RILEM Bookseries

Eduardo B. Pereira
Joaquim A. O. Barros
Fabio P. Figueiredo *Editors*

Proceedings of the 3rd RILEM Spring Convention and Conference (RSCC2020)

Volume 1: Strategies for a Resilient Built Environment

Springer

Proceedings of the 3rd RILEM Spring Convention and Conference (RSCC2020)

RILEM BOOKSERIES

Volume 32

RILEM, The International Union of Laboratories and Experts in Construction Materials, Systems and Structures, founded in 1947, is a non-governmental scientific association whose goal is to contribute to progress in the construction sciences, techniques and industries, essentially by means of the communication it fosters between research and practice. RILEM's focus is on construction materials and their use in building and civil engineering structures, covering all phases of the building process from manufacture to use and recycling of materials. More information on RILEM and its previous publications can be found on www.RILEM.net.

Indexed in SCOPUS, Google Scholar and SpringerLink.

More information about this series at http://www.springer.com/series/8781

Eduardo B. Pereira · Joaquim A. O. Barros ·
Fabio P. Figueiredo
Editors

Proceedings of the 3rd RILEM Spring Convention and Conference (RSCC2020)

Volume 1: Strategies for a Resilient Built Environment

Springer

Editors
Eduardo B. Pereira
ISISE, Civil Engineering
University of Minho
Guimarães, Portugal

Joaquim A. O. Barros
ISISE, Civil Engineering
University of Minho
Guimarães, Portugal

Fabio P. Figueiredo
ISISE, Civil Engineering
University of Minho
Guimarães, Portugal

ISSN 2211-0844 ISSN 2211-0852 (electronic)
RILEM Bookseries
ISBN 978-3-030-76546-0 ISBN 978-3-030-76547-7 (eBook)
https://doi.org/10.1007/978-3-030-76547-7

This Springer imprint is published by the registered company Springer Nature Switzerland AG
The registered company address is: Gewerbestrasse 11, 6330 Cham, Switzerland

Committee

Executive Chair
Eduardo B. Pereira, ISISE, University of Minho, Portugal

Vice-chair
Fabio P. Figueiredo

Honorary Chair
Joaquim A. O. Barros

Topic 1: Strategies for a Resilient Built Environment

Topic Lead

Daman Panesar, University of Toronto, Canada

Topic Scientific Committee

Cise Unluer, Nanyang Technological University, Singapore
Cristina Zanotti, The University of British Columbia, Canada
Daniel Straub, Technical Univeristy of Munich, Germany
Fausto Minelli, University of Brescia, Italy
Guillaume Habert, ETH Zurich, Switzerland
Manu Santhanam, IIT Madras, Chennai-India
Miguel Ferreira, VTT Technical Research Centre of Finland, Finland
Antonio Caggiano, Darmstadt University of Technology, Germany
Carlos Bettencourt, LNEC, Portugal
Carlos Chastre Rodrigues, Universidade Nova de Lisboa, Portugal

Daniel Oliveira, University of Minho, Portugal
Jorge Branco, University of Minho, Portugal
José Matos, University of Minho, Portugal
Klaas van Breugel, Delft TU, Netherlands
Luc Tarweve, University of Ghent, Belgium
Marko Bartolac, University of Zagreb, Croacia
Mette Geiker, Norwegian University of Science and Technology, Norway
Paulo Cachim, Universidade de Aveiro, Portugal

Preface

The RILEM Spring Convention and Conference 2020 (RSCC2020) adopted as theme 'Ambitioning a sustainable future for built environment: comprehensive strategies for unprecedented challenges'. Current challenges posed to the built environment are extremely demanding and generate great concern. The individuals of a growing global population consume resources at increasing and unsustainable paces, with irrecoverable damage to the planet systems. It is clear that the current development models are not sustainable and require committed and common action. Extreme events, as a consequence of global changes, are also more frequent and lead to unprecedented devastation and disruptions. The theme of RSCC2020 was even premonitory, with an event confronted with an exceptional pandemic that tested the RILEM community to its essence. The difficulties were many, but insignificant when compared to what the future holds. Our society is facing an unprecedented challenge, perhaps the greatest of our century, and it should make us consider to which extent our action on the planet is the cause, as a driver of change.

It is unquestionable that there is an urgent need to intensify this debate, fostering a comprehensive roadmap of actions that lead to sustainable development paths. In this context, the main objective of RSCC2020 was to contribute to preparing the new generation of materials and structures for future environmental requirements and societal challenges. Additionally, RSCC2020 also aimed at Identifying and disseminating innovative technologies for more efficient and less resource-intensive construction and maintenance.

The topic 'Strategies for a Resilient Built Environment', to which this volume is dedicated, covered the different aspects related to current and emerging approaches that lead to an optimised design and maintenance of constructions and systems. It included also the development of service life models and life cycle design, in order to maximise longevity and service requirements while minimising the environmental impact of constructions and systems. The analysis and design of larger systems, such as communities, cities or regions, aiming at reducing risk and increasing resilience were also part of this topic. The following subtopics were covered: *resilience and robustness of the built environment and communities at local and global scales; risk-based inspection and maintenance; life cycle analysis*

and service models; performance-based design; improved design strategies by integrating materials and structures. Within this topic, attendees from thirteen countries presented 27 papers.

The editors would like to acknowledge the authors for their outstanding commitment and persistency, for their participation under unprecedented circumstances, during the outbreak of a pandemic without memory. Your contribution was critical; your efforts were very much appreciated!

Guimarães, Portugal

Eduardo B. Pereira
Joaquim A. O. Barros
Fabio P. Figueiredo

Contents

RILEM Publications

The following list is presenting the global offer of RILEM Publications, sorted by series. Each publication is available in printed version and/or in online version.

RILEM Proceedings (PRO)

PRO 1: Durability of High Performance Concrete (ISBN: 2-912143-03-9; e-ISBN: 2-351580-12-5; e-ISBN: 2351580125); *Ed. H. Sommer*

PRO 2: Chloride Penetration into Concrete (ISBN: 2-912143-00-04; e-ISBN: 2912143454); *Eds. L.-O. Nilsson and J.-P. Ollivier*

PRO 3: Evaluation and Strengthening of Existing Masonry Structures (ISBN: 2-912143-02-0; e-ISBN: 2351580141); *Eds. L. Binda and C. Modena*

PRO 4: Concrete: From Material to Structure (ISBN: 2-912143-04-7; e-ISBN: 2351580206); *Eds. J.-P. Bournazel and Y. Malier*

PRO 5: The Role of Admixtures in High Performance Concrete (ISBN: 2-912143-05-5; e-ISBN: 2351580214); *Eds. J. G. Cabrera and R. Rivera-Villarreal*

PRO 6: High Performance Fiber Reinforced Cement Composites—HPFRCC 3 (ISBN: 2-912143-06-3; e-ISBN: 2351580222); *Eds. H. W. Reinhardt and A. E. Naaman*

PRO 7: 1st International RILEM Symposium on Self-Compacting Concrete (ISBN: 2-912143-09-8; e-ISBN: 2912143721); *Eds. Å. Skarendahl and Ö. Petersson*

PRO 8: International RILEM Symposium on Timber Engineering (ISBN: 2-912143-10-1; e-ISBN: 2351580230); *Ed. L. Boström*

PRO 9: 2nd International RILEM Symposium on Adhesion between Polymers and Concrete ISAP '99 (ISBN: 2-912143-11-X; e-ISBN: 2351580249); *Eds. Y. Ohama and M. Puterman*

PRO 10: 3rd International RILEM Symposium on Durability of Building and Construction Sealants (ISBN: 2-912143-13-6; e-ISBN: 2351580257); *Ed. A. T. Wolf*

PRO 11: 4th International RILEM Conference on Reflective Cracking in Pavements (ISBN: 2-912143-14-4; e-ISBN: 2351580265); *Eds. A. O. Abd El Halim, D. A. Taylor and El H. H. Mohamed*

PRO 12: International RILEM Workshop on Historic Mortars: Characteristics and Tests (ISBN: 2-912143-15-2; e-ISBN: 2351580273); *Eds. P. Bartos, C. Groot and J. J. Hughes*

PRO 13: 2nd International RILEM Symposium on Hydration and Setting (ISBN: 2-912143-16-0; e-ISBN: 2351580281); *Ed. A. Nonat*

PRO 14: Integrated Life-Cycle Design of Materials and Structures—ILCDES 2000 (ISBN: 951-758-408-3; e-ISBN: 235158029X); (ISSN: 0356-9403); *Ed. S. Sarja*

PRO 15: Fifth RILEM Symposium on Fibre-Reinforced Concretes (FRC)—BEFIB'2000 (ISBN: 2-912143-18-7; e-ISBN: 291214373X); *Eds. P. Rossi and G. Chanvillard*

PRO 16: Life Prediction and Management of Concrete Structures (ISBN: 2-912143-19-5; e-ISBN: 2351580303); *Ed. D. Naus*

PRO 17: Shrinkage of Concrete—Shrinkage 2000 (ISBN: 2-912143-20-9; e-ISBN: 2351580311); *Eds. V. Baroghel-Bouny and P.-C. Aïtcin*

PRO 18: Measurement and Interpretation of the On-Site Corrosion Rate (ISBN: 2-912143-21-7; e-ISBN: 235158032X); *Eds. C. Andrade, C. Alonso, J. Fullea, J. Polimon and J. Rodriguez*

PRO 19: Testing and Modelling the Chloride Ingress into Concrete (ISBN: 2-912143-22-5; e-ISBN: 2351580338); *Eds. C. Andrade and J. Kropp*

PRO 20: 1st International RILEM Workshop on Microbial Impacts on Building Materials (CD 02) (e-ISBN 978-2-35158-013-4); *Ed. M. Ribas Silva*

PRO 21: International RILEM Symposium on Connections between Steel and Concrete (ISBN: 2-912143-25-X; e-ISBN: 2351580346); *Ed. R. Eligehausen*

PRO 22: International RILEM Symposium on Joints in Timber Structures (ISBN: 2-912143-28-4; e-ISBN: 2351580354); *Eds. S. Aicher and H.-W. Reinhardt*

PRO 23: International RILEM Conference on Early Age Cracking in Cementitious Systems (ISBN: 2-912143-29-2; e-ISBN: 2351580362); *Eds. K. Kovler and A. Bentur*

PRO 24: 2nd International RILEM Workshop on Frost Resistance of Concrete (ISBN: 2-912143-30-6; e-ISBN: 2351580370); *Eds. M. J. Setzer, R. Auberg and H.-J. Keck*

PRO 25: International RILEM Workshop on Frost Damage in Concrete (ISBN: 2-912143-31-4; e-ISBN: 2351580389); *Eds. D. J. Janssen, M. J. Setzer and M. B. Snyder*

PRO 26: International RILEM Workshop on On-Site Control and Evaluation of Masonry Structures (ISBN: 2-912143-34-9; e-ISBN: 2351580141); *Eds. L. Binda and R. C. de Vekey*

PRO 27: International RILEM Symposium on Building Joint Sealants (CD03; e-ISBN: 235158015X); *Ed. A. T. Wolf*

PRO 28: 6th International RILEM Symposium on Performance Testing and Evaluation of Bituminous Materials—PTEBM'03 (ISBN: 2-912143-35-7; e-ISBN: 978-2-912143-77-8); *Ed. M. N. Partl*

PRO 29: 2nd International RILEM Workshop on Life Prediction and Ageing Management of Concrete Structures (ISBN: 2-912143-36-5; e-ISBN: 2912143780); *Ed. D. J. Naus*

PRO 30: 4th International RILEM Workshop on High Performance Fiber Reinforced Cement Composites—HPFRCC 4 (ISBN: 2-912143-37-3; e-ISBN: 2912143799); *Eds. A. E. Naaman and H. W. Reinhardt*

PRO 31: International RILEM Workshop on Test and Design Methods for Steel Fibre Reinforced Concrete: Background and Experiences (ISBN: 2-912143-38-1; e-ISBN: 2351580168); *Eds. B. Schnütgen and L. Vandewalle*

PRO 32: International Conference on Advances in Concrete and Structures 2 vol. (ISBN (set): 2-912143-41-1; e-ISBN: 2351580176); *Eds. Ying-shu Yuan, Surendra P. Shah and Heng-lin Lü*

PRO 33: 3rd International Symposium on Self-Compacting Concrete (ISBN: 2-912143-42-X; e-ISBN: 2912143713); *Eds. Ó. Wallevik and I. Níelsson*

PRO 34: International RILEM Conference on Microbial Impact on Building Materials (ISBN: 2-912143-43-8; e-ISBN: 2351580184); *Ed. M. Ribas Silva*

PRO 35: International RILEM TC 186-ISA on Internal Sulfate Attack and Delayed Ettringite Formation (ISBN: 2-912143-44-6; e-ISBN: 2912143802); *Eds. K. Scrivener and J. Skalny*

PRO 36: International RILEM Symposium on Concrete Science and Engineering —A Tribute to Arnon Bentur (ISBN: 2-912143-46-2; e-ISBN: 2912143586); *Eds. K. Kovler, J. Marchand, S. Mindess and J. Weiss*

PRO 37: 5th International RILEM Conference on Cracking in Pavements—Mitigation, Risk Assessment and Prevention (ISBN: 2-912143-47-0; e-ISBN: 2912143764); *Eds. C. Petit, I. Al-Qadi and A. Millien*

PRO 38: 3rd International RILEM Workshop on Testing and Modelling the Chloride Ingress into Concrete (ISBN: 2-912143-48-9; e-ISBN: 2912143578); *Eds. C. Andrade and J. Kropp*

PRO 39: 6th International RILEM Symposium on Fibre-Reinforced Concretes—BEFIB 2004 (ISBN: 2-912143-51-9; e-ISBN: 2912143748); *Eds. M. Di Prisco, R. Felicetti and G. A. Plizzari*

PRO 40: International RILEM Conference on the Use of Recycled Materials in Buildings and Structures (ISBN: 2-912143-52-7; e-ISBN: 2912143756); *Eds. E. Vázquez, Ch. F. Hendriks and G. M. T. Janssen*

PRO 41: RILEM International Symposium on Environment-Conscious Materials and Systems for Sustainable Development (ISBN: 2-912143-55-1; e-ISBN: 2912143640); *Eds. N. Kashino and Y. Ohama*

PRO 42: SCC'2005—China: 1st International Symposium on Design, Performance and Use of Self-Consolidating Concrete (ISBN: 2-912143-61-6; e-ISBN: 2912143624); *Eds. Zhiwu Yu, Caijun Shi, Kamal Henri Khayat and Youjun Xie*

PRO 43: International RILEM Workshop on Bonded Concrete Overlays (e-ISBN: 2-912143-83-7); *Eds. J. L. Granju and J. Silfwerbrand*

PRO 44: 2nd International RILEM Workshop on Microbial Impacts on Building Materials (CD11) (e-ISBN: 2-912143-84-5); *Ed. M. Ribas Silva*

PRO 45: 2nd International Symposium on Nanotechnology in Construction, Bilbao (ISBN: 2-912143-87-X; e-ISBN: 2912143888); *Eds. Peter J. M. Bartos, Yolanda de Miguel and Antonio Porro*

PRO 46: Concrete Life'06—International RILEM-JCI Seminar on Concrete Durability and Service Life Planning: Curing, Crack Control, Performance in Harsh Environments (ISBN: 2-912143-89-6; e-ISBN: 291214390X); *Ed. K. Kovler*

PRO 47: International RILEM Workshop on Performance Based Evaluation and Indicators for Concrete Durability (ISBN: 978-2-912143-95-2; e-ISBN: 9782912143969); *Eds. V. Baroghel-Bouny, C. Andrade, R. Torrent and K. Scrivener*

PRO 48: 1st International RILEM Symposium on Advances in Concrete through Science and Engineering (e-ISBN: 2-912143-92-6); *Eds. J. Weiss, K. Kovler, J. Marchand, and S. Mindess*

PRO 49: International RILEM Workshop on High Performance Fiber Reinforced Cementitious Composites in Structural Applications (ISBN: 2-912143-93-4; e-ISBN: 2912143942); *Eds. G. Fischer and V. C. Li*

PRO 50: 1st International RILEM Symposium on Textile Reinforced Concrete (ISBN: 2-912143-97-7; e-ISBN: 2351580087); *Eds. Josef Hegger, Wolfgang Brameshuber and Norbert Will*

PRO 51: 2nd International Symposium on Advances in Concrete through Science and Engineering (ISBN: 2-35158-003-6; e-ISBN: 2-35158-002-8); *Eds. J. Marchand, B. Bissonnette, R. Gagné, M. Jolin and F. Paradis*

PRO 52: Volume Changes of Hardening Concrete: Testing and Mitigation (ISBN: 2-35158-004-4; e-ISBN: 2-35158-005-2); *Eds. O. M. Jensen, P. Lura and K. Kovler*

PRO 53: High Performance Fiber Reinforced Cement Composites—HPFRCC5 (ISBN: 978-2-35158-046-2; e-ISBN: 978-2-35158-089-9); *Eds. H. W. Reinhardt and A. E. Naaman*

PRO 54: 5th International RILEM Symposium on Self-Compacting Concrete (ISBN: 978-2-35158-047-9; e-ISBN: 978-2-35158-088-2); *Eds. G. De Schutter and V. Boel*

PRO 55: International RILEM Symposium Photocatalysis, Environment and Construction Materials (ISBN: 978-2-35158-056-1; e-ISBN: 978-2-35158-057-8); *Eds. P. Baglioni and L. Cassar*

PRO 56: International RILEM Workshop on Integral Service Life Modelling of Concrete Structures (ISBN 978-2-35158-058-5; e-ISBN: 978-2-35158-090-5); *Eds. R. M. Ferreira, J. Gulikers and C. Andrade*

PRO 57: RILEM Workshop on Performance of cement-based materials in aggressive aqueous environments (e-ISBN: 978-2-35158-059-2); *Ed. N. De Belie*

PRO 58: International RILEM Symposium on Concrete Modelling—CONMOD'08 (ISBN: 978-2-35158-060-8; e-ISBN: 978-2-35158-076-9); *Eds. E. Schlangen and G. De Schutter*

PRO 59: International RILEM Conference on On Site Assessment of Concrete, Masonry and Timber Structures—SACoMaTiS 2008 (ISBN set: 978-2-35158-061-5; e-ISBN: 978-2-35158-075-2); *Eds. L. Binda, M. di Prisco and R. Felicetti*

PRO 60: Seventh RILEM International Symposium on Fibre Reinforced Concrete: Design and Applications—BEFIB 2008 (ISBN: 978-2-35158-064-6; e-ISBN: 978-2-35158-086-8); *Ed. R. Gettu*

PRO 61: 1st International Conference on Microstructure Related Durability of Cementitious Composites 2 vol., (ISBN: 978-2-35158-065-3; e-ISBN: 978-2-35158-084-4); *Eds. W. Sun, K. van Breugel, C. Miao, G. Ye and H. Chen*

PRO 62: NSF/ RILEM Workshop: In-situ Evaluation of Historic Wood and Masonry Structures (e-ISBN: 978-2-35158-068-4); *Eds. B. Kasal, R. Anthony and M. Drdácký*

PRO 63: Concrete in Aggressive Aqueous Environments: Performance, Testing and Modelling, 2 vol., (ISBN: 978-2-35158-071-4; e-ISBN: 978-2-35158-082-0); *Eds. M. G. Alexander and A. Bertron*

PRO 64: Long Term Performance of Cementitious Barriers and Reinforced Concrete in Nuclear Power Plants and Waste Management—NUCPERF 2009 (ISBN: 978-2-35158-072-1; e-ISBN: 978-2-35158-087-5); *Eds. V. L'Hostis, R. Gens and C. Gallé*

PRO 65: Design Performance and Use of Self-consolidating Concrete—SCC'2009 (ISBN: 978-2-35158-073-8; e-ISBN: 978-2-35158-093-6); *Eds. C. Shi, Z. Yu, K. H. Khayat and P. Yan*

PRO 66: 2nd International RILEM Workshop on Concrete Durability and Service Life Planning—ConcreteLife'09 (ISBN: 978-2-35158-074-5; ISBN: 978-2-35158-074-5); *Ed. K. Kovler*

PRO 67: Repairs Mortars for Historic Masonry (e-ISBN: 978-2-35158-083-7); *Ed. C. Groot*

PRO 68: Proceedings of the 3rd International RILEM Symposium on 'Rheology of Cement Suspensions such as Fresh Concrete (ISBN 978-2-35158-091-2; e-ISBN: 978-2-35158-092-9); *Eds. O. H. Wallevik, S. Kubens and S. Oesterheld*

PRO 69: 3rd International PhD Student Workshop on 'Modelling the Durability of Reinforced Concrete (ISBN: 978-2-35158-095-0); *Eds. R. M. Ferreira, J. Gulikers and C. Andrade*

PRO 70: 2nd International Conference on 'Service Life Design for Infrastructure' (ISBN set: 978-2-35158-096-7, e-ISBN: 978-2-35158-097-4); *Eds. K. van Breugel, G. Ye and Y. Yuan*

PRO 71: Advances in Civil Engineering Materials—The 50-year Teaching Anniversary of Prof. Sun Wei' (ISBN: 978-2-35158-098-1; e-ISBN: 978-2-35158-099-8); *Eds. C. Miao, G. Ye and H. Chen*

PRO 72: First International Conference on 'Advances in Chemically-Activated Materials—CAM'2010' (2010), 264 pp., ISBN: 978-2-35158-101-8; e-ISBN: 978-2-35158-115-5; *Eds. Caijun Shi and Xiaodong Shen*

PRO 73: 2nd International Conference on 'Waste Engineering and Management—ICWEM 2010' (2010), 894 pp., ISBN: 978-2-35158-102-5; e-ISBN: 978-2-35158-103-2, *Eds. J. Zh. Xiao, Y. Zhang, M. S. Cheung and R. Chu*

PRO 74: International RILEM Conference on 'Use of Superabsorsorbent Polymers and Other New Addditives in Concrete' (2010) 374 pp., ISBN: 978-2-35158-104-9; e-ISBN: 978-2-35158-105-6; *Eds. O.M. Jensen, M.T. Hasholt, and S. Laustsen*

PRO 75: International Conference on 'Material Science—2nd ICTRC—Textile Reinforced Concrete—Theme 1' (2010) 436 pp., ISBN: 978-2-35158-106-3; e-ISBN: 978-2-35158-107-0; *Ed. W. Brameshuber*

PRO 76: International Conference on 'Material Science—HetMat—Modelling of Heterogeneous Materials—Theme 2' (2010) 255 pp., ISBN: 978-2-35158-108-7; e-ISBN: 978-2-35158-109-4; *Ed. W. Brameshuber*

PRO 77: International Conference on 'Material Science—AdIPoC—Additions Improving Properties of Concrete—Theme 3' (2010) 459 pp., ISBN: 978-2-35158-110-0; e-ISBN: 978-2-35158-111-7; *Ed. W. Brameshuber*

PRO 78: 2nd Historic Mortars Conference and RILEM TC 203-RHM Final Workshop—HMC2010 (2010) 1416 pp., e-ISBN: 978-2-35158-112-4; *Eds. J. Válek, C. Groot and J. J. Hughes*

PRO 79: International RILEM Conference on Advances in Construction Materials Through Science and Engineering (2011) 213 pp., ISBN: 978-2-35158-116-2, e-ISBN: 978-2-35158-117-9; *Eds. Christopher Leung and K.T. Wan*

PRO 80: 2nd International RILEM Conference on Concrete Spalling due to Fire Exposure (2011) 453 pp., ISBN: 978-2-35158-118-6; e-ISBN: 978-2-35158-119-3; *Eds. E.A.B. Koenders and F. Dehn*

PRO 81: 2nd International RILEM Conference on Strain Hardening Cementitious Composites (SHCC2-Rio) (2011) 451 pp., ISBN: 978-2-35158-120-9; e-ISBN: 978-2-35158-121-6; *Eds. R.D. Toledo Filho, F.A. Silva, E.A.B. Koenders and E.M. R. Fairbairn*

PRO 82: 2nd International RILEM Conference on Progress of Recycling in the Built Environment (2011) 507 pp., e-ISBN: 978-2-35158-122-3; *Eds. V.M. John, E. Vazquez, S.C. Angulo and C. Ulsen*

PRO 83: 2nd International Conference on Microstructural-related Durability of Cementitious Composites (2012) 250 pp., ISBN: 978-2-35158-129-2; e-ISBN: 978-2-35158-123-0; *Eds. G. Ye, K. van Breugel, W. Sun and C. Miao*

PRO 84: CONSEC13—Seventh International Conference on Concrete under Severe Conditions—Environment and Loading (2013) 1930 pp., ISBN: 978-2-35158-124-7; e-ISBN: 978-2- 35158-134-6; *Eds. Z.J. Li, W. Sun, C.W. Miao, K. Sakai, O.E. Gjorv and N. Banthia*

PRO 85: RILEM-JCI International Workshop on Crack Control of Mass Concrete and Related issues concerning Early-Age of Concrete Structures—ConCrack 3—Control of Cracking in Concrete Structures 3 (2012) 237 pp., ISBN: 978-2-35158-125-4; e-ISBN: 978-2-35158-126-1; *Eds. F. Toutlemonde and J.-M. Torrenti*

PRO 86: International Symposium on Life Cycle Assessment and Construction (2012) 414 pp., ISBN: 978-2-35158-127-8, e-ISBN: 978-2-35158-128-5; *Eds. A. Ventura and C. de la Roche*

PRO 87: UHPFRC 2013—RILEM-fib-AFGC International Symposium on Ultra-High Performance Fibre-Reinforced Concrete (2013), ISBN: 978-2-35158-130-8, e-ISBN: 978-2-35158-131-5; *Eds. F. Toutlemonde*

PRO 88: 8th RILEM International Symposium on Fibre Reinforced Concrete (2012) 344 pp., ISBN: 978-2-35158-132-2; e-ISBN: 978-2-35158-133-9; *Eds. Joaquim A.O. Barros*

PRO 89: RILEM International workshop on performance-based specification and control of concrete durability (2014) 678 pp., ISBN: 978-2-35158-135-3; e-ISBN: 978-2-35158-136-0; *Eds. D. Bjegović, H. Beushausen and M. Serdar*

PRO 90: 7th RILEM International Conference on Self-Compacting Concrete and of the 1st RILEM International Conference on Rheology and Processing of Construction Materials (2013) 396 pp., ISBN: 978-2-35158-137-7; e-ISBN: 978-2-35158-138-4; *Eds. Nicolas Roussel and Hela Bessaies-Bey*

PRO 91: CONMOD 2014—RILEM International Symposium on Concrete Modelling (2014), ISBN: 978-2-35158-139-1; e-ISBN: 978-2-35158-140-7; *Eds. Kefei Li, Peiyu Yan and Rongwei Yang*

PRO 92: CAM 2014—2nd International Conference on advances in chemically-activated materials (2014) 392 pp., ISBN: 978-2-35158-141-4; e-ISBN: 978-2-35158-142-1; *Eds. Caijun Shi and Xiadong Shen*

PRO 93: SCC 2014—3rd International Symposium on Design, Performance and Use of Self-Consolidating Concrete (2014) 438 pp., ISBN: 978-2-35158-143-8; e-ISBN: 978-2-35158-144-5; *Eds. Caijun Shi, Zhihua Ou and Kamal H. Khayat*

PRO 94 (online version): HPFRCC-7—7th RILEM conference on High performance fiber reinforced cement composites (2015), e-ISBN: 978-2-35158-146-9; *Eds. H.W. Reinhardt, G.J. Parra-Montesinos and H. Garrecht*

PRO 95: International RILEM Conference on Application of superabsorbent polymers and other new admixtures in concrete construction (2014), ISBN: 978-2-35158-147-6; e-ISBN: 978-2-35158-148-3; *Eds. Viktor Mechtcherine and Christof Schroefl*

PRO 96 (online version): XIII DBMC: XIII International Conference on Durability of Building Materials and Components (2015), e-ISBN: 978-2-35158-149-0; *Eds. M. Quattrone and V.M. John*

PRO 97: SHCC3—3rd International RILEM Conference on Strain Hardening Cementitious Composites (2014), ISBN: 978-2-35158-150-6; e-ISBN: 978-2-35158-151-3; *Eds. E. Schlangen, M.G. Sierra Beltran, M. Lukovic and G. Ye*

PRO 98: FERRO-11—11th International Symposium on Ferrocement and 3rd ICTRC—International Conference on Textile Reinforced Concrete (2015), ISBN: 978-2-35158-152-0; e-ISBN: 978-2-35158-153-7; *Ed. W. Brameshuber*

PRO 99 (online version): ICBBM 2015—1st International Conference on Bio-Based Building Materials (2015), e-ISBN: 978-2-35158-154-4; *Eds. S. Amziane and M. Sonebi*

PRO 100: SCC16—RILEM Self-Consolidating Concrete Conference (2016), ISBN: 978-2-35158-156-8; e-ISBN: 978-2-35158-157-5; *Ed. Kamal H. Kayat*

PRO 101 (online version): III Progress of Recycling in the Built Environment (2015), e-ISBN: 978-2-35158-158-2; *Eds I. Martins, C. Ulsen and S. C. Angulo*

PRO 102 (online version): RILEM Conference on Microorganisms-Cementitious Materials Interactions (2016), e-ISBN: 978-2-35158-160-5; *Eds. Alexandra Bertron, Henk Jonkers and Virginie Wiktor*

PRO 103 (online version): ACESC'16—Advances in Civil Engineering and Sustainable Construction (2016), e-ISBN: 978-2-35158-161-2; *Eds. T.Ch. Madhavi, G. Prabhakar, Santhosh Ram and P.M. Rameshwaran*

PRO 104 (online version): SSCS'2015—Numerical Modeling—Strategies for Sustainable Concrete Structures (2015), e-ISBN: 978-2-35158-162-9

PRO 105: 1st International Conference on UHPC Materials and Structures (2016), ISBN: 978-2-35158-164-3; e-ISBN: 978-2-35158-165-0

PRO 106: AFGC-ACI-fib-RILEM International Conference on Ultra-High-Performance Fibre-Reinforced Concrete—UHPFRC 2017 (2017), ISBN: 978-2-35158-166-7; e-ISBN: 978-2-35158-167-4; *Eds. François Toutlemonde and Jacques Resplendino*

PRO 107 (online version): XIV DBMC—14th International Conference on Durability of Building Materials and Components (2017), e-ISBN: 978-2-35158-159-9; *Eds. Geert De Schutter, Nele De Belie, Arnold Janssens and Nathan Van Den Bossche*

PRO 108: MSSCE 2016—Innovation of Teaching in Materials and Structures (2016), ISBN: 978-2-35158-178-0; e-ISBN: 978-2-35158-179-7; *Ed. Per Goltermann*

PRO 109 (2 volumes): MSSCE 2016—Service Life of Cement-Based Materials and Structures (2016), ISBN Vol. 1: 978-2-35158-170-4; Vol. 2: 978-2-35158-171-4; Set Vol. 1&2: 978-2-35158-172-8; e-ISBN : 978-2-35158-173-5; *Eds. Miguel Azenha, Ivan Gabrijel, Dirk Schlicke, Terje Kanstad and Ole Mejlhede Jensen*

PRO 110: MSSCE 2016—Historical Masonry (2016), ISBN: 978-2-35158-178-0; e-ISBN: 978-2-35158-179-7; *Eds. Inge Rörig-Dalgaard and Ioannis Ioannou*

PRO 111: MSSCE 2016—Electrochemistry in Civil Engineering (2016); ISBN: 978-2-35158-176-6; e-ISBN: 978-2-35158-177-3; *Ed. Lisbeth M. Ottosen*

PRO 112: MSSCE 2016—Moisture in Materials and Structures (2016), ISBN: 978-2-35158-178-0; e-ISBN: 978-2-35158-179-7; *Eds. Kurt Kielsgaard Hansen, Carsten Rode and Lars-Olof Nilsson*

PRO 113: MSSCE 2016—Concrete with Supplementary Cementitious Materials (2016), ISBN: 978-2-35158-178-0; e-ISBN: 978-2-35158-179-7; *Eds. Ole Mejlhede Jensen, Konstantin Kovler and Nele De Belie*

PRO 114: MSSCE 2016—Frost Action in Concrete (2016), ISBN: 978-2-35158-182-7; e-ISBN: 978-2-35158-183-4; *Eds. Marianne Tange Hasholt, Katja Fridh and R. Doug Hooton*

PRO 115: MSSCE 2016—Fresh Concrete (2016), ISBN: 978-2-35158-184-1; e-ISBN: 978-2-35158-185-8; *Eds. Lars N. Thrane, Claus Pade, Oldrich Svec and Nicolas Roussel*

PRO 116: BEFIB 2016—9th RILEM International Symposium on Fiber Reinforced Concrete (2016), ISBN: 978-2-35158-187-2; e-ISBN: 978-2-35158-186-5; *Eds. N. Banthia, M. di Prisco and S. Soleimani-Dashtaki*

PRO 117: 3rd International RILEM Conference on Microstructure Related Durability of Cementitious Composites (2016), ISBN: 978-2-35158-188-9; e-ISBN: 978-2-35158-189-6; *Eds. Changwen Miao, Wei Sun, Jiaping Liu, Huisu Chen, Guang Ye and Klaas van Breugel*

PRO 118 (4 volumes): International Conference on Advances in Construction Materials and Systems (2017), ISBN Set: 978-2-35158-190-2; Vol. 1: 978-2-35158-193-3; Vol. 2: 978-2-35158-194-0; Vol. 3: ISBN:978-2-35158-195-7; Vol. 4: ISBN:978-2-35158-196-4; e-ISBN: 978-2-35158-191-9; *Ed. Manu Santhanam*

PRO 119 (online version): ICBBM 2017—Second International RILEM Conference on Bio-based Building Materials, (2017), e-ISBN: 978-2-35158-192-6; *Ed. Sofiane Amziane*

PRO 120 (2 volumes): EAC-02—2nd International RILEM/COST Conference on Early Age Cracking and Serviceability in Cement-based Materials and Structures, (2017), Vol. 1: 978-2-35158-199-5, Vol. 2: 978-2-35158-200-8, Set: 978-2-35158-197-1, e-ISBN: 978-2-35158-198-8; *Eds. Stéphanie Staquet and Dimitrios Aggelis*

PRO 121 (2 volumes): SynerCrete18: Interdisciplinary Approaches for Cementbased Materials and Structural Concrete: Synergizing Expertise and Bridging Scales of Space and Time, (2018), Set: 978-2-35158-202-2, Vol.1: 978-2-35158-211-4, Vol.2: 978-2-35158-212-1, e-ISBN: 978-2-35158-203-9; *Eds. Miguel Azenha, Dirk Schlicke, Farid Benboudjema, Agnieszka Knoppik*

PRO 122: SCC'2018 China—Fourth International Symposium on Design, Performance and Use of Self-Consolidating Concrete, (2018), ISBN:

978-2-35158-204-6, e-ISBN: 978-2-35158-205-3; *Eds. C. Shi, Z. Zhang, K. H. Khayat*

PRO 123: Final Conference of RILEM TC 253-MCI: Microorganisms-Cementitious Materials Interactions (2018), Set: 978-2-35158-207-7, Vol.1: 978-2-35158-209-1, Vol.2: 978-2-35158-210-7, e-ISBN: 978-2-35158-206-0; *Ed. Alexandra Bertron*

PRO 124 (online version): Fourth International Conference Progress of Recycling in the Built Environment (2018), e-ISBN: 978-2-35158-208-4; *Eds. Isabel M. Martins, Carina Ulsen, Yury Villagran*

PRO 125 (online version): SLD4—4th International Conference on Service Life Design for Infrastructures (2018), e-ISBN: 978-2-35158-213-8; *Eds. Guang Ye, Yong Yuan, Claudia Romero Rodriguez, Hongzhi Zhang, Branko Savija*

PRO 126: Workshop on Concrete Modelling and Material Behaviour in honor of Professor Klaas van Breugel (2018), ISBN: 978-2-35158-214-5, e-ISBN: 978-2-35158-215-2; *Ed. Guang Ye*

PRO 127 (online version): CONMOD2018—Symposium on Concrete Modelling (2018), e-ISBN: 978-2-35158-216-9; *Eds. Erik Schlangen, Geert de Schutter, Branko Savija, Hongzhi Zhang, Claudia Romero Rodriguez*

PRO 128: SMSS2019—International Conference on Sustainable Materials, Systems and Structures (2019), ISBN: 978-2-35158-217-6, e-ISBN: 978-2-35158-218-3

PRO 129: 2nd International Conference on UHPC Materials and Structures (UHPC2018-China), ISBN: 978-2-35158-219-0, e-ISBN: 978-2-35158-220-6

PRO 130: 5th Historic Mortars Conference (2019), ISBN: 978-2-35158-221-3, e-ISBN: 978-2-35158-222-0; *Eds. José Ignacio Álvarez, José María Fernández, Íñigo Navarro, Adrián Durán, Rafael Sirera*

PRO 131 (online version): 3rd International Conference on Bio-Based Building Materials (ICBBM2019), e-ISBN: 978-2-35158-229-9; *Eds. Mohammed Sonebi, Sofiane Amziane, Jonathan Page*

PRO 132: IRWRMC'18—International RILEM Workshop on Rheological Measurements of Cement-based Materials (2018), ISBN: 978-2-35158-230-5, e-ISBN: 978-2-35158-231-2; *Eds. Chafika Djelal, Yannick Vanhove*

PRO 133 (online version): CO2STO2019—International Workshop CO2 Storage in Concrete (2019), e-ISBN: 978-2-35158-232-9; *Eds. Assia Djerbi, Othman Omikrine-Metalssi, Teddy Fen-Chong*

PRO 134: 3rd ACF/HNU International Conference on UHPC Materials and Structures—UHPC'2020, ISBN: 978-2-35158-233-6, e-ISBN: 978-2-35158-234-3; *Eds. Caijun Shi and Jiaping Liu*

RILEM Reports (REP)

Report 19: Considerations for Use in Managing the Aging of Nuclear Power Plant Concrete Structures (ISBN: 2-912143-07-1); *Ed. D. J. Naus*

Report 20: Engineering and Transport Properties of the Interfacial Transition Zone in Cementitious Composites (ISBN: 2-912143-08-X); *Eds. M. G. Alexander, G. Arliguie, G. Ballivy, A. Bentur and J. Marchand*

Report 21: Durability of Building Sealants (ISBN: 2-912143-12-8); *Ed. A. T. Wolf*

Report 22: Sustainable Raw Materials—Construction and Demolition Waste (ISBN: 2-912143-17-9); *Eds. C. F. Hendriks and H. S. Pietersen*

Report 23: Self-Compacting Concrete state-of-the-art report (ISBN: 2-912143-23-3); *Eds. Å. Skarendahl and Ö. Petersson*

Report 24: Workability and Rheology of Fresh Concrete: Compendium of Tests (ISBN: 2-912143-32-2); *Eds. P. J. M. Bartos, M. Sonebi and A. K. Tamimi*

Report 25: Early Age Cracking in Cementitious Systems (ISBN: 2-912143-33-0); *Ed. A. Bentur*

Report 26: Towards Sustainable Roofing (Joint Committee CIB/RILEM) (CD 07) (e-ISBN 978-2-912143-65-5); *Eds. Thomas W. Hutchinson and Keith Roberts*

Report 27: Condition Assessment of Roofs (Joint Committee CIB/RILEM) (CD 08) (e-ISBN 978-2-912143-66-2); *Ed. CIB W 83/RILEM TC166-RMS*

Report 28: Final report of RILEM TC 167-COM 'Characterisation of Old Mortars with Respect to Their Repair (ISBN: 978-2-912143-56-3); *Eds. C. Groot, G. Ashall and J. Hughes*

Report 29: Pavement Performance Prediction and Evaluation (PPPE): Interlaboratory Tests (e-ISBN: 2-912143-68-3); *Eds. M. Partl and H. Piber*

Report 30: Final Report of RILEM TC 198-URM 'Use of Recycled Materials' (ISBN: 2-912143-82-9; e-ISBN: 2-912143-69-1); *Eds. Ch. F. Hendriks, G. M. T. Janssen and E. Vázquez*

Report 31: Final Report of RILEM TC 185-ATC 'Advanced testing of cement-based materials during setting and hardening' (ISBN: 2-912143-81-0; e-ISBN: 2-912143-70-5); *Eds. H. W. Reinhardt and C. U. Grosse*

Report 32: Probabilistic Assessment of Existing Structures. A JCSS publication (ISBN 2-912143-24-1); *Ed. D. Diamantidis*

Report 33: State-of-the-Art Report of RILEM Technical Committee TC 184-IFE 'Industrial Floors' (ISBN 2-35158-006-0); *Ed. P. Seidler*

Report 34: Report of RILEM Technical Committee TC 147-FMB 'Fracture mechanics applications to anchorage and bond' Tension of Reinforced Concrete Prisms—Round Robin Analysis and Tests on Bond (e-ISBN 2-912143-91-8); *Eds. L. Elfgren and K. Noghabai*

Report 35: Final Report of RILEM Technical Committee TC 188-CSC 'Casting of Self Compacting Concrete' (ISBN 2-35158-001-X; e-ISBN: 2-912143-98-5); *Eds. Å. Skarendahl and P. Billberg*

Report 36: State-of-the-Art Report of RILEM Technical Committee TC 201-TRC 'Textile Reinforced Concrete' (ISBN 2-912143-99-3); *Ed. W. Brameshuber*

Report 37: State-of-the-Art Report of RILEM Technical Committee TC 192-ECM 'Environment-conscious construction materials and systems' (ISBN: 978-2-35158-053-0); *Eds. N. Kashino, D. Van Gemert and K. Imamoto*

Report 38: State-of-the-Art Report of RILEM Technical Committee TC 205-DSC 'Durability of Self-Compacting Concrete' (ISBN: 978-2-35158-048-6); *Eds. G. De Schutter and K. Audenaert*

Report 39: Final Report of RILEM Technical Committee TC 187-SOC 'Experimental determination of the stress-crack opening curve for concrete in tension' (ISBN 978-2-35158-049-3); *Ed. J. Planas*

Report 40: State-of-the-Art Report of RILEM Technical Committee TC 189-NEC 'Non-Destructive Evaluation of the Penetrability and Thickness of the Concrete Cover' (ISBN 978-2-35158-054-7); *Eds. R. Torrent and L. Fernández Luco*

Report 41: State-of-the-Art Report of RILEM Technical Committee TC 196-ICC 'Internal Curing of Concrete' (ISBN 978-2-35158-009-7); *Eds. K. Kovler and O. M. Jensen*

Report 42: 'Acoustic Emission and Related Non-destructive Evaluation Techniques for Crack Detection and Damage Evaluation in Concrete'—Final Report of RILEM Technical Committee 212-ACD (e-ISBN: 978-2-35158-100-1); *Ed. M. Ohtsu*

Report 45: Repair Mortars for Historic Masonry—State-of-the-Art Report of RILEM Technical Committee TC 203-RHM (e-ISBN: 978-2-35158-163-6); *Eds. Paul Maurenbrecher and Caspar Groot*

Report 46: Surface delamination of concrete industrial ffioors and other durability related aspects guide—Report of RILEM Technical Committee TC 268-SIF (e-ISBN: 978-2-35158-201-5); *Ed. Valerie Pollet*

Integrated Model for Predicting the Flexural Capacity of Concrete Elements Reinforced with Non-corrodible Discrete Reinforcements

Tiago Valente, Christoph de Sousa, Inês Costa, Felipe Melo, and Joaquim A. O. Barros

Abstract The present work describes an integrated approach that leads to the development of a new model capable of describing the tensile behavior (mode I) of fiber reinforced concrete (FRC), considering the orientation of the fibers, the fibers segregation along the cross-section of the FRC members and the pullout constitutive model of each fiber bridging the two faces of a crack. The possibility of the numerical model to capture the flexural behavior of non-metallic fiber reinforced concrete members is explored by simulating the response of polypropylene fiber reinforced concrete notched beams submitted to 3-point bending tests.

Keywords Polypropylene fibers · Fiber reinforced concrete · Flexural capacity

1 Introduction

The use of short and randomly distributed fibers increases concrete's post-cracking tensile capacity, its ductility, energy absorption capacity and impact resistance when compared to plain concrete [1, 2]. Additionally, the restrain to crack opening, provided by the different fiber reinforcement mechanisms at fracture, enhances the durability and integrity of cement based materials. The fundamental reinforcement mechanism of fibers consists in the capacity of ensuring relatively high stress transfer between the faces of cracks, by restraining the degeneration of micro-cracks in meso- and macro-cracks, which increases the stiffness and load carrying capacity of concrete structures in their cracking stage, as well as their durability [3–6].

T. Valente · C. de Sousa · I. Costa · F. Melo
CiviTest-Pesquisa de Novos Materiais para a Engenharia Civil, Lda., Vila Nova de Famalicão, Portugal
e-mail: tiagovalente@civitest.com

J. A. O. Barros (✉)
ISISE, Department of Civil Engineering, Structural Division, University of Minho, 4800-058 Guimarães, Portugal
e-mail: barros@civil.uminho.pt

E. B. Pereira et al. (eds.), *Proceedings of the 3rd RILEM Spring Convention and Conference (RSCC 2020)*, RILEM Bookseries 32,
https://doi.org/10.1007/978-3-030-76547-7_1

The fiber contribution after cracking depends mainly on the content of fibers, their orientation and distribution towards the potential cracks [7–10], the material and geometric characteristics of the fibers [11–13], and the quality of the concrete [14], which are designated as the variables that mainly affect the fiber reinforcement mechanisms. The present work presents the main aspects of an integrated model to predict the tensile behavior (mode I) of fiber reinforced concrete (FRC) by considering these variables in the form of a fiber orientation profile model, a fiber segregation model and a fiber pullout constitutive model. It is believed that the followed approach can simulate more realistically the post-cracking response of FRC in comparison to the already available models, e.g. cohesive stress-crack width constitutive law.

Considering that the proposed model has already shown good agreement to simulate the flexural behavior of steel fiber reinforced concrete elements [15], the present work explores the potential of the model to capture the behavior of non-metallic fiber reinforcements, as is the case of polypropylene fibers (PP).

PP fibers have been used mainly in non-structural applications for limiting crack width due to shrinkage effects of cement-based materials. Being non-susceptible to corrosion, PP fibers can also be regarded as viable discrete reinforcement elements for the production of thin concrete elements. The relatively low elasticity modulus, tensile strength and almost frictional-based reinforcing nature of PP fibers have been pointed out as the main arguments for preventing their use in structural applications, as a total or even partial replacement of conventional steel reinforcements. However, significant improvements have been made, not only on the material properties of PP fibers, but also on their surface treatment, that provide the means to develop fiber reinforced concrete (FRC) with toughness levels capable of being used for structural applications, according to the requirements of fib Model Code 2010.

2 Integrated Model for Predicting Flexural Capacity of FRC Structural Elements

In order to predict the flexural capacity of FRC members, a numerical tool was developed that considers the influence of the orientation and segregation of fibers along the cross-section of the FRC members and the pullout constitutive law of each fiber bridging the two faces of a crack.

The integrated model was implemented in *DOCROS*, an already existing software for the analysis of cross-sections of R-FRC members failing in bending [16]. In *DOCROS* a cross-section is discretized in N layers, for which is assigned specific constitutive laws to describe the material behavior of the layers. In this scope, the fiber orientation profile, fiber segregation and fiber pullout constitutive law were coupled to form a new material model to simulate the nonlinear material behavior of FRC.

For the simulation of the tensile behavior of the FRC, a linear elastic stress–strain response was considered, up to tensile strength, f_{ct}, is reached. For the post-cracking

tensile response of FRC, the contribution of the fiber pullout resistance, $P(w)$, was added to the post-cracking residual strength of FRC matrix, $\sigma_{ct}(w)$, namely:

$$\sigma^j = \frac{P^j\left(w^j\right)}{b^j \cdot t^j} + \sigma_{ct}^j\left(w^j\right) \tag{1}$$

where b^j and t^j are, respectively, the width and thickness of the generic jth layer that discretizes the cross-section, and w^j is the crack width at the level of the geometric center of the jth layer.

The adopted stress-crack width relationship of the concrete matrix is based on the model presented in [20].

For the usual fiber dosages used in FRC's, its compressive behavior is similar to the one observed in plain concrete. Therefore, the simulation of the behavior of FRC in compression was done by adopting the model proposed in [17].

2.1 Fiber Orientation Profile Model

The model for predicting the distribution of orientation angles of the fibers, φ_i, is based on the definition of an orientation factor, η. The orientation factor corresponds to the average length of the projection of all fibers crossing a crack plane on its orthogonal direction, divided by the fiber length [18]. The fiber orientation factor can vary between 0.0 and 1.0, corresponding, respectively, to fibers parallel and orthogonal to the analyzed cross-section (herein representing the crack plane) [19]. The fiber orientation factor relates the theoretical number of fibers, N_{th}, contained in the concrete medium with the number of fibers to be encountered in a cross-section, N_f, according to the expression [20]:

$$N_f = N_{th} \cdot \eta = \frac{A_{\text{sec}}}{A_f} \cdot V_f \cdot \eta \tag{2}$$

where A_{sec} is the cross-section area of the FRC element, A_f is the cross sectional area of a fiber, and V_f is the fiber volume dosage.

The fiber orientation profile model is based on the work of [18], where the distribution of the orientation of the fibers in a cross-section is arranged in discrete intervals, $n\Delta\varphi$, and the number of fibers within each orientation angle interval, $N_{f,\overline{\varphi_i}}$ is determined according to the expression:

$$N_{f,\overline{\varphi_i}} = C(\overline{\varphi_i}) \cdot N_f \tag{3}$$

where $C(\overline{\varphi_i})$ is the ratio between the number of fibers within each interval range with a mean orientation angle $\overline{\varphi_i}$ and the total number of fibers in the cross-section. The

parameter $C(\varphi_i)$ can be determined by the expression [18]:

$$C(\overline{\varphi_i}) = f(\overline{\varphi_i}) \cdot F_{RE}(\eta) \tag{4}$$

where $f(\overline{\varphi_i})$ is the frequency of fibers within the interval of orientation angles $\varphi_i \pm \Delta\varphi_i/2$, $\Delta\varphi_i = 90/n\Delta\varphi$, considering a Gaussian law to describe the frequency distribution, and $F_{RE}(\eta)$ is a coefficient to account to the error resultant of adopting discrete ranges of fiber orientation angles rather than considering a continuous function, which is determined with Eq. (5).

$$F_{RE} = \begin{cases} 1.29 - 0.38 \cdot \eta & ; \eta < 0.75 \\ 1.0 & ; \eta \geq 0.75 \end{cases} \tag{5}$$

Based on the orientation factor is possible to determine the average orientation angle of the fibers in the cross-section, φ_m, and the corresponding standard deviation, $\sigma(\varphi_m)$, using the following equations [18]:

$$\varphi_m = \arccos(\eta) \cdot 180/\pi \quad [^\circ] \tag{6}$$

$$\sigma(\varphi_m) = 90 \cdot \eta \cdot (1 - \eta) \quad [^\circ] \tag{7}$$

The methodology adopted to determine the fiber orientation factor, η, is based on the work of Krenchel [20] for stiff fibers. Due to the wall effect on the orientation of the fibers, the cross-section of the FRC member is divided in three zones with different orientation factors (Fig. 1). The fiber orientation factor of the cross-section is determined by the expression:

$$\eta = \frac{\eta_1 \cdot (b - l_f) \cdot (h - l_f) + \eta_2 \cdot l_f \cdot \left[(b - l_f) + (h - l_f)\right] + \eta_3 \cdot l_f^2}{b \cdot h} \tag{8}$$

where l_f is the length of the adopted fiber type, and $\eta_z (z = 1,\ 2,\ 3)$ is the fiber orientation factor for each zone of the cross-section.

The values of the orientation factor for each zone of the cross-section are based on previous research, namely: $\eta_1 = 0.50$ [21, 22]; $\eta_2 = 2/\pi$ [22]; $\eta_3 = 0.84$ [21].

2.2 Fiber Segregation Model

In order to simulate the fiber segregation phenomena that can occur during FRC casting, a segregation model is proposed, that assumes a linear variation of the fiber's distribution along the depth of the cross-section. The model solely defines the segregation factor, ξ, varying between -1.0 and $+1.0$. Considering the thickness

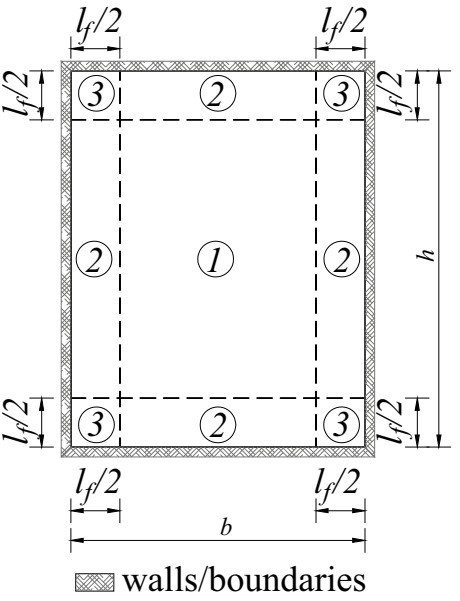

Fig. 1 Zones of cross-section for the determination of the fiber orientation factor due to wall effect

$t^j (j = 1, \ldots, N)$ and depth of the geometric center of each layer of the cross-section $d^j (j = 1, \ldots, N)$, the number of fibers in each layer is determined by the following expression:

$$N_f^j = \left(N_f^{\text{top}} \left(1 - \frac{d^j}{h} \right) + N_f^{\text{bot}} \cdot \frac{d^j}{h} \right) \cdot t^j \; ; \; j = 1, \ldots, N \tag{9}$$

where h is the cross-section height, N_f^{top} and N_f^{bot} are, respectively, the number of fibers at top and bottom faces of the cross-section that are determined according to:

$$N_f^{\text{top}} = \frac{N_f}{h} \cdot (1 - \xi) \tag{10}$$

$$N_f^{\text{bot}} = \frac{N_f}{h} \cdot (1 + \xi) \tag{11}$$

where N_f is the total number of fibers in the cross-section.

For a homogenous distribution of the fibers in the cross-section, the segregation factor assumes a value of $\xi = 0$, and $N_f^{\text{top}} = N_f^{\text{bot}}$. If $\xi = 1.0$ is assumed, $N_f^{\text{top}} = 0$, while $N_f^{\text{bot}} = 0$ if $\xi = -1.0$.

2.3 Fiber Pullout Constitutive Model

The considered fiber pullout constitutive model is based on the Unified Variable Engagement Model (UVEM) proposed by [12, 23, 24] for steel fiber reinforced concrete (SFRC). The UVEM combines Mode I and Mode II fracture process of SFRC. The present section presents the main aspects of the proposed model, while further details can be obtained elsewhere [15].

The proposed model adopts an uniform bond strength, τ_b, along the fiber embedded length that is a function of the slip displacement of the fiber. The adopted bond strength versus slip model ($\tau_{b,0} - \delta$), illustrated in Fig. 2a, is idealized for the pullout response of an aligned fiber ($\varphi = 0°$). The bond strength versus slip model is defined by the following four parameters (Fig. 2a; Eq. 12): the peak bond strength, $\tau_{b,o,p}$; the slip corresponding to the peak bond strength, δ_p; and the exponents α and β, which define the $\tau_{b,0} - \delta$ variation in its pre-peak and post-peak stage.

$$\tau_{b,o} = \begin{cases} \tau_{b0,p} \cdot \left(\frac{\delta}{\delta_p}\right)^{\alpha} & \delta \leq \delta_p \\ \tau_{b0,p} \cdot \left(\frac{\delta}{\delta_p}\right)^{-\beta} & \delta > \delta_p \end{cases} \tag{12}$$

In order to consider the snubbing effect in the pullout resistance of the fiber, the expression presented in [24] is adopted:

$$\tau_b(\delta) = \tau_{b,0}(\delta) + 0.25 \cdot \gamma^3 \tag{13}$$

where γ is the fiber bending angle, being defined as the angle between the fiber longitudinal axis and pullout force direction (Fig. 2b). For Mode I fracture, fiber bending angle is equal to the fiber orientation angle ($\gamma = \varphi$).

The model admits that all the fiber slippage from the matrix occurs from the shorter embedded length of the fiber, and the slip between the longer embedded part of the fiber and its surrounding matrix is negligible. This assumption leads to the

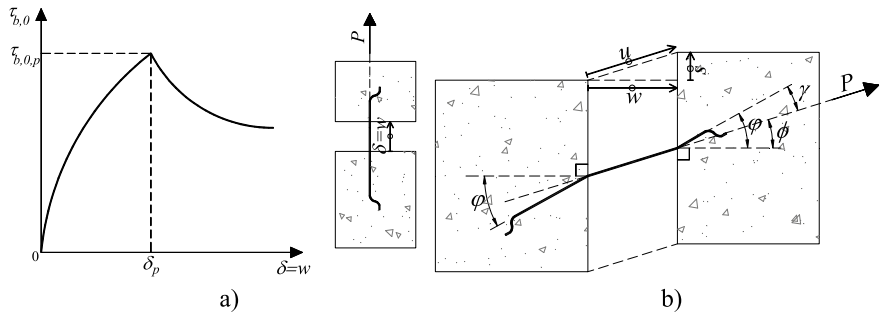

Fig. 2 **a** Idealized bond stress versus slip ($\tau_{b,0} - \delta$) for the pullout response of an aligned fiber. **b** Definition of fiber bending angle, γ

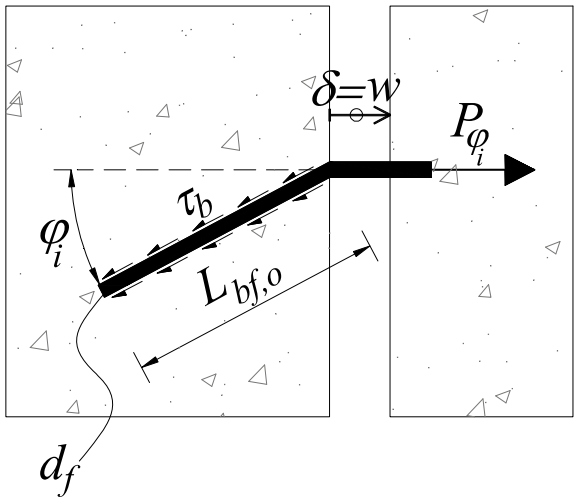

Fig. 3 Pullout force of a fiber with the orientation φ_i

slip of the shorter embedded length being equal to the crack opening displacement of the cimentitious matrix. As illustrated in Fig. 3, the pullout force of a fiber with an orientation angle φ_i, P_{φ_i}, corresponding to a crack opening displacement, w, is equal to:

$$P_{\varphi_i}(w) = \cdot\pi \cdot d_f \cdot \tau_b(\varphi_i, \delta = w) \cdot L_{bf,o}(w) \tag{14}$$

where d_f is the diameter of the fibers; τ_b is the average fiber bond strength determined according to Eq. (13), function of the crack width and orientation angle of the fiber; $L_{bf,o}$ is the fiber embedment length that is equal to its initial value minus the crack opening displacement. For the initial value of the fiber embedment length, which corresponds to a crack width equal to zero ($w = 0$), it is assumed that $L_{bf,o} = l_f/4$ for the shortest embedment side, considering that it has been verified to be the average length of embedment of the fibers according to the work of [25].

During the pullout process, fibers may be susceptible to rupture, particularly in the case of the most inclined fibers. The present model considers that a fiber rupture if the tensile stress, σ_f, reaches the effective ultimate tensile strength of the fiber, $\overline{\sigma_{fu}}$. The effective ultimate tensile strength of the fibers is determined through the expression considered in the UVEM model, namely [24]:

$$\overline{\sigma_{fu}} = \sigma_{fu} \cdot \frac{\pi}{2 \cdot \gamma_{\max}} \tag{15}$$

where σ_{fu} is the fiber tensile strength.

The failure criterion of the fibers with circular (or equivalent circular in case o non perfectly circular, such is the case of the adopted PP fibers in the present work)

cross-section is verified by the following expression:

$$\overline{\sigma_{fu}} \geq \sigma_f = \frac{4 \cdot \tau_b \cdot L_{bf,o}(w)}{d_f} \tag{16}$$

Considering that the cross-section of a FRC member is discretized in N layers ($j = 1, ..., N$), and that the fiber orientation domain is divided into $n\Delta\varphi$ intervals, at the jth cracked layer, the pullout resistance is equal to:

$$P^j(w) = \sum_{i=1}^{n\Delta\varphi} P^j_{\overline{\varphi_i}}(w) \tag{17}$$

$$P^j_{\overline{\varphi_i}}(w) = N^j_{f,\overline{\varphi_i}} \cdot \pi \cdot d_f \cdot \tau_{bu,i} \cdot L_{bf,o}(w) \tag{18}$$

where $P^j_{\overline{\varphi_i}}(w)$ is the pullout resistance of the $N^j_{f,\overline{\varphi_i}}$ fibers with a mean orientation angle $\overline{\varphi_i}$ at the jth cracked layer, determined according to the fiber orientation and segregation models.

3 Assessment of the Predictive Performance of the Model

The predictive performance of the proposed model is assessed by comparing the flexural response of polypropylene fiber reinforced concrete (PPFRC) notched beams submitted to 3-point bending tests, according to [26], with the numerical response determined with software *DOCROS*. Although the proposed numerical model was originally proposed to simulate the flexural behavior of steel fiber reinforced concrete elements, this research work verifies if it has potential to be applicable to other non-metallic discrete fibers reinforcements in concrete.

The PPFRC composition presented in Table 1 was considered, while two mixes with different fiber reinforcement dosages were studied: 6.0 and 3.0 kg/m^3.

A new type of PP fibers for structural reinforcement that is being developed in the scope of a R&D project carried out by *Exporplás* and *CiviTest*, is used, which has 0.7 mm of equivalent diameter, length equal to 54 mm, modulus of elasticity of 6GPa and ultimate tensile strength of 500 MPa.

Table 1 PPFRC mix composition

Portland cement CEM I 52.5R (kg/m^3)	Fly ash (kg/m^3)	Aggregate 6/14 mm (kg/m^3)	Aggregate 0/4 mm (kg/m^3)	Aggregate 0/2 mm (kg/m^3)	Superplasticizer [l/m^3]	Water (l/m^3)
330.0	20.0	750.0	885.0	300.0	7.2	140.0

In order to characterize the relevant mechanical properties of both PPFRC mixes that were considered in this study, an experimental program was carried out to determine the concrete compressive strength (NP EN 12390-3:2009 [27]), modulus of elasticity (NP EN 12390-13:2013 [28]) and post-cracking residual flexural strength (EN 14651:2005 [26]) at the age of 28 days. The results of the mechanical characterization of the PPFRC are summarized in Table 2.

Since at the present stage of the research activities, the local bond-slip relationship (Fig. 2a) of the used PP fibers are not yet available from experimental tests (by adopting inverse analysis with the results from fiber pullout tests), the parameters that define this local law were obtained by a fitting procedure implemented in *DOCROS*, that resorts to the nonlinear least squares fitting routine *MPFIT* [29]. The data considered in the fitting procedure corresponded to the average of the moment versus crack tip opening displacement (CTOD) relationship that was derived from the experimental results of 3 samples submitted to the bending tests.

Figure 4a, b present the comparison between the experimental and numerical response of the force versus CTOD relationship of the PPFRC prisms submitted to 3-point bending, while Fig. 4c presents the bond stress versus slip relationship, $\tau_{b,0} - \delta$, for the pullout response of the aligned PP fibers obtained by the fitting procedure, for each PPFRC mix. As demonstrated in Fig. 4, the proposed model captures with very good agreement the flexural behavior of the PPFRC prisms.

To be noticed that the derived peak bond strength of pullout response of fibers is dependent on the fiber dosage of the PPFRC, with the peak bond strength being inversely proportional to the employed fiber dosage. This phenomenon points to a detrimental effect of the increased number of fibers on the pullout response of each individual fiber.

4 Conclusions

This study presents a new integrated model capable of describing the flexural behavior of 1D type FRC members considering the orientation of the fibers, the fiber segregation along the cross-section of these members, and the pullout constitutive model of each fiber bridging the two faces of a crack.

Nonetheless the proposed numerical model has been originally developed to simulate the behavior of steel fiber reinforced concrete, it is shown that it can also capture with very satisfactory accuracy the behavior of concrete reinforced with non-metallic discrete fibers, as is the case of the studied PP fibers.

The accuracy of the model would greatly benefit from the characterization of the pullout response of aligned and inclined fibers, including a more in-depth study regarding the influence of the number of fibers bridging a crack on the pullout response of each individual fiber.

For the particular case of members made by concrete reinforced with flexible fibers such is the case of PP fibers), an upgrade to the fiber orientation and distribution model is under development, which will also contribute to improve the predictive

Table 2 Average values of the mechanical properties of the PPFRC mixes

Mixture	f_{cm} (MPa)	E_{cm} (GPa)	f_{Lm} (MPa)	f_{R1m} (MPa)	f_{R2m} (MPa)	f_{R3m} (MPa)	f_{R4m} (MPa)
Mix with 6 kg/m^3 of PP fibers	35.1 (1%)[a]	24.9 (4%)[a]	3.25 (7%)[a]	1.88 (20%)[a]	1.97 (26%)[a]	2.04 (27%)[a]	2.07 (27%)[a]
Mix with 3 kg/m^3 of PP fibers	33.4 (1%)[a]	25.6 (1%)[a]	3.70 (7%)[a]	1.48 (21%)[a]	1.41 (30%)[a]	1.44 (34%)[a]	1.40 (31%)[a]

[a]Coefficient of variation

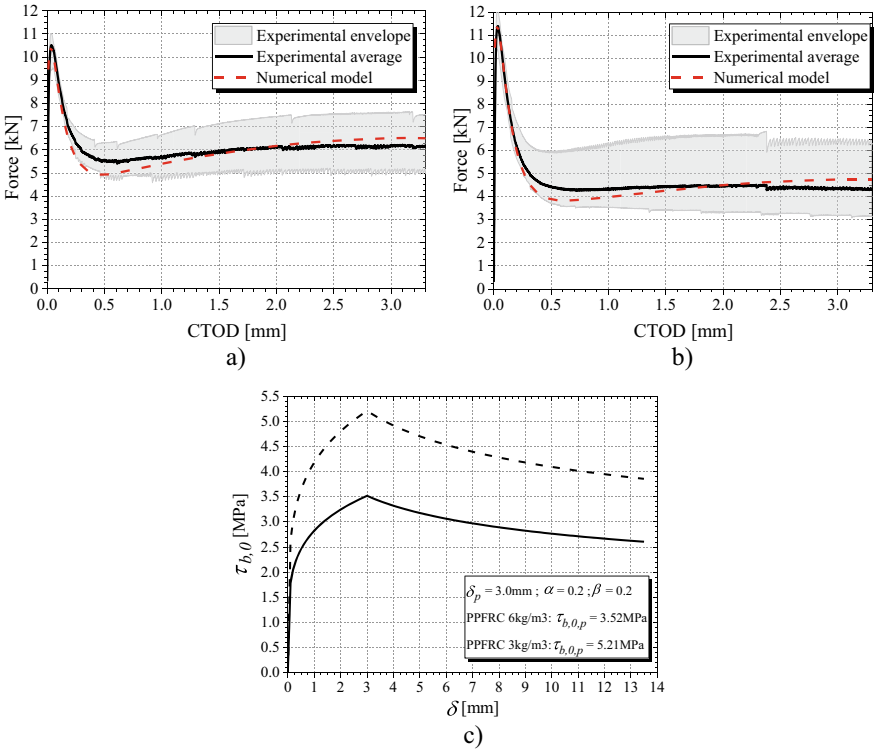

Fig. 4 Experimental and numerical model comparison of force versus CTOD relationship for PPFRC with: **a** 6 kg/m^3 of PP fibers; **b** 3 kg/m^3 of PP fibers; **c** Derived bond stress versus slip ($\tau_{b,0} - \delta$) of the pullout response of the aligned PP fibers

performance of the integrated model to simulate the flexural behavior of PPFRC members.

Acknowledgements The authors would like to acknowledge the support provided by *Exporlás*, regarding the provision of the PP fibers to conduct the study. This work is supported by the European Regional Development Fund (FEDER) through the Competitiveness and Internationalization Operational Program—COMPETE under the NG_TPfib project POCI-01-0247-FEDER-033719.

References

1. Barros, J.A.O.: Comportamento do betão reforçado com fibras—análise experimental e simulação numérica (Behavior of fiber reinforced concrete–experimental and numerical analysis). Ph.D. Thesis, Department of Civil Engineering, FEUP (1995)
2. Barros, J.A.O., Sena, J.: Fracture energy of steel fiber-reinforced concrete. Mech. Compos. Mater. Struct. **8**, 29–45 (2001)

3. Brandt, A.M.: Cement based composites: materials, mechanical properties, and performance, 2nd edn. Taylor & Francis, Milton Park, Abingdon, Oxon (2009)
4. Banthia, N.: Fiber reinforced concrete. ACI SP-142ACI Detroit MI 91–119 (1994)
5. Mazaheripour, H., Barros, J.A.O., Soltanzadeh, F., Sena, J.: Deflection and cracking behavior of SFRSCC beams reinforced with hybrid prestressed GFRP and steel reinforcements. Eng. Struct. **125**, 546–565 (2016). https://doi.org/10.1016/j.engstruct.2016.07.026
6. Frazão, C., Barros, J., Camões, A., Alves, A.C., Rocha, L.: Corrosion effects on pullout behavior of hooked steel fibers in self-compacting concrete. Cem. Concr. Res. **79**, 112–122 (2016). https://doi.org/10.1016/j.cemconres.2015.09.005
7. Ferrara, L., Meda, A.: Relationships between fibre distribution, workability and the mechanical properties of SFRC applied to precast roof elements. Mater. Struct. **39**, 411–420 (2007). https://doi.org/10.1617/s11527-005-9017-4
8. Ferrara, L., Park, Y.-D., Shah, S.P.: Correlation among fresh state behavior, fiber dispersion, and toughness properties of SFRCs. J. Mater. Civ. Eng. **20**, 493–501 (2008)
9. Stähli, P., Custer, R., van Mier, J.G.M.: On flow properties, fibre distribution, fibre orientation and flexural behaviour of FRC. Mater. Struct. **41**, 189–196 (2008). https://doi.org/10.1617/s11527-007-9229-x
10. Abrishambaf, A., Cunha, V.M.C.F., Barros, J.A.O.: The influence of fibre orientation on the post-cracking tensile behaviour of steel fibre reinforced self-compacting concrete. Fract. Struct. Integr. J. **31**, 38–53 (2015)
11. Cunha, V.M.C.D., Barros, J.A.O., Sena, J.M.: Pullout behavior of steel fibers in self-compacting concrete. J. Mater. Civ. Eng. **22**, 1–9 (2010). https://doi.org/10.1061/(ASCE)MT.1943-5533.0000001
12. Ng, T.S., Foster, S.J., Htet, M.L., Htut, T.N.S.: Mixed mode fracture behaviour of steel fibre reinforced concrete. Mater. Struct. **47**, 67–76 (2014). https://doi.org/10.1617/s11527-013-0045-1
13. Voo, J.Y.L., Foster, S.J.: Tensile-fracture of fibre-reinforced concrete: variable engagement model. In: Sixth RILEM Symposium on Fibre-Reinforced Concrete (FRC)—BEFIB 2004. RILEM, Varenna, Italy, pp. 874–884 (2004)
14. Htut, T.N.S., Foster, S.J.: Unified model for mixed mode fracture of steel fibre reinforced concrete. In: Proceedings of the 7th International Conference on Fracture Mechanics Concrete and Concrete Structures (FramCoS-7), Jejyu, Korea, pp. 1469–1477 (2010)
15. Valente, T.: Advanced tools for design and analysis of fiber reinforced concrete structures. Ph.D. Thesis, University of Minho (2019)
16. Häßler, D., Barros, J.A.O.: Exploring the possibilities of steel fibre reinforced self-compacting concrete for the flexural strengthening of masonry structural elements. Int. J. Arch. Herit. Conserv. Anal. Restor. 26–53
17. Barros, J.A.O., Varma, R.K., Sena, J.M., Azevedo, A.F.M.: Near surface mounted CFRP strips for the flexural strengthening of RC columns: experimental and numerical research. Eng. Struct. **30**, 3412–3425 (2008). https://doi.org/10.1016/j.engstruct.2008.05.019
18. Laranjeira de Oliveira, F.: Design-oriented constitutive model for steel fiber reinforced concrete. Ph.D. Thesis, Universitat Politècnica de Catalunya (2010)
19. Laranjeira, F., Aguado, A., Molins, C., Grünewald, S., Walraven, J., Cavalaro, S.: Framework to predict the orientation of fibers in FRC: a novel philosophy. Cem. Concr. Res. **42**, 752–768 (2012). https://doi.org/10.1016/j.cemconres.2012.02.013
20. Krenchel, H.: Fibre spacing and specific fibre surface. In: Proceedings of Rilem Symposium on Fibre Reinforced Cement and Concrete, pp. 69–79. Construction Press (1975)
21. Dupont, D., Vandewalle, L.: Distribution of steel fibres in rectangular sections. Cem. Concr. Compos. **27**, 391–398 (2005). https://doi.org/10.1016/j.cemconcomp.2004.03.005
22. Alberti, M.G., Enfedaque, A., Gálvez, J.C.: On the prediction of the orientation factor and fibre distribution of steel and macro-synthetic fibres for fibre-reinforced concrete. Cem. Concr. Compos. **77**, 29–48 (2017). https://doi.org/10.1016/j.cemconcomp.2016.11.008
23. Htut, T., Foster, S.J.: Fracture of steel fibre reinforced concrete—the unified variable engagement model. The University of the New South Wales, UNSW Sydney, Australia (2012)

24. Htut, T.: Fracture processes in steel fibre reinforced concrete. Ph.D. Thesis, School of Civil and Environmental Engineering, The University of New South Wales, UNSW Sydney (2010)
25. Marti, P., Pfyl, T., Sigrist, V., Ulaga, T.: Harmonized test procedures for steel fibre-reinforced concrete. ACI Mater. J. **96**, 676–685 (1999)
26. European Committee for Standardization.: Test method for metallic fibered concrete—measuring the flexural tensile strength (limit of proportionality (LOP), residual) (2005)
27. European Committee for Standardization.: Testing hardened concrete—Part 3: compressive strength of test specimens (2009)
28. European Committee for Standardization.: Testing hardened concrete—Part 13: determination of secant modulus of elasticity in compression (2013)
29. Markwardt, C.B.: Non-linear least squares fitting in IDL with MPFIT. In: Astronomical Data Analysis Software and Systems XVIII. ASP Conference Series, Quebec, Canada, pp. 251–254 (2009)

An Analytical Approach for Evaluating the Impact Response of Steel Fiber Reinforced Concrete Beam

Mohammad Bakhshi, Honeyeh Ramezansefat, Mohammadali Rezazadeh, Isabel Valente, and Joaquim A. O. Barros

Abstract In this paper, a new approach is proposed for predicting reaction force in simply supported steel fiber reinforced concrete (SFRC) beams under impact loading (drop weight test) considering the energy conservation approach. If SFRC beams completely fail under impact load, it can be found that the total reaction force is equal to force capacity of SFRC beams. The force-deflection relationship can show the peak force that the SFRC beam can carry under impact load. Since concrete is a material sensitive to loading rates, the strain rate of loading and also the volume fraction of steel fiber will influence the beam's response. The force-deflection relationship of the SFRC beam under impact loading is obtained using the proposed model. This model considers the effect of volume fraction of steel fiber and also the strain rate on the concrete properties. The model is then verified with the results collected from the literature that include 189 SFRC beams tested under drop-weight impacts and included in a database. The results obtained show that this method can estimate the maximum impact force with acceptable accuracy.

Keywords Steel fiber reinforced concrete · Concrete beam · Drop weight test · Strain rate

1 Introduction

Steel fiber reinforced concrete (SFRC) is a composite material that includes cement, aggregates, and steel fibers in its composition [1]. Normal concrete is usually a brittle material, so the addition of fibers causes an increase in its post-cracking tensile capacity and prevents the early cracking of concrete. According to [2–4], SFRC has an improved behavior, which includes: resistance to the combination of wear—tear damage and weathering, high resistance to fatigue stress, excellent impact resistance, excellent tensile strength, ductility, high load capacity after cracking, and high shear

M. Bakhshi (✉) · H. Ramezansefat · M. Rezazadeh · I. Valente · J. A. O. Barros
Structural Division, Department of Civil Engineering, ISISE, University of Minho, 4800-058 Guimarães, Portugal
e-mail: Mohammad.Bakhshi.ngd@gmail.com

E. B. Pereira et al. (eds.), *Proceedings of the 3rd RILEM Spring Convention and Conference (RSCC 2020)*, RILEM Bookseries 32,
https://doi.org/10.1007/978-3-030-76547-7_2

strength. The ACI code [1] recognizes the possibility of using a volume content of 0.75% of deformed steel fibers for minimum shear reinforcement in common structural applications under quasi-static loading conditions.

On the other hand, concrete is a material that is sensitive to the strain rate [5–8] imposed during the loading process and, consequently, its mechanical properties are dependent to this rate. The effect of strain rate on concrete for each type of loading is also different (i.e., compressive, tensile, and flexural) [9–12]. Existing experimental results on the dynamic behavior of SFRC have shown that both the tensile strength and the mode I fracture energy increase with strain rate [2, 3]. Moreover, based on the experimental results, the strain rate influences on the reaction force and energy dissipation capacity of SFRC beam. The dynamic increase factor (DIF) of compressive, tensile and flexural strength of SFRC are defined to evaluate the effect of strain rate on the SFRC characterizations [6–9]. Although there are some experimental studies for understanding the flexural behavior of SFRC under impact load [5–12], due to include several aspects, analytical models for predicting the impact response of SFRC beams are still scarce. To accurately predict the impact response of SFRC beams under the drop-weight impact, some analytical methods for concrete beams reinforced with conventional steel bars (RC beams) can be adapted for SFRC beams. There are generally three approaches for predicting the impact response of a RC beam, namely, contact law, energy-based approach, and spring-mass model [13]. These approaches are used in RC beams because complete fracture of this beams does not occur. In SFRC beams under impact load, the total energy applied by the impactor is dissipated by the inertial energy caused by existing acceleration and deflection of the beam. If SFRC beams completely fail under impact load, it can be found that the total reaction force is equal to force capacity of SFRC beams. In this condition, the impactor passes the beam and the remaining energy of the impactor is released to the test setup frame. Consequently, for each SFRC beam, critical initial kinetic energy can be defined as the maximum initial kinetic energy that the beam can dissipate. A simplified method is established in this paper for predicting the maximum reaction force of simply supported SFRC beams under impact load (Fig. 1). Appropriate assumptions and theoretical derivation are utilized to establish this simplified method. Moreover, the results of 189 SFRC beams under impact load acting at midspan are compiled in a database to validate the proposed method [14–16].

2 Analytical Method

In the impact loading condition, due to the existing accelerations on the beam, the inertia force is mobilized along the beam, and its direction is contrary to the direction of the beam's movement. The total impact force (P_t) in a simply supported beam is equal to the sum of the total inertia forces (P_i) and reaction forces R_1 and R_2 in its supports ($P_b = R_1 + R_2$), (Fig. 1). By assuming the linear acceleration distribution, the inertia force is calculated by the Eq. (2) [4].

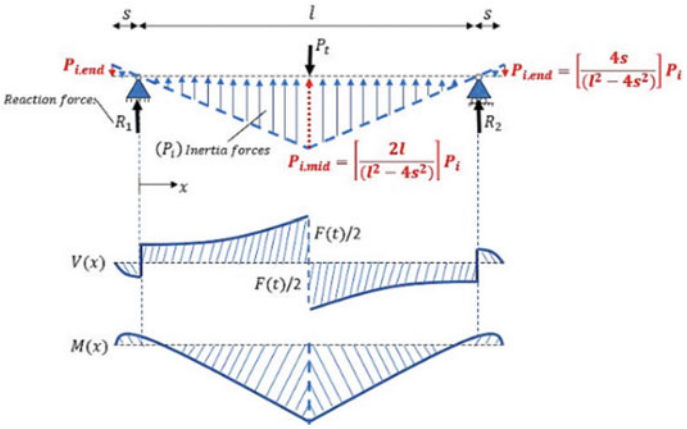

Fig. 1 Loadings and generated shear and bending moment diagrams in an impact situation

$$P_t = P_b + P_i \tag{1}$$

$$P_i = \rho A \ddot{\delta}(t)\left[\frac{l}{3} + \frac{8}{3}\frac{s^3}{l^2}\right] \tag{2}$$

where ρ, A, l, s and $\ddot{\delta}(t)$ are the beam's material density, cross section area, span length, overhanging length (Fig. 2), and the time dependent acceleration of beam at its midspan, respectively.

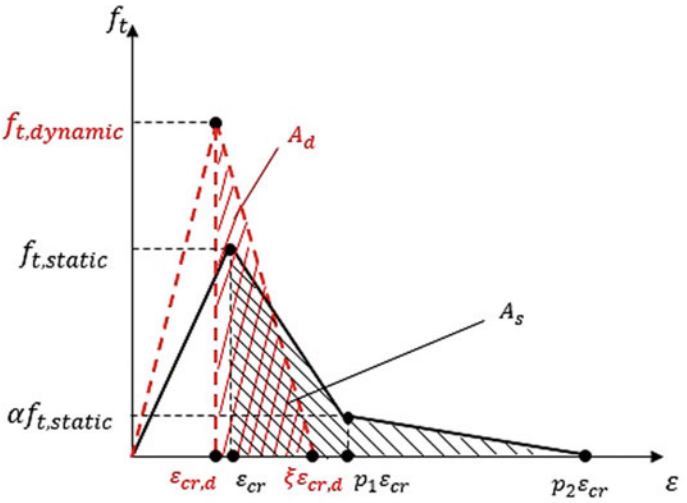

Fig. 2 Dynamic tensile behavior of the SFRC

The acceleration is depended on the materials properties, geometry of the beam, and the height and mass of impactor. Unfortunately, there are not enough data about the maximum acceleration in the midspan of the beam. The statistical analysis of the available experimental studies [6, 8, 11, 22] shows that the effects of the stiffness of the beam and mass of impactor have a marginal impact on the maximum acceleration, while by increasing the height of the impactor, the acceleration increases significantly. Considering the lack of experimental investigations, a simple empirical equation is proposed by using the available experimental data for calculating the maximum acceleration at midspan ($\ddot{\delta}_{\max}$) based on the height of the impactor (H) as follows:

$$\ddot{\delta}_{max} = \left(-6.404 \times 10^3\right)H^3 + \left(1.776 \times 10^4\right)H^2 - \left(3.665 \times 10^3\right)H + 4980 \quad (3)$$

In the current study, first, the force-deflection relation of SFRC simply supported beam is analytically predicted using the proposed model, whose governing variables are function of the strain rate of loading, and then a simplified approach is proposed to determine its loading capacity.

2.1 Force-Deflection Relationship of SFRC

Several studies in the literature focused on the stress-strain relation of SFRC materials. The model proposed by Barros et al. [18] was selected in the present research because it considers the effect of steel fiber volume as the main parameter (Table 1). Since concrete is a sensitive material to the strain rate of loading, its static constitutive quantities must be updated when exposed to loading conditions that generate high strain rates. In the current study, for considering the effect of the strain rate on the compressive strength and modulus of elasticity, *fib*-Model code 2010 formulation is adopted, by considering Eqs. (4) and (5) [17]. On the other hand, since the effect of fiber reinforcement mostly influence the tensile behavior of concrete, rather than the compressive behavior, to consider the strain rate effect on the tensile strength of SFRC, the model proposed by Malver and Ross is adopted (Eq. (6)) [19], because their proposed model is supported on results from experimental tests with SFRC specimens.

$$\frac{f'_{cd}}{f'_{cs}} = \begin{cases} \left(\dfrac{\dot{\varepsilon}_c}{30 \times 10^{-6}}\right)^{0.014}, & \dot{\varepsilon}_c \le 30\ s^{-1} \\ 0.012\left(\dfrac{\dot{\varepsilon}_c}{30 \times 10^{-6}}\right)^{1/3}, & \dot{\varepsilon}_c > 30\ s^{-1} \end{cases} \quad (4)$$

$$\frac{E_{cd}}{E_{cs}} = \left(\frac{\dot{\varepsilon}_c}{30 \times 10^{-6}}\right)^{0.026} \quad (5)$$

Table 1 Stress-strain model of SFRC suggested by Barros [18]

Compressive	Tensile
$\frac{\sigma_{cf}}{f'_{cf}} = \frac{\left(\frac{\varepsilon_c}{\varepsilon'_{cf}}\right)}{(1-p-q)+q\left(\frac{\varepsilon_c}{\varepsilon'_{cf}}\right)+p\left(\frac{\varepsilon_c}{\varepsilon'_{cf}}\right)^{(1-q)/p}}$ $p+q=1-\frac{f'_{cf}}{E_c\varepsilon'_c}$ $\varepsilon'_{cf}=2.2\times10^{-3}+0.0002W_f$ $p=1-0.919\exp(-0.394W_f)$ $W_f \simeq 3\ V_f$	$\sigma=\begin{cases} E_{ci}\varepsilon, & \varepsilon \le \varepsilon_{cr} \\ E_{ci}\left(\frac{\alpha-1}{p_1-1}\right)(\varepsilon-\varepsilon_{cr})+f_{ct}, & \varepsilon_{cr} < \varepsilon \le p_1\varepsilon_{cr} \\ E_{ci}\left(\frac{\alpha}{p_1-p_2}\right)(\varepsilon-p_2\varepsilon_{cr}), & p_1\varepsilon_{cr} < \varepsilon \le p_2\varepsilon_{cr} \end{cases}$ $E_{ci}=\left(\frac{f_{ct}}{\varepsilon_{cr}}\right),\quad \varepsilon_{cr}=\frac{f_{ct}}{E_{ci}},\quad f_{ct}=1.4\left(\frac{f'_c-8}{10}\right)^{\frac{2}{3}}$ $E_{ci}=2.15\times10^4\left[\frac{f'_c}{10}\right]^{\frac{1}{3}},\quad \alpha=\frac{L(beam\ length)}{l(span\ length)}-1,\quad \frac{G_f}{G_{f0}}=19.953+3.213W_f$ $G_{f0}(N.mm^{-1})=f\left(\max.agg.size\ and\ f'_c\right),\quad G_{f0}=\begin{cases}0.025, & d=8\,mm\\ 0.030, & d=16\,mm\\ 0.058, & d=32\,mm\end{cases}$ $l_b=\frac{G_fE_{ci}}{f_{ct}^2}=10970\,G_{f0}\frac{\left(f'_c/10\right)^{1.03}}{\left[\left(f'_c/10\right)-0.8\right]^{4/3}},\quad p_2=\frac{2G_f}{\alpha l_b f_{ct}\varepsilon_{cr}}-\frac{p_1-\alpha}{\alpha},\quad p_1=1\sim3\simeq2$

$$\frac{f'_{td}}{f'_{ts}} = \begin{cases} \left(\frac{\dot{\varepsilon}_t}{1\times10^{-6}}\right)^{\delta}, & \dot{\varepsilon}_c \le 1\ s^{-1} \\ \beta\left(\frac{\dot{\varepsilon}_t}{1\times10^{-6}}\right)^{1/3}, & \dot{\varepsilon}_c > 1\ s^{-1} \end{cases}, \quad \log(\beta) = 6\delta - 2, \quad \delta = 1/\left(1 + 0.6 f'_c\right) \tag{6}$$

In Eqs. (4) to (6), f'_{cd} and f'_{cs} are, respectively, the dynamic and static compressive strength, f'_{td} and f'_{ts} are, respectively, the dynamic and static tensile strength, E_{cd} and E_{cs} are, respectively, the dynamic and static modulus of elasticity, while $\dot{\varepsilon}_c$ and $\dot{\varepsilon}_t$ are, respectively, the compressive and tensile strain rate. Since the concrete compressive strength is about ten times higher its tensile strength, the overall behavior of the SFRC beam is often controlled by the tensile behavior. In this regard, the tensile strength, fracture energy, and modulus of elasticity of the SFRC are essential parameters for calculating the overall behavior of the beam under impact load. According to the experimental results [9–12], the post peak tensile behavior of SFRC under impact load can be considered linear concerning the effect of strain rate on the fracture energy. Based on the experimental stress-strain curves of the SFRC under various strain rates, the value of fracture energy under static and dynamic loading can be calculated by Eq. (7) [12, 23]. The first term of the equation represents the fracture energy externally supplied to propagate the crack across the specimen. The second term of Eq. (7) corresponds to the fracture energy supplied by the beam weight, causing to reduce the prediction error compared to the recommendation of RILEM TC50-FMC Technical Committee [24] which did not consider the influence of the cantilever of the beam:

$$G_f = \frac{W_0}{b(h-a)} + \frac{mg\left(1 - \frac{l}{2s}\right)\delta_u}{b(h-a)} \tag{7}$$

where W_0, b, h, a, s, l, m, δ_u, and g are the area under the experimental load-displacement curve, width, cross section's height, notch depth, span, length, mass of the beam between the supports (length l), final deflection of the beam and gravitational acceleration, respectively. For the case of impact loading, due to the existing inertia force, W_0 is the area under the reaction force-displacement curve [23]. To consider the effect of the strain rate of loading on the fracture energy of SFRC, the model proposed by Zhang et al. [12] for determining the DIF of fracture energy is adopted as follows:

$$DIF_G = \frac{G_{fd}}{G_{fs}} = 1 + (7.6\times10^{-6})\left(\frac{\dot{\delta}_d}{\dot{\delta}_s}\right)^{1.54}; \qquad \dot{\delta}_s = 1\ (\text{mm/s}) \tag{8}$$

where G_{fd} and G_{fs} are fracture energy of the SFRC beam under dynamic and static loading, respectively, which can be calculated by Eq. (7). $\dot{\delta}_d$ and $\dot{\delta}_s$ (=1 mm/s) are the dynamic and static loading rate in mm/s, respectively. On the other hand, according to three-point bending test, the strain rate ($\dot{\varepsilon}$) can be obtained based on the beam bending theory by using the displacement rate ($\dot{\delta}$) as follows [22]:

$$\dot{\varepsilon} = \frac{6h\dot{\delta}}{L^2} \tag{9}$$

where h and l are the cross section's height and span length of the beam, respectively. After determining the fracture energy parameter, to define the post cracking tensile behavior, the softening constitutive relationship must be derived from the fracture parameters, namely, the tensile strength, the width of the fracture process zone (l_b), the mode I fracture energy (G_f), and the shape of the softening diagram. The area under the post-cracking tensile stress-strain curve (g_f) can be defined from the following equation, proposed by Barros et al. [18]:

$$g_f = \frac{G_f}{l_b} \tag{10}$$

where l_b can be taken as approximately three times the maximum aggregate size, as proposed by Bazant and Oh [20], for plain concrete [18]. By ignoring the effect of strain rate on l_b, the DIF of the area under the tensile stress-strain curve was assumed to be the same as DIF of the fracture energy (Fig. 3).

$$\begin{aligned} DIF_G = DIF_{g_f} &= \frac{A_d}{A_s} \\ &= \frac{0.5 f'_{td} \times (\xi - 1)\varepsilon_{cr,d}}{\left[0.5 f'_{ts}\, \varepsilon_{cr}(\alpha + 1)(p_1 - 1)\right] + \left[0.5 f'_{ts}\, \varepsilon_{cr} \times \alpha(p_2 - p_1)\right]} \end{aligned} \tag{11}$$

where A_d and A_s are the area under the dynamic and static post-cracking tensile stress-strain curve, respectively (Fig. 3). In Eq. (11) ε_{cr} and $\varepsilon_{cr,d}$ are the strain at concrete crack initiation in static and dynamic loading conditions, respectively, α, p_1 and p_2 are coefficients defining the bilinear configuration of the constitutive law.

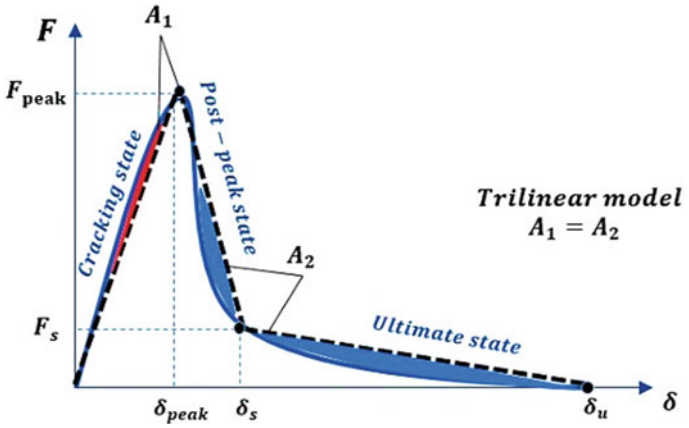

Fig. 3 Moment-curvature relationship

For defining the tensile behavior of SFRC under impact load, it should be considered that the fracture mechanism of steel fibers in SFRC composite material is different in the various rate of loading. For example, for hooked end fibers, by increasing the rate of loading the mechanism of steel fibers changes from pull-out to rupture resulting in post-cracking the slope of the tensile stress-strain curve SFRC increases. In high strain rate loading, hooked end steel fibers mostly fail by tensile rupture, while under static loading the fibers are pulled out, enhancing the maximum deflection of SFRC under tensile and bending tests. In this regard, the tensile stress-strain curve of SFRC under impact load can be simplified by two linear branches, as shown Fig. 3. The linear behavior up to the peak point can be defined by Eqs. (5) and (6), and the post-peak behavior, can be obtained by Eqs. (8) to (11) considering the effect of strain rate on fracture energy of SFRC. By adopting the model proposed by Barros et al. [18] for the tensile behavior of SFRC under static loading and the model suggested by Malver and Ross [19] for the effect of strain rate on the tensile strength of SFRC materials, ξ can be calculated by Eqs. (8) to (11).

In general, the nonlinear analysis of beams can be conducted with the moment-curvature relationship based on the layered-section approach. In the present study, to determine the moment-curvature relationship of a cross-section, the sectional analysis software DOCROS has been used [21]. The compressive and tensile stress-strain relations of SFRC have been modified for dynamic loading, and they are utilized as a material model in DOCROS. Figure 3 presents a schematic representation of the moment-curvature relationship of a SFRC beam's section, including the cracking, post-peak, and ultimate state. The moment-curvature diagram can be simplified to a trilinear curve that the area under the moment-curvature curve remains constant. For achieving the force-deflection diagram of the SFRC beam under impact load, the moment distribution on the beam must be calculated considering the effect of inertia force. Because the inertia force along the beam changes the moment distribution. The moment distribution can be obtained using the ratio of inertia force to total force (Fig. 2). The ratio of inertia force to total force (β) was defined because analyzing the beam under impact load is completely different from analyzing the beam under static load. In the Eq. (12), the inertia force (P_i) is obtained by Eq. (1) and β is a function of P_b. Thus, P_b could be achieved through a try and error process. $M(x)$ is the moment distribution along the beam and is the total force that in

$$\beta = \frac{P_i}{P_t} = \frac{P_i}{P_i + P_b}; \qquad M(x) = \left(\frac{2}{3}\beta\right)\left(\frac{F}{l^2}\right)x^3 + \left(\frac{1-\beta}{2}\right).F.x \tag{12}$$

where F is the total force that is increasing smoothly from zero up to peak value and then decreases up to zero at the ultimate deflection. By considering the peak moment (M_{peak}), the peak force (F_{peak}) in the midspan ($x = l/2$) can be obtained (Fig. 4). The post-peak force (F_s) can be obtained by the same approach considering the M_s instead of M_{peak}. Using the conjugate beam method, the curvature can be considered as a load (Fig. 5). In this condition, the moment of every point of the conjugate beam is equal to the deflection of the main beam. There are three necessary points to draw the force-deflection diagram; (a) peak point (δ_{peak}, F_{peak}); (b) post-peak point (δ_s,

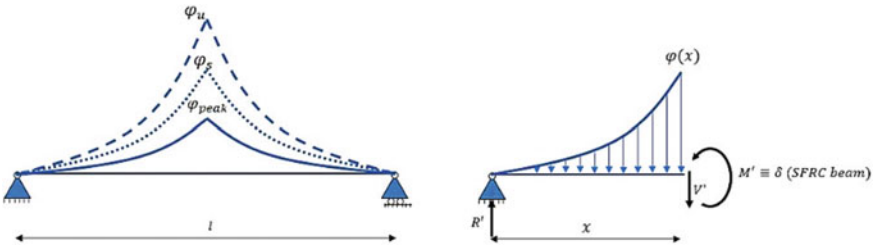

Fig. 4 Conjugate beam method

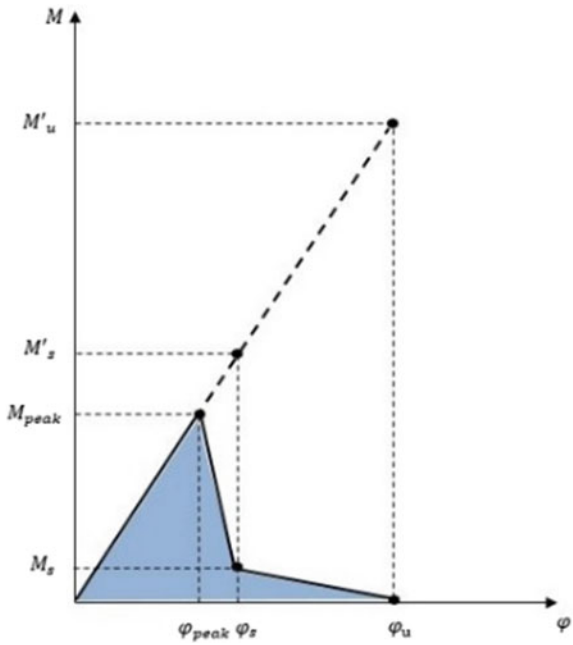

Fig. 5 Defining the assumed moments, F'_s and F'_u

F_s); and (c) ultimate point (δ_u, 0). As was mentioned, the force values of these three points can be calculated by Eq. (12). The peak deflection (δ_{peak}) can be achieved by Eq. (15). For calculating the post-peak deflection (δ_s) and ultimate deflection (δ_u) firstly two hypothetical moments (M'_s and M'_u) are defined. These moments are equivalent curvatures ϕ_s and ϕ_u in linear and rigid behavior of the beam (Fig. 6). Two equivalent forces (F'_s and F'_u) can be defined by Eq. (12) based on the moment of M'_s and M'_u. Accordingly, the post-peak deflection (δ_s) and ultimate deflection (δ_u) are calculated by using the Eq. (16).

$$\phi(x) = M(x).\left(\frac{\phi_{peak}}{M_{peak}}\right) \tag{13}$$

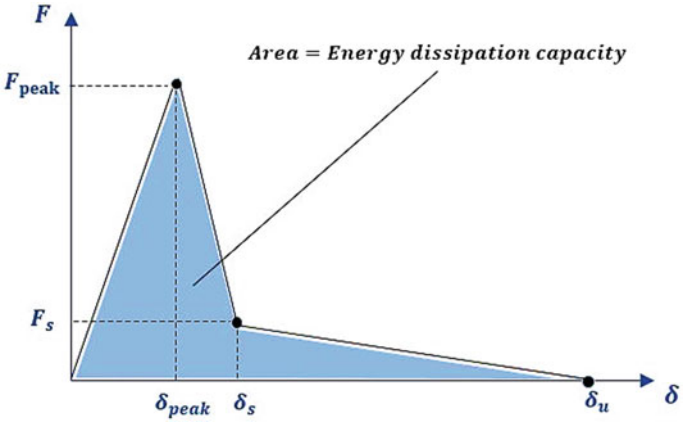

Fig. 6 Force-deflection diagram of SFRC

$$R' = \frac{1}{2}\int_0^l M(x).\left(\frac{\phi_{peak}}{M_{peak}}\right)dx = \left(Fl^2\right)\left(\frac{3-\beta}{24}\right)\left(\frac{\phi_{peak}}{M_{peak}}\right) \tag{14}$$

$$\delta_{peak} = \frac{(10-\beta)}{240} \times l \times \frac{\phi_{peak}}{M_{peak}} \times F_{peak}\, l^2 \tag{15}$$

$$\delta_s = \frac{(10-\beta)}{240} \times l \times \frac{\phi_{peak}}{M_{peak}} \times F_s'\, l^2; \quad \text{and}$$

$$\delta_u = \frac{(10-\beta)}{240} \times l \times \frac{\phi_{peak}}{M_{peak}} \times F_u'\, l^2 \tag{16}$$

In Eq. (13), $\phi(x)$ is the distribution curvature along the beam. Finally, based on the previously calculated moment-curvature diagram, the force-deflection diagram of the beam under dynamic loading is finalized, as shown in Fig. 7.

The following equation provides the area under the $F - \delta$ diagram, which represents the energy dissipation capacity of the SFRC beam under impact loading.

$$\int_0^{\delta_u} F(\delta)\, d\delta = \left[\frac{F_{peak}.\delta_{peak}}{2}\right] + \left[\frac{\left(F_{peak}+F_s\right)\left(\delta_s-\delta_{peak}\right)}{2}\right] + \left[\frac{F_s.(\delta_u-\delta_s)}{2}\right] \tag{17}$$

where $F_{peak}, \delta_{peak}, F_s, \delta_s$, and δ_u are the peak force, deflection at peak force, post-peak force, deflection at post-peak force, and ultimate deflection, respectively.

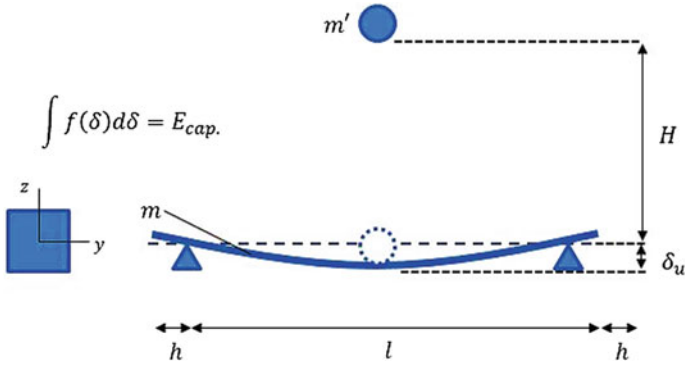

Fig. 7 Schematic shape of the beam under impact load

2.2 Maximum Reaction Force

The energy balance equation can be written for the SFRC beam under the dropping down of the impactor. It should be noted that the complete fracture may happen in the SFRC beam under impact loading. In this condition, extra kinetic energy of impactor after passing the beam releases to the test setup frame. Consequently, for each SFRC beam, critical initial kinetic energy ($E_{k,cr}$) can be defined as the maximum initial kinetic energy that the beam can dissipate. In other words, the critical initial kinetic energy is the minimum energy to fracture the SFRC beam completely. The critical initial kinetic energy can be calculated using the energy balance equation:

$$E_{k,cr} + U = E_{cap.} \tag{18}$$

$$E_{k,cr} = E_{cap.} - U = \int_0^{\delta_u} F(\delta)d\delta - \left(m + m'\right)g\delta_u \tag{19}$$

where U is the potential energy of the beam caused by deflection (Fig. 8), and $E_{cap.}$ is the energy dissipation capacity of the beam. In Eq. (19) g, m' and m are the gravity acceleration, the mass of impactor and the mass of the beam, respectively (Fig. 8). The energy balance equation, can be written for each value of initial kinetic energy:

$$\begin{aligned} E_{k,1} + U = E_c \quad &\rightarrow \quad \frac{1}{2}m'V_1^2 + \left(m + m'\right)g\delta_{\max} \\ &= \int_0^{\delta_{\max}} F(\delta)d\delta; \qquad E_{k,1} \le E_{k,cr} \end{aligned} \tag{20}$$

$$E_{k,1} + U = E_{cap.} + E_{k,2} \quad \rightarrow \quad \frac{1}{2}m'V_1^2 + \left(m + m'\right)g\delta_u$$

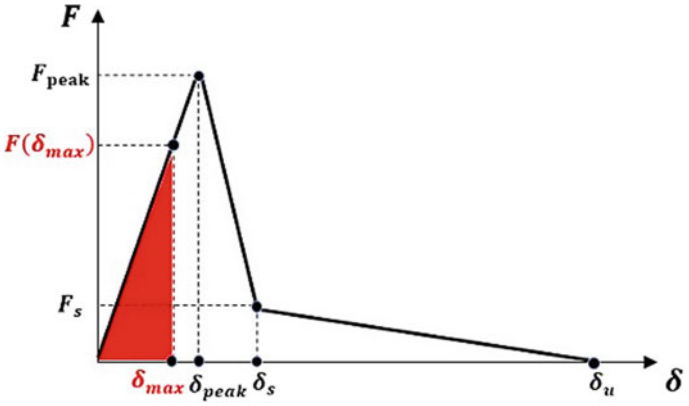

Fig. 8 The maximum response of beam

$$= \int_0^{\delta_u} F(\delta)d\delta + \frac{1}{2}m'V_2^2; \qquad E_{k,1} > E_{k,cr} \tag{21}$$

where $E_{k,1}$ is the initial kinetic energy that impactor applies to the beam at V_1 initial velocity, $V_1 = \sqrt{2gH}$ (H is the distance of the impactor to the beam's surface of impact). If the beam after impact loading does not fail, the initial energy is completely dissipated by the beam, being applicable Eq. (20). However, if the beam fails and separates into two segments, the difference between the initial kinetic energy and the energy dissipation capacity of the beam releases to test set up frame. In this case, the extra energy is considered as the second kinetic energy. In this condition, the velocity of the impactor is V_2. Consequently, there are generally two conditions: (a) the initial kinetic energy is more than the critical kinetic energy ($P_b = F_{peak} - P_i$) and (b) the initial kinetic energy is less than the critical kinetic energy, Eq. (22). If the initial kinetic energy is less than the critical kinetic energy, the maximum total force depends on the maximum deflection that can be obtained by Eqs. (20) and (21). Clearly, due to the softening behavior of SFRC composite after the peak force, after the peak deflection, the maximum force that the beam has experienced is equal to the peak force (Fig. 9). Thus, the maximum force can be calculated by Eq. (22).

$$P_b = \begin{cases} F(\delta_{max}) - P_i, & \delta_{max} < \delta_{peak} \\ F_{peak} - P_i, & \delta_{max} \geq \delta_{peak} \end{cases} \tag{22}$$

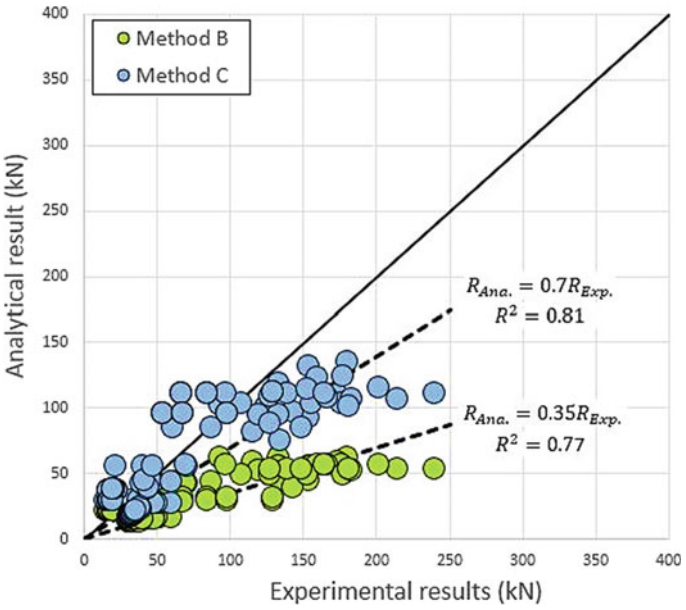

Fig. 9 Comparison of the methods C and B

3 Assessment of the Proposed Method

To validate the proposed method for predicting the peak response of SFRC beams under impact loading, a database of 189 SFRC beams tested under drop-weight impact at midspan is collected from other studies in the literature [6–12]. All the specimens considered in this study are simply supported SFRC beams with rectangular cross-section, and the impactors have two types of nose shape: spherical and flat impact surface.

Method C (considering the proposed model for tensile post-peak behavior (Fig. 3) and the model proposed by Malver and Ross [19] for calculating the effect of strain rate on the tensile strength) was selected to determine the force-deflections curve of SFRC beam under impact loading. For understanding the effect of DIF formulation on the force-deflection diagram, the Method B (considering the proposed model for tensile post-peak behavior (Fig. 3) and the model proposed by *fib* Model Code [17] for calculating the effect of strain rate on the tensile strength) was selected. Moreover, for evaluating the effect of the tensile post-peak behavior of SFRC on the force-deflection curve, Method A (using the equation of Barros et al. [18] for post-peak behavior (Table 1) and the model proposed by Malver and Ross [19] for calculating the effect of strain rate on the tensile strength) was also performed. Thus, three methodologies were selected to evaluate the force-deflection diagrams (Figs. 9 and 10).

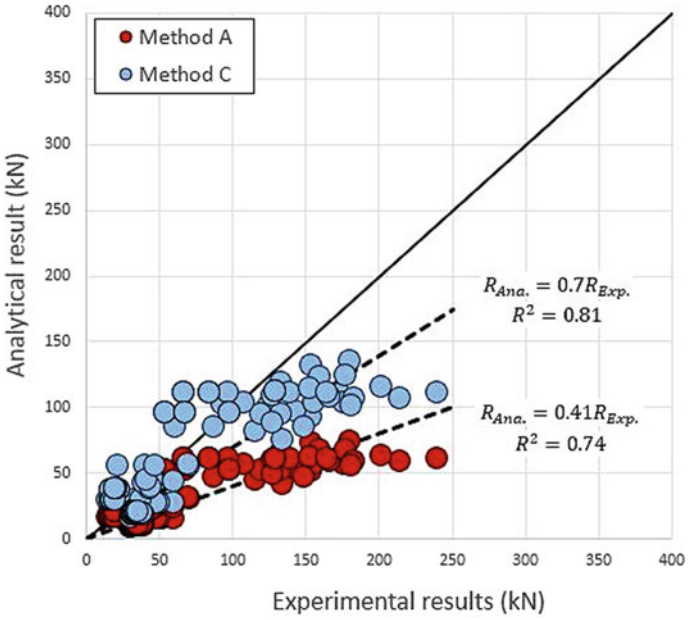

Fig. 10 Comparison of the methods C and A

Generally, the analytical results of all methods underestimated the experimental results. However, by considering the suggested approach (Method C) for predicting the maximum impact force of the SFRC beam on the simple supports, the tensile behavior of SFRC is updated based on different strain rates (Eqs. (6) and (11)). In this condition, the results have shown much higher accuracy than the Methods A and B (Figs. 9 and 10). As can be seen in the present paper, based on the proposed approach, the minimum energy for the failure of the SFRC beam can be estimated by the properties and the geometry of material, Eqs. (20) and (21). There are several methods for evaluating the accuracy of the model to predict the reaction force of the SFRC beam under impact loading. In the present study, the mean absolute deviation (MAD) and mean absolute percentage error (MAPE) have been used.

$$MAD = \frac{\sum_{1}^{N} |pre_i - exp_i|}{N}, \quad and$$
$$MAPE = \frac{1}{N} \sum_{1}^{N} \left| \frac{pre_i - exp_i}{exp_i} \right| \times 100 \tag{23}$$

where pre is the model predictions, exp is the experimental results, and N is the total number of specimens. The value of MAD and MAPE for the proposed model (Method C) are 23. 52 and 41.69 respectively while for the Method A are 40.99 and

52.82 and for Method B are 38.18 and 50.44 respectively. Obviously, by increasing the number of data, the precision of the model may be enhanced. It can be seen that method C can predict the results more precisely.

4 Conclusion

In the current study, the impact response of steel fiber reinforced concrete (SFRC) beams has been analytically investigated and a new approach for predicting reaction force of simply supported SFRC beams under impact loading (drop weight test) has been proposed. Based on the work carried out, the conclusions are:

(1) The proposed method consider the effect of strain rate on the tensile strength and also the post-peak behavior of SFRC. Moreover, this model can be used for a wide range of impact weight and velocity, geometry of beam, and volume fraction of steel fiber.
(2) A comparison with 189 experimental tests has shown that the proposed method is able to estimate the reaction forces of SFRC beams under impact loading. The reaction force is shown to be slightly underestimated.
(3) Based on the existed experimental tests, the results have shown the proposed method can predict the experimental results more precisely and realistic than the other method that consider the static function for the impact loading.

Acknowledgements The study reported in this paper is part of the project "PufProtec—Prefabricated Urban Furniture Made by Advanced Materials for Protecting Public Built" with the reference of (POCI-01-0145-FEDER-028256) supported by FEDER and FCT funds. The third author also acknowledges the support provided by FEDER and FCT funds within the scope of the project StreColesf (POCI-01-0145-FEDER-029485).

References

1. American Concrete Institute: ACI 318-11: Building Code Requirements for Structural Concrete and Commentary. American Concrete Institute, Framington Hills, MI (2011)
2. Thomas, R.J., Sorensen, A.D.: Review of strain rate effects for UHPC in tension. Constr. Build. Mater. **153**, 846–856 (2017)
3. Fujikake, K., Senga, T., Ueda, N., Ohno, T., Katagiri, M.: Effects of strain rate on tensile behavior of reactive powder concrete. J. Adv. Concrete Technol. **4**(1), 79–84 (2006)
4. Banthia, N., Chokri, K., Ohama, Y., Mindess, S.: Fiber-reinforced cement based composites under tensile impact. Adv. Cem. Based Mater. **1**(3), 131–141 (1994)
5. Wang, N., Mindess, S., Ko, K.: Fibre reinforced concrete beams under impact loading. Cem. Concr. Res. **26**(3), 363–376 (1996)
6. Ulzurrun, G., Zanuy, C.: Flexural response of SFRC under impact loading. Constr. Build. Mater. **134**, 397–411 (2017)

7. Millard, S.G., Molyneaux, T.C.K., Barnett, S.J., Gao, X.: Dynamic enhancement of blast-resistant ultra-high performance fibre-reinforced concrete under flexural and shear loading. Int. J. Impact Eng **37**(4), 405–413 (2010)
8. Zanuy, C., Ulzurrún, G.S.: Rate effects of fiber-reinforced concrete specimens in impact regime. Procedia engineering **193**, 501–508 (2017)
9. Hao, Y., Hao, H., Chen, G.: Experimental investigation of the behaviour of spiral steel fibre reinforced concrete beams subjected to drop-weight impact loads. Mater. Struct. **49**(1–2), 353–370 (2016)
10. Yoo, D.Y., Yoon, Y.S., Banthia, N.: Flexural response of steel-fiber-reinforced concrete beams: effects of strength, fiber content, and strain-rate. Cement Concr. Compos. **64**, 84–92 (2015)
11. Banthia, N., Gupta, P., Yan, C.: Impact resistance of fiber reinforced wet-mix shotcrete part 1: beam tests. Mater. Struct. **32**(8), 563 (1999)
12. Zhang, X.X., Elazim, A.A., Ruiz, G., Yu, R.C.: Fracture behaviour of steel fibre-reinforced concrete at a wide range of loading rates. Int. J. Impact Eng **71**, 89–96 (2014)
13. Pham, T.M., Hao, H.: Prediction of the impact force on reinforced concrete beams from a drop weight. Adv. Struct. Eng. **19**(11), 1710–1722 (2016)
14. Hazizan, M.A., Cantwell, W.J.: The low velocity impact response of an aluminium honeycomb sandwich structure. Compos. B Eng. **34**(8), 679–687 (2003)
15. Lu, G., & Yu, T. X. (2003). Energy absorption of structures and materials. Elsevier
16. Wu, M., Chen, Z., Zhang, C.: Determining the impact behavior of concrete beams through experimental testing and meso-scale simulation: I Drop-weight tests. Eng. Fract. Mech. **135**, 94–112 (2015)
17. Model Code 2010-Final draft: volume 1. Vol. 65. fib Fédération internationale du béton, 2012
18. Barros, J.A., Figueiras, J.A.: Flexural behavior of SFRC: testing and modeling. J. Mater. Civ. Eng. **11**(4), 331–339 (1999)
19. Malvar, L.J., Ross, C.A.: Review of strain rate effects for concrete in tension. ACI Mater. J. **95**, 735–739 (1998)
20. Bažant, Z.P., Oh, B.H.: Crack band theory for fracture of concrete. Matériaux et construction **16**(3), 155–177 (1983)
21. Ramezansefat, H., Barros, J., Rezazadeh, M.: A model for the simultaneous prediction of the flexural and shear deflections of statically determinate and indeterminate reinforced concrete structures. Struct. Concrete **18**(4), 618–633 (2017)
22. Othman, H., Marzouk, H., Sherif, M.: Effects of variations in compressive strength and fibre content on dynamic properties of ultra-high performance fibre-reinforced concrete. Constr. Build. Mater. **195**, 547–556 (2019)
23. Zhang, X., Ruiz, G., Tarifa, M., Cendón, D., Gálvez, F., Alhazmi, W.: Dynamic fracture behavior of steel fiber reinforced self-compacting concretes (SFRSCCs). Materials **10**(11), 1270 (2017)
24. RILEM TC 50-FMC Determination of the fracture energy of mortar and concrete by means of three-point bend tests on notched beams. Mater. Struct. **18**, 99–101, (1985)

Microstructural and Chemical Effects of Accelerated Carbonation of High-Volume Fly Ash Binders in View of Carbon Sequestration

Philip Van den Heede and Nele De Belie

Abstract According to the Intergovernmental Panel on Climate Change (IPCC), global climate change induced temperature rise should remain below 1.5 °C by 2100 to guarantee the livability of our planet. This can only be achieved by immediate action by all sectors, including the cement and concrete industry. Carbonation of cementitious materials in presence of atmospheric CO_2 can on the one hand hamper the durability when used in steel-reinforced applications prone to corrosion. On the other hand, the binding of CO_2 through carbonation in non-steel reinforced applications could actually be of interest. When considering the worldwide application of cement-bound materials in construction along with their CO_2 sequestration potential, CO_2 emissions inherent to Portland cement production can partly be compensated for. Obviously, for such CO_2 uptake estimations to be reliable, a thorough understanding of the carbonation behavior is imperative. In this paper, this was studied for high-volume fly ash (HVFA) binder systems with a low production related carbon footprint. HVFA mortar was subjected to accelerated carbonation experiments at 1% and 10% CO_2. Carbonation-induced changes in microstructure were assessed using mercury intrusion porosimetry (MIP) while the changes in proportioning of CH and C–S–H carbonation reaction products were measured with thermogravimetric analysis (TGA). A carbonation-induced coarsening of the pore structure was observed which is more pronounced at 10% CO_2 levels and attributable to more dominant C–S–H carbonation. Also the calcium carbonate content in the carbonated zone tends to significantly increase with the applied CO_2%.

Keywords Carbonation · Fly ash · Accelerated testing · Mercury intrusion porosimetry (MIP) · Thermogravimetric analysis (TGA)

P. Van den Heede (✉) · N. De Belie
Magnel-Vandepitte Laboratory for Structural Engineering and Building Materials, Ghent University, Ghent, Belgium
e-mail: philip.vandenheede@ugent.be

E. B. Pereira et al. (eds.), *Proceedings of the 3rd RILEM Spring Convention and Conference (RSCC 2020)*, RILEM Bookseries 32,
https://doi.org/10.1007/978-3-030-76547-7_3

1 Introduction

Recent reports by the Intergovernmental Panel on Climate Change (IPCC) indicate that CO_2 emissions should be reduced as much as needed to keep global temperature increase relative to pre-industrial levels below 1.5 °C by 2100. This is required for Earth to remain livable. Therefore, global net CO_2 emissions need to decline by about 45% from 2010 levels, reaching net zero around 2050 [1]. The cement industry, accountable for no less than 8% of the global anthropogenic CO_2 emissions [2], is thus being encouraged strongly to cut down on its carbon footprint. This can be done by shifting more to binders with considerable portions of carbon-intensive Portland clinker replaced by supplementary cementitious materials (SCMs). On the one hand this will often result in concrete that is more susceptible to carbonation-induced corrosion of embedded reinforcing steel. On the other hand, the reduced CO_2 buffering capacity of these binders may diminish the considerable CO_2 sequestration potential during the use and end-of-life phase. As calculated by Xi et al. [3], the global carbon uptake between 1930 and 2013 through cement carbonation during service life and after demolition and secondary use of concrete waste represents a large and growing net sink of CO_2, growing from 0.10 GtCarbon yr^{-1} in 1998 to 0.25 GtCarbon yr^{-1} in 2013. The study shows that besides focusing on the CO_2 emissions in the production stage of cement-bound materials, also their CO_2 sequestration potential should be addressed. However, Van den Heede and De Belie further investigated this for binder systems with a high SCM content, i.e. High-Volume Fly Ash (HVFA) binders in which 50% of the carbon intensive ordinary Portland cement (OPC) content was replaced by pozzolanic fly ash from coal-fired electrical power plants. They found that for these types of binders the CO_2 sequestration potential as estimated from accelerated carbonation tests may be significantly higher than the natural one at atmospheric CO_2 concentration [4]. This can probably be attributed to differences in carbonated phase proportioning (%CH carbonation versus %C–S–H carbonation) and the resulting response of the microstructure. These aspects have been studied in this paper via comparative Mercury Intrusion Porosimetry (MIP) and thermogravimetric analysis (TGA) experiments on HVFA mortar that was carbonated in a slightly accelerated way at 1% CO_2 and in a highly accelerated way at 10% CO_2.

2 Materials and Methods

2.1 Mix Proportions

All tests were performed on HVFA mortar. The proportioning of the sand and binder for one batch of mortar was the same as for the standard mortar specified in NBN EN 196–1 and amounted to 1350 g and 450 g, respectively. The binder portion consisted for 50% of Ordinary Portland Cement CEM I 52.5 N and for 50% of class F fly

ash. The applied water-to-binder (W/B) ratio equaled 0.55, which is higher than the 0.50 value which is normally prescribed for a standard mortar but in agreement with the NBN EN 206–1 maximum W/B requirements for exposure class XC3. A high cement replacement level was used to make sure there was less carbonatable material, i.e. portlandite, available. This ensures a lower buffer capacity for the penetrating CO_2 and thus a faster inward movement of the carbonation front [5]. A W/B ratio of 0.55 facilitated a higher porosity, and thus also a faster ingress of CO_2.

2.2 Sample Preparation, Preconditioning and Carbonation Tests

HVFA mortar cubes with a 100 mm side were cast. Next, they were stored in a curing chamber conditioned at 20 °C and 95% RH. Demolding took place after 24 h whereupon the cubic samples were stored again in the same curing chamber until the age of 7 days. Then, they were dried in an oven at 40 °C for 4 days to ensure a uniform moisture distribution. Subsequently, they were carefully sealed on all sides except for one exposure side. In this condition, they remained in a climate room at 20 °C and 60% RH for 3 days. At this point, all specimens were ready to be subjected to the envisaged carbonation experiments: a slightly accelerated carbonation test at 1% CO_2 and a highly accelerated carbonation test at 10% CO_2. For both carbonation experiments, temperature and relative humidity amounted to 20° C and 60% RH during exposure. The total exposure period amounted to 9 weeks.

2.3 Sample Collection and Preparation for MIP and TGA

When reaching the full carbonation exposure period, one cube per test series was split and the carbonation front was visualized with phenolphthalein (colorless area: carbonated; purple area: non-carbonated; cf. carbonation-induced pH drop). From the central area of each split cube half a 15 mm wide slice was taken containing both the carbonated and uncarbonated zone of the sample. Where possible the carbonated zone was subdivided into multiple layers to further explore carbonation induced changes in microstructure as a function of carbonation depth. This resulted in two carbonated layers for the sample exposed to 1% CO_2 for 9 weeks and 4 carbonated layers for the sample exposed to 10% CO_2 for 9 weeks. For each cube half a sample was also taken from the non-carbonated area. Each slice was cut in multiple pieces with a thickness of around 6–7 mm. The obtained prismatic pieces were preconditioned as follows. In accordance with Durdzinski et al. [6], the slices were immersed in isopropanol for 7 days to stop hydration by solvent exchange. Afterwards, they were stored in vacuum desiccators at −1.0 bar for 7 days to remove the isopropanol. Next, the samples were kept in vacuum sealed plastic bags until the time of MIP and TGA.

2.4 Mercury Intrusion Porosimetry (MIP)

Overall porosity and average pore diameter were determined using a PASCAL 140 + 440 Series MIP apparatus of Thermo Fischer Scientific and the software application SOL.I.D. The mercury pressure range considered during testing equaled 200 kPa–200 MPa. The pore size range of interest ranged from 0.01 to 10 μm. This corresponds with the capillary pore system [7]. Per exposure condition and available depth from the exposure surface two replicates were tested.

2.5 Thermogravimetric Analysis (TGA)

Per exposure condition and available depth from the exposure surface three samples were mechanically crushed until all material could pass a sieve with a 63 μm mesh size. Powder samples were collected from them and subjected to TGA. For each analysis around 50 mg was heated from 20 °C to 1100 °C at a rate of 10 °C/min under an inert atmosphere (nitrogen). The mass change as a function of temperature was recorded with a Netzsch Sta 449 F3 Jupiter TGA apparatus. The results of the TGA measurements were analyzed in the Proteus software provided by Netzsch. To enable adequate comparison between the three carbonation conditions under investigation, the recorded mass losses during TGA were expressed in % m/m relative to the residual mass of the powdery sample at 1100 °C whereupon everything was recalculated relative to the binder portion of this residual mass. Also note that the mass losses recorded during TGA were always corrected for the concurrent dehydration of other hydrated compounds. This was done in accordance with Baert [8]. For the determination of the calcium carbonate (CC) content for each studied carbonation condition, the same calculation approach of determining the total carbonation-induced CC content and the proportioning of %CH carbonation to %C–S–H carbonation was used as in Van den Heede et al. [9]. The latter calculation approach is very similar to the one proposed by Borges et al. [10].

3 Results and Discussion

3.1 Overall Porosity and Average Pore Diameter

With respect to the porosity that corresponds with the capillary pore size range (0.01 μm < pore diameter < 10 μm) the most obvious differences can be observed between the carbonated and non-carbonated layers (Fig. 1a).

For each considered CO_2 concentration during exposure (1% and 10% CO_2) the non-carbonated layer (1%N: 16.4 ± 0.6%, 10%N: 16.3 ± 0.1%) is always characterized by a lower porosity than the carbonated layers (1%L1: 18.1 ± 0.4%, 10%L1:

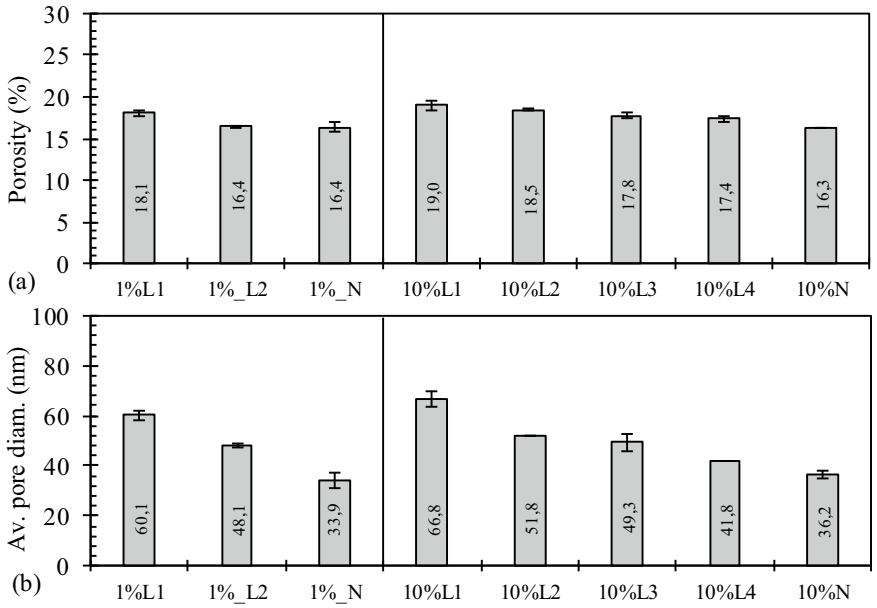

Fig. 1 Porosity (**a**) and average pore diameter (Av. pore diam.) (**b**) as determined with MIP

19.0 ± 0.6%). Literature usually speaks of a densification of the pore structure due to carbonation, yet mainly with respect to OPC binder systems. CH carbonation has the upper hand in such systems. The volumetric increase that goes with it tends to partially fill the pore system. For binder systems that contain high volumes of SCMs, the limited availability of CH leads to more carbonation of the C–S–H instead which tends to coarsen the pore structure [10]. The HVFA mortar under investigation belongs to the latter group. Thus, it seems quite logical that the carbonated layers are characterized by a higher porosity than the corresponding non-carbonated area. When looking at the sample series with more than one carbonated layer available, the porosity also seems to decrease as a function of carbonation depth. Comparison of the results obtained at 1% and 10% CO_2 reveals for the outer carbonated layer an increase in porosity from 18.1 ± 0.4% (1%L1) to 19.0 ± 0.6% (10%L1). When looking at corresponding layers L2, one notices an increase from 16.4 ± 0.6% (1%L2) to 18.5 ± 0.1% (1%L2).

Apart from inspecting overall porosity, one can also look at the average pore diameters calculated by the SOL.I.D. software for the same capillary pore size range (Fig. 1b). This analysis could reveal whether a shift in governing pore size range occurs that is dependent on the applied CO_2 concentration. In line with the porosity results, the average pore diameters (34–36 nm) for the samples taken from the non-carbonated region of the cubic specimens after carbonation at 1% and 10% CO_2, are substantially lower than the values recorded for the samples taken from the carbonated region. For the layers carbonated at 1% CO_2 (1%L1, 1%L2) and 10% CO_2 (10%L1,

10%L2, 10%L3, 10%L4), the average pore diameters clearly decrease as a function of carbonation depth. For 1% CO_2, the average diameters drop from 60 (1%L1) to 48 nm (1%L2). For 10% CO_2, the corresponding values drop from 67 (10%L1) to 42 nm (10%L4). The average pore diameters for corresponding carbonated layers (e.g. L1) tend to increase with the applied CO_2 concentration from 60 for 1% CO_2, to 67 nm for 10% CO_2. In other words, carbonation at elevated CO_2 concentrations results in a coarsening of the pore structure for the capillary pore range.

3.2 Calcium Carbonate Content and CH to C–S–H Carbonation Proportioning

The recorded CC contents with TGA show that for corresponding layers (e.g. L1) and the same sample age there is an obvious increase with the imposed CO_2 concentration (Fig. 2a: 1%L1: 32%, 10%L1: 38%). This dependency on the applied CO_2 concentration also follows from the comparison between 1%L2 and 10%L2. The TGA results do not suggest a dependency on the carbonation depth. When going from L1 to L2 one can observe an increase in total CC content after being carbonated at 1% and 10% CO_2. At higher carbonation depths it then tends to decrease again for 10% CO_2.

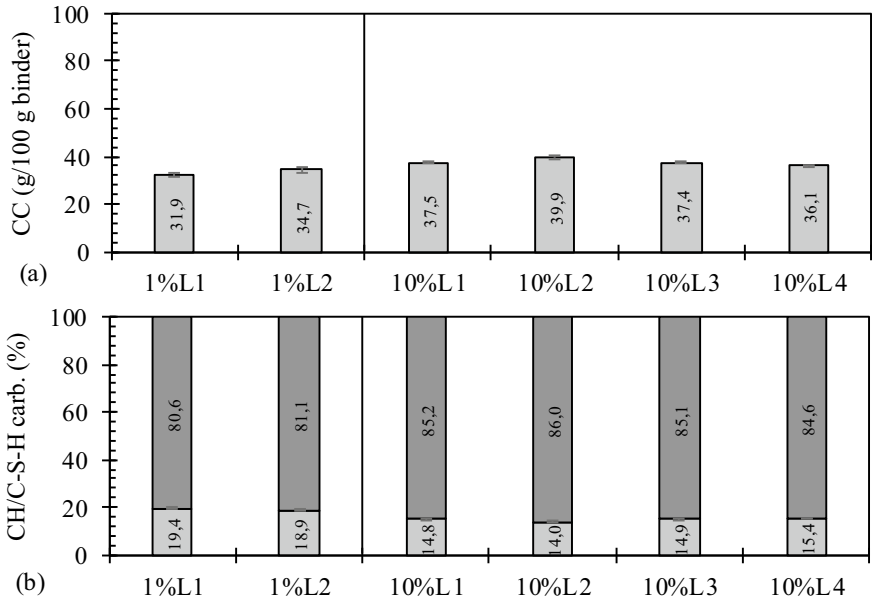

Fig. 2 Calcium carbonate (CC) content (**a**) and CH to C–S–H carbonation proportioning (CH/C–S–H carb.: light grey/dark grey) (**b**) after CO_2 exposure as determined with TGA

When comparing the calculated proportioning of %CH carbonation and %C–S–H carbonation for corresponding layers with the same sample age (Fig. 2b), one notices a decrease in % of carbonated CH with increasing CO_2 concentration. For the first layer containing the exposure surface, the %CH carbonation goes from 19.4 ± 0.5% at 1% CO_2 (1%L1) to 14.8 ± 0.3% at 10% CO_2 (10%L1). A similar decreasing trend is also observed for the corresponding layers L2 after carbonation at 1% CO_2 (1%L2) and 10% CO_2 (10%L2). From comparison of the values obtained for the 4 subsequent layers carbonated at 10% CO_2, the proportioning of %CH carbonation and %C–S–H carbonation does not seem to be a clear function of the considered depth from the exposure surface. This also seems to be the case for carbonation at 1% CO_2. Subsequent layers L1 and L2 are characterized by a very similar proportioning of %CH carbonation and %C–S–H carbonation.

4 Conclusions

The use of highly accelerated carbonation experiments at elevated CO_2 levels to estimate the CO_2 sequestration potential of HVFA binders systems may induce important changes in the microstructure and carbonated phase. Going from slightly accelerated carbonation at 1% CO_2 to highly accelerated carbonation tests at 10% CO_2 causes clear changes. MIP experiments showed a coarsening of the pore structure involving a larger overall porosity and a shift towards larger average pore diameters. TGA experiments seem to indicate that this is to be attributed to an increase in %C–S–H carbonation at the expense of %CH carbonation.

Acknowledgements Philip Van den Heede is a postdoctoral research fellow of the Research Foundation—Flanders (FWO) (project No. 3E013917). The financial support of FWO is gratefully acknowledged.

References

1. Masson-Delmotte, V., et al. (eds.): Global warming of 1.5 °C, an IPCC special report on the impacts of global warming of 1.5 °C above pre-industrial levels and related global greenhouse gas emission pathways in the context of strengthening the global response to the threat of climate change, sustainable development, and efforts to eradicate poverty. IPCC (2018)
2. Andrew, R.M.: Global CO_2 emissions from cement production. Earth Syst. Sci. Data **10**, 2213–2239 (2018)
3. Xi, F., et al.: Substantial global carbon uptake by cement carbonation. Nat. Geosci. **9**, 880–883 (2016)
4. Van den Heede, P., De Belie, N.: CO_2 sequestration potential of High-Volume Fly Ash (HVFA) mortar when based on accelerated carbonation tests. In: Djerbi, A., et al. (eds.) International Workshop on CO_2 Storage in Concrete (CO_2s to 2019), pp. 186–192. Iffstar, Marne La Vallée (2019)

5. Lammertijn, S., De Belie, N.: Porosity, gas permeability, carbonation and their interaction in high-volume fly ash concrete. Mag. Concr. Res. **60**, 535–545 (2008)
6. Durdzinski, P.T., et al.: Outcomes of the RILEM round robin on degree of reaction of slag and fly ash in blended cements. Mater. Struct. **50**, 1–15 (2017)
7. Gruyaert, E.: Effect of blast-furnace slag as cement replacement on hydration, microstructure, strength and durability of concrete. Ph.D. thesis. Ghent University, Ghent (2011)
8. Baert, G.: Physico-chemical interactions in Portland cement—(high volume) fly ash binders. Ph.D. thesis. Ghent University, Ghent (2009)
9. Van den Heede, P., De Schepper, M., De Belie, N.: Accelerated and natural carbonation of concrete with high volumes of fly ash: chemical, mineralogical and microstructural effects. R. Soc. Open Sci. **6**(181665), 17 (2019)
10. Borges, P.H.R., Costa, J.O., Milestone, N.B., Lynsdale, C.J., Streatfield, R.E.: Carbonation of CH and C–S–H in composite cement pastes containing high amounts of BFS. Cem. Concr. Res. **40**, 284–292 (2010)

Durability of Slag-Blended Cementitious Materials Interacts with High Concentration of Sodium Sulphate

Yogarajah Elakneswaran, Chuang Li, Tomohiro Kajio, Eiji Owaki, Masataka Ogino, and Toyoharu Nawa

Abstract The low-level waste generated from boiling water reactor (BWR) power plant consists of very high concentration of sodium sulphate, higher than 25 mass% of Na_2SO_4. These liquid wastes are solidified with cementitious materials at elevated temperature. A critical concern of highly concentrated sodium sulphate nuclear waste with co-hydrating of cementitious materials is the degradation of the materials by chemical interaction of sulphate with cement hydrates and crystallisation of sodium sulphate as well as the deterioration due to external sulphate attack. Sulphate ions cause a serious chemical deterioration to cement matrix through either forming expansive products of ettringite and gypsum or sodium sulphate crystallization. In addition, a very high concentration of sodium sulphate solution could induce to form U-phase $[(CaO)_4(Al_2O_3)_{0.9}(SO_3)_{1.1}(Na_2O)_{0.5}{:}16H_2O]$ and this may cause deterioration to cement matrix. A potential variation of the physicochemical properties of the materials because of internal and external sulphate interaction is the important factor to maintain the performance over the time scale required. The purpose of this study is to investigate the degradation of hydrated Portland cement and slag-blended cementitious materials, where the cement is replaced by 42% hydrated with 13% of Na_2SO_4 by weight, in sodium and magnesium sulphate solutions. The hydrated samples having diameter between 2.38 and 4.75 mm were immersed in 1300 mmol/L Na_2SO_4 and $MgSO_4$ for 28 days and phase changes as a result of sulphate interaction were investigated. In addition, the hydrated samples exposed to water and 1300 mmol/L of Na_2SO_4 and $MgSO_4$ for 6 months and spatial mineralogical distribution due to sulphate ingress from the external source or from the pore solution was determined. The results of shows a significant formation of ettringite due to sulphate

Y. Elakneswaran (✉) · C. Li
Division of Sustainable Resources Engineering, Faculty of Engineering, Hokkaido University, Kita 13, Nishi 8, Kita-ku, Sapporo 060-8628, Japan
e-mail: elakneswaran@eng.hokudai.ac.jp

T. Kajio · E. Owaki · M. Ogino
Civil Structure and Material Research Section, Civil Engineering Research Institute Technology Centre, Taisei Corporation, Shinjuku, Japan

T. Nawa
Hokkaido University, Kita 8, Nishi 5, Kita-ku, Sapporo 060-0808, Japan

E. B. Pereira et al. (eds.), *Proceedings of the 3rd RILEM Spring Convention and Conference (RSCC 2020)*, RILEM Bookseries 32,
https://doi.org/10.1007/978-3-030-76547-7_4

ingress and U-phase instability. The type of exposure solution and the replacement of slag influence the dissolution of U-phase and consequent formation of ettringite causes severe degradation.

Keywords Sulphate attack · Leaching · U-phase · Hydration

1 Introduction

Cementitious materials play an important role in solidifying low- or intermediate-level nuclear waste repositories mainly because it can act as barrier for transport of radioactive waste from repositories to external environment [1–3]. The liquid radioactive waste is evaporated before solidifying with cementitious materials, which induces to form high concentration of salts such as sodium sulphate in the waste [4]. In addition, sulfuric acid has been used to remove the precipitates formed in the cooling pipes, leading to form very high concentration of sodium sulphate higher than 25% by weight in the low-level radioactive waste [5]. Solidification of high content of sodium sulphate into the cementitious materials may deteriorate the material and the nuclear waste repository facilities. Therefore, physicochemical interaction of high concentration of sodium sulphate with hydrating cementitious materials is necessary to propose a suitable material for the solidification.

Internal or external sulphate attack is a serious durability problem for the cementitious materials exposed to sulphate environments. Many studies have reported the physical and chemical sulphate attack in cementitious materials, but the associated mechanisms and influencing parameters are incomplete [1–3]. Elakneswaran et al., has recently performed modelling study to evaluate the long-term performance of cementitious materials under sodium sulphate interaction [6]. The interaction of sulphate with cement hydrates form expansive products of ettringite, gypsum, and thaumasite [1]. In addition, the sodium sulphate crystals such as mirabilite ($Na_2SO_4{:}10H_2O$) and thenardite (Na_2SO_4) or their phase changes (mirabilite to thenardite or vice versa) can cause the deterioration [2]. The reaction of cement hydrates with high concentration of sodium sulphate induces in the formation of U-phase [$(CaO)_4(Al_2O_3)_{0.9}(SO_3)_{1.1}(Na_2O)_{0.5}{:}16H_2O$ [7–10]. The stability of U-phase and its conversion to ettringite have not fully understood because of limited studies. Authors' recent research has studied the thermodynamic properties of U-phase and its stability in various environments [10–12]. The objective of this study is to analysis the hydration of white Portland cement (WPC) and slag-blended cement (42% of cement replacement) in sodium sulphate solution as well as their deterioration in sodium and magnesium sulphate solution.

2 Experimental

White Portland cement and blast furnace slag were used for experiments. WPC and slag-blended WPC (42% of slag replacement) were mixed with 13% of Na_2SO_4 solution with water to binder ratio of 0.6 to determine the amount of hydrates formed as a function of curing period. After the curing, the specimens were grinded to fine powders and analysed by X-ray diffraction (XRD). In the Rietveld analysis, clinkers, ettringite, monosulphate, portlandite, calcite, hydrotalcite, and thenardite were used as targets. The known amount of synthesised U-phase was mixed with the hydrated WPC and XRD patterns were obtained to draw the calibration curve for the intensity of U-phase. The amount of U-phase in hydrates was calculated by the ratio of intensity of XRD pattern. The specimens were crushed and sieved to provide samples of diameter between 2.38 and 4.75 mm. Around 25 g of the sample was immersed into known sulphate concentration of 500 mL solution for a period of 3, 7, and 28 days. The adopted sulphate solutions were 1300 mmol/L of Na_2SO_4 and $MgSO_4$. Once the specified exposure period was completed, the samples were ground, and the powders were used for XRD and Rietveld analysis to determine the phases and its composition.

The summary of sample preparation and exposure conditions for external sulphate ingress experiment are given in Table 1. The cylindrical specimens after the curing were sealed with epoxy resin except the bottom of circular surface which will face to exposure solution. The sealed specimens were exposed to pure water and 1300 mmol/L of Na_2SO_4 and $MgSO_4$ solution for 6 months (Table 1). The epoxy resin of the specimen was removed after the exposure period, and the specimen was ground using file from the exposure surface in 2 mm depth. The collected powder was used for XRD measurement to determine mineralogical composition.

Table 1 Experimental outline

Cement	WPC
Slag replacement ratio (%)	0, 42
Mixing solution	13% Na_2SO_4 solution
Water to binder	0.6
Curing condition	Sealed curing for 28 days at 50 °C
Exposure solution	• Pure water
	• 1300 mmol/L Na_2SO_4
	• 1300 mmol/L $MgSO_4$
Exposure period	6 months
Exposure solution to solid ratio	3:1

3 Results and Discussion

3.1 Solid Products of Slag-Blended Cement Hydrating in Na_2SO_4 Solution

The XRD/Rietveld analysis was used to characterise the hydration products formed, and the results are shown in Fig. 1 as a function of hydration time. The presence of Na_2SO_4 in the solution could influence the hydration of clinker minerals and the reaction of slag. In addition to the main hydration products of C–S–H, portlandite, and ettringite, U-phase and thenardite were formed for the hydration of slag-blended cement hydrated with high concentration of sodium sulphate, but the formation of monosulphate could not observe. Although the types of hydration products are the same in both hydrating WPC and slag-blended WPC, the reaction of slag modifies

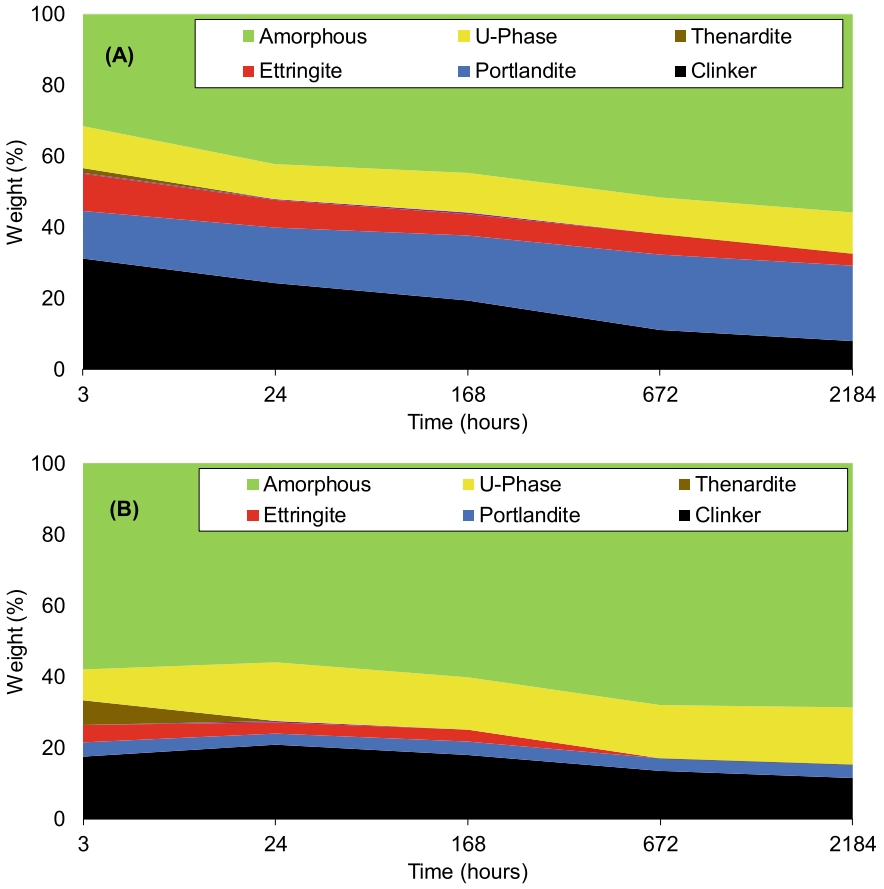

Fig. 1 Phase distribution of hydrating, **a** WPC; **b** slag-blended WPC, in 13% of Na_2SO_4 solution

its amount. The formation of U-phase in highly concentrated Na_2SO_4 environments consistent with previous studies [7–9], but it co-exists with ettringite which contradicts the previous studies' results. The hydration of cement and a partial replacement of cement by slag enhance the U-phase formation at later age.

3.2 *Effect of Sulphate Solution on the Stability of Hydration Products*

Figure 2 shows the change of phases in the hydrated WPC, which was hydrated in 13% of Na_2SO_4 solution for 28 days, exposed to sulphate solution for a period of 3, 7, and 28 days. The stability of U-phase and its conversion to ettringite depend on the type of solution. Magnesium sulphate solution converts the U-phase at early age, but the Na_2SO_4 gradually changing the U-phase to ettringite and consumes longer period for the transformation; the U-phase is completely changed to ettringite at 28 days of exposure. As observed in the hydration (Fig. 1), both U-phase and ettringite are exist together in the sodium sulphate solution before the U-phase converted to ettringite at 28 days. Further, the sulphate solution induces portlandite dissolution and correlates with gypsum formation. Magnesium sulphate solution significantly influences the portlandite dissolution and gypsum formation and destabilizes the amorphous as well. The dissolved portlandite leads to form brucite when the samples exposed to magnesium sulphate solution.

The results of slag-blended exposed to 1300 mmol/L Na_2SO_4 and $MgSO_4$ are shown in Fig. 3. The addition of slag affects amounts of phases present in the hydrated samples before it exposed to sulphate solution: lower portlandite and higher U-phase compared to hydrated WPC. Although the phase-changes of slag-blended cement exposed to sulphate solution is similar to WPC, the initial amount of hydrates due to the slag reaction affect the behaviour. Again, as observed in WPC, U-phase dissolution and ettringite formation relate to type of the sulphate solution. Magnesium sulphate solution causes severe degradation, but it limits brucite formation due to lower amount of initial portlandite in the hydrated slag-blended cement. Based on the results, it can be inferred that the U-phase is not stable in sodium or magnesium sulphate solution up to 1300 mmol/L.

3.3 *Degradation Due to External Sulphate Ingress*

The hydrated WPC and slag-blended WPC, which were hydrated in 13% of Na_2SO_4 solution for 28 days, immersed in water and sulphate solution for 6 months. The quantified solid phase changes as a function of depth in terms of weight percentage is shown in Fig. 4, and the visual image of exposed surface is shown in Fig. 5. The deterioration for WPC exposed to sodium sulphate is very severe and the results

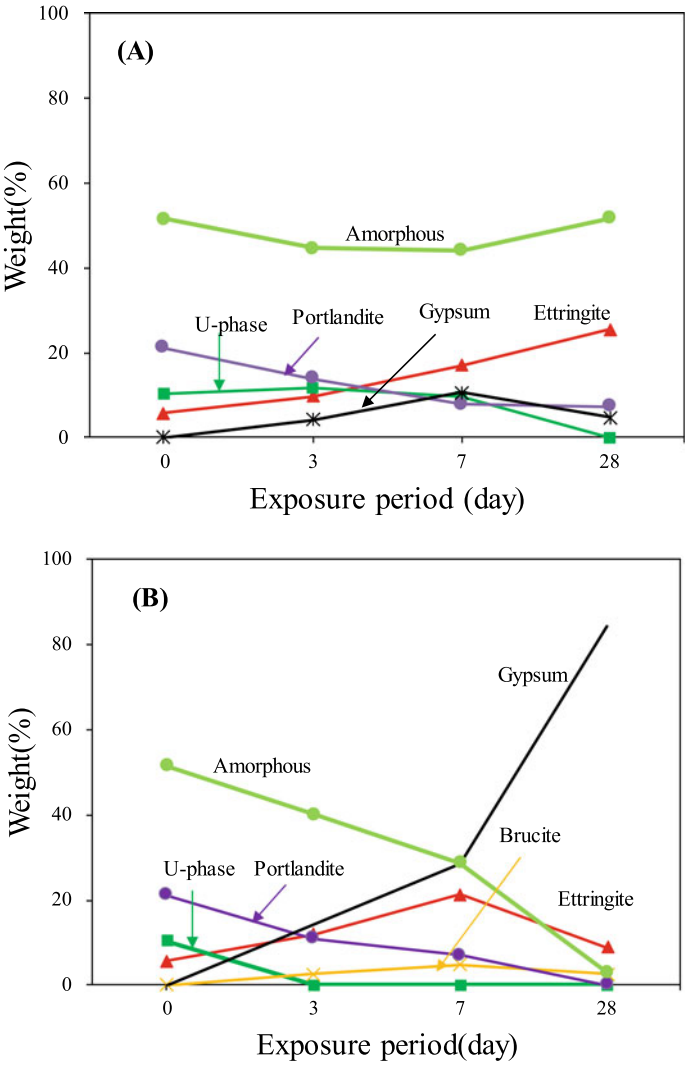

Fig. 2 Change of hydration products in hydrated WPC exposed to **a** 1300 mmol/L Na_2SO_4; **b** 1300 mmol/L $MgSO_4$

are plotted until 18 mm while other results are shown up to 9 mm. The distribution of ettringite, portlandite, clinker, gypsum, and gypsum are plotted in the figure. The replacement of WPC by slag modifies the mineralogy of hydration products as well as their amount during the hydration reaction with sodium sulphate solution. The dissolution of portlandite was observed close to the exposure surface and it is disappeared at the surface of slag-blended case as the initial content of the phase is much lower than WPC. The dissolution of portlandite induces to form gypsum for

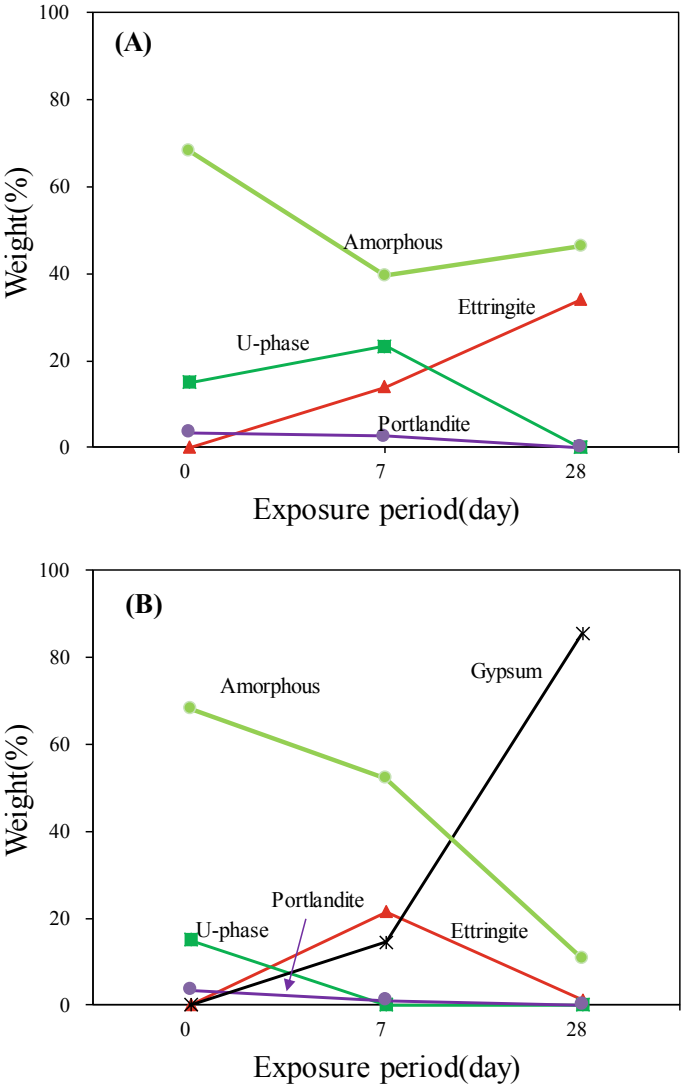

Fig. 3 Change of hydration products in slag-blended WPC exposed to **a** 1300 mmol/L Na_2SO_4; **b** 1300 mmol/L $MgSO_4$

the samples exposed only to magnesium sulphate solution. As expected, the clinker miners do not affect by the ingress of sulphate.

The U-phase is not stable as the hydrated paste exposed to water or sulphate solution; it dissolves and transforms to ettringite during the exposure. In WPC, it is completely dissolved as a result of exposure for 6 months. The type of exposure

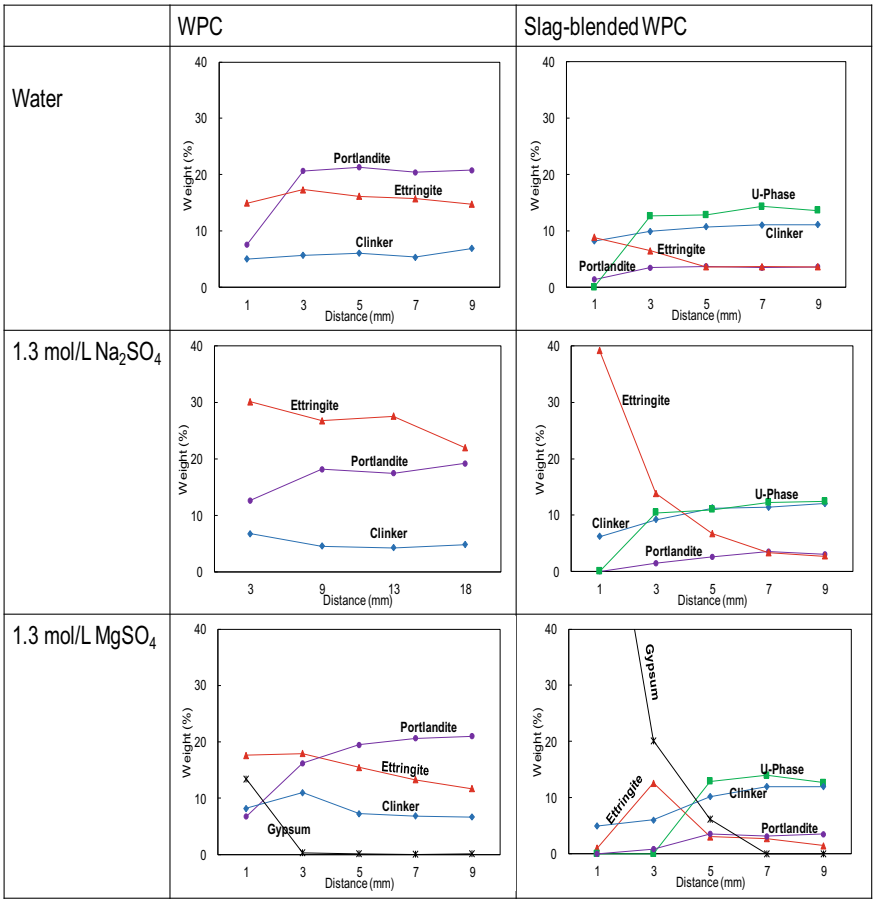

Fig. 4 Spatial distribution of solid phases deduced by XRD/Rietveld analysis in WPC and slag-blended WPC exposed to water, 1300 mmol/L Na_2SO_4, and 1300 mmol/L $MgSO_4$ water for 6 months

solution significantly influences the U-phase dissolution and thus ettringite formation. The samples immersed in water show higher instability of U-phase than that exposed to sulphate solution. The diffusion of ions from pore solution to external solution causes the instability of U-phase as it is in equilibrium at very high sodium and sulphate solution [7–10]. The surface of hydrated WPC exposed to water shows cracks in Fig. 5, which validates U-phase to ettringite transformation. The ettringite formation due to external sulphate ingress and destabilisation of U-phase influence the deterioration of WPC and the quantity of ettringite determines the severity of the damage (Fig. 5). Although brucite did not show in Fig. 4, it is precipitated at the surface as shown in Fig. 5 and acts as barrier for further sulphate ingress. Higher dissolution of portlandite and lower formation of ettringite in Fig. 4 are the proof of brucite formation and its role on the surface.

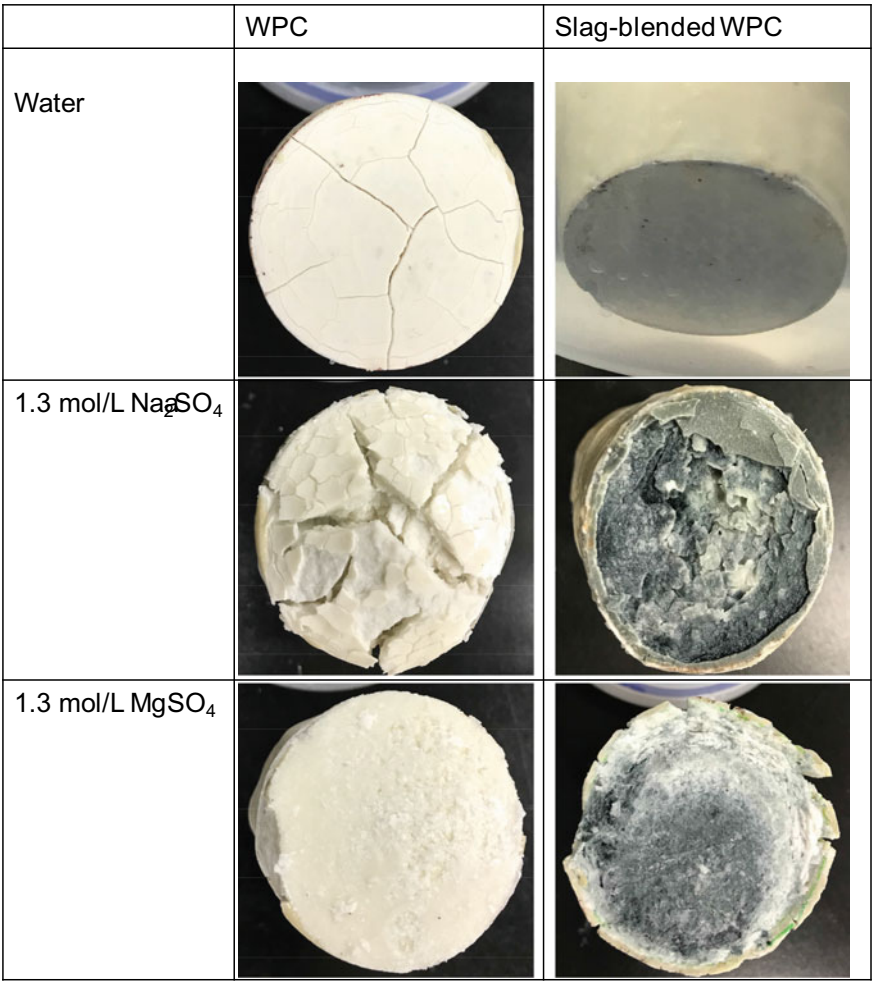

Fig. 5 Surface appearance of WPC and slag-blended WPC exposed to water, 1300 mmol/L Na_2SO_4, and 1300 mmol/L $MgSO_4$ water for 6 months

The slag-blended WPC shows severe deterioration than WPC for the samples exposed to sulphate solution. The formation of ettringite in sodium sulphate solution and gypsum formation in magnesium sulphate solution cause the deterioration. Initial of U-phase in slag-blended WPC, which is higher than WPC, contributes to form a large amount of ettringite. In addition, the slag-blended case has significant amount of stable U-phase in the core of the sample. Although the surface of slag-blended cement deteriorates severely, the degradation depth in slag-blended cement is smaller than WPC for the case of water and sodium sulphate.

4 Conclusions

The hydration and performance of WPC and slag-blended WPC hydrated with 13% of Na_2SO_4 are evaluated in this study. Based on the experimental results, the following conclusions were made.

- Both hydrated WPC and slag-blended WPC produce similar hydrates with time, but the U-phase in slag is higher than that of without slag.
- The U-phase is dissolved and transformed to ettringite as the hydrated cement exposed to water or sulphate solution. The kind of sulphate solution affects the stability U-phase and thus ettringite formation.
- When the U-phase containing WPC and slag-blended samples exposed to water and sulphate solution, the U-phase is fully dissolved and converted to ettringite in WPC, but not in slag-blended case.
- In both types of cement, ettringite formation due to sulphate reaction with cement hydrates and/or destabilisation of U-phase is the main deterioration mechanism in the sample exposed to water and sodium sulphate solution, however the gypsum formation controls the degradation in the magnesium sulphate case.

References

1. Scrivener, K., Skalny J.: International RILEM workshop on internal sulphate attack and delayed ettringite formation. In: Proceeding: RILEMPublications (2004)
2. Rodriguez-Navarro, C., Doehne, E., Sebastian, E.: How does sodium sulfate crystallize? Implications for the decay and testing of building materials. Cem. Concr. Res. **30**(10), 1527–1534 (2000)
3. IAEA: Near surface disposal of radioactive waste. IAEA Safety Standards Series, Requirements (1999)
4. Li, G., et al.: The U phase formation in cement-based systems containing high amounts of Na_2SO_4. Cem. Concr. Res. **26**, 27–33 (1996)
5. Owaki, E., Niwase, K., Akatsuka, M., Kudo, J.: Effect of curing temperature on cement paste containing sodium sulphate. JSCE Ann. Meet. **67**, 57–58 (2012)
6. Elakeswaran, Y., et al.: Modelling long-term durability performance of cementitious materials under sodium sulphate interaction. Appl. Sci. **8**, 2597 (2018)
7. Li, G., et al.: Synthesis of the U phase ($4CaO{\cdot}0.9Al_2O_3{\cdot}1.1SO_3{\cdot}0.5Na_2O{\cdot}16H_2O$). Cem. Concr. Res. **27**, 7–13 (1997)
8. Li, G., et al.: Expansion mechanism associated with secondary formation of the U phase in cement-based systems containing high amounts of Na_2SO_4. Cem. Concr. Res. **26**, 195–201 (1994)
9. Champenois, J.B., et al.: Influence of sodium borate on the early age hydration of calcium sulfoaluminate cement. Cem. Concr. Res. **70**, 83–93 (2015)
10. Kajio, T., et al.: Characterization of U-phase and its prediction in cementitious materials. In: NUWCEM (2018)
11. Elakneswaran, Y., et al.: Formation and stability of u-phase in cementitious materials under sulphate attack. In: SSMS (2019)
12. Li, C., et al.: Sulphate attack in slag-blended cementitious materials hydrated with sodium sulphate. In: SCMT5 (2019)

Design for Disassembly of Super-Light Concrete Structures

Philip S. Halding and Kristian D. Hertz

Abstract Concrete structures are sometimes believed to be less sustainable and difficult to disassemble properly compared to structures of other materials. However, when a holistic design approach and novel technology is applied in the design of concrete structures, they can be more sustainable than other solutions and designed for disassembly. A novel concrete technique, developed at the Technical University of Denmark, the Super-Light Deck, is one example of this new green generation of concrete. Pre-stressed deck elements of Super-Light concrete consist of a combination of light aggregate concrete and normal concrete. The flat decks can be used individually in buildings as horizontal divisions, or several decks can be joined together by post-tensioning in an arch shape for use in bridges or in vaulted roofs (the pearl-chain method). The technology makes it possible to create beamless structures by having blade joints between deck and support in buildings. Furthermore, an arch shaped structure consisting of several Super-Light Decks can be joined to the supporting structure by a designed "end-element" with a behaviour comparable to a concrete hinge. Both of these solutions are presented in the paper. They are novel designs, where the disassembly process is taken into account, and it will be possible to dismantle and reuse the Super-Light Deck elements, at the end of the lifetime of the structure.

Keywords Arch · Connection · Sustainable · Beamless building · Pearl-chain method

1 Introduction

Professor Kristian D. Hertz invented and patented the concept of Super-Light Structures at the Technical University of Denmark a decade ago. The basis of the technology is to optimize resources by utilizing a normal strong concrete where it is

P. S. Halding (✉) · K. D. Hertz
Department of Civil Engineering, Technical University of Denmark (DTU), Kongens Lyngby, Denmark
e-mail: phsh@byg.dtu.dk

E. B. Pereira et al. (eds.), *Proceedings of the 3rd RILEM Spring Convention and Conference (RSCC 2020)*, RILEM Bookseries 32,
https://doi.org/10.1007/978-3-030-76547-7_5

required to take compression in a structure, and fill out the remaining space with a less strong stabilizing light-aggregate concrete. The total structure will then be less heavy compared to a typical concrete structure, and furthermore, production and transportation of the super-light concrete structures emits only approximately 1/2 to 2/3 of the CO_2 compared to regular concrete structures [1].

The first practical use of the technology was in pre-cast and pre-tensioned deck elements for buildings—so called SL-Decks [2]. The SL-Deck have been through a development process in the past years, but it still relies on the combination of a bottom of light-aggregate concrete (LAC) blocks with normal concrete poured over to form the top of the deck cross-section, see Fig. 1.

In SL-Decks for buildings, the greener combination of normal- and light-aggregate concrete has several advantages compared to other deck types:

- It has better acoustical properties due the combination of the two types of concrete.
- It can span longer and be lifted further by crane.
- It has outstanding fire resistance because of the light-aggregate concrete in the bottom.
- It allows building services to be included.
- It can be flexible in the sense that it e.g. can be curved, cantilevered, made with blade connections etc.

Especially, the latter is important in regards to being able to dismantle SL-Decks. The flexibility comes into play when one or more of the light-aggregate concrete blocks are omitted, and it is possible to put in normal concrete and reinforcement steel instead. This means that it is possible to e.g. integrate beams inside SL-Decks

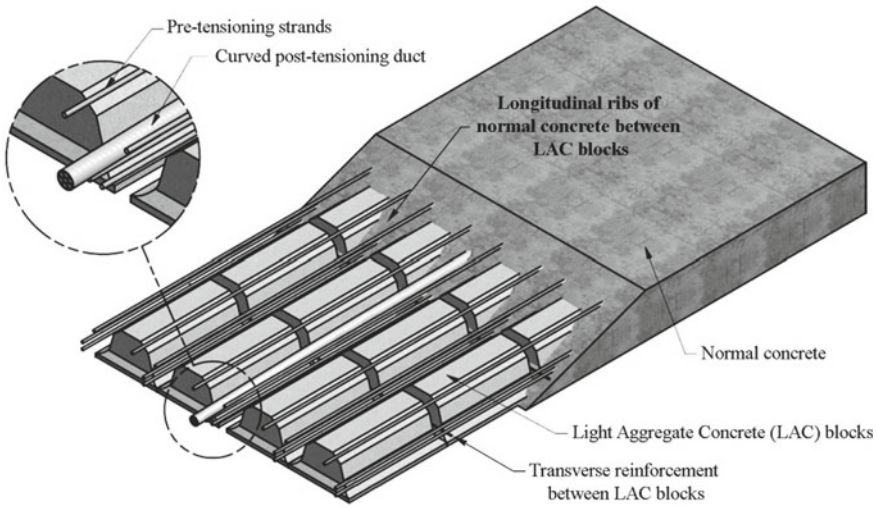

Fig. 1 View inside SL-Deck with pre-tensioning strands, transverse mild steel reinforcement and a duct (optional) for post-tensioning

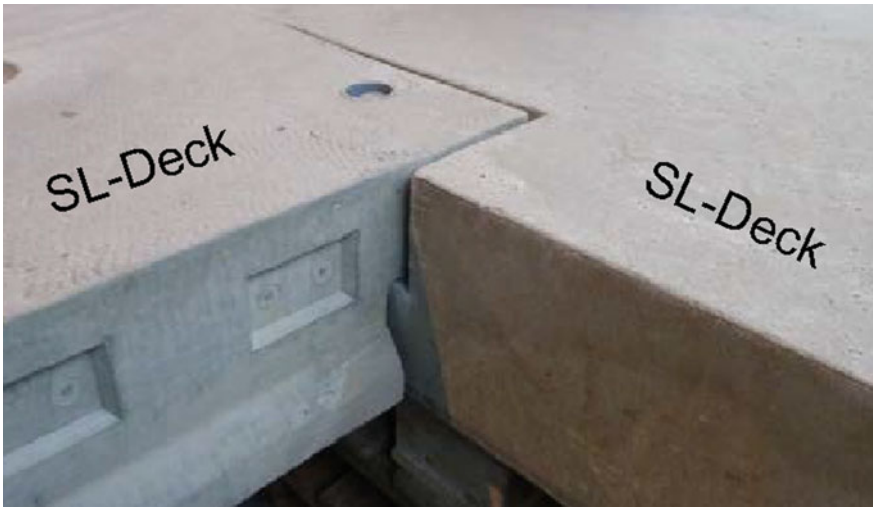

Fig. 2 Blade connection of a SL-Deck resting on the side of another SL-Deck

or have blade connections (decks resting on decks without increasing the structural height), see Fig. 2.

As documented in Hertz [3], the SL-Decks have a fire resistance time of 240 min. Combined with the beam-less design, they are suitable for establishing horizontal fire barriers.

Furthermore, several SL-Decks can be joined together by post-tensioning to form spacious shapes when combined. We call this, the pearl-chain method. It can for instance be used for arch bridges or vaulted roofs [4–6], see Fig. 3.

For such joined pearl-chain arches, it is necessary to design special end-elements where the arch structure rest on a foundation. Due to the arch shape, the connection to the foundation is in compression, and it is possible to utilize this when designing the end-elements for disassembly.

In the paper, a novel method for assembly (and easy disassembly) of the mass produces SL-Deck by blade connections are shown. This method can be used to create longer spans and beamless buildings, which is not possible with other mass produces pre-cast concrete deck solution like hollow core slabs.

The paper also includes a novel semi-hinged connection solution with simple disassembly, made of lightweight pre-fabricated element arches. Not only will the connection detail be easy to dismantle, a study shows that the resistance to rotation in the “hinge” can be adjusted by the thickness of the mortar joint, and the stiffness of the mortar.

Fig. 3 Top: SL-Deck elements and end-elements post-tensioned together in an arch shape. Used for full-scale load testing. Bottom: first ever constructed bridge based on arches using the pearl-chain method

2 Beamless Buildings with Super-Light Decks

Normally, larger concrete buildings of pre-fabricated elements consist of decks (often hollow core slabs) that rest on beams that rest on columns. Both the corbels on the columns, the beams, and the decks add potentially unwanted height to each story and everything must be cast together with transverse and longitudinal reinforcement due to robustness demands. Also, to hide the construction and services, and to have sufficient acoustic damping, hung down ceilings are put in.

If the beamless alternative is used, columns are joined with a quadratic concrete platform on which strong massive concrete decks can be attached to form a frame with the columns. This frame can be designed with enough integrity to withstand horizontal loads in one or two directions corresponding to the requirements for robustness. The sides of the massive concrete decks are prepared for blade connections to SL-Decks. Such setup is illustrated in Fig. 4, and example calculations verify the method with a SL-Deck span of 12 m. The blade connections correspond to a simple support of the SL-Decks, and disassembly of the SL-Decks in this solution is simple. Since the simple supports of the deck elements are placed a distance from the column centerlines, this represents an increased span-width of a deck element of between 2.4 and 3.6 m. Also, hung-down ceilings can be avoided, since services can be cast into the SL-Decks, the quadratic platform and potentially also the columns. The bottom of

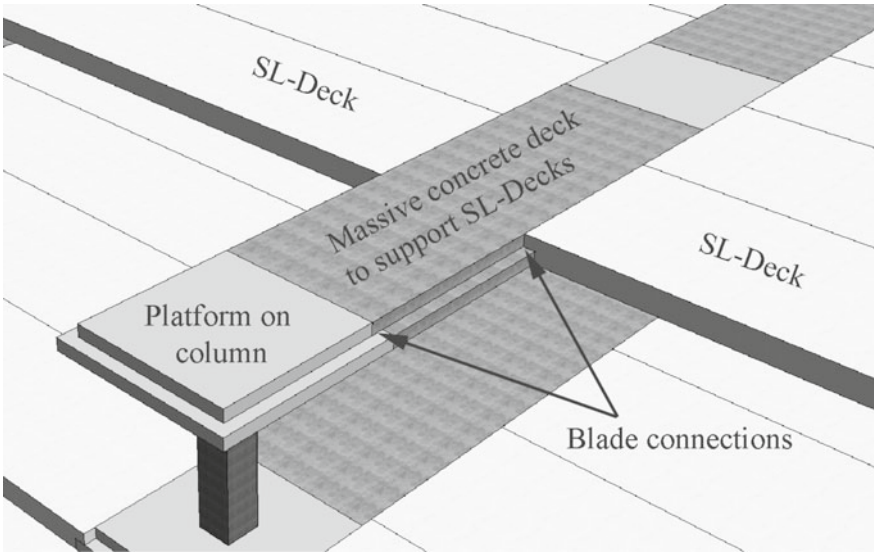

Fig. 4 Beamless building consisting of a frame of platforms, columns and massive concrete decks. The frame supports SL-Decks by blade connections

the SL-Decks with the exposed light-aggregate concrete provides sufficient acoustic damping.

2.1 Blade Connection Details

In Fig. 5, one reinforcement solution to the connection detail is shown for use in buildings with a span of the SL-Decks of 12 m. One row of light-aggregate concrete

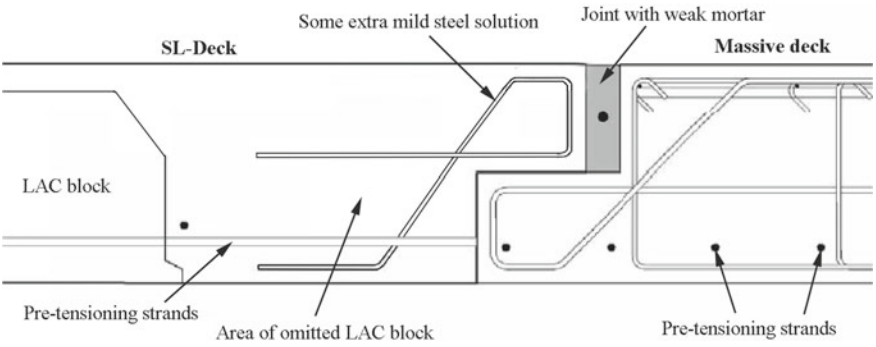

Fig. 5 Example of solution in blade connection where SL-Deck rests on a massive deck spanning in the opposite direction

blocks are omitted in the SL-Deck, and instead mild steel reinforcement is inserted to be able to transfer the increased local shear force at the support. In the figure, pre-tensioning strands are shown as well. SL-Decks with blade connections are cast in the same molds and together with other SL-Deck elements. The only difference is the separating cross-mold pieces placed before the normal concrete is cast.

A combined cement and lime mortar can be used on the grooves being poured at the building site to transfer in-plane shear in the combined deck. This weaker mortar is much easier to remove when the building is dismantled.

3 End-Elements for Pearl-Chain Arch Structures

The pearl-chain method is to post-tension several concrete elements together like pearls on a string. When the string is tightened at the end of a row of elements, the "pearls" will join in an angle, made by the mold piece separating the elements at the factory, and create a shape depending on the equilibrium in the joint between each pearl. It is possible to join SL-Decks by this method. A post-tensioning duct is cast into each plane SL-Deck element and is positioned with a shape corresponding to the desired curvature of the joined structure. The post-tensioning duct is placed perpendicular to the inclined end surface of each SL-Deck element. See an example of such Super-Light pearl-chain construction in Fig. 6.

At the end of a pearl-chain arch, the vertical and horizontal reaction must be resisted by an adjacent structure, and the connection is done via a specially designed end-element. The end-element is the link from the arch to the support, but is also where the large concentrated force from the anchorage of the post-tensioning cable (that runs through the duct) is resisted. A design proposal for such end-element used in an arch bridge is seen in Fig. 7. This element has two orthogonal sides that should fit to two similar orthogonal surfaces on the supporting structure, and the connection should act as a hinge but with some rotational resistance. The orthogonal connection

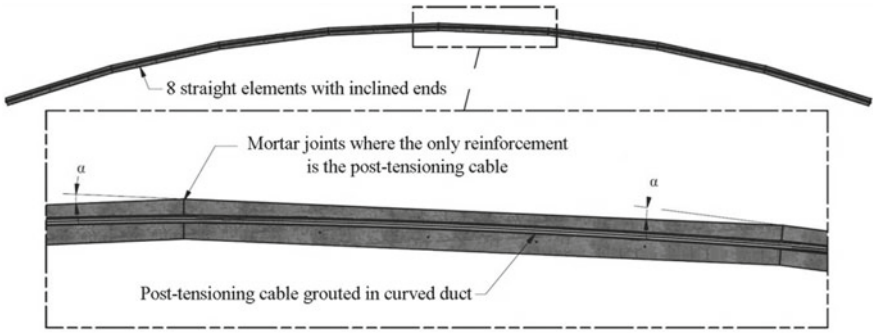

Fig. 6 Pearl-chain arch consisting of eight straight elements post-tensioned together. Each element has a curved duct with the shape of the combined arch

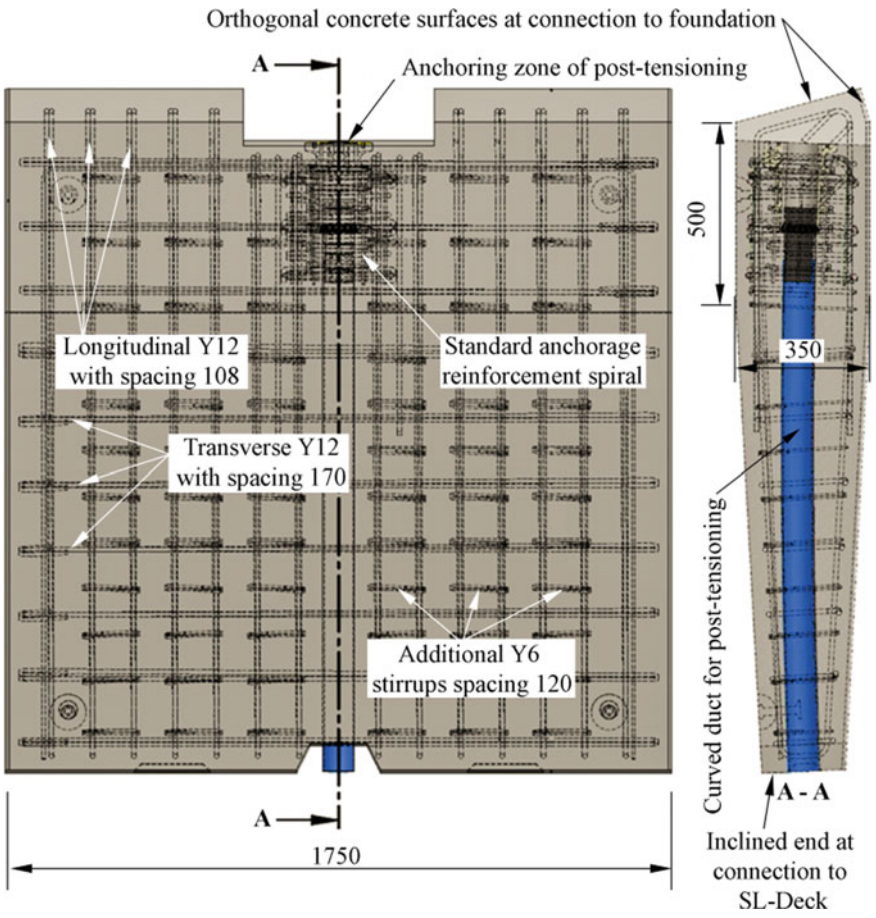

Fig. 7 Example of end-element geometry and reinforcement solution

is ideal for disassembly, since there is no reinforcement in the connection—only the mortar.

3.1 Brief Assessment of End-Element Connection Behavior

When a pearl-chain arch is lifted and positioned on the supports, some shims, wedges or flat jacks are placed between the arch and the supports to ensure that the arch shape can be adjusted correctly. Subsequently, a mortar is poured in the void, and the stiffness of the mortar has influence on the rotational resistance of the "hinge".

Figure 8 shows strain results from Digital Image Correlation (DIC) measurements of the end-element joint during load-testing of a full-scale pearl-chain arch. The

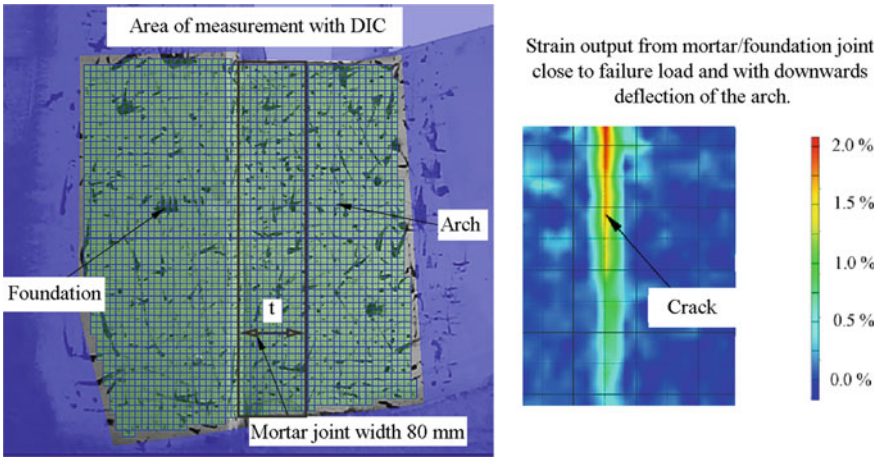

Fig. 8 DIC-measurements position in joint area with mortar between end-element and foundation. Measurements of both deflections and deformations are possible

software ARAMIS was used for DIC measurements in both the elastic and plastic regime. In this case, the horizontal distance from the end-element to the foundation, t, was 80 mm, and the Young's modulus of the mortar was 23 GPa. The Young's modulus of the concrete in the foundation and the end-element was 36 GPa and 39 GPa, respectively. Other measurement techniques and instruments were used as well to verify DIC-results and to find the deflection of the arch in other locations.

A FE-model is created to see what happens in the elastic domain to the level of resistance to rotation in the un-cracked joint, if the thickness of the mortar layer or the stiffness of the mortar is changed. In Fig. 9, the result of the behavior is seen together with the actual measured rotation from the full-scale test (red dot). The model has been applied the same value of normal force, N, and deflection as in the actual test (load level before cracking). For instance, the level of deflection was measured by a LVDT in the same location as it is applied to the model. In the model, the normal force is applied as a uniform load over the height of the end-element, and the foundation is fixed along the horizontal and vertical boundary. Quadrilateral elements are used, and several element sizes were checked to find the optimal tradeoff between calculation time and precision.

The rotation is found based on deformations in the mortar alone (the bottom curves), and based on deformations in the mortar and foundation combined (the top curves). The deformation in the small part of the end-element seen in the figure, is not included as part of the rotation of the connection.

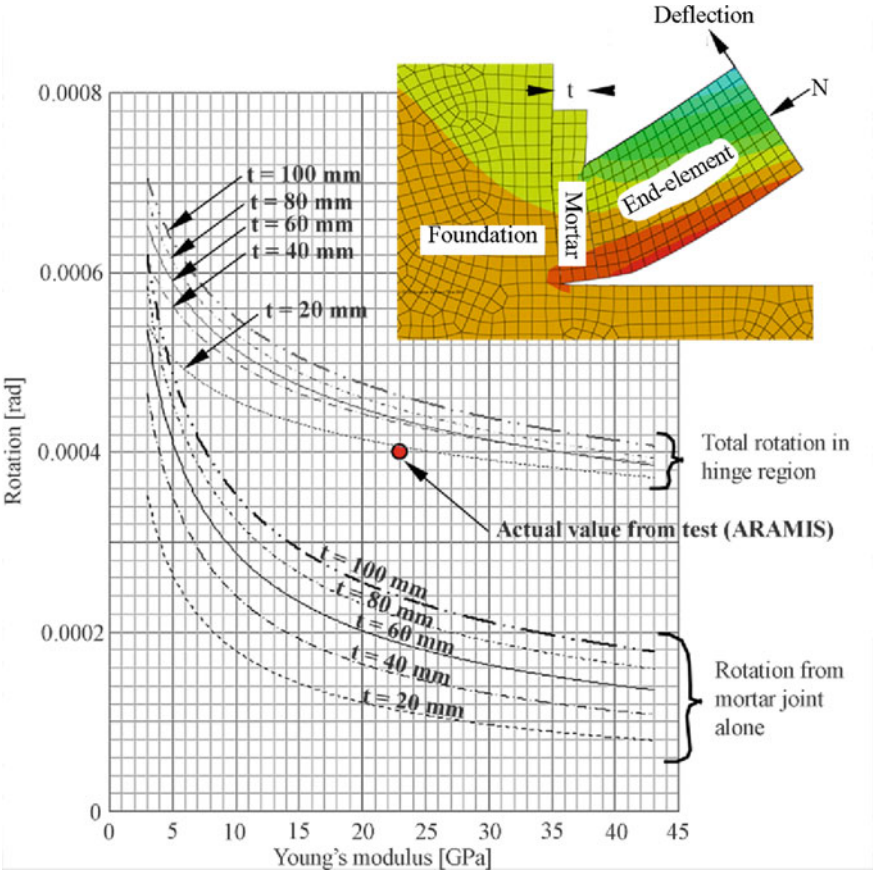

Fig. 9 FE-model example with results from changing the stiffness and thickness of the mortar joint between foundation and end-element. In this case the arch deflects upwards

4 Conclusion

Super-Light concrete is used in different structural solutions, and the flexibility of the technology makes is possible to design for disassembly. Two specific structural situations were presented: The beamless building, and pearl-chain arch connections.

A concept of how to design beamless buildings was shown. The idea is to create strong frames of concrete columns, platforms and massive concrete decks, where SL-Decks can rest on the sides of the frame by blade connections. The unique combination of light-aggregate concrete and normal concrete makes the SL-Decks flexible to use, and by omitting a row of light-aggregate concrete blocks, extra mild steel reinforcement can be put in to ensure a proper load carrying capacity near the blade connection. In the small void in the joint between the SL-Deck and the frame, a weak mortar can be used for easier demounting. Except for being designed for disassembly,

the beamless building concept also avoids the use of hung down ceilings, since the SL-Decks have excellent fire- and acoustic performance.

The pearl-chain method is to connect pre-fabricated elements in any joined shape by post-tensioning. The joined "pearl-chain" can be lifted in place by crane, and to design for disassembly, the joint between pearl-chain and foundation is in focus. For arch structures made of pearl-chains, the last element (the end-element) towards the foundation is specially created to work as a hinge with some degree of resistance to rotation. At the same time, the solution enables easy disassembly with orthogonal sides of the end-elements, and a weaker mortar joint between the end-element and the foundation. A brief assessment of the behavior of such solution was presented and it was based on full-scale tests and a FE-model.

References

1. Hertz, K., Bagger, A.: CO2 emissions from super-light structures. In: International Association for Shell and Spatial Structures (IABSE-IASS) Symposium 2011
2. Hertz, K., Castberg, A., Christensen, J.: Super-light concrete decks for building floor slabs. Struct. Concr. **15**(4), 522–529 (2014)
3. Hertz, K.: Design of Fire-Resistant Concrete Structures, 1st edn. Thomas Telford, UK (2019)
4. Halding, P., Hertz, K., Wittrup, J., Kennedy, B.: Full-scale load tests of Pearl-Chain arches. Eng. Struct. **131**, 101–114 (2017)
5. Halding, P., Hertz, K., Wittrup, J.: Precast Pearl-Chain concrete arch bridges. Eng. Struct. **103**, 214–227 (2015)
6. Halding, P., Hertz, K., Viebæk, N., Kennedy, B.: Assembly and lifting of Pearl-Chain arches. In: FIB Symposium Proceedings 2015

Electromagnetic Properties of Concrete: Bottom-Up Modeling from the Molecular Scale

Tulio Honorio, Farid Benboudjema, Thierry Bore, Helena Carasek, Oswaldo Cascudo, Mehdi Ferhat, and Eric Vourc'h

Abstract The electromagnetic response of concrete can be used to the non-destructive testing of structures and to follow early-age property development. Fundamental understanding of the physical origins of the electromagnetic response of cement-based materials is critical to reduce the empirism in the interpretation of electromagnetic-based techniques. The pore solution is the main contribution to the electrical conductivity and dielectric response of porous geomaterials. Specific ion effects are known to impact the dynamics of ions in aqueous salt solutions. In this context, molecular dynamics (MD) simulation is a well-suited technique to compute and understand how the ionic composition of the pore solution affects the electromagnetic properties of concrete. Here, we discuss recent results of MD simulation on bulk solution mimicking concrete pore solution. Then, we upscale the information from the molecular scale up to the concrete scale in order to provide a multiscale model of the electrical conductivity and frequency-dependent dielectric response of cement-based materials.

Keywords Dielectric properties · Electrical conductivity · Frequency-dependent response · Molecular dynamics simulation · Micromechanics.

T. Honorio (✉) · F. Benboudjema
LMT - Laboratoire de Mécanique et Technologie, Université Paris-Saclay, ENS Paris-Saclay, CNRS, 94235 Cachan, France
e-mail: tulio.honorio-de-faria@ens-paris-saclay.fr

T. Bore
School of Civil Engineering, The University of Queensland, Brisbane, Australia

H. Carasek · O. Cascudo
Universidade Federal de Goiás, Escola de Engenharia Civil e Ambiental, PPG-GECON, Goiânia, Brazil

M. Ferhat · E. Vourc'h
SATIE, UMR CNRS 8029, ENS Paris Saclay, Université Paris Saclay, Cachan, France

E. B. Pereira et al. (eds.), *Proceedings of the 3rd RILEM Spring Convention and Conference (RSCC 2020)*, RILEM Bookseries 32,
https://doi.org/10.1007/978-3-030-76547-7_6

1 Introduction

Measurements of the electromagnetic response of concrete have been extensively used for monitoring purposes. The related techniques, including resistivity and high-frequency electromagnetic (ground-penetrating radar, L-band remote sensing, capacitive probe, etc.) measurements, are non-destructive. Electromagnetic probing of concrete can also be used to follow the development of the material property at early age. Fundamental understanding of the electromagnetic properties of the phases present in cement-based materials, especially the pore solution, is critical to enhance the performance of these techniques and to improve the confidence in the corresponding results.

In this paper, we propose a multiscale strategy to model both resistivity and dielectric response of concrete informed by the dynamics of water and ion at the molecular scale [9]. We have previously deployed molecular simulation to get information with atomic-level detail on the physical origins of various properties of microporous materials [4, 12, 13] The dynamics and dielectric response based on molecular simulations of bulk system mimicking pore solutions are discussed. The frequency-dependent response of the susceptibility and conductivity of the pore solutions are analyzed. Micromechanics theory is then deployed to upscale the information obtained from molecular dynamics simulations.

2 Theory and Calculation

2.1 Electrical Conductivity and Dielectric Response from Fundamentals

For a system with n particles i with charge q_i, the total system polarization $\mathbf{P}$ is the sum of the polarization (or dipole moment) $\boldsymbol{\mu}_i(t)$ of the each particle i at time t [16]: $\mathbf{P}(t) = \sum_{i=1}^{n} \boldsymbol{\mu}_i(t) = \sum_{i=1}^{n} q_i \mathbf{r_i}(t)$, with $\mathbf{r_i}(t)$ being the position of the (center of) particle i. The total system polarization $\mathbf{P}$ is related to the electric field $\mathbf{E}$ via the complex frequency-dependent dielectric susceptibility $\chi(f) = \chi'(f) - i\chi''(f)$ by $\mathbf{P}(f) = \chi(f)\epsilon_0\mathbf{E}(f)$, where ϵ_0 is the vacuum permittivity. The dielectric susceptibility $\chi(f)$ can be computed from the auto-correlation of equilibrium polarization fluctuations using [14]:

$$\chi(f) = -\frac{1}{3Vk_BT\epsilon_0}\int_0^\infty e^{-2\pi i f t}\left\langle \mathbf{P}(0).\dot{\mathbf{P}}(t)\right\rangle dt \tag{1}$$

where V and T are the volume and temperature of the system, respectively; k_B is the Boltzmann constant and $\dot{\mathbf{P}}(t)$ is the time-derivative of the total polarization.

For a salt aqueous solution, the total polarization is the sum of the contributions of the water $\mathbf{P}_W$ and ionic $\mathbf{P}_I$ polarizations: $\mathbf{P} = \mathbf{P}_W + \mathbf{P}_I$. The ionic current $\mathbf{J}_I$ is related to the ionic polarization by: $\mathbf{J}_I(t) = \dot{\mathbf{P}}_I(t)$. This ionic current $\mathbf{J}_I$ is linked to

the electric field $\mathbf{E}$ via the frequency-dependent ionic conductivity $\sigma(f) = \sigma'(f) - i\sigma''(f)$ by

$$\mathbf{J}_I(f) = \sigma(f)\epsilon_0\mathbf{E}(f) \tag{2}$$

The frequency-dependent ionic conductivity can be computed using the cross correlations [2, 17]:

$$\sigma(f) = \frac{1}{3Vk_BT}\int_0^\infty e^{-2\pi ift}\left\langle \mathbf{J}_I(0).\dot{\mathbf{P}}(t)\right\rangle dt \tag{3}$$

The contributions of water-water, ion-water and ion-ion correlations can be separated using the following auto- and cross-correlations functions of the water polarization and ionic current can be defined [17]:

$$\phi_W(t) = \frac{\langle \mathbf{P}_W(0).\mathbf{P}_W(t)\rangle}{3Vk_BT\epsilon_0} \tag{4}$$

$$\phi_{IW}(t) = \frac{\langle \mathbf{P}_W(0).\mathbf{J}_I(t) - \mathbf{J}_I(0).\mathbf{P}_W(t)\rangle}{3Vk_BT\epsilon_0} \tag{5}$$

$$\phi_I(t) = \frac{\langle \mathbf{J}_I(0).\mathbf{J}_I(t)\rangle}{3Vk_BT\epsilon_0} \tag{6}$$

The regularized susceptibility $\Delta\chi(f)$ can be decomposed into three separate contributions:

$$\Delta\chi(f) = \chi_W(f) + \chi_{IW}(f) + \Delta\chi_I(f) \tag{7}$$

where

$$\chi_W(f) = \phi_W(0) - i2\pi f\int_0^\infty e^{-2\pi ift}\phi_W(t)dt \tag{8}$$

$$\chi_{IW}(f) = -2\int_0^\infty e^{-2\pi ift}\phi_{IW}(t)dt \tag{9}$$

$$\Delta\chi_I(f) = -\frac{i}{2\pi f}\int_0^\infty \left(e^{-2\pi ift} - 1\right)\phi_I(t)dt \tag{10}$$

The frequency-dependent ionic conductivity can be decomposed into the two terms:

$$\sigma(f) = \sigma_{IW}(f) + \sigma_I(f) \tag{11}$$

with

$$\sigma_{IW}(f) = -i2\pi f \epsilon_0 \int_0^\infty e^{-2\pi i f t} \phi_{IW}(t) dt \tag{12}$$

$$\sigma_I(f) = \epsilon_0 \int_0^\infty e^{-2\pi i f t} \phi_I(t) dt \tag{13}$$

Therefore, the static conductivity can be computed via $\sigma(f = 0) = \sigma_I(f = 0) = \epsilon_0 \int_0^\infty \phi_I(t) dt$.

2.2 Homogenization of the Electrical Conductivity and Dielectric Permittivity

Micromechanics is the study of the mechanical, thermal, electromagnetic and mass transport behavior of the materials with a microstructure [15]. The homogenization of the electrical conductivity is analogous to the homogenization of the thermal conductivity, dielectric permittivity, and diffusion coefficient [18]. In this section, we recall three homogenization schemes—namely Mori-Tanaka (MT, or Maxwell-Garnett) and Self-Consistent (SC, or Bruggeman) schemes—that we have extensively used (e.g. [5, 6, 8, 20]) to estimate the effective properties of cement-based materials accounting for the hierarchical microstructure of the material. With these homogenization schemes, it is possible to account for the random nature of cement-based materials microstructure and interactions among the different phases in a simplified way. The estimations are not computer-intensive compared to numerical homogenization based on finite element methods.

In a matrix/inclusion morphology, for a $(N + 1)$-phase heterogeneous material with N isotropic spherical inclusions randomly distributed in a representative elementary volume, the Mori-Tanaka estimation of the effective electrical conductivity σ^{MT} (resp. dielectric permittivity) can be computed from [18]:

$$\frac{\sigma^{MT} - \sigma_0}{\sigma^{MT} + 2\sigma_0} = \sum_{r=1}^{N} f_r \frac{\sigma_r - \sigma_0}{\sigma_r + 2\sigma_0} \tag{14}$$

where f_r is the volume fraction of the phase r, and the subscript $_0$ denotes the (isotropic) matrix phase.

In a polycrystalline-like morphology, for a N-phase heterogeneous materials with N isotropic equiaxed inclusions randomly distributed in representative elementary volume, the Self-Consistent estimation of the effective electrical conductivity σ^{SC} (resp. dielectric permittivity) can be computed from the implicit formula [18]:

$$\sum_{r=1}^{N} f_r \frac{\sigma_r - \sigma^{SC}}{\sigma_r + 2\sigma^{SC}} = 0 \tag{15}$$

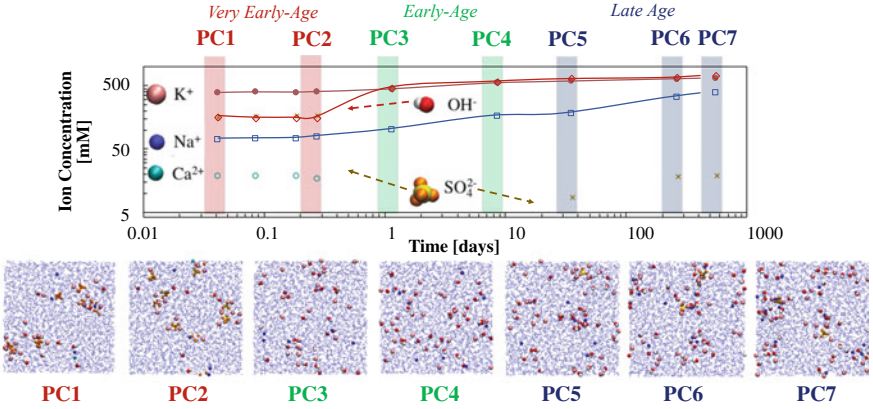

Fig. 1 Age-dependent ionic composition of the pore solution based on the experimental results of Vollpracht et al. [19]. Snapshot of the atomic configuration obtained in the MD simulations reported in Ref. [9]

The presence of interphases (i.e. the volume in-between two phases—in contrast with an "interface", which is a surface between two surfaces) can be modeled with the Generalized Self-Consistent (GSC) scheme based on the composite-sphere morphology. For the sake of simplicity, ITZ is not taken into account here. See [11] for a detailed analysis of the influence of ITZ in the electrical conductivity of mortars.

3 Results

3.1 Dielectric Response and Conductivity from Molecular Dynamics

Figure 1 shows the age-dependent ionic composition of the pore solution based on the experimental results of Vollpracht et al. [19] for CEM I system with w/c=0.4. Bulk solution with the selected compositions is modeled using classical molecular dynamics as detailed in Honorio et al. [9]. PC1 and PC2 correspond to typical pore solution at the very early age (before setting). PC3 and PC4 correspond to pore solution at early-age *per se* (after setting), and PC5–PC7 correspond to late ages pore solutions.

The frequency-dependent DC-conductivity and dielectric spectra of the age-dependent pore solutions are shown in Fig. 2. As discussed in Ref. [10], the contribution of water-water interactions, are predominant in the dielectric response. The dielectric spectra can be fitted using the Cole-Cole model with the parameters gathered in Table 1. For comparison, we also provide the fits for SPC/E water that are in agreement with experiments [1] and previous simulation with SPC/E water model

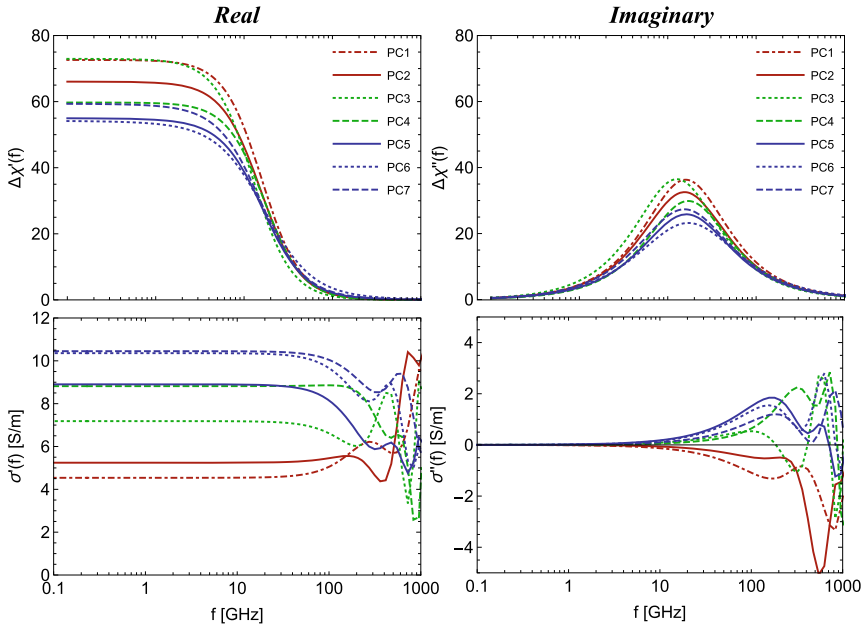

Fig. 2 Frequency-dependent susceptibility $\Delta\chi = \epsilon - 1 = \Delta\chi'(f) - i\Delta\chi''(f)$ (top) and DC-conductivity $\sigma = \sigma'(f) - i\sigma''(f)$ (bottom) of age-dependent pore solutions from correlation functions computed using MD simulations [10].

Table 1 Cole-Cole fit parameters from MD simulations of pore solution and SPC/E water [10]. The variability/uncertainty associated with the fittings were computed suing Pearson's correlations

	ϵ_{CC} [−]	τ_{CC} [ps]	α [−]
PC1	73.6 ± 2.9	9.97 ± 0.97	0.000 ± 0.060
PC2	67.1 ± 2.6	10.26 ± 0.97	0.009 ± 0.060
PC3	73.9 ± 3.2	12.55 ± 1.33	0.000 ± 0.061
PC4	60.7 ± 2.7	9.33 ±1.14	0.000 ± 0.050
PC5	56.0 ± 2.1	9.80 ± 0.96	0.040 ± 0.056
PC6	55.2 ± 2.4	9.33 ± 1.27	0.098 ± 0.055
PC7	60.4 ± 3.0	10.30 ± 1.52	0.052 ± 0.063
SPC/E	68.2 ± 2.7	8.35 ± 0.94	0.033 ± 0.055

[17] . We observe that the variability of the ion composition of the pore solution leads to significant variations of the dielectric response: on the order of tens units of relative dielectric permittivity.

3.2 *Upscaling the Electromagnetic Properties*

The self-consistent scheme was used to get the effective properties of the cement paste since it captures the complex liquid-solid transition observed in cement paste at early-ages [10, 11]. Mori-Tanaka is deployed to homogenize mortar and concrete scales, in which a clear matrix/inclusion morphology is observed. The volume fractions of sand (at the mortar scale) and of coarse aggregates (at the concrete scale) are each 40%. To upscale the effective permittivity $\epsilon = \Delta\chi + 1$ of the cement paste we use the Cole-Cole fits with the parameters in Tab. 1 to describe the dielectric permittivity of each pore solution ϵ_{PS}. Powers cement hydration model is deployed to estimate the evolution of the capillary porosity (i.e. the volume fraction associated to the pore solution phase) in the system:

$$f_{PS}(\xi, w/c) = \phi^0_{cap}(w/c) - 1.32(1 - \phi^0_{cap}(w/c))\xi \tag{16}$$

where the degree of hydration $\xi = 0.9\left[1 - e^{-t/7}\right]$ is described by an exponential (in agreement with boundary nucleation and growth models [7]) for t in days [11], and $\phi^0_{cap}(w/c) = (w/c)/\left(\rho_w/\rho_c + (w/c)\right)$ is the initial porosity computed from the w/c and densities of water and cement (ρ_c and ρ_w, respectively).

Figure 3 shows the homogenized values of the static conductivity and dielectric permittivity at the cement paste, mortar, and concrete scales. The electrical conductivity of the hydrates adopted is of 0.0246 S/m as obtained from Monte Carlo Micromechanics in Ref. [11]. The (non-porous-aggregates are considered perfect insulators ($\sigma(0) = 0$). The three stages associated with the pore solution composition, namely, the very early-age, early-age and late age, are retrieved in the trends observed in the static electrical properties. At the very early age, the conductivity reaches its maximum at all scales, drops drastically in the early-age stage and

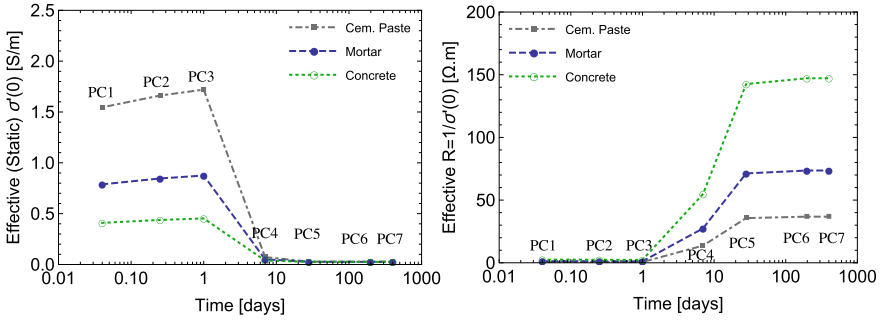

Fig. 3 Upscaling the static conductivity and resistivity at cement paste, mortar, and concrete scales. The properties of the pore solution refers to a cement paste with a w/c of 0.4. We assumed a volume fraction of sand at the mortar scale of 40% and of coarse aggregate at the concrete scale of 40%. The electrical conductivity of the hydrates adopted is of 0.0246 S/m as obtained from Monte Carlo micromechanics in Ref. [11]. The aggregates are considered perfect insulators ($\sigma(0) = 0$).

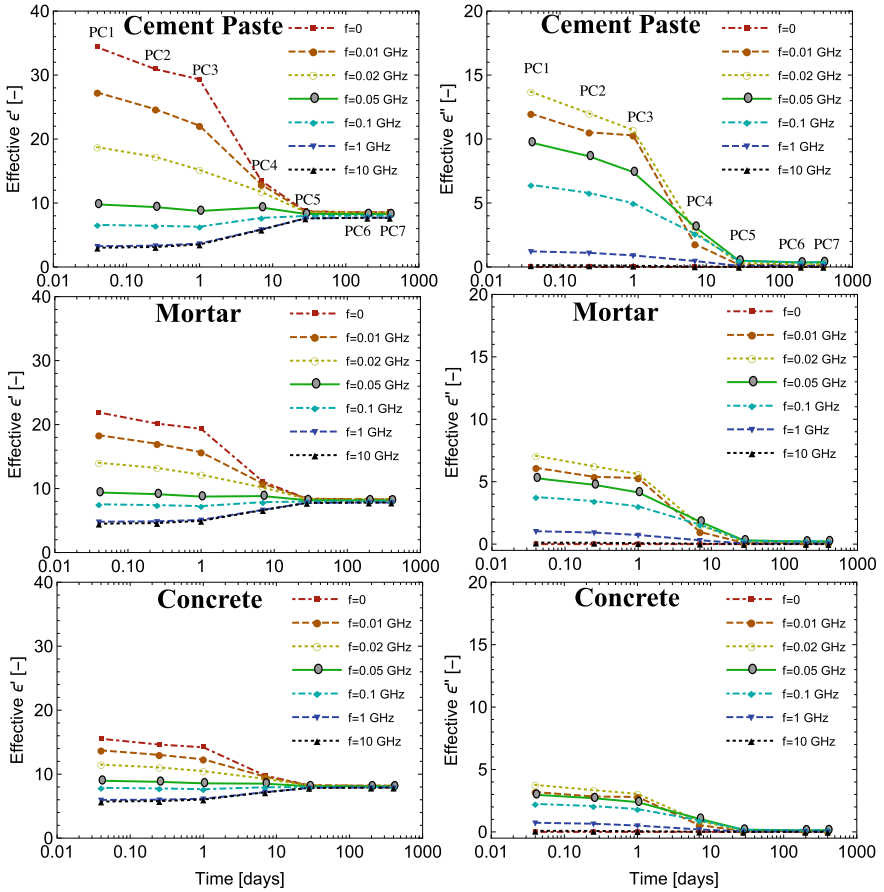

Fig. 4 Upscaling the frequency-dependent dielectric spectra $\epsilon = \epsilon'(f) - i\epsilon''(f)$ at cement paste, mortar and concrete scales: real part (left) and imaginary (right) parts. We assumed a volume fraction of sand at the mortar scale of 40% and of coarse aggregate at the concrete scale of 40%. We considered a dielectric permittivity of solids of 8 [3].

remains close to zero at late ages. The inverse tendency is observed with respect to the resistivity $R = 1/\sigma$ (which is the reciprocal of the conductivity). At larger scales, for a given age, the conductivity decreases. Again, the inverse is observed with the resistivity.

Figure 4 shows the effective frequency-dependent dielectric spectra at cement paste, mortar, and concrete scales. We considered a dielectric permittivity of solids of 8 based on experimental evidence from the literature [3]. The real part of the dielectric permittivity decreases with age for frequencies below 0.05 GHz and slightly increases with age for higher frequencies. This behavior is observed in all scales considered, being more pronounced at the cement paste scale. The imaginary part of the permittivity reaches a maximum at the very early age and for a frequency of

0.02 GHz, which shows the non-monotonous evolution of the imaginary part with the frequency. In larger scales, the differences between the results at the different frequencies are reduced, which is expected given the reduction in the relative volume fraction of cement paste present in the material at larger scales.

4 Conclusions

The electromagnetic response of concrete is closely related to the nanoscale processes associated with water and ion interactions. The combination of molecular simulations and micromechanics provides a robust and powerful framework to link the composition and (micro-)structure to the macroscopic electromagnetic properties of cement-based materials. In this work, we showed that such a framework provided estimations of the electromagnetic properties of cement-based materials across scales that are consistent with the experimental evidence. In particular, we quantified the effects of the variability of the ionic composition of the pore solution on effective electrical conductivity and frequency-dependent dielectric response. Our results suggest that the characterization of the pore solution is a critical step in reducing the empirism of the interpretations of the resistivity and HF measurement in concrete.

References

1. Buchner, R., Hefter, G.T., May, P.M.: Dielectric relaxation of aqueous NaCl solutions. J. Phys. Chem. A **103**(1), 1–9 (1999) https://doi.org/10.1021/jp982977k, http://pubs.acs.org/doi/abs/10.1021/jp982977k
2. Caillol, J.M., Levesque, D., Weis, J.J.: Theoretical calculation of ionic solution properties. J. Chem. Phys. **85**(11), 6645–6657 (1986)
3. Guihard, V., Taillade, F., Balayssac, J.P., Steck, B., Sanahuja, J.: Permittivity measurement of cementitious materials and constituents with an open-ended coaxial probe: combination of experimental data, numerical modelling and a capacitive model. RILEM Tech. Lett. **4**, 39–48 (2019). https://doi.org/10.21809/rilemtechlett.2019.77, https://letters.rilem.net/index.php/rilem/article/view/77
4. Honorio, T.: Monte Carlo molecular modeling of temperature and pressure effects on the interactions between crystalline calcium silicate hydrate layers. Langmuir **35**(11), 3907–3916 (2019). https://doi.org/10.21809/rilemtechlett.2019.77, https://letters.rilem.net/index.php/rilem/article/view/77
5. Honorio, T., Bary, B., Benboudjema, F.: Multiscale estimation of ageing viscoelastic properties of cement-based materials: A combined analytical and numerical approach to estimate the behaviour at early age. Cem. Concr. Res. **85**, 137–155 (2016)
6. Honorio, T., Bary, B., Benboudjema, F.: Thermal properties of cement-based materials: Multiscale estimations at early-age. Cem. Concr. Compos. **87**, 205–219 (2018)
7. Honorio, T., Bary, B., Benboudjema, F., Poyet, S.: Modeling hydration kinetics based on boundary nucleation and space-filling growth in a fixed confined zone. Cem. Concr. Res. **83**, 31–44 (2016)

8. Honorio, T., Bary, B., Sanahuja, J., Benboudjema, F.: Effective properties of n-coated composite spheres assemblage in an ageing linear viscoelastic framework. Int. J. Solids Struct. **124**, 1–13 (2017)
9. Honorio, T., Benboudjema, F., Bore, T., Ferhat, M., Vourc'h, E.: The pore solution of cement-based materials: structure and dynamics of water and ions from molecular simulations. Phys. Chem. Chem. Phys. **21**, 11111–11121 (2019)
10. Honorio, T., Bore, T., Benboudjema, F., Vourc'h, E., Ferhat, M.: Dielectric properties of the pore solution in cement-based materials. J. Mol. Liq. 112548 (2020). https://doi.org/10.1016/j.molliq.2020.112548, http://www.sciencedirect.com/science/article/pii/S0167732219360593
11. Honorio, T., Carasek, H., Cascudo, O.: Electrical properties of cement-based materials: multi-scale modeling and quantification of the variability. Constr. Build. Mater. **245**, 118461 (2020). https://doi.org/10.1016/j.conbuildmat.2020.118461
12. Honorio, T., Lemaire, T., Tommaso, D.D., Naili, S.: Anomalous water and ion dynamics in hydroxyapatite mesopores. Comput. Mater. Sci. **156**, 26–34 (2019)
13. Honorio, T., Lemaire, T., Tommaso, D.D., Naili, S.: Molecular modelling of the heat capacity and anisotropic thermal expansion of nanoporous hydroxyapatite. Mater. 100251 (2019)
14. Köhler, F., Findenegg, G.H.: The Liquid State, vol. 1. Wiley-VCH (1972)
15. Milton, G.W.: The Theory of Composites. Cambridge University Press, Cambridge (2002)
16. Praprotnik, M., Janežič, D.: Molecular dynamics integration and molecular vibrational theory. III. The infrared spectrum of water. J. Chem. Phys. **122**(17), 174103 (2005). https://doi.org/10.1063/1.1884609, http://aip.scitation.org/doi/10.1063/1.1884609
17. Rinne, K.F., Gekle, S., Netz, R.R.: Dissecting ion-specific dielectric spectra of sodium-halide solutions into solvation water and ionic contributions. J. Chem. Phys. **141**(21), 214502 (2014)
18. Torquato, S.: Random Heterogeneous Materials: Microstructure and Macroscopic Properties. Springer Science & Business Media (2002)
19. Vollpracht, A., Lothenbach, B., Snellings, R., Haufe, J.: The pore solution of blended cements: a review. Mater. Struct. **49**(8), 3341–3367 (2016)
20. Wyrzykowski, M., Sanahuja, J., Charpin, L., Königsberger, M., Hellmich, C., Pichler, B., Valentini, L., Honório, T., Smilauer, V., Hajkova, K., Ye, G., Gao, P., Dunant, C., Hilaire, A., Bishnoi, S., Azenha, M.: Numerical benchmark campaign of COST Action TU1404—microstructural modelling. RILEM Tech. Lett. **2**, 99–107 (2017)

Interfacial Performance of Coating Polymer on Calcium–Silicate–Hydrates During Different Stages of Cement Hydration

Ashwin Konanur Nagesh and Pijush Ghosh

Abstract Polymers are widely used for concrete coating applications such as surface coating materials for buildings, preventing penetration of water or air, aesthetic purpose like glazing finish, conservation materials for mural paintings and many more. In the field, the common practice is to coat concrete after it has set completely (28 days), but it is not well understood if this will maximize the interfacial strength. Hence there is a need to determine at what time after the addition of water, the coating should be applied and also how surface characteristics influence interfacial strength. The reason for better interfacial performance at the interface between coating polymers and cement paste is due to the physical and chemical interactions between the cement hydration products and the different functional groups in coating polymer. In the present work, the physical interaction and molecular mechanisms between functional groups of two different coating polymer (Epoxy and poly(methyl methacrylate) (PMMA)) and cement hydration products during early stages of cement hydration is studied using molecular dynamics simulation. The mechanical response and the physical interaction of functional groups of two different coating polymer Epoxy and PMMA are significantly influenced by (a) pore solution calcium (b) C–S–H substrate calcium and (c) adsorbed water layer.

Keywords Epoxy · PMMA · Calcium silicate hydrates · Interface · Molecular dynamics

1 Introduction

Polymer coatings on concrete surface find many modern-day applications such as protection and functional material, preventing the penetration of water or air, aesthetic purpose like glazing finish, surface coating materials for buildings and conservation materials for mural paintings and many more [1–8]. Other than flooring, polymer coatings are essentially used in swimming pools, car parking spaces, warehouses,

A. K. Nagesh (✉) · P. Ghosh
Nanomechanics and Nanomaterials Laboratory, Indian Institute of Technology Madras, Tamil Nadu, Chennai 600036, India

E. B. Pereira et al. (eds.), *Proceedings of the 3rd RILEM Spring Convention and Conference (RSCC 2020)*, RILEM Bookseries 32,
https://doi.org/10.1007/978-3-030-76547-7_7

garages etc. The most commonly used coating polymer can be broadly classified as epoxies, acrylics, urethanes, polyureas and siloxanes [7, 8]. They possess some inherent properties such as good adhesion with most of the substrates, relatively high mechanical strength, cure at ambient temperature etc.

In such type of applications, adhesion between the cementitious substrate and the organic material is usually required to ensure the effectiveness of the coating and its durability. Therefore, it is essential to investigate the surface interactions of organic polymer coatings with the cementitious substrate. The interfacial strength and adhesion between the coating and the substrate (C–S–H) determines the performance of the system as a whole.

C–S–H is the most important hydration product of cement-based materials and it occupies about 60–70% of cement paste volume. This C–S–H is virtually X-ray amorphous, compositionally and structurally very variable, and generally finely intermixed with other phases, all of which make it difficult to study. NMR studies have shown varying proportions of Q^0 (anhydrous Silica tetrahedral), Q^0(h) (hydroxylated Silica tetrahedral), Q^1 (Silica polymerized in one of the four oxygen atoms) and Q^2 (Silica polymerized in two of the four oxygen atoms) silica over the first few hours of hydration. For instance, during the induction period (1–2 h) Q^0(h) silica is the predominant phase. This indicates an atomic structure where the surface silicates of C_3S are simply hydroxylated. During the acceleration stage (<10 h) Q^1 starts forming indicating a dimer predominant atomic structure. It is during the deceleration period (10–20 h) of hydration that the Q^2 finally starts forming giving rise to atomic structure with a higher degree of polymerization [9]. This information provides us different approximate atomic structures of C–S–H during the three different stages of hydration. Richardson [10] had developed idealized models for C–S–H which represents different mean chain lengths of silicates (i.e., Dimer (T2), Trimer (T3), Pentamer (T5), Undecamer (T11), and Infinite Chain (Tinf)). This Dimer (T2) C–S–H model has been used in our study.

In this work, a molecular dynamics study is performed to determine the interfacial properties between PMMA (as a coating polymer) and hydrating cement paste. Different factors contributing to interfacial shear strength between two different coating polymer (Epoxy and poly(methyl methacrylate) (PMMA)) and hydrating cement paste include physical interaction, chemical bonds, mechanical interactions and heat dissipation. At the molecular level, physical interaction and chemical bonds contributes to interfacial shear strength. Primarily, the role of (a) pore solution calcium and (b) C–S–H substrate calcium (c) monolayer of wáter (adsorbed water) which influence the interfacial mechanism between two different coating polymer (Epoxy and poly(methyl methacrylate) (PMMA)) and C–S–H substrate during the initial period of cement hydration is studied.

2 Model Construction and Simulation Details

A multiscale perspective for cement paste/polymer are as shown in Fig. 1. Figure 1a shows schematic representation of Cement/Polymer coating at macrolevel and Fig. 1b shows schematic representation of atomistic interaction between functional group of polymer with (i) pore solution calcium and (ii) C–S–H substrate calcium.

The atomistic model consists of T2_sc_LS2 (Dimer) idealized C–S–H model [10] was used. A T_2 C–S–H structure have a unit cell dimension of a = 11.35 Å, b = 7.3 Å, c = 19 Å, with $\alpha = 90°$, $\beta = 98.4°$, $\gamma = 90°$. The entire T_2 C–S–H substrate was constructed from repeating the unit cell as shown in Fig. 2 in x, y, and z-directions with dimension a = 22.7 Å, b = 102.2 Å, c = 266 Å, with $\alpha = 90°$, $\beta = 98.4°$, $\gamma = 90°$. The [1 0 0] cleavage plane was exposed to the surface interaction. The structure of PMMA and Epoxy are shown in Fig. 3. A one chain of PMMA with 50 repeating units and one chain of Epoxy with 4 repeating units was considered in simulation.

In this work, the Interface Force Field (IFF) [11] was applied for C–S–H structures. For Epoxy and PMMA polymer, the Consistent Valence Force Field (CVFF) [12] was adopted. A simple point charge (SPC) [13] model was used for the water molecule.

A monolayer of water was modeled at the top of T_2 C–S–H substrate and this represents adsorbed water of thickness 3 Å and density 1 g/cm^3. To understand the effect of Ca ion in pore solution, a surplus of calcium ion was added in adsorbed water/monolayer water. A total of 1000 Ca ions was added along monolayer/adsorbed water in a model using PACKMOL [14, 15]. To ensure the charge neutrality, the extra positive charge of Ca ion is distributed evenly throughout the T_2 C–S–H substrate.

The simulations were implemented using the massively parallelized modeling code LAMMPS [16] (http://lammps.sandia.gov/). In all the systems, the T2 CSH substrate was constrained whereas water molecules, pore solution calcium, PMMA

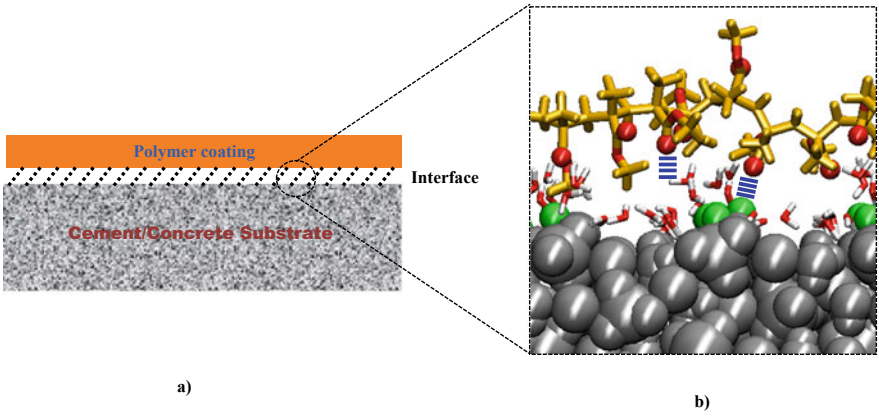

Fig. 1 Shows a multiscale perspective for cement paste/polymer **a** Schematic representation of Cement/ Polymer coating at macrolevel **b** Schematic showing atomistic interaction between functional group of polymer with (i) pore solution calcium and (ii) C–S–H substrate calcium

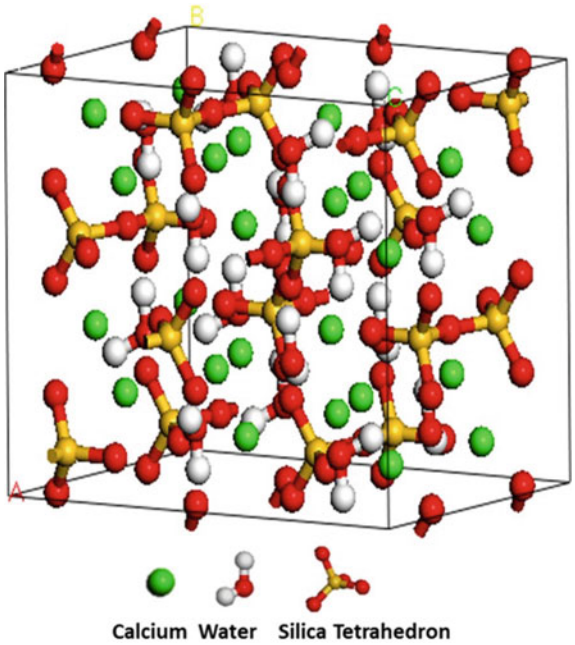

Fig. 2 Shows Unit cell of T_2 C–S–H with dimension of a = 11.35 Å, b = 7.3 Å, c = 19 Å, with α = 90°, β = 98.4°, γ = 90°

and Epoxy were free. The energy minimizations were performed using conjugate gradient method with energy and force cut-off tolerances set close to zero (10^{-10}). The system was equilibrated for 200 ps in the NVT ensemble at 300 K using Nose–Hoover thermostat. Time step of 1 fs was adopted in MD simulations. Initial configurations were prepared using Packmol.

The equilibrated system was considered as an initial model for Steered molecular dynamics (SMD). The basic objective behind the application of SMD was to apply an external force to one or a group and pull it over mineral substrate. In our simulation, only the T_2 C–S–H substrate was fixed. All atoms in PMMA polymer were allowed to move freely. The end monomer in the Epoxy/PMMA was connected to a virtual spring in the entire process of SMD and pulled. A spring constant of 5 kcal/mol/Å was used with a timestep of 1 fs per iteration step. The magnitude of the velocity of 0.5 Å/ps was applied. Visualization was carried out using the Visual Molecular Dynamics (VMD) visualization package [17].

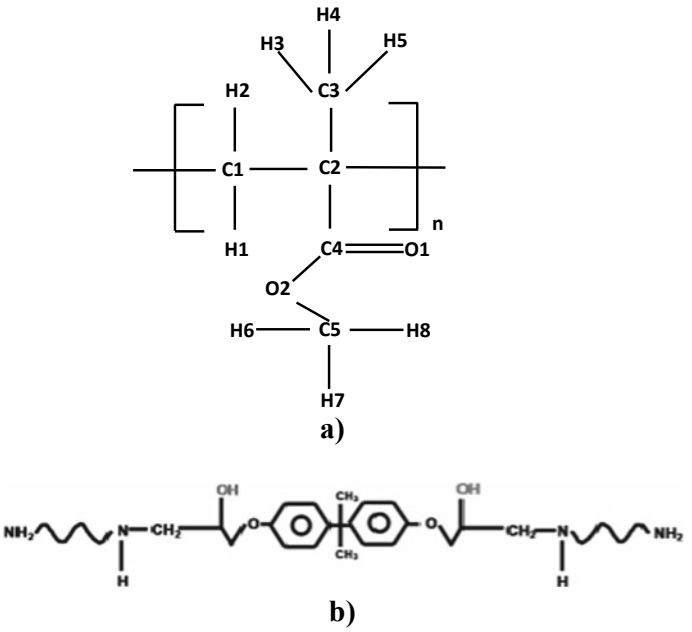

Fig. 3 Shows the structure of **a** PMMA and **b** Epoxy

3 Result and Discussion

3.1 Systems Considered for Interaction Study Applying SMD

The systems considered in the simulation are as shown in Fig. 4. In system 1, the combination of the T_2 C–S–H substrate, a monolayer of water and calcium represents closely the cement hydration products. The monolayer layer of water considered here is the adsorbed water present in cement hydration product and calcium ions represent the calcium present in pore solution. System 2 is considered to study the effect of water between the Epoxy/PMMA and T_2 C–S–H substrate in the absence of pore solution calcium.

3.2 Total Energy Comparison of Two Systems

The total energy required to pull PMMA and Epoxy polymer completely out of substrate for 2 different systems is as shown in Fig. 5. Refer Sect. 3.3 for the calculation of total energy. By performing multiple repetitions of simulation, the mean of total energy was calculated and the standard deviation was plotted for the same in all four systems. So the standard deviation represents an error bar in Fig. 5.

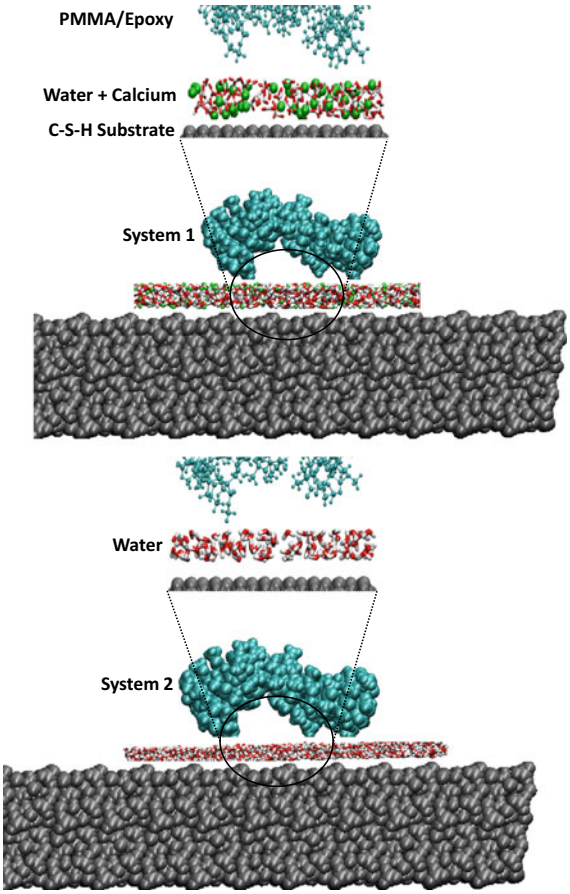

Fig. 4 Schematic showing the two systems considered in the simulation. In system 1, the combination of the T_2 C–S–H substrate, a monolayer of water and calcium represents closely the cement hydration products. System 2 is considered to study the effect of water between the PMMA and T_2 C–S–H substrate in the absence of pore solution calcium

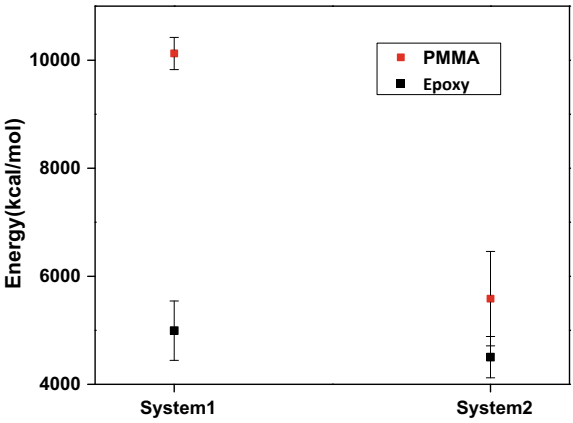

Fig. 5 Shows the total energy required to pull PMMA and Epoxy polymer completely out of substrate for two systems

Let TE_1 and TE_2 represent the total energy required to pull PMMA polymer completely out of substrate from system 1 to 2 respectively. The average value of TE_1 is 10124 kcal/mol. Most of the energy required for pulling PMMA in system 1 is due to the interaction between (a) Ca1 ions present in pore solution with O1 of PMMA (b) Hw1 (hydrogen of wáter) with O1. The average value of TE_2 is 5584 kcal/mol. Here $TE_2 < TE_1$ which clearly indicates that interaction between Ca1 with O1 PMMA is predominant.

Let TE_i and TE_{ii} represent the total energy required to pull Epoxy polymer completely out of substrate from system 1 to 2 respectively. The average value of TE_i and TE_{ii} is 4494 kcal/mol and 4503 kcal/mol respectively. Most of the energy required for pulling Epoxy in system 1 and 2 is due to the formation of hydrogen bond between (a) Ow1 oxygen of water with Ho (hydroxyl hydrogen) of Epoxy and (b) Ow1 oxygen of water with Hn (hydrogen of amine) of Epoxy.

From Fig. 5 it is evident that the electrostatic interaction, which results from the presence of calcium in pore solution as well Hw1 (hydrogen of wáter) with of PMMA, is the main cause of the energy spent in pulling PMMA over CSH or cement paste substrate. From Fig. 5 it is also evident that formation of hydrogen bond between (a) Ow1 oxygen of water with Ho (hydroxyl hydrogen) of Epoxy (b) Ow1 oxygen of water with Hn (hydrogen of amine) of Epoxy, is the main cause of the energy spent in pulling Epoxy over CSH or cement paste substrate.

Thus it can be concluded that the total energy (TE_2) required to pull PMMA polymer completely out of substrate is less in presence of monolayer of water (system 2). In system 1, though the solvation shell is formed over pore solution calcium, the total energy (TE_1) is high compared to TE_2. For epoxy TE_i and TE_{ii} is almost same since the energy spent in pulling Epoxy over CSH or cement paste substrate is due to formation of hydrogen bond between (a) Ow1 oxygen of water with Ho (hydroxyl hydrogen) of Epoxy (b) Ow1 oxygen of water with Hn (hydrogen of amine) of Epoxy.

3.3 Total Energy Calculation

The total energy is calculated as shown in Fig. 6 which is area under the curve of Load-Displacement (L-D) for one system ie system 1. This total energy is the energy required to pull single chain PMMA with 50 repeating units completely out of the substrate. Now this value is converted to kcal/mol which means that to pull one mole of single chain PMMA with 50 repeating units completely out of the substrate. So, per mol means one mole of single chain of PMMA with 50 repeating units.

4 Conclusions

In this work, a molecular dynamics study is carried out to determine interfacial properties between PMMA (as a coating polymer) and hydrating cement paste.

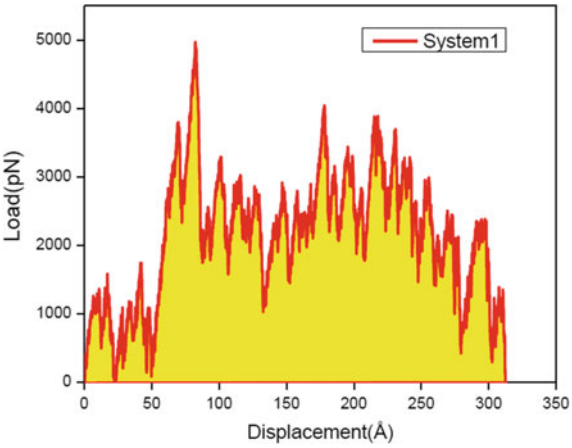

Fig. 6 Shows load-displacement (L-D) plot of system 1. Yellow colour represents area under the curve

The total energy required for pulling PMMA polymer completely out of substrate in presence of pore solution calcium and water is due to the interaction between pore solution calcium (Ca1) and hydrogen (Hw1) with double bond oxygen (O1) present in –COO functional group of PMMA. The formation of water solvation shell around pore solution calcium reduces the number of interactions between pore solution calcium with double bond oxygen (O1) of PMMA and thereby decreases the total energy.

Similarly, the total energy required for pulling Epoxy polymer completely out of substrate in presence of pore solution calcium and water is due formation of hydrogen bond between (a) Ow1 oxygen of water with Ho (hydroxyl hydrogen) of Epoxy (b) Ow1 oxygen of water with Hn (hydrogen of amine) of Epoxy.

References

1. Swamy, R.N., Tanikawa, S.: An external surface coating to protect concrete and steel from aggressive environments. Mater. Struct. **26**, 465–478 (1993)
2. Swamy, R.N., Suryavanshi, A.K., Tanikawa, S.: Protective ability of an acrylic-based surface coating system against chloride and carbonation penetration into concrete. ACI Mater. J. **95**(2), 101–112 (1998)
3. Carretti, E., Dei, L., Baglioni, P.: Solubilization of acrylic and vinyl polymers in nanocontainer solutions. Application of microemulsions and micelles to cultural heritage conservation. Langmuir **19**(19), 7867–7872 (2003)
4. Yang, Z., Peng, H., Wang, W., Liu, T.: Crystallization behavior of poly(ε-caprolactone)/layered double hydroxide nanocomposites. J. Appl. Polym. Sci. **116**(5), 2658–2667 (2010)
5. Tam, L., Lau, D.: Moisture effect on the mechanical and interfacial properties of epoxy-bonded material system: an atomistic and experimental investigation. Polymer (Guildf) **57**, 132–142 (2015)
6. Bedi, R., Chandra, R., Singh, S.: Reviewing some properties of polymer concrete. Indian Concr. J. (October 2002), 0–8 (2015)

7. Almusallam, A.A., Khan, F.M., Dulaijan, S.U., Al-Amoudi, O.S.B.: Effectiveness of surface coatings in improving concrete durability. Cem. Concr. Compos. **25**(4–5), 473–481 (2003) (SPEC)
8. Yan, L., Yang, Y., Jiang, H., Zhang, B., Zhang, H.: The adsorption of methyl methacrylate and vinyl acetate polymers on α-quartz surface: a molecular dynamics study. Chem. Phys. Lett. **643**, 1–5 (2016)
9. Pustovgar, E., et al.: Understanding silicate hydration from quantitative analyses of hydrating tricalcium silicates. Nat. Commun. **7**, 10952 (2016)
10. Richardson, I.G.: Model structures for C-(A)-S-H(I). Acta Crystallogr. Sect. B Struct. Sci. Cryst. Eng. Mater. **70**(6), 903–923 (2014)
11. Mishra, R.K., et al.: cemff: a force field database for cementitious materials including validations, applications and opportunities. Cem. Concr. Res. **102**(April), 68–89 (2017)
12. Cornell, W.D., et al.: A second generation force field for the simulation of proteins, nucleic acids, and organic molecules. J. Am. Chem. Soc. **117**(19), 5179–5197 (1995)
13. Teleman, O., Jönsson, B., Engström, S.: A molecular dynamics simulation of a water model with intramolecular degrees of freedom. Mol. Phys. **60**, 193–203 (1987)
14. Marti, M., Marti, L.: Packing optimization for automated generation of complex system's initial configurations for molecular dynamics and docking. J. Comput. Chem. **24**, 819–825 (2003)
15. Martínez, J.M.M.L., Andrade, R., Birgin, E.G.: Software news and update packmol: a package for building initial configurations for molecular dynamics simulations. J. Comput. Chem. **30**, 2157–2164 (2009)
16. Plimton, S.: Fast parallel algorithms for short-range molecular dynamics. J. Comput. Phys. **117**, 1–19 (1995)
17. Humphrey, W., Dalke, A., Schulten, K.: VMD: visual molecular dynamics. J. Mol. Graph. Graph. **14**(October 1995), 33–38 (1996)

CarboDB—Open Access Database for Concrete Carbonation

Charlotte Thiel, Alexander Haynack, Sebastian Geyer, Alexander Braun, and Christoph Gehlen

Abstract Sustainable service life design of reinforced concrete structures relies on accurate input values. However, in the field of carbonation induced corrosion some input parameters and statistical distributions still need to be validated for worldwide climate conditions. Furthermore, many well-published literature data is not considered due to different storage conditions. At the suggestion of CEN/TC 104/SC1/WG1 the database "CarboDB" was created providing open access to extensive information on concrete carbonation under different storage conditions. The natural carbonation coefficient as well as the minimum concrete cover can be calculated for chosen situations. CarboDB provides reliable data on concrete carbonation in order to increase existing knowledge on concrete carbonation. The database is available online at http://carbodb.bgu.tum.de/#/. By registration further contribution is possible and appreciated. New insights can be gained by merging several sources. For natural carbonation, testing only up to 140 days underestimates the carbonation progress of concretes with limestone fillers and high amount of ground granulated blast furnace slag.

Keywords Carbonation · Service life design · Data management · Compliance testing · Supplementary cementicious materials

1 Background

Concrete carbonation leads to chemical and physical changes in the concrete. Here, CO_2 from the environment diffuses inside the pore structure of concrete and dissolves to carbonic acid. Portlandite, C-S-H as well as all phases in the cement matrix react

C. Thiel (✉) · A. Haynack · C. Gehlen
Centre for Building Materials, Technical University of Munich, Munich, Germany
e-mail: charlotte.thiel@tum.de

S. Geyer
Engineering Risk Analysis Group, Technical University of Munich, Munich, Germany

A. Braun
Computational Modeling and Simulation, Technical University of Munich, Munich, Germany

E. B. Pereira et al. (eds.), *Proceedings of the 3rd RILEM Spring Convention and Conference (RSCC 2020)*, RILEM Bookseries 32,
https://doi.org/10.1007/978-3-030-76547-7_8

with carbonic acid leading to significant changes in the pore structure [1–4] and a reduction of the alkalinity of the pore solution. The latter leads to depassivation of the reinforcement so that it is no longer protected from corrosion.

Reinforced concrete structures are designed to avoid damage during their anticipated service life. Therefore, for concrete carbonation the concrete cover (resistance) needs to remain higher than the carbonation depth (stress) over the anticipated service life. In order to ensure high durability four different concepts exist:

- By compliance to rules and minimum requirements for concrete composition, concrete cover and construction [5, 6],
- by compliance with recognized laboratory test methods (e.g. for approvals in individual cases) [7],
- by semiprobabilistic design approaches, see [8–10],
- by fully probabilistic design approaches. In this case, the structural resistance R for the planned service life must be higher than the load S with a certain reliability [11, 12].

  While descriptive rules limit the use of new material, there is still no consensus about one single European compliance test. Greve-Dierfeld et al. [8–10] suggested testing under natural conditions up to an age of 140 d. DIN EN 12390-10 [13] suggests testing for one year and extending the test procedure to two years for carbonation depth <5 mm which is not feasible for real building projects. The semiprobabilistic concept is derived from the fully probabilistic one, which is included in the database and therefore shortly described below.

The carbonation rate can be described by Eq. 1:

$$x_c(t) = k_{NAC} * \sqrt{k_e * k_c * k_a} * \sqrt{t} * W(t) \tag{1}$$

k_{NAC} (mm/year$^{0.5}$) is the carbonation rate for $W(t) = k_e = k_c = k_a = 1$ and a relative humidity of 65%.

$W(t)$ is the weather function accounting for the effect of rain that will reduce the carbonation rate due to pore clogging with water (CO_2 diffusion in liquid is about 10,000 times slower as in gas). $W(t)$ depends on the time of wetness ToW and the probability of wind-driven rain p_{DR}. It takes into account the exposure orientation of vertical components to wind-driven rain.

k_e is a parameter describing the effect of relative humidity of exposure on the gaseous CO_2 diffusion coefficient,

k_c describes the effect of curing duration on the carbonation resistance.

k_a considers the effect of the CO_2-concentration on the carbonation resistance.

Influencing parameters like the type of curing or the transferability of accelerated test methods to alternate binders are still subject to current research. Therefore, the aim of this work was to create an online carbonation database that is freely accessible to the public. The database collects and organizes experimental results, which can be compared by providing analysis and visualization tools. Thus, the user can compare the performance of concretes for different boundary and environmental conditions

and obtain a recommendation for the required concrete cover. The database facilitates approvals and standardization activities. In the following the structure of the database and the webpage are introduced and an application example is given.

2 Database Structure

2.1 Overview

CarboDB consists of five main tables which store the data under a unique code (ID), thus enabling later allocation. Concrete recipes are documented together with specific storage conditions under precisely defined boundary conditions over the test period and can be clearly traced back to its source. This is depicted in the following scheme.

Each table requires certain input data. The required data

- are necessary to calculate the carbonation resistance of concrete represented by the carbonation coefficient k_{NAC} (Eq. 1),
- are needed to calculate the minimum concrete cover c_{nom},
- enable the unique assignment of the data (reference).

In addition, if available, further data is collected, increasing the knowledge on the carbonation mechanism and allowing alternative service life prediction than proposed in the fib model code [11]. The individual tables are briefly discussed below. Required fields are marked in bold.

2.2 Included Data

The *Materials* table saves information on the concrete composition as well as fresh and hardened concrete properties. The cement type as well as the w/b-ratio are the only mandatory data here.

In addition, information on aggregate size (max. grain size, grading curve, natural or crushed aggregate, density and water absorption) can be included. As the compressive strength of concrete is determined throughout Europe according to different storage conditions on different specimen geometries (cubes or cylinders), the strength class as well as the 28d compressive strength are requested.

Since edges, and whether a samples is laterally sealed or not affect the carbonation progress, see [14, 15], the CO_2 transport is also taken into account. Papadakis [16] showed that it is possible to predict the service life of concrete structures by combining the O_2 diffusion coefficient and the binding capacity, which is also implemented. In addition, physical parameters like porosity and permeability are included.

At last, the contributor finds two columns with "Other" and Specify" where additional parameters that we did not think of so far can be included.

The database table *Conditionings* stores information on the storage conditions (curing, pre-conditioning). The only information required is the curing duration. The type of curing can also be specified (under water at 20 °C, membrane curing, covering with plastic sheets, etc.). Furthermore, information regarding duration, temperature, relative humidity and CO_2 concentration during pre-conditionings can be given.

The table *Exposure Conditions* stores information on the environmental conditions. the following two cases are distinguished:

Case A: Laboratory

Under laboratory conditions, NAC (natural carbonation) and ACC (accelerated carbonation are mandatory in the column carbonation type. Furthermore, the CO_2-concentration, the temperature as well as the relative humidity ***NAC/ACC RH (%)*** are needed. The temperature during the carbonation test becomes necessary if no information on the curing time is available from the *Conditionings* table. In this case, the required curing time can be calculated from the temperature and the ratio of the concrete compressive strengths after 2 and 28 days [17].

Case B: Field

Table 1 summarizes the required data for field data.

The *References* table is used to store the references of the respective experiments. Authors resp. Institute and year are mandatory while title (i..e project title in case of internal and unpublished data) as well as ISBN or DOI are voluntary.

Finally, the *Results* table stores mean value (**carbonation depth average)** and standard deviation of the carbonation depths over time.

Each table also has a column labelled *id_table name* relating the different tables, Fig. 1. Other than the excel template provided for data upload (see Sect. 3.2), the code ID is automatically generated for each table row in the online database. This code is unique for each concrete recipe, each storage condition and each environmental condition during CO_2 exposure. These codes are reflected in the results table and thus

Table 1 Required data in the *Exposure Conditions* table for field investigations

Heading	Description	Example
Carbonation type	Experimental conditions	Field
CO_2 (%)	CO_2-concentration during exposure	0.04
Field RH medium (%)	Average relative humidity during exposure time	79
Field Temperature medium (°C)[a]	Average Temperature during field exposure	6
Field compass direction	Orientation	East, South-East, …

[a]Necessary when information on the curing conditions is missing

Fig. 1 Database relations (mandatory input data are marked bold; hatched columns are not visible in the frontend)

refer to the corresponding database table. Furthermore, the Code ID of the respective table acts as a control column to avoid duplicates. Since the Code IDs are unique, it is not possible, for example, to store two identical concrete compositions in the *Materials* table. This serves on the one hand to increase clarity and on the other hand to reduce the memory requirement of the online database.

3 Webpage

3.1 Structure

The webpage https://carbodb.bgu.tum.de/ provides six different pages that are accessible via an overview menu on each site. Furthermore, each site contains links needed in order to meet the corporate design requirements of the Technical University of Munich, Fig. 2.

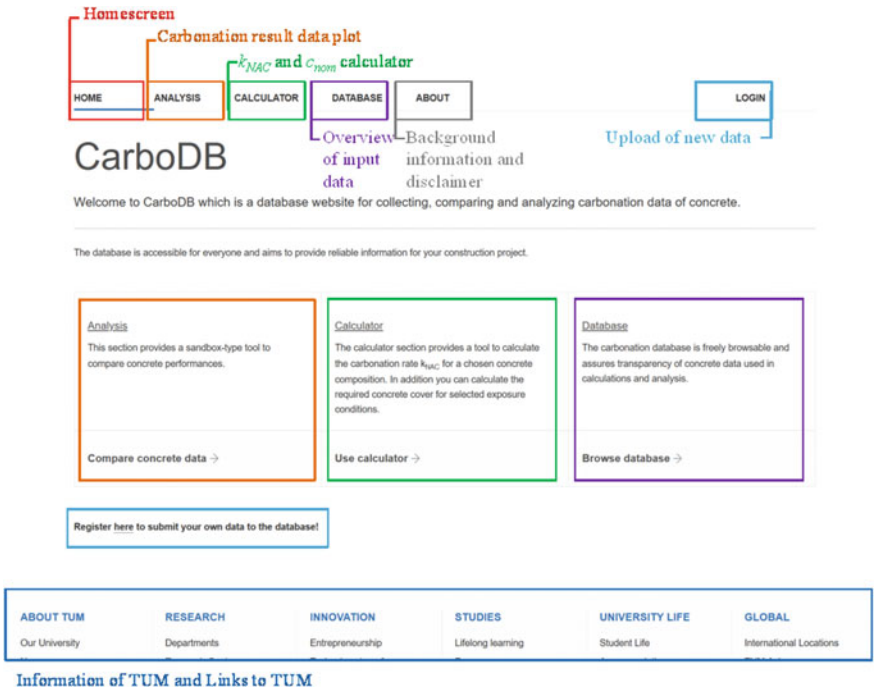

Fig. 2 Webpage structure

The home screen (Fig. 2) provides a general overview and links to the five different database tools: The tool *Analysis* visuals selected results, Fig. 3. The *Calculator* enables the determination of the natural carbonation rate and the concrete cover. In addition, the *Database* tab allows searching through the existing data. The *Register* and *Login* function enables registered users to upload their own data and compare it directly online with existing data, see Sect. 4.

In order to guarantee the durability and safety of the project, the MySQL database of the LRZ [18] was chosen for the database system. This provides the project with a web server with a storage capacity of 10 GB, which is more than enough for the current amount of data and offers sufficient capacity for the near future. Thus, the project is limited to the use of the PHP programming language (version 7.1) [19]. The application user operates the website via the so-called *frontend*. This was implemented with the help of the framework *React* in the programming languages *JavaScript* and *HTML* and is mainly used for the visualization of the database functionalities. The processing of the functionalities, which are triggered by *frontend requests*, is done in the PHP-based *backend* (Framework *Laravel*). The main functions of the backend are the data query in the relational MySQL database (queries), user authentication, file upload and download as well as the implementation of the included functions:

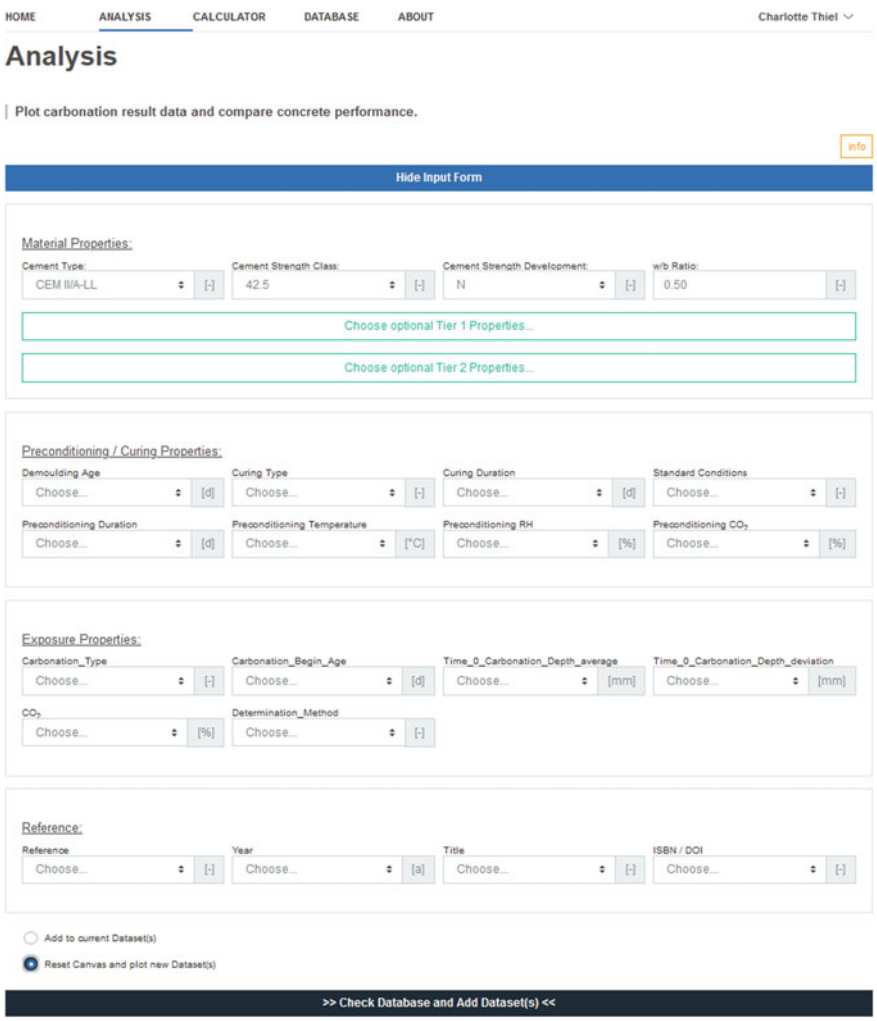

Fig. 3 Analysis (left) tool within the database CarboDB

- Calculation of the carbonation rate k_{NAC}
- Calculation of the minimum concrete cover c_{nom} including the determination of the weather function and the transfer parameters k_e as well as the calculation of the curing time t_c.

Further details can be found in the orange "Info"-boxes within the database.

3.2 How to Contribute

In order to contribute to CarboDB please register at https://carbodb.bgu.tum.de. Your registration will be confirmed within seven days. Hereby, you will receive an excel template as well as detailed information on the data needed. It is also possible, to send data in the existing form to *admin@carbodb.eu.*

4 Application Example

An open question in research and practice is still the transferability of accelerated carbonation tests to natural conditions. Gehlen [12] proposed a transfer function at 2% by vol. for the transferability of experiments according to fib model code [11], Fig. 4.

Figure 4 also shows that the performance of OPC concretes is underestimated and SCM concretes are overestimated. Therefore, the correction factor can be calculated dynamically for each concrete in the database. In order to test the transferability of fine-grained concretes, the mortars shown in Table 2 were produced, stored five years in saturated lime solutions. The sides of the cylinders were sealed with epoxy resin in order to guarantee 1-dimensional CO_2 diffusion. The sample were pre-conditioned in an argon filled chamber at 20 ± 1 °C, 65 ± 2% RH, $CO_2 \leq 0.0005\%$ by vol. Afterwards, the samples were exposed to 20 ± 1 °C, 65 ± 2% RH and different CO_2

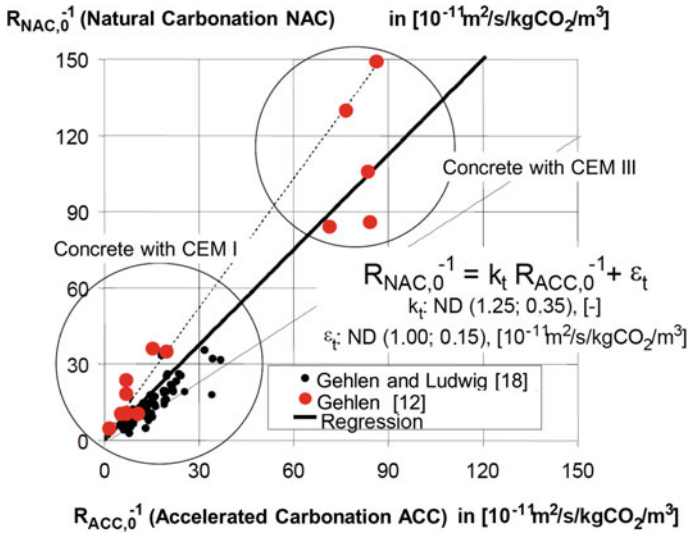

Fig. 4 Relationship between inverse carbonation resistances that were determined under natural conditions (NAC) and under accelerated conditions (ACC) [12]

Table 2 Investigated mortar compositions (more details can be found in the online database)

Label	Cement type	w/b ratio (–)	Air content (% by vol.)	28d compressive strength (N/mm^2)
M1	CEM I 42.5 R	0.50	2.5	55.8
M2	CEM III/B 42.5 N	0.50	2.9	53.2

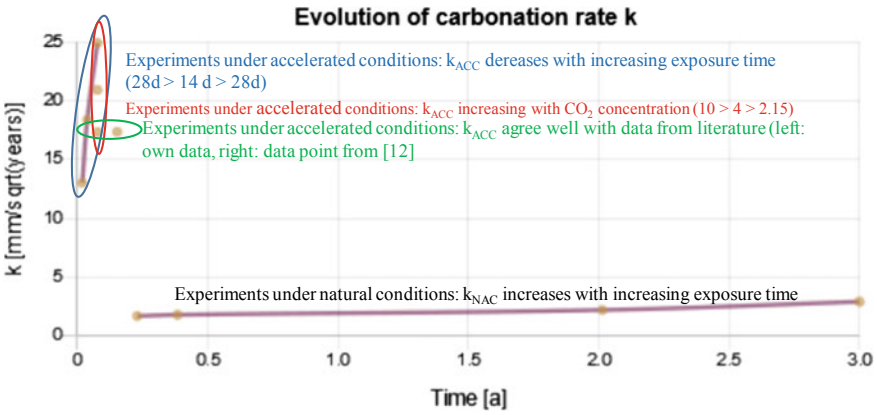

Fig. 5 Carbonation coefficients (uncorrected) for "CEM III/B 42.N and w/b-ratio of 0.50" as displayed in CarboDB in the calculation menu

concentration of 0.045 (NAC), 2.15, 4.0 and 10.0% by vol. for up to three years in the case of NAC and 28d in the case of accelerated CO_2 concentrations. The carbonation depth was determine indirectly using a phenolphthalein-based color indicator.

The data were uploaded to CarboDB and the evolution of the carbonation coefficient was visualized in the calculator menu. Figure 5 shows the results for "CEM III/B 42.N with w/b = 0.50.

Accelerated carbonation lead to surprisingly inconstant values with increasing exposure time, see Table 3. When relating the carbonation coefficients under accelerated conditions k_{ACC} by the square root of the ratio of the accelerated concentration to the natural one, the carbonation coefficient is clearly underestimated, as illustrated in Table 3. This agrees with the observations of Hunkeler et al. [14], who determined increasing correction parameters for higher CO_2 concentrations in their investigations. The carbonation coefficients are not constant over time—especially at high CO_2 concentrations. However, a single correction factor is not suitable for the different types of concretes. Future research should therefore focus on developing a correlation based on physio-chemical relationships. Especially for concrete with high amount of slag, increasing CO_2 concentration led to an increased deviation of expected results, Table 3.

By visualizing natural and accelerated carbonation coefficients over time, accelerated coefficients tended to decrease with time while natural increased with time. Most concrete recipes agreed well with the recommendation to terminate the natural

Table 3 Carbonation coefficients under different conditions

Label	CO_2 concentration during exposure (% by vol.)	Exposure time (d)	$K = x_c(t)/\mathrm{sqrt}(t)$	$K = K_{ACC} * \mathrm{sqrt}([CO_2]_{NAC}/[CO_2]_{ACC})$
M1	0.045	140	1.3	3
M1	0.045	1095	1.4	
M1	2.15	28	5.8	0.8
M1	4.00	28	11.9	1.2
M1	10.00	28	14.4	0.9
M1	10.00	14	11.7	0.9
M1	10.00	7	13.7	0.7
M2	0.045	140	1.8	
M2	0.045	1095	2.9	
M2	2.15	28	17.3	2.4
M2	4.00	28	20.9	2.1
M2	10.00	28	24.9	1.6
M2	10.00	14	13.0	0.8
M2	10.00	7	18.4	1.2

test after 140d. However, for concretes with CEM II/A-LL as well as CEM III/B the natural carbonation coefficient further increased from 2.75 to 3.2 for CEM II/A-LL and for CEM III/B from 2.0 to 2.9 (2 year value). This clearly shows that further data evaluation is needed, to come to a general conclusion and recommendation for further durability assessment in the field of concrete carbonation. Here, the database can serve as a valuable tool to collect, organize and analyze existing data.

5 Conclusions

An open database was created in order to connect field and research results for concrete carbonation and draw recommendation for future standardization. The database enables filtering and calculation of the natural carbonation coefficient as well as displaying different carbonation results. It therefore serves as a decision-aid for choosing optimal concrete compositions or maintenance strategies. In addition, the database collects additional data such as diffusion coefficient and binding capacity increasing the knowledge on the carbonation mechanism and allowing alternative service life prediction than proposed in the fib model code. Furthermore, existing model input parameters or statistical distributions could now be adapted to real experimental results.

In order to ensure the use of CarboDB in the future, the project resources are hosted by the LRZ (Leibniz Rechenzentrum). This allows both database and performance

scaling depending on the demands of increasing data capacity. The database can be adapted to include new insights whenever available and therefore serves as a dynamic decision aid for planners, consultants, approval bodies and researchers.

References

1. Bier, T.A.: Karbonatisierung und Realkalisierung von Zementstein und Beton. Karlsruhe: Institut für Massivbau und Baustofftechnologie. Dissertation (1988)
2. Morandeau, A., Thiéry, M., Dangla, P.: Investigation of the carbonation mechanism of CH and C-S-H in terms of kinetics, microstructure changes and moisture properties. Cem. Concr. Res. **56**, 153–170 (2014)
3. Ashraf, W.: Carbonation of cement-based materials: challenges and opportunities. Build. Mater. **120**, 558–570 (2016). https://doi.org/(10.1016/j.conbuildmat.2016.05.080)
4. Auroy, M., Poyet, S., Le Bescop, P., Torrenti, J.M., Charpentier, T., Moskura, M., Bourbon, X.: Comparison between natural and accelerated carbonation (3% CO_2): impact on mineralogy, microstructure, water retention and cracking. Cem. Concr. Res. **109**, 64–80 (2019)
5. DIN 1045-2:2008-08: Tragwerke aus Beton, Stahlbeton und Spannbeton - Teil 2: Beton - Festlegung, Eigenschaften, Herstellung und Konformität - Anwendungsregeln zu DIN EN 206-1. Beuth Verlag (2008)
6. DIN EN 206:2017 Beton Festlegung, Eigenschaften, Herstellung und Konformität. Beuth verlag (2017)
7. Gehlen, C., Thiel, C.: Specification of building materials for in service durability. In: Proceedings ICSBM 2019: 2nd International Conference of Sustainable Building Materials, Technische Universiteit Eindhoven, S. 31–40 (2019)
8. Von Greve-Dierfeld, S., Gehlen, C.: Performance-based durability design, carbonation. Part 1—Benchmarking of European present design rules. fib Struct. Concr. **17**(3), 309–328 (2016)
9. Von Greve-Dierfeld, S., Gehlen, C.: Performance-based durability design, carbonation. Part 2—Classification of concrete. fib Struct. Concr. **17**(4), 523–532 (2016)
10. Von Greve-Dierfeld, S., Gehlen, C.: Performance-based durability design, carbonation. Part 3: PSF approach and a proposal for the revision of deemed-to-satisfy rules. fib Struct. Concr. **17**(5), 718–728 (2016)
11. Fib: Model Code for Concrete Structures 2010. Bulletin of the fib, Lausanne, Switzerland (2010)
12. Gehlen, C.: Probabilistische Lebensdauerbemessung von Stahlbetonbauwerken-Zuver-lässigkeitsbetrachtungen zur wirksamen Vermeidung von Bewehrungskorrosion. Disser-tation, RWTH Aachen (2000)
13. DIN EN 12390-10:2019, Testing Hardened Concrete—Part 10: Determination of the Relative Carbonation Resistance of Concrete. Beuth Verlag (2018)
14. Hunkeler, F., Lammar, L.: Anforderungen an den Karbonatisierungswiderstand von Betonen: Forschungsauftrag AGB 2008/012 auf Antrag der Arbeitsgruppe Brückenforschung (AGB). Schweizerischer Verband der Strassen- und Verkehrsfachleute (VSS) (2012)
15. Thiel, C., Schön, A., Gehlen, C.: Einfluss der CO_2-Permeation auf die Carbonatisierung zementgebundener Baustoffe. 20. ibausil, Weimar (2018)
16. Papadakis, V.G., Vayenas, C.G., Fardis, M.N.: A reaction engineering approach to the problem of concrete carbonation. Am. Inst. Chem. Eng. J. (AIChE J.) **35**(10), 1639–1650 (1989)
17. Betontechnische Daten. 10.7.3 Nachbehandlungsdauer. Retrieved from https://www.betontechnische-daten.de/de/10-7-3-nachbehandlungsdauer. Accessed 16 Dec 2019

18. Gehlen, C., Ludwig, H.M.: Compliance Testing for Probabilistic Design Purposes. Brussels: European Union – Brite EuRam, 1999. - Contract BRPR-CT95-0132, Project BE95-1347, Document BE95-1347/R8 (1999)
19. Leibniz Rechenzentrum. Webhosting (2019). Retrieved from https://doku.lrz.de/display/PUBLIC/Webhosting. Accessed 16 Dec 2019

Architectural Concrete Versus White Stone: A New Approach to Restoring Historical Heritage

Vyacheslav R. Falikman and Vyacheslav V. Deniskin

Abstract The Russian culture has a rich history and strong traditions, especially when it comes to ancient white-stone architecture. Usually the term "white stone" stands for light carboniferous limestone. White stone was one of the basic building materials in Old Russia and was of great historic importance in the 11th–15th cc. Unfortunately, natural white stone resources are gradually being depleted. Modern concrete technology is able to imitate and replace to the full the natural stones by artificial composites that are not inferior to them in their properties. One of the most promising areas of high-performance concrete (HPC) concept implementation is manufacture of architectural concrete with improved decorative properties based on mechanically activated composite binders and effective admixtures. Architectural concrete frost resistance reaches 300–600 freezing–thawing cycles and more; the open integral porosity does not exceed 2–4% vol. The values of the prism strength factor and the initial tangent modulus of elasticity of modified concretes meet or exceed regulatory requirements. Durability of architectural concrete may be additionally improved by impregnation with special organic silicate compounds. Thereby an optimum combination of construction and technical characteristics of concretes and decorative properties of products is achieved that should considerably expand the field of architectural concrete application, solve the problems of historical heritage preservation, and on the whole facilitate the growth of its social significance and attractiveness. Some of the most valuable of the white-stone architecture objects reconstructed in Russia with use of architectural concrete in the last decade are presented.

Keywords Architectural concrete · White stone · Restoring · Historical heritage · High performance concrete

V. R. Falikman (✉) · V. V. Deniskin
National Scientific Research Centre "Construction", Moscow, Russia
e-mail: vfalikman@yandex.ru

E. B. Pereira et al. (eds.), *Proceedings of the 3rd RILEM Spring Convention and Conference (RSCC 2020)*, RILEM Bookseries 32,
https://doi.org/10.1007/978-3-030-76547-7_9

1 Introduction

From ceremonial stone runes in the European continent, to the polished, white stone in Greco-Roman classical orders, to mountain-shaped stone temples of Southeast Asia, to the stone block pyramids in Latin America, stone is one of the most commonly used building materials.

Russian culture has a rich history and strong traditions, especially when it comes to ancient white-stone architecture: churches, chapels, ancient country estate complexes, apartment houses and household constructions. White stone was one of the basic building materials in Old Russia and was of great historic importance as an expression of the state's power and imperial ideology in the 11th–15th cc. It played a key role not only in the Old Russian Architecture, but in the history of the Old Russia as well. In the pre-Mongolian years 95% of buildings in Vladimir and Suzdal lands were built of white stone.

Usually the term "white stone" stands for light carboniferous limestone (from the Paleozoic Era), occurring in the central regions of European, part of modern Russia. However, it is also often referred to sandstone, dolomite, and Volga limestone of Permian formation, as well as numerous sorts of limestone, travertine, and alabaster lying in Transdniestria. Consequently, a more general definition of white stone is any treatable white-yellowish matt surfaced stone, which is neither marble nor shell rock. Unfortunately, natural white stone resources are being gradually depleted now. The problem of historical heritage preservation becomes especially acute.

Designers and architects are continuously looking for new materials to improve their projects. Resistance and durability take here a starring role. So called "cast stone" or "reconstructed stone" is a concrete masonry form of artificial stone which simulates natural-cut stone. Cast stone frequently was produced with a low water-to-cement ratio mixture with a "dry" (or "earth moist") consistency. The mixture was consolidated into a mold using an air-driven, or electric, tamping device or vibration under pressure.

The concept of high-performance concretes (HPC) formulated in the 80s–90s of the past century has determined the requirements to concretes combining the values of physical and mechanical properties and durability being optimum for specific operating conditions; their development has become one of the basic achievements in the building materials science at the turn of the millennium [2, 10]. The HPC extends the areas of application of artificial mineral composites [9].

One of the most promising areas of HPC implementation is manufacture of architectural concrete with improved decorative properties and performance. Application of concrete technology in decorative façade elements, sculptural plaster, and other elements of buildings requires, as a rule, the use of highly workable and fluid mixes. Additionally, plain and colored cements are used to improve decorative properties of the material, while fine aggregates are required to create complex textured and highly detailed surfaces. A combination of these factors leads to increased water requirements for cement mixes, which in turn instigate the growth of shrinkage strains, increase in permeability and reduction in frost resistance of concrete. The features of

cement chemical, mineralogical, and material composition (for example, increased content of C_3A, increased content of belite, introduction of bleaching mineral agents during grinding, e.g. diatomite, etc.) contribute to the problem.

Within the framework of the HPC concept, an integrated control system for the structural characteristics, hardening rate and strength of concrete has been developed having in mind to obtain a material with set-up physical and mechanical properties and durability in specific operating conditions. It envisages the use of mechanically activated composite binders with multifunctional chemical modifiers for various applications. Thereby a directional impact is possible upon the processes of structure formation and hydration, hardening and strength gain, as well as on parameters of concrete structure and durability.

2 Materials and Test Methods

White cement of CEM I 52.5 R grade produced by the Aalborg cement plant, Denmark, was used (Table 1).

Washed crushed granite aplite of 5–20 mm fraction as coarse aggregate and standard siliceous sand were used for concrete preparation.

A superplasticizer used was polymethylene polynapthalene sulphonates (PNS) type. Titanium dioxide produced by DuPont was used as a pigment.

The test procedures were conformed to the current Russian standards including the concrete mix properties according to GOST 10181-2014, strength—GOST 10180-2012, prism strength and initial tangent modulus of elasticity—GOST 24452-80, frost resistance—GOST 10060-2012, shrinkage—GOST 24544-81*, water absorption and void ratio—GOST 12730.3-78…GOST 12740.4-78, water impermeability—GOST 12730.5-84, characteristics of binders and cements—GOST 310.1-76 … GOST 310.3-76, GOST 310.4-81 and special technical requirements for LWDB TU 5744-002-00369171-97.

To investigate the parameters of the specimen porous structure, the optical method based on the Gallery software was applied.

Composite binders preparation was envisaged by mechanochemical activation of components (the “intergrinding” technique) ensuring reduction of their water demand; in compliance with the established practice, the binders produced are specified as LWDBs (low water-demand binder) with indication of the clinker component per cent content (e.g. LWDB-80, LWDB-90, LWDB-100).

Table 1 Bogue cement composition

Cement	C_3S	C_2S	C_3A	C_4AF	R_2O*
CEM I 52.5 R	77.26	15.52	4.5	1.0	0.25

*Alkali content ($Na_2O + 0.658\ K_2O$)

3 Results and Discussion

3.1 Low Water Demand Binders

The main principle of low water demand binder production is mechanical and chemical activation of a rationally selected raw mix including clinker components, mineral additives, gypsum and an organic modifying agent which contains a water-reducing component [5]. The production of low water demand binder (LWDB) is carried out under pre-specified conditions in the grinding mills which are traditionally used in the cement industry i.e. tube mills with special ball charges. In such a case, preference is given to closed cycle grinding with the use of separator mills, which are rather widespread. Grinding with modifying agent provides for a variety of advantages which secure certain properties to a ready-made product, including considerable increase in hydraulic activity of the clinker minerals under the simultaneous decrease in water consumption of the binder.

The LWDB technology [6] makes it possible to produce binders with a wide range of material composition and properties varying from multicomponent low-clinker binders with 15…25% of clinker consumed (LWDB-15…LWDB-25) to pure clinker binders, the mineral part of which is presented only by the clinker component and gypsum (LWDB-100).

LWDB-100 differs in the increased physical and mechanical properties and durability. That's why, the use of concrete on its basis when constructing important and unique engineering structures is considered to be technically reasonable and economically viable. The "specific consumption of aggregates" in concrete based on LWDB is so great in comparison with an ordinary Portland cement (max. 13 vs. max. 27) that this allows considering LWDB as a next-generation cement [15].

It should be noted that the organic mineral compounds formed on the clinker grain surface in the activation process determine such technological properties of composite binder-based mixes as resistance to bleeding, a high degree of thixotropic shear thinning and increased reproductive performance, i.e. the ability to reproduce the finest details of the relief or texture without the formation of large air pores and defects on the front surface, which is especially important for decorative elements made from architectural concrete [7, 8].

The use of mechanochemical activation provides for the considerable increase in the hardening rate and strength of white cement, which n turn would be used as a basis of composite binders with 60–100 MPa activity (strength quality of cement) depending on the initial cement quality; this corresponds to the strength rise about 41–53% at 28 days, about 30–70% at 2–7 days and over 2 times at 1 day. Alongside the above, the essential reduction (by 17–25%) of cement paste water demand is provided in spite of the rise in binder dispersivity as compared to initial cements. Introducing at the stage of binder production, mineral additives, such as natural alumina-containing pozzolana to reduce shrinkage or granulated blast furnace slag to control heat release and to increase sulfate resistance, does not result in considerable reduction of binder activity.

Below the test results are given based on composite binders from LWDB-90–LWDB-100 test batches that were produced in a ball mill with 0.5 t/h capacity from white cements. In compliance with the established practice, for composite binders LWDB designation is used, i.e. the binder having low water demand, the numeral in the designation denotes the content of clinker component in % note that the first paragraph of a section or subsection is not indented. The first paragraphs that follows a table, figure, equation etc. does not have an indent, either.

3.2 Fresh Concrete and Structure Formation of Concrete

In accordance with the reduced water demand of binders the making of flowable (or self-compacting) fresh concrete on their basis is achieved at significantly lower—by 20–30%—mixing water consumption (Table 2). At the same time, the specific rheological properties of composite binders associated with mechanochemical activation provide the minimum bleeding, reduction of air entrainment in concrete mixes and increase in their density, suggesting improvements of concrete structural characteristics.

Control of structure formation processes as well as performance and decorative properties of architectural concrete envisages at the stage of concrete mix preparation, first of all, a regulation of their slump loss and introduction of various chemical and mineral admixtures (mineral pigments, shrinkage reducing admixtures, etc.) when mixing. The slump loss of concrete mixes with composite binders, i.e. the rate and time of initial flow reduction, as a rule, corresponds to the slump loss of mixes with ordinary cements. However, all that may not be sufficient when concreting complex elements, for example, large-scale sculptural reliefs. Besides, the rapid loss of workability is in line with accelerated structure formation of concrete and intensive heat release during the first hours after placement. Introduction of retarding agents (for example, based on sodium tripolyphosphate) may be good solution. Subsequent paragraphs, however, are indented.

3.3 Positive Role of Titanium Dioxide

Along with admixtures controlling the rate of structure formation, coloring agents, in the first turn, titanium dioxide TiO_2, are introduced when mixing. Even when using binders based on white cement, the introduction of TiO_2 allows neutralizing the color distortion due to contamination of the fillers and aggregates, and makes the mix color more susceptible to the introduction of small doses of mineral pigments for accurate reproduction of colors. Adding small amounts of TiO_2 (up to 3–5% of cement mass) does not actually affect water demand and rheology of concrete mixes, while it affects positively the concrete strength. The data presented in Table 2 show that for all periods of hardening, the strength of concretes increases with the growth

Table 2 The impact of binders and admixtures used in architectural concrete mixtures preparation on technological properties and strength of concrete

№	Quality index, measuring unit	Indicator values					
		White CEM I 52.5R		LWDB-100*			LWDB-90**
	Composition №	1	2	3	4	5	7
1	Material consumption, kg/m^3						
1.1	Cement	490	496	480	485	490	469
1.2	Sand	542	595	710	717	725	1641
1.3	Aggregate	1068	1071	1100	1110	1124	–
1.4	Water	226	198	160	162	146	159
2	Admixture dosage, % cement mass						
2.1	PNS	–	0.6	–	–	0.5	–
2.2	TiO_2	–	–	–	1	1	3
3	W/C	0.46	0.4	0.33	0.33	0.3	0.34
4	Slump, cm	18.5	20	15	5–9	14	14
5	Fresh concrete density, kg/m^3	2326	2360	2450	2475	2490	2288
6	Air content, %	2.5	3.0	2.7	2.3	2.3	4.5
7	Compressive strength, MPa, at age						
	1 day	20.5	25.7	55.0	69.7	72.8	39.8
	2 days	36.4	47.4	64.8	70.5	78.4	55.2
	3 days	40.2	51.0	72.1	76.7	83.0	59.5
	7 days	47.6	58.4	83.3	90.0	90.6	73.4
	28 days	55.6	67.3	93.7	103.8	112.6	81.0

*Based on white CEM I 52.5 R
**Based on white CEM I 52.5 R, mineral additive—granulated blast furnace slag

of TiO_2 dosage. In combination with PNS the introduction of TiO_2 is accompanied by even greater increase in strength.

Using titanium dioxide sensibilized through nanotechnology gives additional benefits [13].

3.4 Hardened Concrete

The analysis of the data in Table 2 shows that the use of mechanically activated binders is accompanied in all cases by an essential increase of the hardening rate as compared to concretes based on initial cements. Indeed, the strength of modified concretes reaches 49–67% of the quality class strength as early as 1 day aging,

while for concretes based on initial cements this value does not exceed 36–38%. These high hardening rates of concrete cured at ambient air confirm once more a possibility to produce architectural concrete articles without steam curing when used both sand and crushed stone (compositions 1–5) and graded sand mixtures as aggregates (composition 7).

3.5 Mechanical Properties and Durability

The increased hydraulic activity of mechanically activated binders and efficient mix design of architectural concretes predetermine their high physical and mechanical properties and durability. The data presented in Table 2 shows that the values of physical and mechanical properties of concrete correspond to high values of their strength.

The values of the prism strength factor and the initial tangent modulus of elasticity of modified concretes meet regulatory requirements or exceed them according to National Building Code SP 63.13330 [18].

The value of volumetric water absorption of modified architectural concretes may also serve as an indicator of improvement of their structural characteristics. The data in Table 3 indicates that the mentioned value does not exceed 8%, thus allowing attributing the obtained concretes to materials with a compact structure.

Combination of high density and strength of modified concrete determines, in turn, their high frost-resistance. A frost-resistance factor, K_{fr}, of concretes based on LWDB (i.e. the ratio of strength of key samples after a given number of alternate freezing and thawing cycles to the strength of control samples) is over 1 even after

Table 3 Main characteristics of architectural concrete depending on binder and admixture types

№	Quality index, measuring unit	Indicator values	
		White CEM I 52.5R	LWDB-100*
1	Admixtures and dosage, % cement mass	PNS (0.6%)	TiO_2 (1%) PNS (0.5%)
2	Compressive strength, MPa, in age 28 days		
2.1	Cubic R_c	67.3	112.6
2.2	Prism R_{pr}	48.5	85.6
3	Prism strength factor, R_{pr}/R_c	0.71	0.76
4	Initial tangent modulus of elasticity $E \times 10^{-3}$, MPa		
4.1	Experimental	38.1	57.7
4.2	Normative	39.0	–
5	Volumetric water absorption	12.8	7.1

*Based on white CEM I 52.5 R

300–400 test cycles, that indicates to the available reserve of durability and to the predominance of constructive processes in the concrete structure over destructive ones. In contrast, the frost resistance of concrete based on initial white cements does not exceed 100–250 cycles depending on the type of cement.

3.6 Impregnation with Special Organic Silicate Compounds

In real building practice, ornamental concrete products are exposed to pollution to some extent even prior to the beginning of maintenance—during transportation, warehousing and especially at installation which is carried out frequently without appropriate protection of exterior surfaces. Surface treatment of architectural concrete with special organic-silicate compounds, which partially or completely seal the pores with high density air-silica-gel, improves performance and durability of material, decreases water absorption up to 20–37% and increases freezing–thawing resistance up to 20–50% [12].

With reference to architectural concrete it means also an increase of durability of the surface of ornamental elements to fouling and makes easy the process of their cleaning, and also possibility of protective coating while in service that is confirmed by experience of practical application.

4 Case Study

High performance architectural concrete was used for the manufacture of external decoration with a texture and color simulating a natural white stone in restoration work of many historical monuments and buildings in the City of Moscow and the Moscow Region, including churches, chapels, ancient country estate complexes, apartment houses and household constructions: The Center of Orthodox Heritage in Peredelkino near Moscow (early 19th c.) where more than 24,000 purpose-made details of outside architectural decoration were installed, Tsaritsino (18th c.) near Moscow (Fig. 1), the St. George Church in Romanovo (early 18th c.), the Church of the Iveron Icon of the Mother of God, the church tower of the Ascension of Christ at Rogozhky Barrier (19th c.), etc.

As usual, elements of external decoration had highly rich ornaments of the front surface that reached 3/4 of the total surface of the product (Fig. 2). The main objective was to obtain a high quality, defect-free surface with a given texture and color, when the size of individual items was sometimes more than 3.0—1.5 m with a thickness not exceeding 80 mm.

A unique example of the implementation of the developed architectural concrete (LWDB-100—480 kg/m^3; sand—723 kg/m^3; coarse aggregates—1120 kg/m^3; water—149 kg/m^3; TiO_2—14.6 kg/m^3; admixtures—4 kg/m^3) was the making of the high relief of St. Princess Olga, Equal-to-the-Apostles for the Cathedral of Christ the

Fig. 1 Tsaritsino near Moscow

Fig. 2 The church tower of the Ascension of Christ at Rogozhky Barrier, Moscow

Savior with height more than 5 m. The characteristics of the sculpturesque concrete are shown in Table 4.

Calculation of durability of such architectural concrete for climatic conditions of Moscow based on fracture mechanics parameters show that the time within which

Table 4 The concrete for the St. Princess Olga, Equal-to-the-Apostles high relief

Properties	Quality index	Units	Values
Aesthetic	Whiteness	%	Reference (dolomite)
	Surface quality	–	A2
Physical and mechanical	Specific gravity	kg/cm^3	2.503
	Compressive strength	MPa	149.8
	Modulus of elasticity	MPa	5.6×10^4
	Shrinkage	mm/m	0.137
Durability	Frost resistance	grade	F_1800
	Watertightness	grade	W16

the structural characteristics of the concrete have reached its limit state, is 152 years [16].

As usual, elements of architectural decoration are manufactured by vibratory casting method, with the use of vibrators and vibrating table (frequent vibration in the range 10–60 Hz), in a specially designed rigid composite matrix with an outer layer of silicone compounds meeting the requirements of dimensional stability (not more than 0.01%) that allows producing details with very precise geometric dimensions. At the age of 24 h after curing in a humid chamber under controlled conditions (T = 40–45 °C; RH = 80–95%) the products were demolded and treated by water-repellent composition.

5 Standardization Issues

Unfortunately, architectural concrete did not fully comply with the Russian standards, so it was necessary to develop a set of new standards dedicated to cast stones or to update already published standards, including technical requirements, test methods, specifications for architectural concrete, durability and execution of concrete structures and units, especially in severe conditions and under fire hazard.

Today, the would-known industry standard for physical properties and raw materials constituents of architectural cast stone is ASTM C 1364 [4]. In the UK and Europe, it is more normal to use the British Standard BS 1217:2008 “Cast stone—Specification”. The European Commission’s “Construction Products Regulations” legislation states that by mid-2013 CE marking becomes mandatory for certain construction products sold in Europe, including some cast stone items.

Deutscher Beton- und Bautechnik-Verein (DBV) and Bundesverband der Deutschen Zementindustrie (BDZ) published in 2015 the last edition of Code of Practice for Architectural Concrete [11]. It defines four concrete classes (SB1-SB4) which have different demands for texture (demand classes T1-T3), porosity (demand

classes P1-P4); steadiness of shade (demand classes FT1-FT3); surface evenness (demand classes E1-E3); quality of formwork skin (demand classes SHK1-SHK3), and quality of formwork joints (demand classes AF1-AF4). The DBV Code of Practice presents the current state of technology and gives specific instructions for practical implementation. Some requirements are available also in ACI 303R-12 [1] and ICOMOS/ISCARSAH Recommendations [14].

In 2010, Russia started the process of creating new building regulations, revising building codes and standards, and reestablishing the corresponding enforcement mechanism to ensure regulatory compliance. This presents a unique opportunity to rebuild its regulatory framework from the ground up on the premise of integration and interoperability. Implementation of international norms is the main objectives. Currently, within the framework of programs of standardization, a group of standards has to be developed referring to specification and test methods of architectural concrete. Russian specialists hope to start long-running professional cooperation with representatives of international professionals and business to solve very important problems in the development of the next generation of standards and determination of what standards need to be implemented foremost.

These kinds of joint actions will help us to work with new documents without any problems for international or Russian business. With research progresses and the technical regulations development, the field of architectural concrete application will undoubtedly expand.

6 Conclusions

Thus, modern concrete technology is able to imitate and replace to the full the natural stones by authenticable and compatible artificial composites that are not inferior to them in their properties. For this reason, the Association for preservation technology was describing cast stone materials as being "fully accepted" [3]. Only recently, architectural concrete has developed into one of the most important means of design in modern architecture. No other building material can be used and processed in such a versatile manner. Therefore, architectural concrete is used now for almost all construction tasks. Through the design capabilities of the fresh concrete, virtually any shape and quality can be economically realized with the help of appropriate formwork systems and form lining.

SCC shows additional great potential to obtain good surfaces, in a way which is hard to get with vibrated concrete. However, SCC seems to be more sensitive than vibrated concrete with regard to surface finishing, due to the way it is cast, the nature of the formwork, the type and thickness of applied release agent, temperature of the formwork and weather conditions.

The above mentioned methods of modifying the architectural concrete provide an opportunity to control its structure and properties as well as concrete mix workability and hardening rate at all stages of its manufacture—from selection of initial materials to surface treatment at the final stage of manufacture or even at the operational stage.

Thereby an optimum combination of construction and technical characteristics of concretes and decorative properties of products is achieved that should considerably expand the field of architectural concrete application, solve the problems of historical heritage preservation, and on the whole facilitate the growth of its social significance and attractiveness.

According to Scott [17], "…through technological advances and rigorous testing regimes, the quality of cast stone is undoubtedly higher and more consistent than has been created at any time in the history of artificial stone. One can only wonder how historians will review the works of present day manufacturers in the centuries to come, for it would appear that it is only with hindsight that we are prepared to properly judge this material".

Growth in the codes, standards, guidelines, and training and certification programs will play a significant role in the development and acceptance of architectural concrete versus stone. An emphasis-shift to long-term cost–benefit analyses and performance-based criteria for designing will result in the selection of this type concrete for a particular application. Ultimately, the realization of the full potential of architectural concrete will depend upon on strategic planning and vision from industry leaders, government and academia alike.

References

1. ACI 303R-12: Guide to cast-in-place architectural concrete practice. ACI, 36 (2013)
2. Aitcin, P.-C.: High performance concrete. E&EN Spon., 140 (2004)
3. APT Bulletin: J. Preserv. Technol. **21**(3/4), APT Int. (1989)
4. ASTM C1364: Standard specification for architectural cast stone, 3 (2019)
5. Babaev, Sh.T., Bashlykov, N.F., Falikman, V.R., et al.: Cementitious materials and method of making the same, US Patent 5,478,391. 1993 (1995)
6. Bashlykov, N.F., Falikman, V.R., Serdyuk, V.N., et al.: Hydraulic cement. Russian Patent № 2096364, 1996, publ. in Bul. No. 32 (1997)
7. Bashlykov, N.F., Falikman, V.R., Serdyuk, V.N., et al.: Method of manufacturing of decorative binder with low water demand. Russian Patent № 2085525, 1991, publ. in Bul. No. 20 (1997)
8. Bashlykov, N.F., Sorokin, Yu.V., Falikman, V.R., et al.: Method of manufacturing of decorative building products and decorative coatings. Russian Patent № 2084416, 1992, publ. in Bul. No. 20 (1997)
9. Boyle, M.J.: Concrete as a substitute for granite cladding attains high performance concrete consideration as the result of exceptional materials and production control. In: International Symposium on High Performance Concrete, Orlando, Florida, U.S.A., pp. 279–293 (2000)
10. Collepardi, M. (2006). The new concrete. Villorba: Grafiche Tintoretto, Italy, 421 pp.
11. DBV: Code of practice "architectural concrete" (Edition 06/2015) (2015)
12. Falikman, V.R., Sorokin, Yu.V., Deniskin, V.V.: Surface protection of high performance architectural concrete. In: Proceedings of Concrete Solutions, 4th International Conference on Concrete Repair, Dresden, Germany, Taylor & Fransis Group, London, UK, pp 813–821 (2011)
13. Falikman, V., Vajner, A., Zverev, I.: New photocatalytic cementitious composites containing modified titanium dioxide nanoparticles. In: Proceedings, 3rd Int. Symposium on High Performance Concrete and Nanotechnology for High Performance Construction Materials (Hipermat), Kassel, Germany, pp 147–152 (2012)
14. ICOMOS/ISCARSAH: Recommendations for the analysis, conservation and structural restoration of architectural heritage, Paris, 39 pp (2005)

15. Ioudovitch, B.E., Dmitriev, A.M., Zoubekhine, S.A., Bashlykov, N.F., Falikman, V.R., Serdyuk, V.N.: Low water requirement binders as new generation cements. In: 10th International Congress on the Chemistry of Cement, Goteborg, Sweden (Pub. No 3iii021) (1997)
16. Piradov, K.A., Guseev, E.A., Falikman, V.R., et al.: The reinforced concrete high reliefs with assured durability more than 100 years for the Cathedral of Christ the Savior. Beton i zhelezobeton (Concrete and Reinforced Concrete) **6**, 22–24 (in Russian) (1998)
17. Scott, S.: Artificial Stone: A Successful Substitute for Natural Stone? Haddonstone Ltd., 120 pp. (2009)
18. SP 63.13330.2018: Code Specification "Concrete and reinforced concrete structures. General provisions". Ministry of Construction, Housing and Utilities of the Russian Federation, 143 pp. (2018)

Earth, Gypsum and Cement-Based Plasters Contribution to Indoor Comfort and Health

T. Santos, P. Faria, and M. I. Gomes

Abstract Indoor air quality is important for comfort and health of buildings inhabitants. The use of environmentally friendly building materials is also very important for sustainable and green buildings. In the present study, mechanical characteristics of five mortars were comparably analyzed: two unstabilized earth mortars, one earth-air lime mortar, one cement mortar and other gypsum mortar. The earthen plasters are nowadays commonly applied unpainted. The gypsum plaster system is composed by the base mortar and a finishing layer; it can be applied unpainted or painted. The cement plaster is generally finished with a paint system. Therefore, the adsorption and desorption capacities were assessed for all the plasters and the influence of the paint system was evaluated for the cement and gypsum plasters. Results show that the earth mortar stabilized with air lime presents lower mechanical strength, in comparison to all other mortars, and lower adsorption capacity, similar to the gypsum system. The unstabilized earth plasters present high adsorption capacity, in comparison to the cement and gypsum plasters. The paint system does not have significant influence on the adsorption capacity of the gypsum plaster but reduced that capacity on the cement plaster. These results demonstrate the important contribution that unstabilized earth plasters may provide as passive indoor hygrothermal buffers, in comparison to other plasters, thus to comfort and occupants health.

Keywords Air lime · Clay · Desorption · Mechanical strength · Mortar · Sorption

1 Introduction

Plasters are applied to coat, protect and decorate indoor walls and ceilings, having a significant surface area. Currently, with existing energy and environmental problems and people's ecological awareness, it is increasingly necessary to use renewable

T. Santos · P. Faria (✉)
CERIS and Department of Civil Eng, FCT, Universidade NOVA de Lisboa, Lisbon, Portugal
e-mail: paulina.faria@fct.unl.pt

M. I. Gomes
CERIS and Department of Civil Eng, ISEL, Instituto Politécnico de Lisboa, Lisbon, Portugal

E. B. Pereira et al. (eds.), *Proceedings of the 3rd RILEM Spring Convention and Conference (RSCC 2020)*, RILEM Bookseries 32,
https://doi.org/10.1007/978-3-030-76547-7_10

and/or environmentally friendly building materials, with low CO_2 emissions and embodied energy, which may also contribute to improve the comfort and health of inhabitants.

Around the world, cement-based construction is very common. About 900 kg of CO_2 are emitted into the atmosphere during the production of 1 ton of cement [1]. Cement, after water, is the second most consumed substance in the world by weight [1].

Earth plastering mortars present several technical and environmental advantages: the raw material is a natural and abundant local resource; without need of transportation because it should be a local material; it is inexpensive, easy to work, non-toxic, not renewable but reusable (when not chemically stabilized); with low CO_2 emissions to manufacture and apply as a building material and, consequently, low embodied energy. Relatively small amount of energy is necessary to produce earth plasters, compared to conventional plasters, namely based on cement because the production of this binder requires very high temperature [2]. Thus, earth plasters can significantly contribute to the sustainability of buildings.

Furthermore, earth plasters are becoming recognized by their high hygroscopic capacities, conferred by clays, which provide an important contribution to act as passive humidity buffers, adsorbing and releasing a significant content of water vapor, contributing to balance indoor relative humidity (RH) and temperature [3–11]. Minke [10] and Morton [11] refer that the earth can absorb and bind pollutants dissolved in water, due to the hygroscopic capacity of the clay. Thus, it is deduced that the pollutants in the water vapor can be captured by the earth plasters.

The RH inside the buildings should vary from 40% to 70%, promoting the comfort and health of its occupants. In this range of RH there is a reduction of the fine dust content in the air, the protection mechanisms of the skin against microbes are active, and the life span of many bacteria and viruses is reduced. The mucous membranes of buildings' occupants can dry, which causes a decrease of resistance to colds and related diseases when inhabitants are exposed to RH < 40%, particularly if this occurs for long periods of time [10, 12]. On the other hand, RH > 70% promotes discomfort, increase of rheumatic pains and fungus formation in poorly ventilated spaces. When inhabitants are exposed to these environments for long periods, it can cause several kinds of disease and allergies [10, 12].

Thermal comfort can be improved by regulation of RH, since the temperature increase as the RH decreases. Maskell et al. [4] analyzed the mass change of clayish earth, lime and gypsum plasters when exposed to different RH and constant temperature, and Minke [10] presents the adsorption curves of clayish earth, lime-cement and gypsum plasters. Nevertheless, earth plasters characteristics are not often tested and analyzed in comparison to common plasters, especially as regards adsorption and desorption capacity.

In this study five plastering mortars are formulated, specimens are produced and tested for shrinkage, dry bulk density, dynamic modulus of elasticity, flexural and compressive strength: two are unstabilized earth mortars; one is an air lime stabilized earth mortar; another is a cement-based mortar; and the last one is a gypsum-based mortar.

Nowadays earthen plasters use to be applied unpainted to profit from their colors and aesthetic appearance and cement plasters are generally finished with a paint system. The tested gypsum plaster system is composed by a base mortar and a finishing layer; it can be applied unpainted or painted. Therefore, the adsorption and desorption capacities were assessed for all the plasters unpainted (the gypsum plaster included the finishing layer) and the influence of the paint system was evaluated for the cement and gypsum plasters. Therefore, these two plasters were tested for hygroscopicity also painted.

2 Materials and Methods

2.1 Materials

In the present study, five mortars were analyzed with a different formulation. One mortar was produced in the laboratory. Four other mortars were pre-mixed mortars that were produced only by water addition to an incompletely known formulation. Table 1 presents the description of tested mortars and plastering systems (when applicable).

Loose bulk density and particle size distribution of raw materials used in the formulation of mortars and of the pre-mixed mortar products were determined and presented by Santos et al. [13]. In short, the constituent materials and pre-mixed products have the following loose bulk densities: 1.36 ± 0.01 kg/dm^3 for RCE, 1.38 ± 0.00 kg/dm^3 for FS, 1.61 ± 0.00 kg/dm^3 for CS, 1.40 ± 0.01 kg/dm^3 for Ep, 1.50 ± 0.00 kg/dm^3 for Cp and 0.81 ± 0.01 kg/dm^3 for Gp.

A standard plastic paint was used to paint some of the cement and gypsum-based specimens.

2.2 Mortars Preparation and Specimens Production

Em, E + CL and Cm mortars (pre-mixed mortars) were produced only by addition of the water content indicated by each producer (Table 1). The producer of the Gm mortar did not define the water content and, therefore, the water content of Gm and E_L mortars (Table 1) was defined by an experienced craftsman to assure good workability.

All mortars were prepared using a mixed blade to reproduce, as much as possible, the method carried out on a construction site: the dry materials were placed in a bucket; water was slowly added; initial mixing of 8 min, approximately, was carried out; removal of mortar adhered to the bucket walls; final mixing of 3 min [13].

E + CL mortar was prepared (as described before) one day before the production of specimens and was supplied ready-mixed. All the remaining mortars were produced

Table 1 Description of mortars analyzed

Mortars	Type of mortar	Production	Description	Water content (%)
E_L	Earth-based	Formulated in laboratory	Composed by a reddish illitic-kaolinitc clayish earth (RCE), fine (FS) and coarse (CS) sands with volumetric ratio of 1:3:1.5 and mass ratio of 1:3.04:1.78 (RCE:FS:CS)	10
Em	Earth-based	Pre-mixed (Embarro Company—Universal)	Composed by a reddish ilitic-kaolinitc clayish earth from Algarve region, 0–2 mm fine sand and cut straw fibers (Ep—proportions of each constituent are not exactly known)	15
E + CL	Earth-air lime based	Pre-mixed (Aldeias de Pedra company)	Composed by a yellow kaolinitic clayish earth (YCE) provided by Sorgila company, coarse sand (CS), limestone powder (LP) and air lime putty (ALP) (proportions of each constituent are not exactly known—supplied ready-mixed)	20
Cm	Cement-based	Pre-mixed (Secil Argamassas company—RHP Manual Interior)	Cementitious Cp product for manually applied indoor plasters (formulation not known)	14
Gm	Gypsum-based	Pre-mixed (Sival company—Project 2010)	Gypsum-based Gp product for indoor plasters; the system includes a finishing gypsum layer with 1 mm thickness that was applied only on the hygroscopicity specimens (formulations not known)	43

on the same day that specimens were prepared. Santos et al. [13] characterized each mortar in the fresh state.

Different types of specimens were produced for each mortar:

- Prismatic specimens, 40 mm × 40 mm × 160 mm, prepared in metallic molds, filled in two layers mechanically compacted with 20 stokes each and manually levelled. These specimens were demolded after 7 days.
- Planar specimens, 200 mm × 500 mm × 15 mm, prepared in metallic molds, and manually compacted and levelled. These specimens were not demolded. The finishing gypsum layer was applied on the Gm mortar planar specimens 24 h after the base mortar. The planar specimens of the Cm and Gm mortars were tested unpainted, painted with two layers of paint after 9 months in laboratory conditions and tested painted.

All specimens were maintained in laboratory conditions of 20 ± 2 °C and 65 ± 5% RH.

2.3 Methods

Shrinkage

Linear shrinkage was determined by the difference of the linear geometrical length of the prismatic specimens before and after drying for 7 days, according to DIN 18947 [14]. During drying and before the hygroscopic test, specimens were visually observed to assess shrinkage.

Dry bulk density, dynamic modulus of elasticity and flexural and compressive strengths

Mortars were characterized for dry bulk density, based on EN 1015-10/A1 [15], dynamic modulus of elasticity (Ed), according to EN 14146 [16] with a ZEUS XRM equipment, and flexural (FStr) and compressive (CStr) strength, according to EN 1015-11 [17] with a Zwick Rowell Z050 equipment. Load cells of 2 kN and 50 kN and velocity of 0.2 mm/min and 0.7 mn/min were used for flexural and compressive tests, respectively. Tests were performed with 6 prismatic specimens and the results of each mortar are its average. Mortars were characterized after 1 month, by dry bulk density, and 2 months, by Ed, FStr and CStr—except E + CL mortar that was characterized after 4 months to assure air lime carbonation.

Adsorption and desorption

The dynamic vapor adsorption and desorption of plasters were determined with three planar specimens, according to DIN 18947 [14]. The specimens were kept in the metallic molds to ensure that adsorption and desorption occurs only on the top exposed surface of the specimens. Mortars were characterized after 4 months, except E + CL mortar that was characterized after 6.5 months.

The specimens were stabilized in a climatic chamber at 50% RH and 23 °C, for about 24 h. After stabilization, the climatic chamber conditions were changed from 50% to 80% RH, initiating the adsorption phase. The specimens were weighed at the following intervals: 0, 1, 3, 6, 12 and 24 h.

After 24 h the chamber conditions changed from 80% to 50% RH, initiating desorption phase, that was assessed with the same time interval protocol used in the adsorption phase.

3 Results and Discussion

3.1 Shrinkage

Linear shrinkage of mortars (average and standard deviation) is presented in Table 2.

By visual analysis of the hygroscopicity test specimens the presence of cracks was not observed (Fig. 1a), except in case of E + CL mortar which specimens had some cracks in the center (Fig. 1b). E + CL mortar has the higher linear shrinkage, which justifies the presence of cracks in these planar specimens.

Table 2 Linear shrinkage, dry bulk density, dynamic modulus of elasticity (Ed) and flexural (FStr) and compressive (CStr) strengths

Mortars	Linear shrinkage (%)	Dry bulk density (kg/dm^3)	Ed (N/mm^2)	FStr (N/mm^2)	CStr (N/mm^2)
E_L	0.1 ± 0.0	1.77 ± 0.04	3781 ± 316	0.20 ± 0.06	1.01 ± 0.20
Em	0.2 ± 0.1	1.82 ± 0.02	4267 ± 139	0.25 ± 0.06	0.96 ± 0.10
E + CL	1.4 ± 0.8	1.78 ± 0.07	2977 ± 101	0.17 ± 0.04	0.51 ± 0.03
Cm	0.1 ± 0.1	1.79 ± 0.01	5571 ± 243	0.84 ± 0.11	2.84 ± 0.17
Gm	0.2 ± 0.1	1.22 ± 0.03	4006 ± 161	1.51 ± 0.11	4.15 ± 0.58

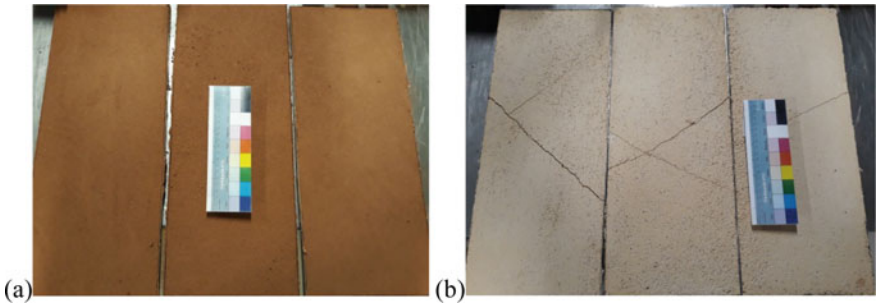

Fig. 1 Distinguish color and shrinkage in three planar specimens of Em (**a**) and E + CL (**b**) mortars

3.2 Dry Bulk Density, Dynamic Modulus of Elasticity, Flexural and Compressive Strength

Table 2 presents the dry bulk density, dynamic modulus of elasticity (Ed) and flexural (FStr) and compressive (CStr) strengths of mortars (average and standard deviation).

Some studies refer that the addition of natural fibers reduces shrinkage, dry bulk density and thermal conductivity [18, 19] and eventually increases compressive strength [20]. But that should depend largely on the type and content of fibers [21]. Despite the presence of fibers, the earth mortar with fibers (Em) presents higher dry bulk density and lower compressive strength, compared to the other unstabilized earth mortar (E_L); however, the CStr values are very close. The Em mortar seems to have a good compactness and, therefore, lower porosity compared to the other analyzed earth mortar. However, this can only be further detailed through an analysis of the porous structure.

According DIN 18947 [14], the E_L mortar can be classified as class 1.8 and the Em mortar as class 2.0 of dry bulk density. Not considering that DIN 18947 [14] refers to unstabilized earth mortars only, the E + CL mortar can be classified as class 2.0. These mortars and the cement-based mortar present similar dry bulk density, while the gypsum-based mortar presents lower dry bulk density.

Dry bulk density of the mortars may be related to the loose bulk density of the raw materials and pre-mixed products (between 1.20 and 1.61 kg/dm^3) [13], which present similar values. The Gp is the exception and present lower loose bulk density (0.81 kg/dm^3) [13]. This can be justified by the lower dry bulk density of Gm mortar.

E + CL mortar presents the lowest strengths (Table 1). This reveals that the addition of air lime does not obligatory improve the mechanical strength of earth mortars. Similar results were obtained in previous studies: Santos et al. [22] concluded that the addition of 5% of air lime in an illitic earth mortar (after 60 days) also decreased its mechanical strength; Gomes et al. [23] obtained similar results with air lime additions up to 15% (after 90 days) in a kaolinitic earth mortar. Low contents of air lime seem to interrupt the clay matrix connection, without creating an air lime network strong enough to replace those clay connections [22, 23]. In the present study, the same phenomena may have happened, although the content of air lime in the E + CL mortar is not known.

EN 998-1 [24] defines different classes for compressive strength, at 28 days, for plastering mortars: CS I for 0.4–2.5 N/mm^2; CS II for 1.5–5.0 N/mm^2; CS III for 3.5–7.5 N/mm^2 and CS IV for $\geq$ 6 N/mm^2. Although all the mortars were not tested at 28 days but at a higher age, earth mortars analyzed in the present study can be classified as CS I class and cement mortar as CS II, meeting the specifications defined by the pre-mixed product technical file. Although the standard [24] is not applied for calcium sulphate binder mortars, the Gm mortar could be also classified as CSII class. These results meet the requirements of mortars for interior and exterior plasters. Gm mortar meets the FStr and CStr defined by pre-mixed product technical file (FStr > 1 N/mm^2 and CStr > 2 N/mm^2) and by EN 13279 [25] (FStr of 1–2 N/mm^2 and CStr of 2–6 N/mm^2).

As expected, the earthen mortars (E_L, Em and E + CL) present lower mechanical strengths (Ed, FStr and CStr) when compared to hydraulic binder mortars (Cm and Gm), except for Em mortar Ed result. This is not necessarily negative if the application of these plasters on substrates with low mechanical properties is considered. In such cases, mortars should not exceed the characteristics of the substrates where they are applied in order to ensure long-term compatibility between the mortar and the substrate. If this compatibility is not verified, premature anomalies and detachment may occur. Other researchers concluded that earth plasters can be applied in different supports, for renovation or in new construction [26, 27].

3.3 Adsorption and Desorption

Figure 2 presents the adsorption and desorption (average and standard deviation) of the plasters, unpainted and, for cement and gypsum-based plasters, also painted, and the limits of sorption classes defined by DIN 18947 [14]: WSI $\geq$ 35 g/m^2; WSII $\geq$ 47.5 g/m^2; WSI $\geq$ 60 g/m^2, after 12 h.

The unstabilized earth plasters (Em and E_L) present significantly higher adsorption and desorption capacity compared to plasters with common binders (cement, gypsum and even earth with added air lime). After 12 h, the Em and E_L mortars present adsorption $\geq$ 60 g/m^2 and, therefore, are classified as WSIII class, by DIN 18947 [14]. Em and E_L plasters adsorb about 104 g/m^2 and 76 g/m^2 water vapor, respectively, after 24 h, and the adsorption curves show an increasing trend at this time (Fig. 2). The presence of illitic clay can justify the higher sorption capacity of these plasters. Illitic clay is characterized by a significant water vapor absorption capacity [7], being only surpassed by montmorillonitic clay, which has a higher adsorption

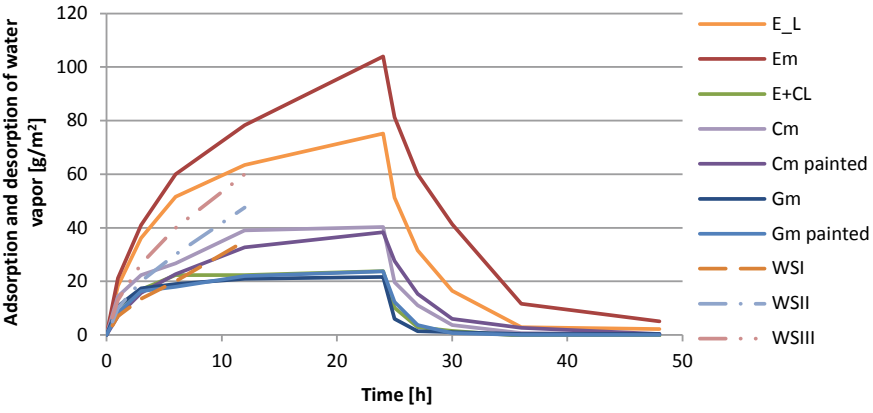

Fig. 2 Adsorption and desorption curves of plasters and WS sorption classes defined by DIN 18947 [14]

capacity than the illitic clay [28]. However, montmorillonitic earth mortars use to present very high shrinkage that enables its application [28].

The higher adsorption capacity demonstrated by Em plaster can also be due the presence of fibers, since fibers may increase the hygroscopicity, the water vapor permeability and the moisture buffering capacity of earth plasters [20, 29]. Moreover, it is necessary to consider that the presence of fibers may also leads to mold growth [30]. For this reason, an adequate drying of plasters must be assured, promoting ventilation to avoid extended conditions of high RH, and prevent the proliferation of mold. Röhlen [31] showed that all earth mortars, with or without fibers, may have presence of fungi, since they can occur when the environment present high levels of humidity.

The adsorption of the Em and E_L plaster is not stabilized after 12 h and is still increasing up to 24 h (when the test stopped), contrarily to what happens with the earth stabilized with air lime, the gypsum and the cement-based plasters. That also confirms the important contribution that unstabilized earth plasters may provide as passive indoor buffers, in comparison to other plasters.

The analysis of the porous structure of the studied mortars may help to understand the differentiated adsorption of the mortars.

Em and E_L plasters also present a good desorption capacity, in comparison to the remaining mortars. However, these plasters present some desorption hysteresis of 3–5%.

Comparing the results obtained with the cement plaster Cm, unpainted and painted (Fig. 2), it is possible to conclude that the painting partially blocked the adsorption and desorption capacity of the cement-based plaster. After 12 h, Cm adsorbed about 39 g/m^2, while Cm painted just adsorbed about 33 g/m^2, 16% less. Nevertheless, after 48 h, Cm and Cm painted desorbed the similar water vapor, about 38–40 g/m^2. The painted and unpainted cement plaster have a desorption hysteresis of about 1%.

Both the gypsum plasters systems do not achieve the lowest sorption class of the DIN 18947 (after 24 h only absorbed about 20 g/m^2 of water vapor). The adsorption capacity of unpainted and painted Gm plasters is similar, although slight differences can be observed: at the beginning and end of adsorption, from 0–9 h to 30–48 h, respectively, the unpainted Gm plaster has adsorption capacity slightly higher than the Gm painted plaster; in the intermediate period (9–30 h) the Gm painted plaster presents higher adsorption capacity (inverse behavior). Thus, it is verified that the painting causes a blockage of adsorption up to 9 h and desorption from 30 h. It is further observed that after 48 h the Gm unpainted plaster presents a slight desorption hysteresis, about 2%, while the Gm painted plaster does not.

Ramos et al. [32] evaluated the experimental mass variation for RH step of 33–75% at 23 °C of a gypsum plaster unpainted and painted (with acrylic and vinyl paints). After 8 h the unpainted gypsum plaster adsorbed about 30 g/m^2, while the painted gypsum plasters adsorbed about 17.5–27.5 g/m^2. In the present study, for different RH variation (step of 50–80%), Gm and Gm painted absorbed slightly less than 20 g/m^2. This can be due to possible admixtures of the pre-mixed gypsum plaster system. The different RH variation or different type of paint may also contribute to the different results obtained. As obtained in the present study (Fig. 2), Ramos et al.

[32] also obtained higher adsorption capacity of the unpainted gypsum plaster in comparison to the painted gypsum plaster, after 8 h.

Minke [10, 12] analyzed the adsorption capacity at 21 °C and RH variation from 50% to 80%, for 24 h, in different materials with 15 mm of thickness and conclude that: undefined clayish earth absorbed about 200 g/m^2; lime-cement and gypsum plaster adsorbed only about 40 g/m^2 and 30 g/m^2 after 24 h, respectively. In the present study, all plasters present lower adsorption capacity after 24 h, except the pre-mixed Cm plaster that present similar adsorption capacity to lime-cement plaster analyzed by Minke [10, 12]. Maskell et al. [4] analyzed the adsorption capacity of a clayish earth plaster, an air lime plaster and a gypsum plaster, at 23 °C, RH variation from 50% to 75% and, after 12 h, obtained adsorption of 30 g/m^2, 15 g/m^2 and 10 g/m^2, respectively. In the present study, the earthen plasters and the gypsum plaster adsorbed higher amount of water vapor (about 22–78.33 g/m^2), after 12 h. The different results obtained in the present study and by these researchers [4, 10, 12] can be justified by eventual different types of clay minerals, formulation of plasters and environmental conditions (temperature and RH).

It is possible to make a comparison between the analyzed plasters when applied in common room during a daily cycle, considering a room with floor dimensions of 3 m × 3 m, with a ceiling height of 3 m, with a door of 2 m^2 and a window of 1 m^2, having walls and ceiling plastered with the seven different systems analyzed for hygroscopicity in the present study, with 15 mm of thickness (Fig. 2).

Considering the room occupied for 8 h during the night at a high RH, the unstabilized earth plasters (E_L and Em) could adsorb about 2–3 l of moisture, whereas the mortars with binders, painted or unpainted (E + CL, Cm and Gm) could only adsorb about 1 l.

The present study demonstrates the ability of clayish earth plasters to adsorb and desorb moisture faster and to a greater extent than common pre-mixed plasters, such as cement and gypsum-based plasters. Nevertheless, the composition of the pre-mixed plasters is not known and eventual admixtures in the formulation may have a significant influence.

4 Conclusions

Plasters have a significant influence on buildings indoor environment. For this reason, plasters must meet some requirements, including aspects that contribute to a healthy and comfortable indoor environment. Thus, the main objective of this study is to quantify some mechanical aspects, but mainly the adsorption and desorption capacity of different plaster systems in order to evaluate the benefits some may have for hygrothermal comfort and indoor air quality.

Analyzing the mechanical characteristics, it is possible to conclude that, as expected, earth mortars present lower mechanical strength comparing to cement and gypsum-based plasters. The addition of air lime, although not directly comparable, does not seem to be mechanically advantageous for an earth mortar.

Unstabilized earth plasters validate their ability to regulate indoor RH since, in comparison to the other plasters, present: a high adsorption and desorption capacity; increasing adsorption after 12 h and at least up to 24 h (when the test stopped), contrarily to what happens with the lime stabilized earth, the gypsum and the cement-based plasters. Thus, the contribution of earth plasters, when applied on indoor walls and ceilings, to the indoor comfort of buildings can be significantly important compared to commonly used plasters, acting as passive hygrothermal buffer systems. This can have positive consequences on indoor air quality but also on energy saving to assure comfort. It was also proved that the tested painting has a negative influence on the adsorption and desorption capacity of the cement-based plaster; however, it does not cause significant influence on the gypsum-based plaster. Further study in needed to justify this different behavior, namely an in depth analysis of the mortars porous structure.

Tests are now being held to observe the capacity of the five plasters to capture pollutants, such as CO_2. Plaster specimens of each type were applied covering five surfaces of air-tight cells, simulating the four walls and the ceiling of a room. The pollutant was injected and it is expected that, soon, results can be presented, hopefully showing a good capacity to capture CO_2 by some of the plasters.

Acknowledgements This study was supported by Operational Programme Competitiveness and Internationalization (COMPETE 2020), by FEDER funds through the Regional Operational Programs of Lisbon and of Center (Lisbon 2020, Center 2020) and by national funds through the Portuguese Foundation for Science and Technology (FCT) in the scope of the project SAICT/23349/2016: INDEEd—Indoor air quality regulation through the usage of eco-efficient mortars. Acknowledgments are due to Aldeias de Pedra, Embarro, Secil Argamassas and Sival companies for providing the materials and pre-mixed mortars.

References

1. Krejcirikova, B., Kolarik, J., Wargocki, P.: The effects of cement-based and cement-ash-based mortar slabs on indoor air quality. Build. Environ. **135**, 213–223 (2018). https://doi.org/10.1016/j.buildenv.2018.03.011
2. Melià, P., Ruggieri, G., Sabbadini, S., Dotelli, G.: Environmental impacts of natural and conventional building materials: a case study on earth plasters. J. Clean. Prod. **80**, 179–186 (2014). https://doi.org/10.1016/j.jclepro.2014.05.073
3. Maddison, M., Mauring, T., Kirsimäe, K., Mander, Ü.: The humidity buffer capacity of clay-sand plaster filled with phytomass from treatment wetlands. Build. Environ. **44**, 1864–1868 (2009). https://doi.org/10.1016/j.buildenv.2008.12.008
4. Maskell, D., Thomson, A., Walker, P., Lemke, M.: Determination of optimal plaster thickness for moisture buffering of indoor air. Build. Environ. **130**, 143–150 (2018). https://doi.org/10.1016/j.buildenv.2017.11.045
5. Bruno, A.W., Gallipoli, D., Perlot, C., Mendes, J.: Effect of stabilisation on mechanical properties, moisture buffering and water durability of hypercompacted earth. Constr. Build. Mater. **149**, 733–740 (2017). https://doi.org/10.1016/j.conbuildmat.2017.05.182

6. Randazzo, L., Montana, G., Hein, A., Castiglia, A., Rodonò, G., Donato, D.I.: Moisture absorption, thermal conductivity and noise mitigation of clay based plasters: the influence of mineralogical and textural characteristics. Appl. Clay Sci. **132–133**, 498–507 (2016). https://doi.org/10.1016/j.clay.2016.07.021
7. Lima, J., Faria, P., Santos Silva, A.: Earthen plasters based on illitic soils from Barrocal region of Algarve: contributions for building performance and sustainability. Key Eng. Mater. **678**, 64–77 (2016). https://doi.org/10.4028/www.scientific.net/KEM.678.64
8. Emiroğlu, M., Yalama, A., Erdoğdu, Y.: Performance of ready-mixed clay plasters produced with different clay/sand ratios. Appl. Clay Sci. **115**, 221–229 (2015). https://doi.org/10.1016/j.clay.2015.08.005
9. Cagnon, H., Aubert, J.E., Coutand, M., Magniont, C.: Hygrothermal properties of earth bricks. Energy Build. **80**, 208–217 (2014). https://doi.org/10.1016/j.enbuild.2014.05.024
10. Minke, G.:, Building with earth. Design and Technology of a Sustainable Architecture, 1st edn. Birkhäuser—Publishers for Architecture, Berlin (2006)
11. Morton, T.: Earth masonry. Design and construction guidelines, 1st edn. IHS BRE Press, UK (2008)
12. Minke, G.: Earth Construction Handbook: The Building Material Earth in Modern Architecture, 1st edn. WIT Press, Boston (2000)
13. Santos, T., Gomes, M.I., Santos Silva, A., Ferraz, E., Faria, P.: Comparison of mineralogical, mechanical and hygroscopic characteristic of earthen, gypsum and cement-based plasters. **254**, 119222 (2020). https://doi.org/10.1016/j.conbuildmat.2020.119222
14. DIN 18947: Earth plasters—Terms and definitions, requirements, test methods (in German) (2013)
15. EN 1015-10: Methods of test for mortars for masonry, Part 10: Determination of dry bulk density of hardened mortar (1999/2006)
16. EN 14146: Natural stone test methods. Determination of the dynamic modulus of elasticity (by measuring the fundamental resonance frequency) (2006)
17. EN 1015-11: Methods of test for mortar for masonry, Part 11: Determination of flexural and compressive strength of hardened mortar (1999/2006)
18. Laborel-Préneron, A., Aubert, J.E., Magniont, C., Tribout, C., Bertron, A.: Plant aggregates and fibers in earth construction materials: a review. Constr. Build. Mater. **111**, 719–734 (2016). https://doi.org/10.1016/j.conbuildmat.2016.02.119
19. Faria, P., Lima, J.: Earth plasters (in Portuguese). Cadernos de Construção com Terra 3, 1st edn. ARGUMENTUM, Lisbon (2018)
20. Palumbo, M., McGregor, F., Heath, A., Walker, P.: The influence of two crop by-products on the hygrothermal properties of earth plasters. Build. Environ. **105**, 245–252 (2016). https://doi.org/10.1016/j.buildenv.2016.06.004
21. Lima, J., Faria, P.: Eco-efficient earthen plasters: The influence of the addition of natural fibers. In: Fangueiro, R., Rana, S. (eds.), Natural Fibres: Advances in Science and Technology Towards Industrial Applications, pp. 315–327. Springer Netherlands, Dordrecht (2016). https://doi.org/10.1007/978-94-017-7515-1_24
22. Santos, T., Nunes, L., Faria, P.: Production of eco-efficient earth-based plasters: influence of composition on physical performance and bio-susceptibility. J. Clean. Prod. **167**, 55–67 (2017). https://doi.org/10.1016/j.jclepro.2017.08.131
23. Gomes, M.I., Faria, P., Gonçalves, T.D.: Earth-based mortars for repair and protection of rammed earth walls. Stabilization with mineral binders and fibers. J. Clean. Prod. **172**, 2401–2414 (2018). https://doi.org/10.1016/j.jclepro.2017.11.170
24. EN 998-1: Specification for mortar for masonry. Part 1: Rendering and plastering mortar (2010)
25. EN 13279-1: Gypsum binders and gypsum plasters. Part 1: Definitions and requirements (2008)
26. Santos, T., Faria, P., Silva, V.: Can an earth plaster be efficient when applied on different masonries? J. Build. Eng. **23**, 314–323 (2019). https://doi.org/10.1016/j.jobe.2019.02.011
27. Delinière, R., Aubert, J.E., Rojat, F., Gasc-Barbier, M.: Physical, mineralogical and mechanical characterization of ready-mixed clay plaster. Build. Environ. **80**, 11–17 (2014). https://doi.org/10.1016/j.buildenv.2014.05.012

28. Lima, J., Faria, P., Santos Silva, A.: Earth plasters: The influence of clay mineralogy in the plasters' properties. Int. J. Archit. Herit. (2020). https://doi.org/10.1080/15583058.2020.1727064
29. Ashour, T., Georg, H., Wu, W.: An experimental investigation on equilibrium moisture content of earth plaster with natural reinforcement fibres for straw bale buildings. Appl. Therm. Eng. **31**, 293–303 (2011). https://doi.org/10.1016/j.applthermaleng.2010.09.009
30. Gomes, M.I., Faria, P., Gonçalves, T.D.: Rammed earth walls repair by earth-based mortars: the adequacy to assess effectiveness. Constr. Build. Mater. **205**, 213–231 (2019). https://doi.org/10.1016/j.conbuildmat.2019.01.222
31. Röhlen, U.: Mould on clay renders. In: 6th International Conference on Building with Earth—LEHM 2012, pp. 113–121. Dachverband Lehm e.V., Weimar, Germany (2012)
32. Ramos, N.M.M., Delgado, J.M.P.Q., de Freitas, V.P.: Influence of finishing coatings on hygroscopic moisture buffering in building elements. Constr. Build. Mater. **24**, 2590–2597 (2010). https://doi.org/10.1016/j.conbuildmat.2010.05.017

Challenges, Opportunities and Potential Solution Strategies for Environmentally and Socially Responsible Urban Development of Megacities in Africa

Wolfram Schmidt, Nonkululeko Radebe, Mike Otieno, Kolawole Olonade, Shirin Fataei, Fatma Mohamed, Gesine Lenore Schiewer, Mareike Thiedeitz, Angela Tetteh Tawiah, Risikat Dauda, Ghada Bassioni, Melissa Telong, and Andreas Rogge

Abstract Cement and concrete construction inevitably impact on societies. By exploiting resources, modifying the landscape and facilitating the mobility of people and movement of goods and services, concrete construction activities are directly linked to climatic effects, local economies, and the socio-economic well-being of urban dwellers. Today's rapidly accelerated urbanisation inevitably coins global societies all over the world, particularly in Africa, where the expected movement from rural to urban environments along with a significant population increase will reach

W. Schmidt (✉) · M. Telong · A. Rogge
Bundesanstalt für Materialforschung und -prüfung, 12205 Berlin, Germany
e-mail: wolfram.schmidt@bam.de

N. Radebe
Karlsruher Institut für Technologie, 76131 Karlsruhe, Germany

M. Otieno
University of the Witwatersrand, Braamfontein 2000, South Africa

K. Olonade · R. Dauda
University of Lagos, 100213 Akoka, Nigeria

S. Fataei
Technische Universität Dresden, 01187 Dresden, Germany

F. Mohamed
University of Dar es Salaam, 35131 Dar es Salaam, Tanzania

G. L. Schiewer
Universität Bayreuth, 95440 Bayreuth, Germany

M. Thiedeitz
Technische Universität München, 81245 Munich, Germany

A. T. Tawiah
MC Bauchemie Ghana, 00233 Accra, Ghana

G. Bassioni
Ain Shams University, 11566 Cairo, Egypt

E. B. Pereira et al. (eds.), *Proceedings of the 3rd RILEM Spring Convention and Conference (RSCC 2020)*, RILEM Bookseries 32,
https://doi.org/10.1007/978-3-030-76547-7_11

unprecedented megacity dimensions. Megacities are already under massive socio-economic, cultural and infrastructural pressure today, and the future predictions indicate that complex challenges will need to be tackled. However, the future developments present both challenges and opportunities at the same time, since due to lacking existing solutions unprecedented environmentally and socio-culturally responsive solutions have to be developed using readily available local resources. The paper discusses challenges related to rapid urbanisation and highlights African distinct differences. Opportunities and potential material and structural solutions are also discussed, along with the associated architectural and socio-economic implications.

Keywords Sustainability · Urban growth · Megacities · Africa · Architecture

1 Introduction

In this century, along with climate challenges, urbanisation is one of the most critical challenges humanity faces. For Africa this challenge is even more pressing than for most other regions in the world. According to the Global Cities Institute [1], by the end of the 21th century 13 of the largest 20 cities in the world are expected to be in Africa (Fig. 1). In 2050 the number of 5-Million-inhabitant cities will rise up from the current number of 10 to ca. 60 [2]. The expected growth should be sustainable.

However, sustainability in the context of urbanisation goes far beyond this. The rapid migration to urban regions, often linked to lack of livelihoods and inaccessibility of health services, poses new challenges such as inequalities, discrimination, social unrest and crime. Furthermore, it puts additional pressure on educational, health, sanitation and supply systems, and is increases environmental pollution.

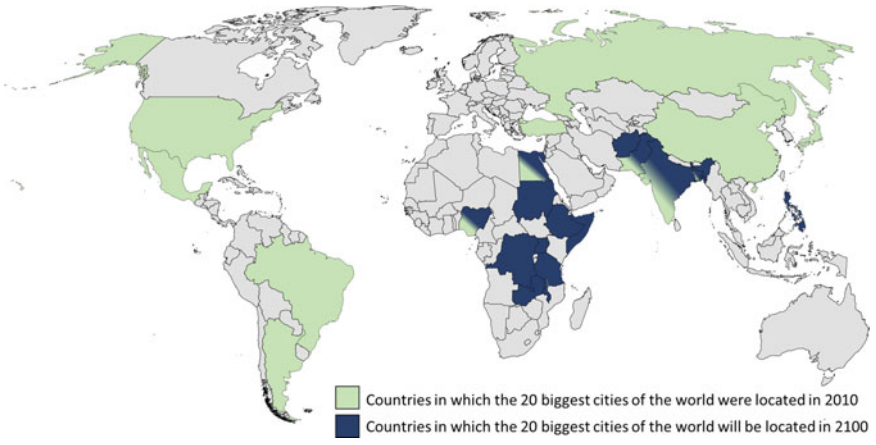

Fig. 1 Countries with the biggest megacities in 2010 and 2100 [1]

Hence, although urbanisation is largely covered by the UN Sustainable Development Goal No. 11 (SDG 11—Sustainable Cities and Communities), urbanisation processes are inevitably linked to all the 17 SDGs [3]. This indicates that environmental challenges of urban growth in Africa are intimately linked to fundamental socio-economic aspects.

2 Challenges, Boundary Conditions and Degrees of Freedom

As much as African megacities share the challenge of rapid growth, historically and geographically they have a vast variety of different boundary conditions. Cities like Cairo, Lagos, or Kumasi for example have unique histories that can be traced back to many centuries. Their past and future growth has been determined by multiple interconnected historical periods. The important maintenance of the cultural heritage limits an unrestricted urban structural development, but in return migration and multiculturalism are not unknown phenomena. Then, the rapid urban growth of many huge cities today was triggered in the end of the 19th century, often in the context of colonial resource exploitation, such as Nairobi, Kampala, or Accra. These cities were conceptualised for a small typically colonial elite and not for the vast majority of the populace, which the city plans often still shows today [4]. Even the separation of the privileged can mostly still be found today, with the difference that separation today depends upon income. Yet there has been permanent amorphous population growth.

Eventually, there are some regions and cities, which were not populated significantly for a long time, but present enormous growth potentials in the future, such as Mtwara and Songea or Blantyre City. These regions provide enormous degrees of freedom for non-traditional urban growth, as new sections can be developed right from the scratch, but new developments must also meet current and future socio-economic demands and intricately blend in with the existing traditional infrastructure.

While historical developments often limit possible and conventional traffic infrastructural developments, the growth can furthermore be limited by topographical and geopolitical factors. Lagos e.g. has reached the state's borders, thus, has limited potentials for lateral urban growth. This forces city planners to extend the land into the lagoon, while Douala or Accra have no severe limitations for lateral growth. Additionally, different boundary conditions are whether the cities are landlocked such as Niamey or Kampala, or located with access to the ocean, such as Lagos or Dar es Salaam. However, a major distinction between African urban growth potentials is the variability in the population density. This parameter needs further discussion.

3 Characteristics and Requirements Depending on Density

3.1 Low Density Situation

Much of Africa's urban expansion occurs through the unplanned and low-density consumption of rural land [1]. Urban sprawl inherently affects areas of low-density population as by definition this is the migration of people from relatively low to high densely populated areas. When developing such areas, it is important to consider different stakeholder groups, such as conservationists and farmers. Regions with more rural characteristics cannot be conceptualised in the same way as larger, more densely populated cities can. The current challenges encountered in existing large cities can be minimised by considering known challenges right from the conceptual planning stages. Such challenges include perpetual traffic jams and the related greenhouse gas emissions and productivity losses, as well as insufficient and inadequate housing. More mixed-use spaces can be built for a more integrated society. This means for example dispersed shopping centres that integrate existing stall-like businesses by expanding their workspace, and railway or rapid transit routes to make relevant areas accessible to people in the growing cities. It is therefore possible to mimic the impact of megacities on smaller more rural areas without over-urbanising it.

In summary, low density urban expansion offers great opportunities to develop more contemporary cities. This also can benchmark the continent as a pioneer in greener, people focused and future oriented city development.

Various principles to build better cities exist [2]. For African urban sprawl the three major principles should be considered and implemented predominantly:

1. **Preservation**: the African continent is rich in natural ecologies and cultural heritage, which should be embraced and integrated in the urban environment.
2. **Diversity**: space should be dynamic and conducive for people of different groups and interests to ensure that all inhabitants benefit from their environment.
3. **Mobility**: a majority of people living in African cities use combinations of non-motorised traffic (NMT), shared vehicles and public transportation. They can build the foundation for more sustainable, integrated systems. African cities can leapfrog past mobility concepts and pioneer future concepts.

3.2 High Density Situation

Urban development in high density cites is a constant challenge because of the exponential population growth. This creates imbalance between demand and supply of services, places and interconnectivity. Furthermore, the disparity between high costs of construction and low household incomes leads to inequitable access to land, shelter and basic services [3]. The high demand of construction usually neglects considerations for ecologically and energy efficient buildings. All of the above-mentioned

challenges are compounded by inefficient transport systems, poor maintenance practices, lack of sufficient clean water and sanitation which is also linked to health aspects.

Reducing the number of vehicles by developing integrated transport systems eventually is the only solution, but the space on grade for traffic axes is typically missing due to the narrow building developments. In most cases, the most reasonable option could be hybrid solutions with trains, buses, multi-passenger shuttles, and possibly unconventional systems such as urban cable cars, which do not require much material, can be built over existing structures and even become tourist attraction.

In general, densely populated urban development, requires much more the careful consideration of both health and environmental aspects. Green areas are mandatory, as urban development seals exposed surfaces and thus reduces their ability to absorb rainwater and surface runoff. This causes problems with urban heat islands, which not only cause environmental problems and higher energy demand, but also increase the fatality and minimises productivity [5]. If this is accompanied by poor drainage and sanitation systems, it creates an increased risk of flooding and outbreak of waterborne diseases. By focusing capital investments on maintaining and upscaling existing sanitation and drainage systems, the effect of flooding can be significantly minimised.

In summary, dense urban development demands for more complex innovative system-based considerations due to limitations of degrees of freedom from existing structures, road maps, commercial areas, and public transportation system capacity.

4 Future Technical Requirements for African Urban Regions

Certain challenges are shared by and will increase for most rising African megacities. These are scarcity of renewable energy and clean water supply as well as today's permanent traffic congestion. In addition, the job creation in most cities cannot catch up match the steady population growth, the food security and resource supply have to be ensured, and the urban heat island phenomenon aggravates the general influence of high temperatures. Therefore, urban planners should focus on innovative and sustainable solutions such as:

- Instead of sealing exposed surfaces as much as possible, cities need to absorb and store as much water as possible, not only in order to secure the water supply but also to counteract the urban heat island phenomenon.
- Energy generation and energy saving, using integral natural ventilation concepts.
- Vertical urban growth requires more material for structural design than horizontal urban growth [6], 50 storeys for example require 24.5 times more material for vertical elements than 50 dispersed units. From an environmental aspect, it is, thus, reasonable to limit the vertical growth as much as is practically possible.

- More sustainable but less intrusive public transportation systems need to be installed. Whether subway, rapid bus or cable car, or hybrid systems are the best solution depends on the urban populations' current and future demands.
- With growing movement of rural population to cities, the question to be answered is "*how sufficient food supply can be generated*". Urban farming, thus, becomes a most important aspect. While there is a synergy between urban agriculture and healthier climate, ecological urban animal farming can become a challenge. However, concepts for the conversion of animal manure into value-added products exist that can either minimise the laterals distance between the animal farm and an urban region or even allow for urban animal farming [7].

A comparison of potentials, challenges and degrees of freedom is provided in Fig. 2. Regardless of the individual best practice solution for each city and city type, the mentioned challenges heavily demand for increased construction activities and the use of enormous amounts of materials. Therefore, urban planners should consider materials saving technologies that help minimising the carbon footprint of the cities as well as their negative environmental impact as much as possible.

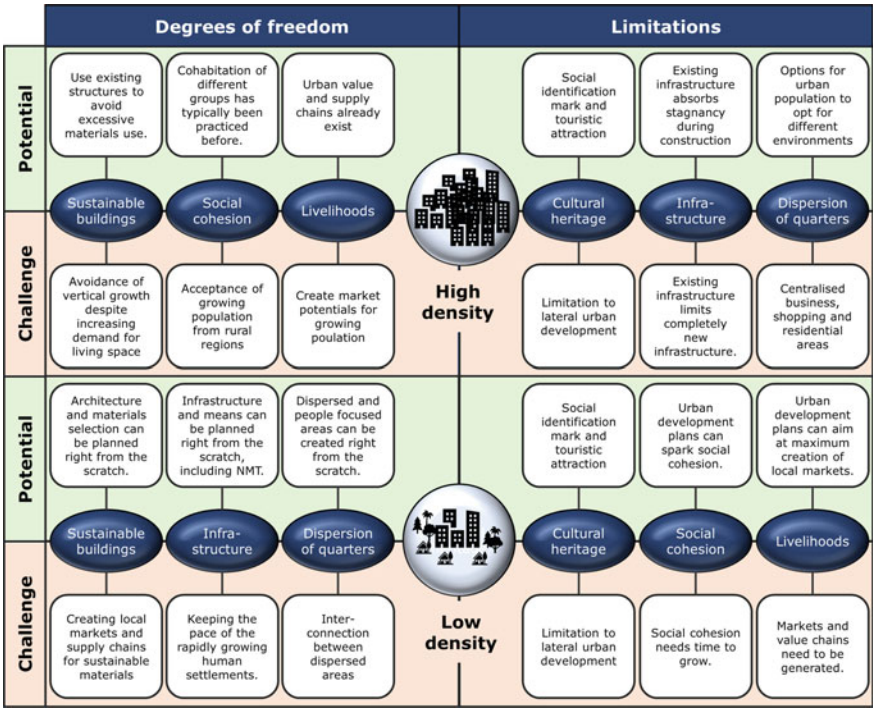

Fig. 2 Challenges and potentials for the growth of differently densely populated cities

5 Materials and Technologies for Local Low Volume Materials Use

Despite its typically negative perception, cementitious materials, particularly concrete, will remain the most feasible option for African urban construction. Compared to any other mass construction material concrete has significantly lower embodied carbon and lower energy demand [8]. Any other materials, hence, would have more negative effects on the global climate than concrete. Particularly in Africa, alternatives are lacking anyway, since timber is scarce, partly due to deforestation, and steel has to be imported. Rammed earth (if no cement is used) and adobe are viable, environmentally friendly, local alternatives, that should absolutely be considered for urban use as well, but they cannot replace cementitious materials for structural application.

Despite their structural and environmental advantages over most materials, cement based materials are responsible for about 10% of the global carbon emissions [9], and the rapid urbanisation in Africa will significantly contribute to the increasing use of cement and concrete in the world.

Due to the inevitability of concrete for urban and infrastructure development, the only option to build more sustainably is using the constituents as efficiently as possible, avoiding overdesign, using low-volume innovative structural systems, using materials according to their strengths and opt for alternatives, where concrete is weak. Recycling of old concrete and other waste building materials, urban mining and circular economic material systems are needed where applicable. These aspects need to be considered right from the beginning and materials aspects have to affect the decision making of project developers, the architects, as well as the structural designers.

Many viable solutions for more sustainable construction have been proposed, e.g. [10]. Locally sourced constituents are most relevant. In Africa, agricultural residues can become an environmentally friendly resource, such as ashes of rice husks, cassava peels, or sugar cane bagasse. Expensive imported chemical admixtures can be replaced by local polysaccharides [11, 12]. Some important materials aspects to build cities more environmentally friendly are listed in Table 1.

6 Education for Sustainable Construction

The implementation of the solutions listed in Table 1 demands for higher levels of materials knowledge at all levels of the construction process [13].

At engineering level, it is important to understand, that today's civil engineer re-quires skills different from those in the past, which should be reflected in more contemporary and responsive curricula. Considering the enormous societal, economic and environmental impact that results from construction activities, today's civil engineers and architects need a deeper understanding of fundamental materials

Table 1 Options to use cementitious materials more efficiently in urban construction

Step	Solutions	Aspects to avoid
Raw materials	• Local materials to avoid transport, e.g. vegetable ashes, local polysaccharides and fibres, mining tailings, recycling aggregates	• Unnecessary import of resources, including staff
Material development	• Replacement of Portland cement by alternatives, e.g. calcined clays, agricultural and industrial ashes • Use of water reducing admixtures to increase concrete properties	• Inefficient use of cement • Consistency control by water addition
Structural design	• Use materials according to its strength • Cross sections acc. to material specifications • Use innovative structural systems	• Excessive construction height • Overdesign
Handling	• Sound curing • Ready-mixed or pre-mixed compounds	• Avoid on-site mixing

knowledge along with acute awareness of their own roles for the global climate [13, 14].

At the level of professional engineers, urban planners, public institutions and policy making bodies, a trait for lifelong learning to sustain permanent knowledge-update is required. With increasing understanding of the implications of materials use in construction, knowledge acquired from the past and standards or codes can quickly be-come obstacle for urgently required innovative solutions. Systems therefore need to be established to transfer and implement new knowledge into the practice.

A most important and influential group are the end-users. Without a broad public awareness of sustainability, and more environmentally friendly technologies, companies and policy makers will not proactively drive innovation. Education on the relevance of construction, thus, needs to address as many people as possible, which also means that scientific communication becomes more relevant for today's engineers.

7 Livelihoods

Since public awareness about and involvement in urban sustainability-related matters are key to global changes, it is important to motivate people to embrace environmentally friendly construction practices. Even more important than governmental incentives for capital investment is the creation of local value chains and market potentials. Particularly, the agricultural sector is strong in Africa and exhibits and

enormous growth potential. With this in mind, and the fact that nearly 60% of the global unused arable land is in Africa, bio-based construction alternatives derived from agricultural wastes are synergistically environmentally friendly and capable of creating new values from formerly unexploited resources. For example, the unused wastes of the cassava production can be converted on the one hand into chemical admixtures to reduce the water content in concrete and on the other hand additionally into reactive cementitious materials to replace ordinary Portland cement [15]. This way, a formerly unused waste material can be converted into value chains without competing with the already existing high demand for food for human consumption. Similar potentials can be found for various plants, and urban farming areas can create synergies between the urban climate and livelihood generation, and partly minimise supply distances.

8 Social Challenges and Potentials

Social aspects, such as the social prerequisites for innovation and social influencing factors, have proven to be a driver of economic dynamics [16] beyond technical innovation that has been considered as the major driver in past social studies [17]. African urban areas have enormous potential for social innovation due to their multicultural, multilingual societies [18]. However, social innovation must find acceptance in the society. The standpoint of religion and cultural customs toward natural resources, the relationship between politics, economy and society, and the integration of technology into daily life are affected by social acceptance and accommodation of tolerance. Peaceful coexistence despite growing social inequalities requires effective and efficient communication, particularly on active participation and conflict mediation in socially heterogeneous and multilingually complex metropoles [19, 20].

All cities have high demands on progressive communication and planning. Nevertheless, depending upon their urban form, each requires a unique but relevant social innovation [21]. Understanding specific urban forms therefore is essential for their implementation. Urban planning, thus, is a powerful control instrument in large cities, which must be adopted with consciousness to balance the economic goals and social progress as harmoniously as possible. The urban planning must be all-inclusive, representing individual groups and communities within a city, considering the interests and objectives of both private and public sector. For the implementation of successful and sustainable urban strategies, joint consultative decisions must be made as far as possible. The focus has to be put on how inevitable conflicting interests can be handled based on differences in income level, gender appreciation, and ethnical, cultural or religious backgrounds [22].

9 Inclusive Growth

Rapid economic growth is often exclusive. The precipitators of this exclusiveness include inequality, large-scale poverty, massive unemployment, and concentration of large proportion of national resources and wealth in the hands of a few [23]. Inclusive growth strategies seek to confront headlong the undesirable distributional effects of the various economic growth strategies, which impair dignity in various forms. Thus, poverty reduction is essential for urban structures to grow without conflicts. Equal opportunity to means of sustenance is inevitable for a stable society, and thus should be central element in urban strategies. Yet, the route to inclusive development in most African countries remains an illusion, since mostly the supporting resources are not equitably distributed and allocated [24]. Cultural diversity, tribal and ethnic inclination, gender and generation perceptions, as well as religious factors are some of the major that have, to date, led to creation of exclusive rather than inclusive frameworks.

Africans are highly diverse in cultures, languages and beliefs. For instance, countries like Nigeria or Cameroon, each have more than 200 ethnic groups with several hundred different languages and cultural inclinations. Nepotism and lack of trust between the ethnic groupings have been major challenge to the implementation of inclusive urban structures, aggravated by tensions arising purely from the growth velocity. Furthermore, the prospects for inclusive urban growth have been constrained by inadequacies in the areas of infrastructure, governance, security, and skill levels of young graduate workers among others.

However, positive examples exist. Dar es Salaam for example combines a population of various cultures, tribes, religion, and languages in relative harmony. Also, various Northern African cities where different quarters have very special characteristics but remain accessible for everyone, show that cultural inclusiveness is possible (yet income-based exclusion still exist). Inclusive urban growth, thus, has to focus on creating bridges rather than barriers between different groups by:

- Creating equal gender opportunities in public, educational and business locations
- Having a sufficient number of cultural meeting and communication points
- Use historic buildings and arts as tools to generate common urban identity
- Creating spaces that attract and fulfil demands of older and younger generations
- Religious interconnectivity hubs, for example by creating spaces where worshippers can meet after service to network.

Urban planners should see cultural diversity as a gift rather than a challenge. It attracts tourists, creates positive attention, and hence livelihoods and business opportunities. These are solid foundations to overcome ethnic, cultural, age and gender bias.

10 Sustainable Architecture

Big cities today often remain hierarchical, and urban planning additionally supports socially disruptive development. Vertical versus lateral building and 'modern' financial quarters versus urban housing are typical challenges of megacities. The rising African megacities offer enormous potentials to overcome hierarchical, oppressive or exclusive habitation and livelihood. Multiplicity, multiculturalism and multilingualism needs to be supported by equitable, sustainable and healthy technical innovation.

The African continent is rich in materials for construction that have been used historically over the years depending mostly on location, need, and the climatic condition [25]. Unfortunately, the buildings found today in many African cities are mostly homogenous in nature, utilising materials, which are deemed to be 'modern' materials. In this context a lot of architecture can be found that is energetically not ideal and lacks architectural local identity. Recent urban African architecture too often uses 'Western' architecture as a role model, in materials and structure. However, architecture that does not serve to the citizens will quickly be replaced and buildings that are wrecked before their expected end of lifetime negatively impact on the global climate.

Thus, neglecting the needs of the urban dwellers as well as their creativity to change the city's landscape according to their preferences from within is definitively not sustainable [4]. Often people create liveable neighbourhoods (e.g. arts, community or innovation centres, or urban gardening spaces) on unused urban areas, which are often projected as interim areas until investors build more profitable structures. This causes alienation of the population from their urban environment. However, if governments allow urban change from within the urban populace, people would much more tend to inherit the spaces they created, and identity with. In the long run this creates more robust urban environments than from direct external capital investment.

For policy makers this means, a trigger point needs to be defined as of which the government decides to put citizens' interest over investors' interest, once the interim space has become systemically too important. While these policies can generate sustainable quarters, the consequences for policy making bodies would be to find laws on how to compensate investors (e.g. offer alternative spaces) as well as financial support for the further development of the quarters.

The construction and construction chemical business, therefore, is an important player in creating synergies between modern construction and local business opportunities. The use of locally available materials (for example from agriculture) is an essential step towards sustainability, even if only utilised in non-load bearing components, e.g. partitioning and finishes. Knowledge in and services on bioclimatic design of buildings is also essential, also considering vernacular and historic solutions, in reducing the overall carbon footprint related to energy use and comfort in buildings. Although the current sustainability rating of African cities is relatively low, there is high potential for a drastic change in future. Until ca. 2050, the current urban structures will only make out ca. 20% of all urban structures, but the architecture has to:

- Meet the needs of today's dwellers while being flexible and dynamic at the same time to adapt to moving targets in urban planning
- Reconsider vernacular architecture and materials, but based on state-of-the art research and best-practice experiences
- Consider infrastructure as an inevitable element to ensure inclusiveness, flexibility and urban livelihood potentials.

11 Summary

Fast urbanisation leads to complex social structures in metropolitan and peri-urban regions. Citizens of today's and future megacities do not only have to deal with insufficient infrastructure, ineffective solutions and inadequate capacity for transportation and energy supply, but with social infrastructure as well. All concepts need to consider that sustainable construction comes at a price which can be compensated for by looking at the financial and social benefits that can be generated in return in the long run. If sustainable urban strategies are systematically developed along with livelihoods and business opportunities, and local potentials are fostered, the inevitably growing African megacities can become global role models.

Important in this is to recognise that sustainable development is multi-faceted, and that no one-fit-all solution is possible. The best practice solutions can be found by creating knowledge and awareness among the key players and influencers in different areas of urban development. Important objectives are climate friendliness, inclusiveness, adaptability, innovation, and local value chain generation (Fig. 3).

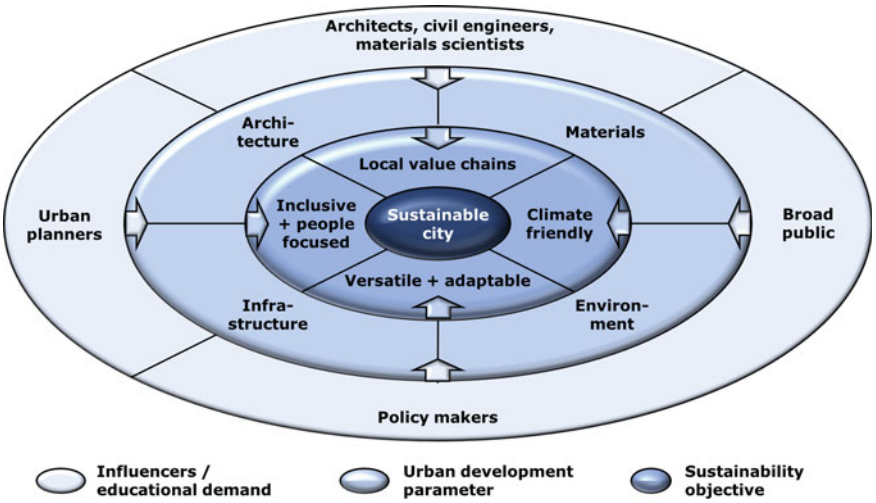

Fig. 3 Key disciplines and relevant parameters for sustainable urban growth

References

1. Hoornweg, D., Pope, K.: Socioeconomic Pathways and Regional Distribution of the World's 101 Largest Cities, vol. 04. Global Cities Institute, Ontario (2014)
2. Metcalfe, M., Ibrahim, N.: Crossroads: sustainable infrastructure + entrepreneurship + online engineering education in 21st century Africa. In: Schmidt, W. (ed.) ISEE Africa—Innovation, Science, Engineering, Education, pp. 32–35. BAM, Berlin, Germany (2019)
3. UN: Res. adopted by the General Assembly on 25 Sept. 2015 vol. A/RES/70/1 UN (2015)
4. Serumaga-Musisi, N.D.: The Griot Introspect—whose Utopia is it anyway? (2018). https://medium.com/@madugian/the-griot-introspect-cbd39de7ac65
5. Barthel, M., Vogler, N., Schmidt, W., Kühne, H.-C.: Outdoor performance tests of self-cooling concrete paving stones for the mitigation of urban heat island effect. Road Mater. Pavement Des. **18**(2), 453–463 (2017)
6. Schmidt, W., Anniser, J., Manful, K.: A sustainability point of view on horizontal and vertical urban growth. In: Schmidt, W. (ed.) ISEE—Innovation, Science, Engineering, Education (Post-conference edition), pp. 189–193. BAM, Berlin, Germany (2019)
7. Fini, E.H., Kalberer, E.W., Shahbazi, G., Basti, M., You, Z., Ozer, H., Aurangzeb, Q.: Chemical characterization of biobinder from swine manure: sustainable modifier for asphalt binder. Mater. Civil Eng. **23**, 1506–1513. American Society of Civil Engineers (ASCE) (2011)
8. Barcelo, L., Kline, J., Walenta, G., Gartner, E.: Cement and carbon emissions. Mater. Struct. **47**(6), 1055–1065 (2014)
9. WBCSD: Getting the numbers right. Project Emissions Report 2014 (2016)
10. Scrivener, K., John, V.M., Gartner, E.M.: Eco-efficient cements: potential economically viable solutions for a low-CO_2 cement-based materials industry. United Nations Environment Programme, Paris (2017) (Revised edition)
11. Schmidt, W., Msinjili, N.S., Kühne, H.-C.: Materials and technology solutions to tackle the challenges in daily concrete construction for housing and infrastructure in sub-Saharan Africa. Afr. J. Sci. Technol. Innov. Dev. 1–15 (2018)
12. Schmidt, W., Tchetgnia Ngassam, I., Olonade, K., Mbugua, R, Kühne, H.-C.: Plant based chemical admixtures—potentials and effects on the performance of cementitious materials. RILEM Tech. Lett. **3**, 124–128 (2019)

13. Schmidt, W., Alexander, M., John, V.: Education for sustainable use of cement based materials. Cement Concr. Res. **114**, 103–114 (2018)
14. Schmidt, W.: Engineering skill requirements to cope with the local and global challenges of the future. In: Schmidt, W. (ed.) ISEE—Innovation, Science, Engineering, Education (Post-conference edition), pp. 16–19. BAM, Berlin, Germany (2019)
15. Schmidt, W., Olonade, K.A., Mbugua, R., Lenz, F.J., Tchetgnia Ngassam, I.L.: Bio-based rheology modifiers for high performance concrete—possible modes of actions and case study for cassava starch in West Africa, pp. 158–166
16. Zapf, W.: Über soziale Innovation. Soziale Welt **40**(1–2), 170–183 (1989)
17. Blättel-Mink, B., Menez, R.: Kompendium der Innovationsforschung (2006)
18. Schiewer, G.L.: Diskurslinguistik, Mehrsprachigkeitsforschung und wirtschaftswissenschaftliche Szenarien-Technik. Prospektive Diskursanalyse am Beispiel urbaner Innovation (‚inclusive innovation'), pp. 41–58. De Gruyter (2014)
19. Schiewer, G.L.: ›Lohnende Kommunikation‹ in komplexen Umfeldern und soziokulturell-mehrsprachigen Metropolen. Zeitschrift für interkulturelle Germanistik **3**(2), 11–23 (2012)
20. Schiewer, G.L.: Nichts Kulturelles ist uns fremd, pp. 153–171. Iudicium (2014)
21. Paddison, R.: Handbook of Urban Studies (2000)
22. Schiewer, G.L.: Discourse and the City. Diskursanalytische Implikationen sozialer Innovationsparadigmen am Beispiel des Urbanismus, pp. 203–219. De Gruyter (2013)
23. Ali, I., Son, H.H.: Measuring inclusive growth. Asian Dev. Rev. **24**(1), 11–31 (2007)
24. Ravallion, M.: Are the world's poorest being left behind? J. Econ. Growth **21**(2), 139–164 (2016)
25. Adekunle, T.O., Odeyale, T.S.: Innovative and sustainable local material in traditional African architecture—socio cultural dimension. In: D'Ayala, D., Fodde, E. (eds.) Structural Analysis of Historic Construction: Preserving Safety and Significance, pp. 991–998. Taylor and Francis (2008)

A Simplified Two-Step Approach for the Seismic Retrofitting Design of Existing Structures Towards a Resiliency Enhancement

Rafael Shehu

Abstract The resilience of a community to come across the natural hazard events is gaining popularity in planning and decision-making strategies. To utmost importance in seismic zones, is the safety and operability of structurally vulnerable existing structures, representing a high portion of the built stock. Manifested low resilience has shown many flaws in planning, managing, retrofitting the damaged structures, which in many cases takes years being completed. The scope of the research is to exploit numerical simulation strategies towards a resiliency enhancement by means of optimized retrofitting solutions. At present, the seismic design is based on elastic analysis. A simplified two-step procedure for the seismic retrofitting design is here proposed, by utilizing the capabilities of FE codes to perform advanced nonlinear analyses. In the first step, it is estimated the structural performance of the structure, whilst the vulnerable elements to be strengthened are indicated. A Retrofitting strategy is selected and implemented into the model, and in the second step, the structure is reanalyzed with the same strategy. Based on the obtained responses, each strengthening element is designed adequately to the required limit state. This strategy is computationally burdening; however, the progress in the numerical analyses makes possible its implementation, and the achieved accuracy is nonpareil. The proposed method is illustrated with a masonry church, severely damaged by the Emilia Romagna (Italy) Earthquake in 2012. The retrofitting strategies adopted for strengthening options, are the surface mounted: (a) FRP sheets; (b) GFRP bars and TRCM. Throughout the investigated case study, it is demonstrated that the vulnerable structures exhibit very low resilient features and the best strategy to enhance their resilience is by means of anterior measures.

Keywords Retrofitting · Design · Seismic analyses · Masonry · Resilience · Composites

R. Shehu (✉)
DICA Department, Politecnico Di Milano, 20133 Milan, Italy
e-mail: rafael.shehu@polimi.it

E. B. Pereira et al. (eds.), *Proceedings of the 3rd RILEM Spring Convention and Conference (RSCC 2020)*, RILEM Bookseries 32,
https://doi.org/10.1007/978-3-030-76547-7_12

1 Introduction

The resiliency and the seismic performance of the built stock is a paramount issue in the present societies because it significally influences the economy in earthquake-prone areas. The economic and social development during the last decades has progressively increased the request for buildings causing a significant increment of the built stock. These buildings are exposed to: (i) deterioration processes, (ii) natural hazards threats and (iii) updates of the technical codes' requirements for adequate seismic performance. Their safety is gaining more interest, due to the correlation between the huge impact of their maintenance in a circular economy, [1]. However, there are many constraints that restrict the capabilities to overcome threats. Three are the most paramount causes, (i) the registered amount of heavy damages to be repaired, (ii) lack of resilient-based strategies and (iii) economic restraints. The last one is out of the scope of this study per se, while all can be correlated with the structural design process.

Addressing structural safety is not an easy task and for what concerns seismic safety the performance-based seismic design is the prevailing approach in design and retrofitting strategies. The structural behavior ante or post-earthquakes, from a probabilistic point of view, exhibit the same level of risk and consequently the same level of required intervention. From a resilient model standpoint, is difficult to distinguish the two cases; however, the social aspects influencing the resilience predominates. The societies tend to pay less attention to measures against possible hazardous events and behave chaotically after disasters. Both these aspects cause a lack of efficient use of resources and decrease the resiliency.

In this research, throughout a case study, it is proposed a simple strategy to achieve a resilience enhancement of the societies against seismic structural damages and losses. A two-step procedure here adopted consists of an inelastic analysis approach for the design of the retrofitting elements. In the first step, the seismic vulnerability is investigated by means of reliable scenarios. At the end of the first step, engineering parameters are collected and used to optimize the retrofitting strategy. In the second step, the strengthening is designed by means of a sophisticated numerical model investigated for the worst scenario in order to obtain the maximum demands on retrofitting elements. The proposed approach might reduce the retrofitting elements and estimate them more accurately by employing a nonlinear design approach. By imposing lower seismic demands in the first step the vulnerability is captured and then the corresponding required strengthening perform efficiently in the second step.

2 A Two-Step Retrofitting Design Approach

The design procedures for the whole structure are principally based on an elastic numerical model and the design forces are derived from a strength-demand equilibrium approach. The most advanced approaches, involving the nonlinear features, are

based on the performance-based design. However, the last procedures estimate the nonlinear properties after a preliminary design based on an elastic approach. This was constrained also by the limitations that numerical procedures had to be implemented practically. Nowadays, the tools have evolved drastically, and many aspects of the computational burdening can be faced, and more advanced simulations can be performed.

Focusing on masonry structures, modeling them with linear elastic procedures brings out unrealistic results. On the other hand, plastic analysis based on the upper bound limit analysis approach limits the number of possible failure mechanisms on those mostly encountered in similar structures, and the dynamic interactions of different elements are lost. Both these aspects are present and crucial issues that should be addressed during the analysis process of masonry structures. Herein, a simple two-step procedure is proposed for the Seismic Retrofitting Design of Existing Structures.

- The first step includes a vulnerability assessment procedure based on the implementation of nonlinear analyses performing multiple scenarios. On the engineer's choice, both nonlinear static procedures and nonlinear dynamic procedures are valid for estimating the performance of the masonry structures corresponding to structural damage formation. The aim of this step is to identify the vulnerability of the structure and to find an optimal retrofitting strategy based on the exhibited vulnerability.
- In the second step, the retrofitted structures are modeled adequately to the retrofitting strategy and the strengthening elements are modeled as elastic materials in order to avoid the loss of strength due to underestimated dimensions. This approach allows the verification of the masonry elements if remain in the safe side and design the strengthening elements in respects to the forces' demands.

The seismic scenarios are chosen based on the seismic hazard and the required safety. For masonry structures, it is very usual to achieve invasiveness strengthening solutions in order to obtain a safety level, thenceforth, it could be an option to address a resilient approach instead.

3 Towards Resiliency

The resiliency deals with the fact that a system, impacted by hazard effects, should not only resist by standing to the hazards and suffer damages, but it should also recover or be strengthened to return within a given period time into acceptable levels of use and serviceability, [2]. A recovery process related to existing masonry structures, mostly for those artifacts part of the cultural heritage, requires a very long time, [3, 4].

The past severe natural disasters have shown that lack of risk aversion measures or interventions that worsen the structural behavior result in a cumbersome situation that becomes difficult to be dealt with, [5]. According to multi-level performance-based seismic design, a structure should be conceived to perform during earthquakes

according to an acceptable level of damage depending on the frequency of the considered earthquake. Table 1 illustrates the distribution of the typical construction performance against the expected earthquakes. In terms of peak ground accelerations, masonry buildings, like fortresses, churches, towers, palaces, old houses in aggregate or not have a very high probability to be severely damaged for a range between 0.1 and 0.2 g, i.e. rare earthquakes. This means that it is very challenging to ensure those buildings performing conform to seismic code design. As a matter of fact, the Italian Code permits that an intervention could be classified as a seismic upgrading even when meets its capacity meets 60% of the seismic demand, [6]. This approach is seen as a reasonable compromise between the seismic demands and the practical capabilities of the masonry structure.

Towards a more resilient society and measures, the risk aversion approach is the predominant one by means of seismic upgrading interventions which are being more preferred compared to the post interventions. The basic principle behind this is to avoid damages, losses or trolls as much as possible, despite difficulties from economical constraints. Figure 1, illustrates different scenarios based on different strategies followed to counter the expected hazard. The worst scenario is when no measure is carried out (i.e. Scenario A) and when a seismic event occurs, the possible damages are the highest possible. This case also corresponds to the lowest measured resilience according to the analytical definition of resilience given in equation (1).

Table 1 Structures performance levels according to seismic design codes

	Fully operational		Operational		Life safety		Near collapse	
Frequent earthquakes (50%, 50 years)								
Rare earthquakes (10%, 50 years)								
Very rare earthquakes (10%, 50 years)								
Ordinary buildings			Seismic code confirm design					
Essential buildings			Seismic code confirm retrofitting					
Hazardous facilities			Existing masonry structures					

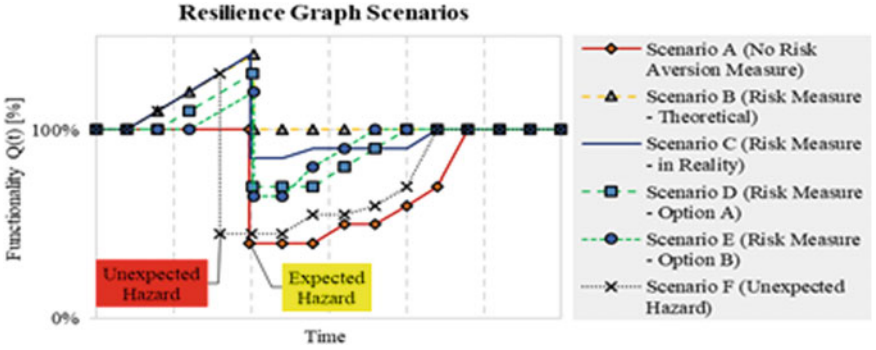

Fig. 1 Resilient scenarios approaches

$$R(\boldsymbol{r}) = \int_{t}^{t+T} \frac{Q_{TOT}(t)}{T_{LC}} dt \tag{1}$$

where Q_{TOT} is the global functionality in region-based; T_{LC} is the control time of the period of interest; t is the initial time of the resilience observation, $\boldsymbol{r}$ is a vector defining the position within the selected region, [7]. The global functionality is the combination of all functionalities related to different facilities, lifelines, etc. However, the measurement of the resilience is not objective of this study per se, thenceforth, will be focused only on the structural functionality in terms of safety and operationality. Two different scenarios are deliberately presented (i.e. scenario B and C) to highlight the uncertainties that exist in the risk and damage assessment. After an intervention it is expected that the structure will not compromise its functionality however, a more severe earthquake or cause of inadequate intervention, a certain damage level is still possible. Two other scenarios are presented, (i.e. D and E) emphasizing the high probability that severe damages will occur despite the interventions, which is particularly probable for masonry structures, as previously mentioned. The approach is based upon a preintervention–postintervention process, however, the level of intervention is not as intense and expensive as for case C. In this way, the amount of investments required is less than case C. In addition, the investment is spread in two periods of time, before the event and after the event, which decreases the immediate impact in the economy. Post-disastrous economies have resulted to be very fragile and the intervention of the public sector has been a necessity. The last scenario, Scenario F, refers to a seismic or hazardous event which occurs before the completion of the interventions.

In terms of resiliency of structures, the most resilient options among the above scenarios referring to masonry structures are D and E. Due to the low resistance in tension and elements interconnections, masonry structures result to be very vulnerable structures, [8], and the predominant behavior is ruled by the macro-elements, [9–12]. In this regard, a minimum intervention in enhancing the interlocking between

elements significantly improves the seismic behavior by prohibiting the mechanism activization, [13–16]. While this approach may not be always true for other typologies of structures, as normally they have better redundancy, ductility, and overall performance.

4 Case Study

The church consists of a single nave, which is over 13 m high. The overall length and width of the church are about 35.6 m and 17.2 m, respectively; the main nave is 28.8 m long and 14.3 m wide, see Fig. 2. On the right side of the nave, there are four rectangular chapels that are separated from each other: the height of the chapel's walls is about 8 m. On the other hand, the left side of the church, without side chapels, is characterized by four rectangular windows and a secondary entrance. The presbytery, which is raised a few steps, is separated from the nave by the triumphal arch and presents sidewalls that are about 7 m high; the back wall behind the altar, which is about 11 m high, exhibits two elongated windows.

The bell tower, which is 17 m high, is incorporated into the presbytery, on the left side of the church. After the 2012 earthquake, in 2016 the ecclesiastic compound was subjected to post-earthquake strengthening interventions, which consisted of steel tie-rods, rigid diaphragms, and consolidation of damaged masonry walls. The masonry is made of clay bricks with lime mortar and the thickness of walls is varies from 30 to 60 cm. Intermediate floors of the structural complex are made of reinforced concrete joists, while the roof is composed of timber beams. The material properties selected for the numerical simulations are conceived to provide a certain reliability of the results and to better fit the results the reality and expected performances. The Italian code recommends some reference values to be utilized during the analysis, i.e., Table C8A.2.1 and Table C8A.2.2 of [6, 17]. The characteristic value of the elastic modulus for the masonry is recommended to be taken E = 1500 MPa in a similar case. The identification of the compressive and tensile strength is even more challenging and uncertain in the absence of experimental tests. According to

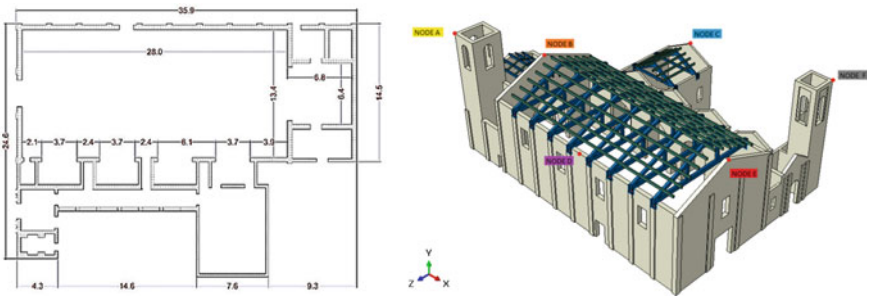

Fig. 2 Plan the layout of the church and the 3D numerical model

the values reported in the aforementioned tables, it is recommended to adopt the minimum value for the compressive strength which is equal to 2.6 MPa. In order to mimic the nonlinear behavior of the masonry material under seismic cyclic loads and characterizing the damage of the material, the Abaqus CAE software is used. The constitutive modeling of masonry in the non-linear phase is approached according to a Concrete Damage Plasticity material model (CDP) [18]. The numerical models are discretized by means of tetrahedron elements that suit best for meshing any irregular shape. The characteristic length of the element is maintained lower than 30 cm to achieve acceptable accuracy.

5 Damage State

The current state of the church exhibits different damages, where some of them were present before the seismic sequence and then expanded further. Damage is mostly diffused under the roof supports, near the interlocking between the elements, arches, and openings, see Fig. 3. These vertical cracks demonstrate low mechanical properties of the masonry wall and the high vulnerability to horizontal loads. The cracks located near the interlockings reveal various mechanisms prone to fail under moderate seismic actions. For instance, a vertical crack in the south nave wall of the church indicates an out-of-plane overturning of the façade. Similar circumstances can be observed also for the apse, the sacristy, and the chapels, where the cracks

Fig. 3 Damage state of the church: **a**, **b** longitudinal section along the nave; **c** transversal section in the nave; **d** transversal section passing through the sacristy; **e** rear view of the church

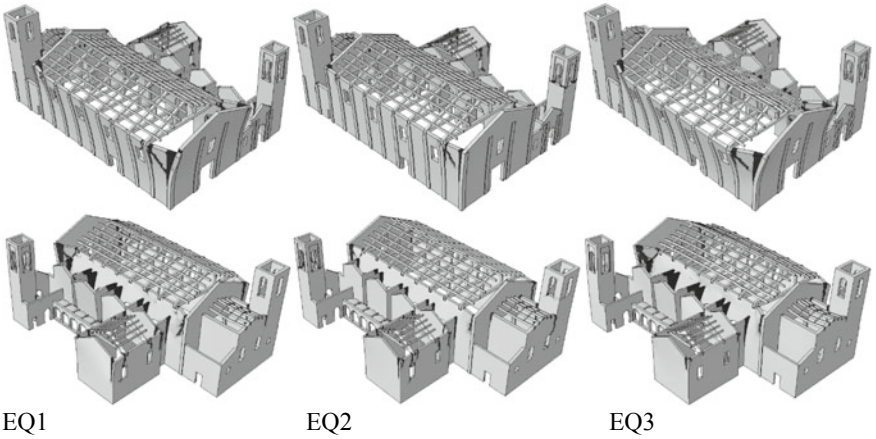

Fig. 4 Induced seismic damage state of Church from three different earthquakes

patterns show possible vulnerabilities. The severe and diffused cracks, deteriorated material and low mechanical properties is a typical picture among the built heritage. From the seismic vulnerability standpoint, those structures are prone to be damaged during horizontal induced loads. Two strategies could be followed: (i) to restore the structure and enhance the quality of material through the repointing or the undo-redo ("scuci-cuci"[1]); (ii) conceive a strengthening that could efficiently ensure structural stability by adequately placing reinforcing systems. The efficiency of the intervention is many times controversial and exhibits many drawbacks. From a numerical point of view, the first strategy does not bring out to a significant improvement of seismic safety, while the second approach is more efficient, [19].

6 Retrofitting Design

6.1 Step 1

As explained in paragraph 2, a two-step procedure is employed. Three earthquakes are deliberately chosen to correspond to a return period of 475y. It corresponds to a seismic severity lower to the required level of safety, i.e. Tr = 715y. This approach conforms to the expected high vulnerability, and the severity of the earthquakes diffuses the structural damages extensively out of the scope of estimating the vulnerability.

Based on the observed vulnerabilities, Fig. 4, detachment of the façade, out of plane bending of the longitudinal walls and the detachment of the chapels the

[1]The Italian term for the restoring the masonry with new material respecting the architectural requirements.

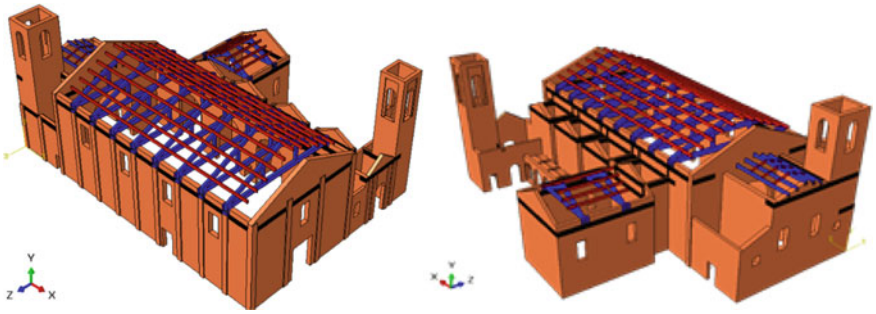

Fig. 5 Retrofitting concept of the Church with surface mounted composites (in black)

following intervention is conceived. Figure 5, depicts in black color the physical position of the retrofitting elements. Horizontal strips are placed close to the top of the church which makes the elements to withstand lower induced forces from the earthquakes and could be easily hidden in the ceilings and the roof. The evasiveness of this intervention is quite acceptable. The next step would be to finalize the design concluding in optimized dimensions in proportion to the required safety.

6.2 Step 2

The same approach, as investigating the vulnerability, is followed for checking the compatibility of the retrofitting. The severity of the earthquake is higher in this step (Tr = 715y), but as can be easily observed in Fig. 6, the level of damage in the masonry material is diminished substantially. The retrofitting design of the seismic upgrading of a masonry element bears many uncertainties due to the quality and the mechanical properties of the masonry. Near-surface mounted high-performance strengthening

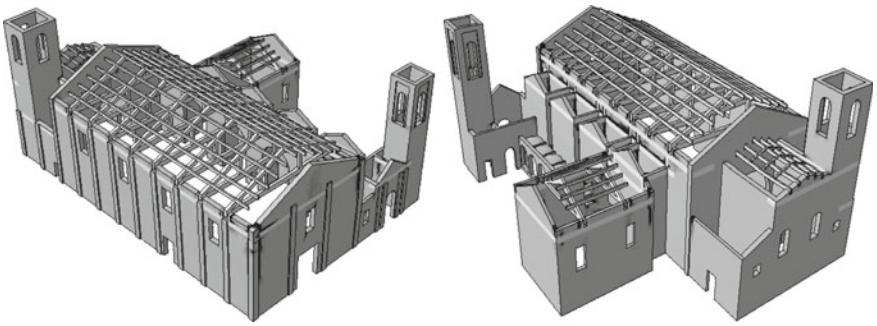

Fig. 6 Damage state of the retrofitted Church from the worst scenario

elements are conceived to carry all the tensile stresses caused by vertical or horizontal bending moments, shear forces or tensile forces. In the present case study, the predominant failure modes are a result of tension and horizontal bending moments.

Figure 7, summarizes the estimated tensile forces due to the nonlinear dynamic analysis. Nine control points are here considered for investigating the maximum design forces of the strengthening elements. In compliance with the damages reported in Fig. 6, the retrofitting elements remain in a permanent state of tension which is due to their contribution of inhibiting the collapse of the macroelements. A simplified mechanical approach is adopted for estimating the capacity of the elements in their ultimate state either of out-of-plane bending or pure tension, according to [20].

Despite the choice of the technology, FRP sheets, GFRP bars or TRCM, it is a mandatory condition to ensure good adhesion between the masonry and the fibers to avoid the delamination and loss of resistance for guaranteeing the long time structural stability, [21]. For the GFRP bars and the TRCM, a perfect bond is assumed between the fibers and the mortar and between the mortar and the existing masonry considering an adequate implementation.

The Italian guideline provides a reliable framework on how to design the retrofitting of existing structures using high-performance materials. Table 2 present the summary of the obtained results of the design procedure from the two-step approach. For the sake of brevity, only 9 points are here considered, as presented in Fig. 7. The details on the adopted strength of the materials and the notations of the symbols, could be referred in the following literature, on the application of the FRP composites CNR-DT200 [22], the application and design with GFRP composites CNR-DT203 [23], and the application of TRCM composites CNR-DT215 [24].

7 Concluding Remarks

This research treats the seismic risk reduction in a resilient approach by proposing a simplified retrofitting design procedure. The emphasis is here focused on the cultural heritage stock, built with masonry which results to be among the most vulnerable assets.

The retrofitting design is very challenging particularly when it is dealt with masonry structures due to a vast amount of uncertainties. Due to a common opinion that the elastic analyses are not suitable for estimating the behavior of a brittle material, a nonlinear design procedure is here implemented with two steps. The first step is to investigate the structural vulnerabilities aiming to have a picture of the strengthening pattern. Then an adequate numerical model, with implemented strengthening elements is reanalyzed to obtain the design forces. Then finally the retrofitting elements are dimensioned in respects to technical norms.

The proposed design strategy encompasses the possibility to properly estimate the vulnerability and optimizes the material for better performance. It is believed that the proposed strategy will help for boosting the resilience towards a seismic risk aversion approach.

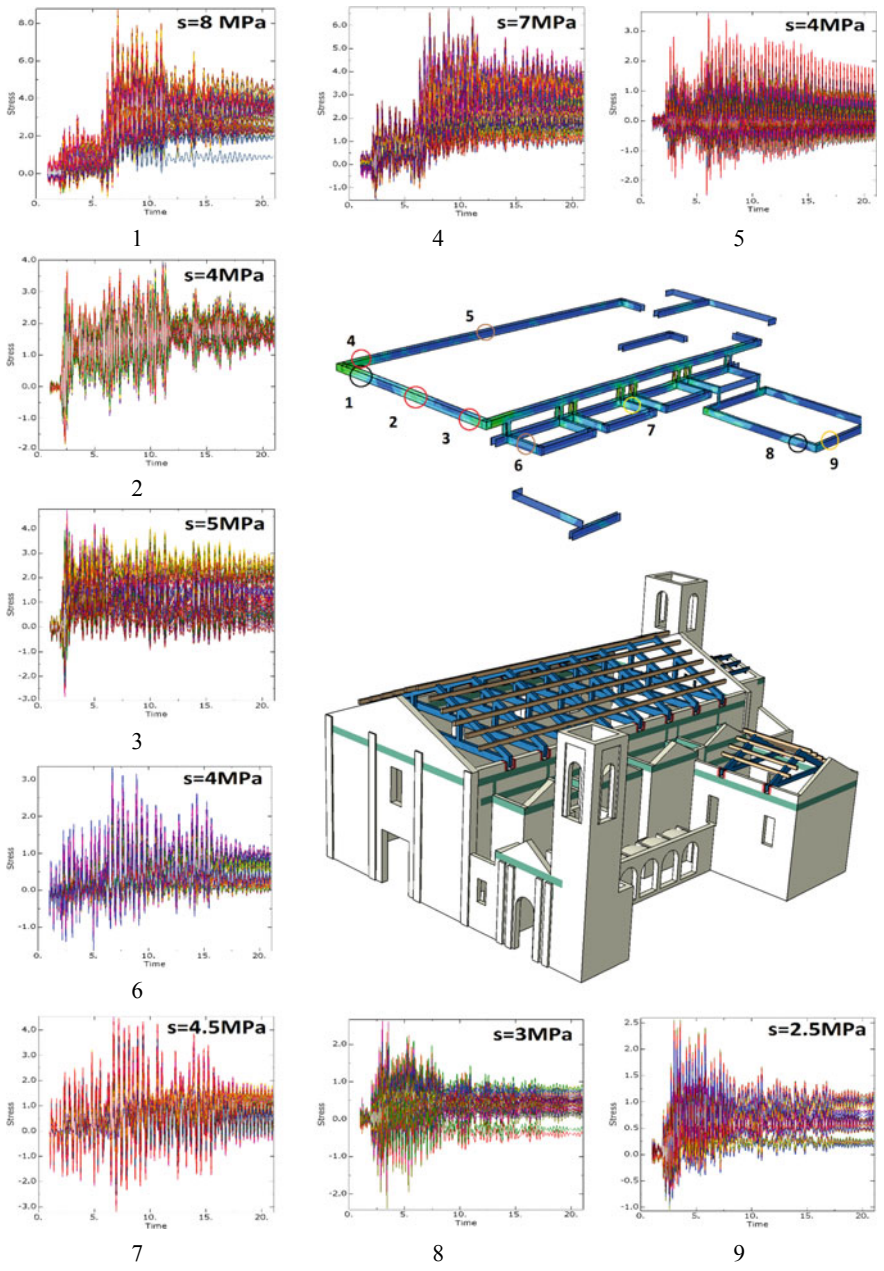

Fig. 7 Homogenized design stresses from the nonlinear dynamic analyses

Table 2 Summary of the retrofitting design for three different options

Point index	σ(h)	T	(FRP)			(TRCM)			(GFRP)		
	(MPa)	(kN)	f_{fdd}	A	b (cm)	$\sigma_{u,f}$	A	b (cm)	f_{fd}	A	no
			(GPa)	(mm^2)	t = 0.15 mm	(GPa)	(mm^2)	t = 0.047 mm	(GPa)	(mm^2)	φ6
1	4	100	0.9	111	74	1.2	83	177	0.8	125	5
2	5	125	1.8	69	46	1.2	104	222	0.8	156	6
3	4	100	0.9	111	74	1.2	83	177	0.8	125	5
4	7	175	0.9	194	130	1.2	146	310	0.8	219	8
5	4	100	1.8	56	37	1.2	83	177	0.8	125	5
6	4	100	0.9	111	74	1.2	83	177	0.8	125	5
7	4.5	112	0.9	125	83	1.2	94	199	0.8	141	5
8	3	75	0.9	83	56	1.2	63	133	0.8	94	3
9	2.5	62.5	0.9	69	46	1.2	52	111	0.8	78	3

References

1. Booth, E.: Dealing with earthquakes: the practice of seismic engineering 'as if people mattered.' Bull. Earthq. Eng. **16**, 1661–1724 (2018)
2. Mebarki, A.: Resilience: theory and metrics—a metal structure as demonstrator. Eng. Struct. **138**, 425–433 (2017)
3. Contreras, D., Forino, G., Blaschke, T.: Measuring the progress of a recovery process after an earthquake: the case of L'Aquila, Italy (2017). ISBN 3464732568
4. Valensise, G., Tarabusi, G., Guidoboni, E., Ferrari, G.: The forgotten vulnerability: a geology- and history-based approach for ranking the seismic risk of earthquake-prone communities of the Italian Apennines. Int. J. Disaster Risk Reduct. **25**, 289–300 (2017)
5. Costa, A., Guedes, J.M., Varum, H.: Structural Rehabilitation of Old Buildings. In: Costa, A., Guedes, J.M., Varum, H. (eds.) Building Pathology and Rehabilitation, vol. 2. Springer, Berlin, Heidelberg (2014). ISBN 978-3-642-39685-4
6. NTC: Aggiornamento delle "Norme Tecniche per le Costruzioni"—NTC 2018, Italy, p. 372 (2018)
7. Reinhorn, A.M., Cimellaro, G.P.: Consideration of resilience of communities in structural design. In: Fischinger, M. (ed.) Geotechnical, Geological and Earthquake Engineering, vol. 32, pp. 401–421. Springer, Netherlands, Dordrecht (2014)
8. Grünthal, G.: European Macroseismic Scale 1998, vol. 15 (1998). ISBN 2879770084
9. D'Ayala, D., Speranza, E.: Definition of collapse mechanisms and seismic vulnerability of historic masonry buildings. Earthq. Spectra **19**, 479–509 (2003)
10. Giuffrè, A.: Monumenti e terremoti. Multigrafica Editrice, Roma (1988)
11. DPCM: Linee guida per la valutazione e la riduzione del rischio sismico del patrimonio culturale con riferimento alle Norme tecniche per le costruzioni di cui al decreto del M.I.T del (2008), Italy (2011)
12. Acito, M., Magrinelli, E., Milani, G., Tiberti, S.: Seismic vulnerability of masonry buildings: numerical insight on damage. J. Build. Eng. 101081 (2019)
13. Milani, G., Shehu, R., Valente, M.: Seismic upgrading of a Masonry Church with FRP composites. Mater. Sci. Forum **866**, 119–123 (2016)
14. Milani, G., Shehu, R., Valente, M.: Effects of FRP application on the seismic response of a masonry church in Emilia-Romagna (Italy). In: Proceedings of the AIP Conference Proceedings, vol. 1790, pp. 130003-1–4. AIP Publishing (2016)
15. Maio, R., Estêvão, J.M.C., Ferreira, T.M., Vicente, R.: Cost-benefit analysis of traditional seismic retrofitting strategies integrated in the renovation of stone masonry buildings. Eng. Struct. **206**, 110050 (2020)
16. Aşıkoğlu, A., Avşar, Ö., Lourenço, P.B., Silva, L.C.: Effectiveness of seismic retrofitting of a historical masonry structure: Kütahya Kurşunlu Mosque, Turkey. Bull. Earthq. Eng. (2019)
17. NTC: Istruzioni per l'applicazione dell'«Aggiornamento delle "Norme tecniche per le costruzioni", vol. 35, p. 337 (2019)
18. Lubliner, J., Oliver, J., Oller, S., Oñate, E.: A plastic-damage model for concrete. Int. J. Solids Struct. **25**, 299–326 (1989)
19. Milani, G., Shehu, R., Valente, M.: Seismic vulnerability reduction of masonry churches: a case study. Procedia Eng. **199**, 272–277 (2017)
20. Ramaglia, G., Fabbrocino, F., Lignola, G.P., Prota, A.: Unified theory for flexural strengthening of masonry with composites. Materials (Basel) **12** (2019)
21. Ramirez, R., Maljaee, H., Ghiassi, B., Lourenço, P.B., Oliveira, D.V.: Bond behavior degradation between FRP and masonry under aggressive environmental conditions. Mech. Adv. Mater. Struct. (2019)
22. CNR DT 200: Istruzioni per la Progettazione, l ' Esecuzione ed il Controllo di Interventi di Consolidamento Statico mediante l ' utilizzo di Compositi Fibrorinforzati Consiglio Nazionale delle Ricerche (2013)

23. CNR-DT 203: Istruzioni per la Progettazione, l'Esecuzione ed il Controllo di Strutture di Calcestruzzo Armato con Barre di Materiale Composito Fibrorinforzato (2007)
24. CNR-DT 215: Istruzioni per la Progettazione, l'Esecuzione ed il Controllo di Interventi di Consolidamento Statico mediante l'utilizo do Compositi Fibrorinforzati a Matrice Inorganica (2018)

Critical Overview and Application of Integrated Approaches for Seismic Loss Estimation and Environmental Impact Assessment

M. Caruso, F. Bianchi, F. Cavalieri, and R. Pinho

Abstract Buildings are among the major contributors to environmental impacts, in terms of non-renewable resource depletion, energy and material consumption, and greenhouse gas (GHG) emissions. For this reason, modern societies are pushing towards the refurbishment of existing buildings aiming at the reduction of their operational energy consumption and at a major use of renewable energy and low-carbon materials. At the same time, buildings are expected to provide population with safe living and working conditions, even when hit by different kinds of hazards during their service life, such as earthquakes. Until recently, life cycle assessment (LCA) procedures tended not to include the effects of natural hazards. However, if considered in a building LCA, earthquake-induced environmental impacts would constitute a very informative performance metric to decision-makers, in addition to the more customarily used monetary losses or downtime indicators. Within this context, therefore, a comprehensive review of the existing literature is presented, with comparisons between available methodologies being carried out in terms of their employed seismic loss estimation method, environmental impact assessment procedure, damage-to-impact conversion, impact-to-cost conversion, and selected decision variable. Further, an illustrative case-study application is also included.

Keywords Seismic loss estimation · Environmental impact assessment · Sustainability · Life cycle assessment

M. Caruso (✉)
University School for Advanced Studies, IUSS Pavia, Pavia, Italy
e-mail: martina.caruso@iusspavia.it

F. Bianchi · F. Cavalieri
European Centre for Training and Research in Earthquake Engineering (EUCENTRE), Pavia, Italy

R. Pinho
Department of Civil Engineering and Architecture, University of Pavia, Pavia, Italy

E. B. Pereira et al. (eds.), *Proceedings of the 3rd RILEM Spring Convention and Conference (RSCC 2020)*, RILEM Bookseries 32,
https://doi.org/10.1007/978-3-030-76547-7_13

1 Introduction

Life cycle assessment (LCA) procedures are intended to estimate the environmental impacts of a process or a product, and they are often employed as a decision-making support instrument. For instance, buildings can be treated as large products with long and uncertain lives. Such procedures are characterised by four main steps, as described in [1] and [2]: (i) definition of goal and scope, (ii) life cycle inventory (LCI) analysis, including the assessment of energy and materials inflows and outflows associated to the building life cycle, (iii) life cycle impact assessment (LCIA), consisting in the quantification of impacts, and (iv) interpretation of the results, with these showing the major contributors, either materials or processes, to global environmental impacts in terms of specific performance metrics. Examples of metrics typically used in LCA procedures include global warming potential (GWP), non-renewable resource use, waste generation, and a wide range of human health impacts.

In the European Union (EU), the construction sector produces significant impacts on the environment, consuming up to 40% of the total EU energy and producing up to 36% of the total greenhouse gas (GHG) emissions [3]. For these reasons, there is a strong need of renovation mainly due to a progressive transition towards low-carbon and eco-efficient societies, as demonstrated by several national and European policies for building stock refurbishment. For instance, the European Green Deal, which is the new growth strategy for Europe, aims at a huge buildings' Renovation Wave, in order to achieve the ambitious energy and GHG reduction targets by 2030 and climate-neutrality by 2050 [4].

The ISO 21931:2010 [5] identifies three main stages in the building life cycle:

- **construction stage**, including raw materials extraction, transportation, component manufacturing and processing, as well as the construction process itself;
- **use stage**, including operational energy usage, building component maintenance, and resource inflow and waste outflow during the building operational phase;
- **end-of-life stage**, including building demolition, together with the transportation of waste or salvaged materials, processing and disposal of waste materials.

Notably, a recent European standard [6] introduced a beyond-life stage, including possible reuse, recycle and recovery of post-demolition materials.

Given that LCA involves the entire building life cycle, particular attention should be addressed to regions that are characterised by high risk of natural hazards, e.g. earthquakes, hurricanes, tornadoes, or floods, where hazardous conditions may result in additional environmental impacts. Until recently, LCA procedures have tended not to include such effects, however, earthquake-induced environmental impacts may constitute a meaningful metric to decision-makers, allowing easier comparisons between alternative design or retrofit strategies and providing tools to evaluate the potential benefits of retrofitting rather than demolishing and reconstructing. There is though still no unique opinion on how to include the additional environmental impacts due to natural hazards into an LCA.

The European building stock, being both earthquake-prone and heavily energy-consuming, needs a comprehensive strategy of renovation, due to its structural deficiencies and to its significant environmental impacts. The region is characterised by wide ranges of seismic areas and of climatic zones with high variability in seismic demands and energy needs for space heating and cooling. Nevertheless, the renovation rate is still very low due to high costs of intervention, downtime, potential need of inhabitants relocation and insufficient hazard-awareness. Furthermore, most of the retrofit interventions on existing building are solely intended to reduce either energy consumption or seismic vulnerability, neglecting potential correlations. However, in seismic prone sites, the vulnerability of buildings can compromise the efficiency and the monetary savings of a sole energy refurbishment. In addition, most of the buildings requiring refurbishment have almost exhausted their service life, being representative of a construction era with building codes lacking of seismic requirements.

Some studies ([7–9], among others) proved that the probability of damaging earthquakes during the building life cycle significantly influences the environmental impact assessment, and that post-earthquake repairs produce additional environmental impacts within a building LCA to be considered as additional construction stages. Earthquake damage can affect the remaining service life of a building and it can result in collapse or abandonment (i.e., end of service life), or in extensive repairs (i.e., extension of service life). Depending on when in the service life of the building the earthquake occurs, damage and repair may be meaningful in the overall LCA.

Furthermore, a minimal seismic retrofit in seismic prone regions may save materials and environmental initial costs, but may be ineffective against future earthquakes. On the contrary, a conservatively designed retrofit with higher initial costs may lead to a much better performance during earthquakes, thus reducing losses during the remaining service life of the building. Moreover, an integrated intervention in which the retrofit system may serve multiple purposes can represent an effective strategy for a better seismic and environmental performance. As an example, reinforced concrete shear walls may contribute not only to the structural upgrade but also to the thermal mass of the building and reduce the HVAC (Heating, Ventilation and Air Conditioning) demands and operational impacts. Also, an efficient choice of materials, for reduced energy demands, for durability, for future potential demolition and recycle, can significantly improve the environmental performance of a building. Thus, the most desirable scenario would be a coupled seismic and energy renovation. Unfortunately, integrated approaches have never been included into design codes due to the lack of a solid methodological framework.

2 Literature Review

Recent interest in sustainability of buildings has motivated a growing number of research endeavours focused on environmental impact assessment methods, and

especially on the integration of those methods into seismic loss estimation frameworks. The differences between the results of the existing approaches is mainly related to the seismic loss estimation framework, the environmental impacts estimation method, the treatment of uncertainty and other aspects, as further discussed in this section.

A comprehensive review of the existing literature is presented herein, also by taking advantage of the similar efforts by Hasik et al. [10] and extending the comparison with a few other works. The aim of this review is to highlight potential strengths and limitations of the existing methodologies for a further understanding on how to properly combine the two aspects of seismic safety and environmental impact. The list of references is reported in Table 1 with information on (i) *authors and year of publication*, highlighting how the available literature on this topic is relatively scarce and recent, (ii) *seismic loss estimation method*, referring to the way the authors estimated the expected annual monetary losses due to potential earthquakes, (iii) *environmental impact assessment method*, indicating how building life cycle environmental impacts are quantified (iv) *damage-to-impact conversion method*, which is needed to assess the contribution to environmental impacts of each damage state defined within the seismic loss assessment, (v) *impact-to-cost conversion method*, which is used to translate the building's environmental impacts into monetary losses, and (vi) *decision variable*, i.e., the performance metric used.

2.1 Seismic Loss Estimation Method

Recent advances in the so-called performance-based earthquake engineering (PBEE) led to the development of the fully probabilistic PEER PBEE methodology [20], proposed by the Pacific Earthquake Engineering Research (PEER) Center, which is a probabilistic approach to estimate damage and the corresponding losses depending on the site-specific seismic hazard and on the structural response of a given building. Most studies included in this review referred to the well-known PEER PBEE framework for seismic loss estimation [21, 22], and used tools developed by the PEER Center to estimate earthquake-induced losses on buildings (e.g., the PACT Tool). The **PEER PBEE** procedure for seismic loss assessment has a four-step main structure: seismic hazard quantification at the site of interest, evaluation of structural performance under seismic hazard, estimation of damage in different building components conditioned on the estimated structural response, and calculation of losses due to repair the damaged components. The results of the procedure are in terms of mean annual frequency of exceedance of a certain value of a decision variable, such as monetary losses, downtime, casualties, or environmental impacts (carbon emissions or embodied energy).

While the PEER PBEE methodology is component-based, the software tool Hazus [23], developed by the Federal Emergency Management Agency (FEMA), is typically used to estimate post-earthquake losses at a local, state and regional scale. Some authors performed the seismic loss assessment using the Advanced Engineering

Table 1 Summary overview of past work on integrated approaches for seismic loss estimation and environmental impact assessment

Authors	Seismic loss estimation method	Env. impact assessment method	Damage-to-impact conversion	Impact-to-cost conversion	Decision variable
Menna et al. (2019) [11]	Other	–	–	Energy consumption	Monetary losses
Chhabra et al. (2018) [9]	Other	BOM LCA	–	Energy consumption and carbon footprint	Monetary losses
Lamperti Tornaghi et al. (2018) [12]	PEER PBEE	–	Damage/repair description + BOM LCA	–	Environmental impacts
Alirezaei et al. (2016) [13]	PEER PBEE	BOM LCA (Tally)	Repair-cost ratio	–	Environmental impacts
Belleri and Marini (2016) [8]	PEER PBEE	eCO_2 factors (references)	Damage/repair description + eCO_2 factors (ICE)	–	Environmental impacts
Calvi et al. (2016) [14]	Other	–	–	Energy consumption	Monetary losses
Padgett et al. (2016) [15]	Other	CO_2 factors (references)	–	Carbon footprint	Monetary losses
Wei et al. (2016) [16]	PEER PBEE	–	EIO LCA (EIO-LCA US 2002)	–	Environmental impacts
Arroyo et al. (2015) [17]	Hazus AEBM	eCO_2 factors (references)	Damage/repair description + eCO_2 factors (references)	–	Environmental impacts
Simonen et al. (2015) [18]	Other	BOM LCA (Athena IE)	Repair-cost ratio	–	Environmental impacts
Menna et al. (2013) [7]	Other	BOM LCA (IMPACT 2002+)	Damage/repair description + BOM LCA (IMPACT 2002+)	–	Environmental impacts
Comber et al. (2012) [19]	Hazus AEBM	EIO LCA (consultant)	EIO LCA (consultant)	–	Environmental impacts

Building Module (**Hazus AEBM**), added in the Hazus-MH Software to allow easier implementation of building-specific damage and loss functions by users.

Lastly, a few authors preferred custom approaches, referred to as **other**, mostly being similar either to PEER PBEE or Hazus. For instance, Menna et al. [11] and Lamperti Tornaghi et al. [12] used simplified versions of the PEER PBEE procedure, described in Vitiello et al. [24] and in Negro and Mola [25], respectively, while Calvi et al. [14] used the Displacement-Based Assessment [26].

2.2 Environmental Impact Assessment Method

Bill-of-materials (BOM), economic input-output (EIO), or hybrid procedures are alternative ways to assess environmental impacts, as described in [27]. In the works included in this review, environmental impacts were assessed with different LCA tools, performing either BOM or EIO LCA, or by applying eCO_2 factors.

BOM-based LCA (referred to as **BOM LCA**) requires individual materials quantities and processing needs and rely on available databases, such as U.S. LCI [28] or Ecoinvent [29]. Several proprietary LCA tools, like Athena Impact Estimator [30], Tally [31], SimaPro [32] or GaBi [33], among others, have been developed, based on ISO guidelines, and are available to perform BOM LCA of buildings.

On the contrary, EIO-based LCA (referred to as **EIO LCA**) requires only product or activity cost information to be used within available tools that translate industry sector-specific costs into the corresponding environmental impacts, such as the U.S. EIO-LCA [34]. This method can be used for a building LCA by either selecting a single sector best representing the building typology (e.g., construction of residential structures) or identifying multiple sectors (e.g., concrete manufacturing, or painting and coating), referred to as Building-EIO and Component-EIO, respectively.

As an alternative, environmental impacts can also be calculated via **eCO_2 factors** or estimates, available in literature or in databases, in which environmental impacts per kilograms of materials o per specific activities are collected. As an example, the Inventory of Carbon and Energy (ICE), developed at the University of Bath [35], collects carbon emissions per kilograms of material applicable to the European area. It is worth mentioning that the LCA boundaries of ICE data are from cradle to gate.

2.3 Damage-to-Impact Conversion Method

Environmental impacts can be treated in the same way as any other consequence function (e.g., economic losses) to be integrated within a seismic loss assessment. To do so, for each damage state (and consequent repair activity) defined in the seismic loss estimation framework for single components (or for an entire building), a damage-to-impact conversion is needed to get an estimate of their environmental impacts.

In the literature, as confirmed by Hasik et al. [10], damage and associated repair were converted into environmental impacts by one of the following three approaches:

- **EIO**: each repair activity is disaggregated into a list of processes to be assigned to specific industry sectors, whose costs are translated into environmental impacts via specific EIO tools, e.g., the U.S. EIO-LCA [34];
- **damage/repair description + BOM or eCO_2 factors**: impact data, resulting from a BOM LCA or via eCO_2 factors, are developed based on custom damage and repair descriptions and then introduced within the seismic loss assessment;
- **repair-cost ratio**: the economic losses due to repair are usually expressed as a percentage of the replacement cost of the building, and the same ratio can be applied to the building pre-use environmental impact to get the impacts of the repair activities.

2.4 Impact-to-Cost Conversion Method and Decision Variable

Some authors preferred to translate environmental impacts into costs so as to deal with a single decision variable, i.e., monetary losses due to both seismic risk and to building energy consumption or carbon footprint. This choice is specific of methods where earthquake-induced environmental impacts are neglected, and only the **energy consumption** of the building is considered from the environmental viewpoint. For instance, Calvi et al. [14] proposed the quantification of the energy annual cost as the ratio between cost of consumed energy and the total building replacement cost to allow a unique classification of seismic resilience and energy efficiency. A few other works translated the building **carbon footprint** into monetary losses by applying existing carbon tax rates.

However, Simonen et al. [36] demonstrated that embodied carbon and embodied energy are acceptable proxies for other environmental metrics, due to the perceived value to practitioners and potential users. For these reasons, in the works collected in this review, the selected decision variable was either in terms of **environmental impacts**, if a damage-to-impact conversion was adopted, or **monetary losses**, if the impact-to-cost conversion was used, neglecting energy-seismic correlations.

3 Application to a Case-Study (Using the FEMA P-58 Approach)

FEMA funded a series of projects, named ATC-86 and ATC-86-1 [37], to incorporate environmental impacts into the well-known FEMA P-58 seismic loss assessment methodology, currently implemented in the PACT Tool [21, 22, 27, 38], and thus to quantify earthquake-induced environmental impacts. This section discusses the application to a case-study of the FEMA P-58 approach.

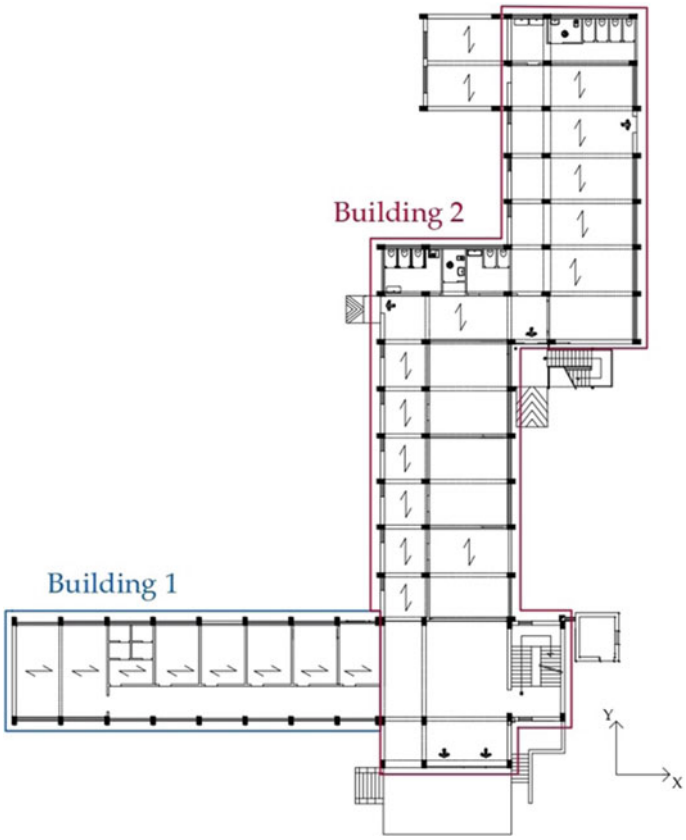

Fig. 1 Floor layout of the case-study

The case-study under scrutiny is one of the buildings of a school complex in Central Italy (i.e., Building 2 in Fig. 1). Although the original design documents are not available, comprehensive reports of in-site inspections and material tests suggest that the complex was built between the 60 s and the 70 s. It is a three-storey structure composed of sixteen reinforced concrete (RC) frames along the shortest direction X, with a U-shaped stair system, whose plan location produces an eccentricity in the building.

3.1 Numerical Modelling

Using the available information on the structural layout and the material properties [39], a refined 3D nonlinear numerical model of the case-study (Fig. 2) was developed with the fibre-based analysis software SeismoStruct [40].

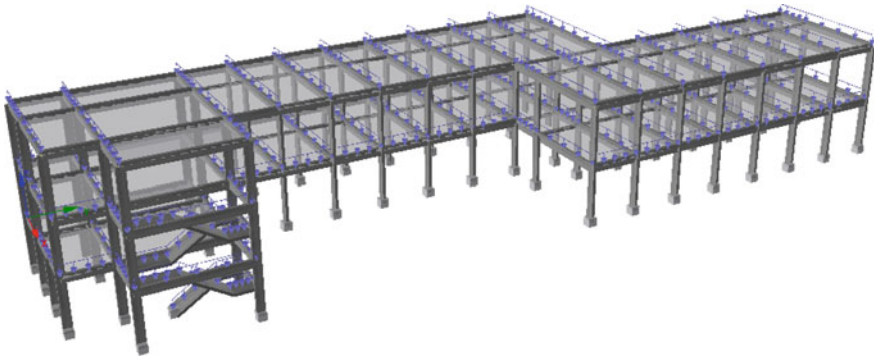

Fig. 2 Overview of the 3D nonlinear model on SeismoStruct [40]

Two materials were defined: existing concrete, with an average cylindrical compressive strength equal to 16.6 MPa and an elastic modulus approximately equal to 25,000 MPa, and existing steel for smooth reinforcement, with mean yielding strength equal to 391 MPa and an elastic modulus equal to 210,000 MPa. The material inelasticity was taken into account through Mander et al. [41] and Menegotto and Pinto [42] constitutive laws for concrete and steel, respectively. Force-based elements were used to model beams and columns, and elastic properties were assigned to the stairs system. Masonry external infills were not modelled explicitly, but only considered as applied loads on perimeter beams. Rigid diaphragms were deemed suitable to represent the rigid behaviour typical of concrete and hollow clay blocks mixed floors.

3.2 Application of Damage-to-Impact Conversion Methods

In the first version of the PACT tool, the results of loss assessments were only available in terms of dollars, deaths and downtime (i.e., the so-called 3Ds). However, in its latest version, environmental impacts, in terms of carbon emissions (CO_2) and embodied energy (EE), are included as consequence functions of damageable components, as suggested by Simonen et al. [36]. This section describes the application of the three damage-to-impact conversion methods introduced above, to estimate the earthquake-induced environmental impacts of the case-study via time-based assessments, based on simplified analysis (i.e., nonlinear static analysis).

Firstly, PACT requires the definition of a building performance model, i.e., a collection of data related to all the structural and non-structural components within the building that may experience damage during an earthquake. Thus, an inventory of drift-sensitive components was collected for the case-study. For RC structural components and masonry non-structural elements, the fragility and repair cost functions developed by Cardone [43] and Cardone and Perrone [44] were deemed appropriate

for the case-study, since they are mostly suitable for pre-70 s RC frame buildings typical of the Italian existing building stock. In terms of environmental impacts, damage-to-impact conversion methods were needed to translate the damage states (DSs) defined for each component into the corresponding environmental impacts due to repair. As explained in Sect. 3.3, dedicated to damage-to-impact conversions, damage and associated repair activities were converted into environmental impacts by the following three approaches:

- **EIO LCA**: the environmental impacts per dollar spent within each specific sector were extrapolated from the web-tool EIO-LCA [31] for the industry sectors of interest and then summed up with their own weight (i.e., the percentage indicating the contribution of a single process to the global costs of the repair activity). The examples found in Simonen et al. [14] and FEMA [36] were taken as a reference to perform the calculations and to define the percentage distribution of cost allocations for the different components. For instance, for exterior masonry infills with windows, the following percentage distribution of costs was assumed for the DS at collapse: 4% adhesive, 10% clay product, 2% cleaning, 2% coating, 2% electrical, 3% glass, 10% piping, 5% plywood, 5% stucco, and 3% windows. The remaining cost percentage was allocated in labour, whose contribution to environmental impact is assumed equal to zero;
- **Repair description + eCO_2 factors**: as suggested by Belleri and Marini [6], the ICE database [32] was used to get the eCO_2 emissions per kg of material (e.g., concrete, glass, clay). Average embodied carbon estimates equal to 0.11, 1.44, 0.24 kg eCO_2 per kg of concrete, glass and clay bricks, respectively, were selected. The main issue related to this approach is the need to estimate the kilograms of material that needs to be replaced during the repair activity associated to specific DSs. A unit volume of material was assumed for the DS at collapse (i.e., in case of full replacement of the component), while partial volumes of material associated to intermediate DSs were scaled down proportionally to DS-specific repair costs to finally assign the eCO_2 at each DS;
- **Repair cost-ratio**: given that the expected annual loss (EAL) ratio is the ratio between the expected value of the loss exceedance curve and the building's replacement value, the environmental impacts due to repair activities were calculated by multiplying the EAL ratio in terms of monetary losses and the replacement value in terms of environmental impacts (estimated through a Building-EIO and equal to approximately 650,000 kg eCO_2). A significant assumption of this approach is related to the fact that also labour costs are included, so the cost percentage allocated to labour should be excluded from the comparison. However, since the estimation of earthquake-induced monetary losses is needed, this procedure was performed after running the loss analysis on PACT and the impacts deriving from this approach are presented in Sect. 3.3.

In conclusion, the environmental impact consequence functions, whose medians in terms of eCO_2 were calculated following the first two approaches above, were assumed lognormally distributed, with dispersion equal to 0.4.

Table 2 eCO_2 resulting from different damage-to-impact (DTI) conversion methods

DTI	eCO_2 (kg eCO_2/yr)	eCO_2 (% ReI)
EIO LCA	1,600	0.24
Description + ICE	1,800	0.28
Repair-cost ratio	2,000	0.30

3.3 Discussion of the Results

The results of time-based performance assessments are mainly expressed in terms of loss curves, which plot the total expected loss as a function of the annual probability of exceedance of that loss. From PACT loss analysis results, an EAL ratio equal to 0.4% was estimated as the ratio between the area underneath the monetary loss curve (approximately equal to € 5,000) and the total replacement cost (approximately equal to € 1.25 million). Concerning environmental impacts, the expected annual carbon emissions obtained by applying the three different damage-to-impact conversion methods described above are shown in Table 2, also expressed as a percentage of the building's replacement impact (ReI). As stated above, labour does not contribute to environmental impacts and its contribution was assumed equal to the 20% of global repair costs. Thus, the impacts due to post-earthquake repairs arising from the repair-cost ratio approach were recalculated as the 80% of the eCO_2 resulting from the approach (i.e., equal to 2.5 t eCO_2). It is worth remembering that the cost percentage assigned to labour may vary significantly depending on the activity of interest.

4 Conclusions

A review of the available literature on integrated approaches for seismic loss estimation and environmental impact assessment was presented, together with the application to a case-study of the FEMA P-58 approach. The critical review of the existing approaches showed that earthquake-related losses and impact may be significant in an overall LCA, thus research is needed to further develop and validate a methodological framework to assess such impact. The application of the FEMA P-58 demonstrated that it can be used to quantify earthquake-induced environmental impact (as done already for monetary losses).

Notably, the three damage-to-impact conversion methods described above lead to very similar estimates of carbon emissions, demonstrating an already relatively satisfactory robustness of the three different approaches despite their very diverse assumptions and required information. It is worth emphasising the lack of comprehensive inventories from where to collect information on environmental impacts of specific components or activities. Furthermore, often the available databases are not updated to the current market prices, thus adjustment factors are needed to adapt the

estimates to the present material or activity prices specific for the site of interest, increasing the uncertainty of the results.

Acknowledgements This work has been carried out within the framework of the WP5 activities (focused on the development and verification of integrated seismic and energy retrofitting solutions) of the ReLUIS-DPC 2019–2021 research project, funded by the Italian Civil Protection Department.

References

1. ISO 14040:2006: Environmental management—Life Cycle Assessment—Principles and framework. International Organization for Standardization (ISO). Geneva (2006)
2. ISO 14044:2006: Environmental management—Life Cycle Assessment—Requirements and guidelines. International Organization for Standardization (ISO). Geneva (2006)
3. European Commission: Energy-efficient Buildings PPP beyond 2013: Research & Innovation Roadmap. Brussels (2012)
4. European Commission: The European Green Deal. Communication from the Commission to the European Parliament, the European Council, the Council, the European Economic and Social Committee of the Regions - COM(2019) 640 final. Brussels (2019)
5. ISO 21931:2010: Sustainability in building construction—Framework for methods of assessment of the environmental performance of construction works—Part 1: Buildings. International Organization for Standardization (ISO). Geneva (2010)
6. EN 15978:2011: Sustainability of construction works—Assessment of environmental performance of buildings—Calculation method. European Committee for Standardization (CEN). Brussels (2011)
7. Menna, C., Asprone, D., Jalayer, F., Prota, A., Manfredi, G.: Assessment of ecological sustainability of a building subjected to potential seismic events during its lifetime. Int. J. Life Cycle Assess. **18**(2), 504–515 (2013)
8. Belleri, A., Marini, A.: Does seismic risk affect the environmental impact of existing buildings? Energy Build. **110**, 149–158 (2016)
9. Chhabra, J.P., Hasik, V., Bilec, M.M., Warn, G.P.: Probabilistic assessment of the life-cycle environmental performance and functional life of buildings due to seismic events. J. Arch. Eng. **24**(1), 04017035 (2018)
10. Hasik, V., Chhabra, J.P., Warn, G.P., Bilec, M.M.: Review of approaches for integrating loss estimation and life cycle assessment to assess impacts of seismic building damage and repair. Eng. Struct. **175**, 123–137 (2018)
11. Menna, C., Vitiello, U., Mauro, G., Asprone, D., Bianco, N., Prota, A.: Integration of seismic risk into energy retrofit optimization procedures: a possible approach based on life cycle evaluation. In: IOP Conference Series: Earth and Environmental Science 290, 012022. IOP Publishing (2019)
12. Lamperti Tornaghi, M., Loli, A., Negro, P.: Balanced evaluation of structural and environmental performances in building design. Buildings **8**(4), 52 (2018)
13. Alirezaei, M., Noori, M., Tatari, O., Mackie, K.R., Elgamal, A.: BIM-based damage estimation of buildings under earthquake loading condition. Procedia Eng. **145**, 1051–1058 (2016)
14. Calvi, G.M., Sousa, L., Ruggeri, C.: Energy efficiency and seismic resilience: A common approach. In: Multi-hazard Approaches to Civil Infrastructure Engineering, pp. 165–208. Springer (2016)
15. Padgett, J.E., Li, Y.: Risk-based assessment of sustainability and hazard resistance of structural design. J. Perform. Construct. Facilities **30**(2), 04014208 (2016)
16. Wei, H.-H., Skibniewski, M.J., Shohet, I.M., Yao, X.: Lifecycle environmental performance of natural-hazard mitigation for buildings. J. Perform. Construct. Facilities **30**(3), 04015042 (2016)

17. Arroyo, D., Ordaz, M., Teran-Gilmore, A.: Seismic loss estimation and environmental issues. Earthquake Spectra **31**(3), 1285–1308 (2015)
18. Simonen, K., Merrifield, S., Almufti, I., Strobel, K., Tipler, J.: Integrating environmental impacts as another measure of earthquake performance for tall buildings in high seismic zones. Struct. Congress **2015**, 933–944 (2015)
19. Comber, M.V., Poland, C., Sinclair, M.: Environmental impact seismic assessment: application of performance-based earthquake engineering methodologies to optimize environmental performance. Struct. Congress **2012**, 910–921 (2012)
20. Porter, K.A., Beck, J.L., Shaikhutdinov, R.V.: Investigation of sensitivity of building loss estimates to major uncertain variables for the Van Nuys testbed. Pacific Earthq. Eng. Res. Center, Berkeley (2002)
21. FEMA: Seismic Performance Assessment of Buildings Volume 1-Methodology. Rep. No. FEMA P-58-1 (2018)
22. FEMA: Seismic Performance Assessment of Buildings Volume 2-Implementation Guide. Rep. No. FEMA P-58-2 (2018)
23. Kircher, C.A., Whitman, R.V., Holmes, W.T.: HAZUS earthquake loss estimation methods. Nat. Hazards Rev. **7**(2), 45–59 (2006)
24. Vitiello, U., Asprone, D., Di Ludovico, M., Prota, A.: Life-cycle cost optimization of the seismic retrofit of existing RC structures. Bull. Earthq. Eng. **15**(5), 2245–2271 (2017)
25. Negro, P., Mola, E.: A performance based approach for the seismic assessment and rehabilitation of existing RC buildings. Bull. Earthq. Eng. **15**(8), 3349–3364 (2017)
26. Welch, D., Sullivan, T., Calvi, G.: Developing direct displacement-based procedures for simplified loss assessment in performance-based earthquake engineering. J. Earthq. Eng. **18**(2), 290–322 (2014)
27. FEMA: Seismic Performance Assessment of Buildings Volume 4- Methodology for Assessing Environmental Impacts. Rep. No. FEMA P-58-4 (2018)
28. National Renewable Energy Laboratory: U.S. LCI, https://www.nrel.gov/lci/ (2012)
29. Swiss Centre for Life Cycle Inventories: Ecoinvent v3.6. https://www.ecoinvent.org/
30. Athena Sustainable Materials Institute: Impact estimator for buildings. http://www.athenasmi.org/
31. KT Innovations: Tally. https://choosetally.com/
32. PRé Consultants: SimaPro 9.0. https://simapro.com/
33. Thinkstep: GaBi v2.0. http://www.gabi-software.com/
34. Weber, C., Matthews, D., Venkatesh, A., Costello, C., Matthews, H.: The 2002 US benchmark version of the economic input-output life cycle assessment (EIO-LCA) model. Green Design Institute, Carnegie Mellon University. http://www.eiolca.net/ (2009)
35. Hammond, G.P., Jones, C.I.: Embodied energy and carbon in construction materials. Proc. Inst. Civil Eng. Energy **161**(2), 87–98 (2008)
36. Simonen, K., Huang, M., Aicher, C., Morris, P.: Embodied carbon as a proxy for the environmental impact of earthquake damage repair. Energy Build. **164**, 131–139 (2018)
37. Court, A., Simonen, K., Webster, M., Trusty, W., Morris, P.: Linking next-generation performance-based seismic design criteria to environmental performance (ATC-86 and ATC-58). Struct. Congress **2012**, 922–928 (2012)
38. FEMA: Seismic Performance Assessment of Buildings Volume 3- Supporting Electronic Materials. Rep. No. FEMA P-58-3 (2018)
39. Prota, A., Di Ludovico, M., Del Vecchio, C., Menna, C., Frascadore, R., Palladino, F., Di Sarno, L.: Caso studio: Scuola "G. Parozzani"—Scheda di sintesi interventi. Progetto DPC_ReLUIS 2019–2021 (WP5)
40. Seismosoft: SeismoStruct—A computer program for static and dynamic nonlinear analysis of framed structures, http://www.seismosoft.com (2020)
41. Mander, J.B., Priestley, M.J., Park, R.: Theoretical stress-strain model for confined concrete. J. Struct. Eng. **114**(8), 1804–1826 (1998)

42. Menegotto, M., Pinto, P. E.: Method of analysis for cyclic loaded R. C. plane frame including changes in geometry and non-elastic behaviour of elements under combined normal force and bending. In: Proceedings of IABSE Symposium on Resistance and Ultimate Deform ability of Structures Acted On by Well Defined Repeated Loads 11, pp. 15–22 (1973)
43. Cardone, D.: Fragility curves and loss functions for RC structural components with smooth rebars. Earthq. Struct. **10**(5), 1181–1212 (2016)
44. Cardone, D., Perrone, G.: Developing fragility curves and loss functions for masonry infill walls. Earthq. Struct. **9**(1), 257–279 (2015)

Behaviour and Characteristics of Construction Materials Subjected to Different Environmental Conditions

E. Menéndez, Y. Salem, E. Hernández Montes, M. C. Alonso, and L. M. Gil

Abstract Through this research it is intended to catalogue different environmental scenarios taking into account extreme climatic actions and what is their mechanical, chemical and physical impact on the main materials used in construction (reinforced concrete, bricks, lime repair mortars, etc.). For this, a qualification of these material deterioration processes will be carried out after having done the data collection, the analysis of the different scenarios and a structural study. To move towards sustainability, where building is better described as a process than a product, a new integrated-design approach that accounts for durability is deemed to be essential. This approach will allow building assessment in a multi-performance perspective. The Sustainable Structural Design (SSD) methodology is presented based on environmental and structural performance parameters in a life-cycle approach. The concept of reuse is a sustainable perspective for extremely durable structures (ESD), new structures and existing structures. In this work we will focused in different building materials characteristics and their potential degradation under extreme events conditions. This work is framed in a research project of the National Plan of Spain, whose purpose is the development of a decision support system based on intelligent management tools for the maintenance of existing buildings and the design of new buildings, in order to extend its working life to cope with climate change and extreme events.

Keywords Extreme climatic actions · Construction materials · Sustainable structural design · Durable structures

E. Menéndez · Y. Salem (✉) · M. C. Alonso
Institute Eduardo Torroja of Construction Science – CSIC, Madrid, Spain
e-mail: yasmin.salem@ietcc.csic.es

E. Hernández Montes · L. M. Gil
Universidad de Granada, Granada, Spain

E. B. Pereira et al. (eds.), *Proceedings of the 3rd RILEM Spring Convention and Conference (RSCC 2020)*, RILEM Bookseries 32,
https://doi.org/10.1007/978-3-030-76547-7_14

1 Introduction

Weather disasters due to climate change are a reality that happens in all seasons. Many of the meteorological phenomena that we considered unusual may become frequent or even vary in intensity. Temperatures will continue to rise in the coming years, which will cause an increase in heat waves and high-temperature days by the end of the century.

The Mediterranean basin is one of the world areas where it is estimated that changes in climatic conditions over the next decades may be more evident according to the study conducted by Jorge Olcina of the University of Alicante [1]. In this area, if climate change forecasts are met, extreme temperature and precipitation events will increase. It could rain less, but at times when it rains, there will be more intense or torrential rainfall.

In Europe, the main effects will probably be manifested in a change in the frequency of extreme events and precipitation, which will cause more droughts in some areas and more river floods in others, especially in the north of the continent.

It is very likely that in the Mediterranean there will be increasingly warm nights, that are called tropical, and whose minimum temperature is above 21 °C, something that has already happened in recent years.

On the other hand, researchers are divided on the amount of hurricanes that will occur in the future. However, in what the scientific community seems to coincide, it is in the fact that those that are formed could be of higher and therefore more destructive categories [2].

Acknowledged near-term climate change events were demonstrated to seriously affect pathologies of historical buildings and, particularly, degradation of materials of external façades [3]. The effect of climate change is acknowledged to be particularly exacerbated in the case of heritage buildings because these are typically low-performance buildings characterized by a weak and ancient structure, old construction techniques, and ineffective if not lacking HVAC systems [4].

Climate change can negatively act on heritage built environment in several ways [5–7]. Among the various material degradation mechanisms associated to climate change, excessive rainfalls play a major role in causing surface recessions of stone [8], as well as surface erosion and surface strength reduction [9]. Moisture content is a critical parameter affecting ageing and durability of fabric materials of historic buildings, with obvious consequences in terms of climate change related effects on heritage preservation [10].

Humidity is another significant driver of degradation phenomena, which can interact with air pollution in causing degradation of limestone in historical buildings [11, 12]. Climate change also affects the frequency of occurrence of freezing-thaw cycles [13] that produce mechanical stress on masonry surfaces, causing surface degradation.

The surface temperature profiles represent one of the key forces for material degradation, together with phenomena related to moisture. In fact, a degraded material results in a lower load capacity of the entire structure which, in general, becomes

more prone to failures under permanent loads such as dead loads or earthquakes. The general evaluation of the health conditions of historical masonry structures is the result of a complex evaluation process that requires multidisciplinary approaches [14]. The seismic vulnerability of historic masonry structures, and their reduction caused by material degradation, is a major concern in Mediterranean countries, where several earthquakes have caused significant damage to these types of buildings [15–20]. Several studies investigated harmful processes that affect historical structures, including advanced diagnostic and monitoring methods [21–23]. On the contrary, structural damage that affects masonry, typically in the form of cracks that pass through layers of mortar and stone or brick elements, results in locally less protected material that is more exposed to uncomfortable environmental conditions and, therefore, to degradation phenomena.

In this work, the effect of extreme events produced by climate change has been related to the most used construction materials, without taking into account the total structure, to be able to feed basic mathematical models and predict the behaviour of these materials individually.

2 Materials

This section defines the main materials used in construction, analysing both its characteristics and its durability over time.

2.1 Steel

Steel is a metal that is derived from the alloy between iron and carbon. It is characterized by its resistance and because it can be hot worked, that is only in a liquid state. Once it hardens, its handling is almost impossible. Depending on the temperature with which one works, the steel can contract, expand or melt. It is a very resistant material and at the same time it is easy to weld. They are high electrical conductors. Steel is recyclable and absolutely biodegradable.

Among its negative aspects is corrosion, since iron tends to oxidize easily when it is outdoors. It has endothermic properties, which causes those structures with steel parts, easily transmit heat and in the event of a fire, it will spread rapidly.

The main types of steel are divided into galvanized, stainless and calm [24].

Different types of steel can also be classified according to the alloy elements that produce different effects on the Steel.

On the one hand, there are carbon steels, which are more than 90% of steels and make up most of the construction structures. On the other hand are alloy steels that are subdivided into structural steels and tool steels. Structural steels contain higher amounts of manganese and other minerals than carbon steels, which improve their strength. They also contain sulphur, phosphorus, silica and vanadium to improve their

weldability and weather resistance. Among its advantages is the great resistance to tension and compression.

Despite the susceptibility to fire and weather, it is the most used structural material for its abundance, ease of assembly and cost.

The high strength of steel per unit weight allows relatively light structures, which is of great importance in the construction of bridges and tall buildings. Its properties do not change over time or vary with the location in the structural elements.

It is the material that is closest to a linearly elastic behaviour, until considerable loads are applied. It allows withstanding large deformations without failure, reaching high stresses. It has the ability to absorb large amounts of energy in deformation (elastic and inelastic) and to easily join with other members (in profiles it can be easily connected through rivets, screws or welding) 21–34.

The strength of the steel can decrease when it is subjected to a large number of load inversions or to frequent changes in the magnitude of tensile stresses (pulsating and alternative loads) [25].

The life of steel is very high. Some studies have estimated that a steel beam with minimal corrosion protection can exceed 60 years. This, if analysed as a material only by component, that is, not as isolated material but as part of a construction system [26].

Steel is the toughest of the commonly used structural materials. The design strength of most steel profiles is 340 MPa in both compression and traction, while in some special qualities they reach 480 MPa.

The fact that the compression and traction strength of structural steel is identical is a decisive factor in the ability of steel to respond to extreme events. In these cases there are unforeseen loads that are applied to the structure, but they are not only an increase in the loads considered in the calculation, but the structures undergo unexpected transitions that lead to their elements as they move from compression to traction. The steel's even ability to handle both traction and compression helps mitigate any failure. Additionally, the real strengths of structural steel exceed the design strengths, thus providing additional resistance to unforeseen extreme loads.

For a given stress (stretching force per unit area), strain is much smaller in steel than other construction materials, resulting in a higher Modulus of Elasticity and an enhanced capability for handling extreme loads without cracking or permanently deforming. Similarly, the ductility of a material such as structural steel allows for the redistribution of forces to provide an alternate load path or to accommodate displacements caused by extreme events. The Elasticity Module of steel is about 200,000 MPa [27].

2.2 Concrete

Depending on the variation of the proportions of the different components, the concrete has different properties. It is possible to differentiate, in this framework,

between light concrete (with a density of 1800 kg/m^3), normal concrete (density of about 2200 kg/m^3) and heavy concrete (density of more than 3200 kg/m^3).

Although it has a very good resistance to compressive stresses, concrete does not react in the same way to other kinds of stress (bending, traction, etc.). Therefore, it is often associated with steel structures, giving rise to the so-called reinforced concrete [28].

The useful or nominal life of a concrete structure according to Article 5 of Chapter I of the Structural Concrete Instruction are the following:

For temporary structures the nominal useful life is estimated between 3 and 10 years; for replaceable elements that are not part of the main structure (railings, pipe supports …) between 10 and 25 years; for agricultural or industrial buildings and maritime works, between 15 and 50 years; for residential or office buildings, bridges or passageways with a total length of less than 10 meters and a civil engineering structure (except maritime works) of low or medium economic impact, 50 years; for buildings of monumental character or of special importance, 100 years; for stands of total length equal to or greater than 10 meters and other civil engineering structures of high economic impact, 100 years.

Concrete being exposed to aggressive environments may have deterioration processes. These can be classified as: physical, caused by exposure to extreme environmental changes such as ice/thaw cycles or artificial changes such as exposure to fire; chemicals, caused by attacks by acids and/or sulphates, water, or alkali-arid reaction; Biological and structural (presence of bacteria, overloads, load cycles, etc.) [29, 30].

The agents that affect the durability of concrete are of various kinds, can be classified into two categories: external agents are those that are in the environment or are due to service conditions, among them are chloride ions, the carbon dioxide, sulphates, bacteria, abrasion and freezing and thawing cycles. Internal agents are found within the same concrete, such as chloride ions incorporated into certain additives and cement alkalis that react with potentially reactive aggregates.

They can be classified by their origin: physical, chemical, biological and mechanical agents. Physicists are due to changes in the environment (freeze-thaw, loads, etc.). Among the chemical agents include attacks by sulphates, acids, seawater and chlorides, the latter inducing the electrochemical corrosion of reinforcing steel.

The biological ones can be microorganisms, algae and mollusks. The mechanics are due to the conditions to which the concrete is exposed (for example, abrasion and erosion). Sometimes, these agents are presented simultaneously, so you can have interesting combinations. Obviously the effect of the damage is due to intrinsic and extrinsic issues of concrete, such as the quality of the concrete and the degree of the active agent to which it is exposed.

The importance of aggressive agents is a function of their environment, penetration speed and means of transport. Such aggressive agents may be gases, liquids or particles that are part of the soils adjacent to the concrete [31].

According with the Structural Concrete Instruction, depending on the type of exposure (non-aggressive, normal, marine or chlorides of non-marine origin, aggressive chemical, with frost and erosion), the minimum compressive strength of the

concrete, depending on whether it is mass concrete, reinforced concrete or prestressed concrete, ranges from 20 to 35 MPa. For the purposes of this instruction, the compressive strength of concrete refers to the results obtained at 28 days. The tensile strength of concrete is about 10% of the compressive strength, and the Modulus of elasticity, which depends on the compressive strength, varies approximately from 23,000 to 28,000 MPa [32].

2.3 Bricks

Brick is an artificial ceramic building component, made of baked clay. It is used for construction in various construction elements, such as walls, partitions, ovens, etc.

Scientists at the University of Illinois (in the United States) create a type of brick called "Smart skin" that monitors the response of the walls once the building is built. The method of use is quite simple: several intelligent bricks are placed, with the sensors, batteries and transmitters housed inside the brick, at strategic points of the building, between normal bricks, connected to a network where possible oscillations are monitored, temperature and movement in responses to external agents such as earthquakes or tornadoes [33].

It is expected that a brick house to last 100 years (or more), there are even buildings built entirely in brick blocks of more than 500 years [34].

Morton [35] proposes that for clay bricks the compressive strength ranges between 10 and 100 MPa, and for calcium silicate bricks between 10 and 45 MPa.

The tensile strength of the pieces of the factory work is related to the flexural strength and the dimensions of the test specimen. In any case, the tensile strength of the brick is very low, and this provides a low tensile strength of the brick-joint assembly. Van der Pluijm [36] found values that ranged from 1.5 to 3.5 MPa for clay bricks and calcium silicate respectively and the elasticity module is about 3000 MPa.

2.4 Lime Mortar

In the past, the only binder of mortars and concrete used in the building was lime, as it not only gave good mechanical strength, but also a certain deformability (lime mortars are less rigid than cement mortars). Most of the architectural heritage of Humanity that has come to this day was executed with lime mortars.

Lime mortar is a very favourable material in buildings due to its compatibility between materials, not chemical aggression against stone and structural ceramics, and in order to avoid excessive rigidity between and within the construction elements. In addition, these types of mortars have a good aging in the face of climatic aggressions, being only the chemical aggression and the mechanical actions of the ice or the crystallization of salts which can degrade their structure [37].

Other important characteristics of lime mortar are the following: Good plasticity and workability. Absence of retraction due to the constant speed in humid conditions. Great elasticity and adaptation to deformations. Avoid condensation. It does not cause efflorescence due to the absence of soluble salts. Good thermal and acoustic insulation. Good resistance to rainwater on exterior vertical walls. Disinfectant product Flame retardant product.

Moreover, not only lime mortars are durable, but also contribute to other materials being durable. This is the case of the protection of stone, ceramics and other materials with thin layers of lime mortar. If we focus on the case of stone, in the face of destructive actions it deteriorates. By applying a thin layer of lime micromortar it protects against atmospheric CO_2, against SO_2 and SO_3, against water and its effects, against destructive mechanical, solar and biological actions, reinforces and consolidates, embellishes and is a material tested by the time having guaranteed his good behaviour. The compressive strength of the lime mortar is about 7.5 MPa, and the tensile strength is about 1 MPa and its modulus of elasticity is approximately 3000 MPa [38].

3 Extreme Weather Events

3.1 Hurricane

Hurricanes originate in the ocean, in warm waters (minimum 26 ° C) and in the presence of high atmospheric humidity. The difference in weight between the masses of hot and cold air that the wind then sets in motion is pushed cyclically to each other forming a spiral (hot air inwards, cold air outwards) until generating a low-pressure centre that makes the circuit grow.

Hurricanes are classified according to their intensity as follows:

Lower intensity: Tropical depression
Medium Intensity: Tropical Storm
Higher intensity: Hurricane.

They are divided into several categories from 1 to 5 ranging from 119 km/h to 252 km/h [39, 42].

3.2 Flood

It is the effect generated by the flow of a current when it exceeds the conditions that are normal for it and reaches extraordinary levels that cannot be controlled in the natural or artificial vessels that contain it, which ordinarily derives the damages that it causes in urban areas, lands productive and in general in valleys and low sites [40].

The origin of the terrestrial floods is usually dual: or the overflow of river currents (rivers, streams, torrents, etc.); or the flooding of flat or endorheic areas due to accumulation of precipitation without circulating on the earth's surface, which is why they are also called "by precipitation in situ".

3.3 Fire

A fire constitutes a threat to life due to suffocation, poisoning and high temperatures, but if a building occurs the danger increases due to the structure of the building itself. In an outdoor enclosure, with fresh air, it is almost impossible to exceed 700 °C. In a closed enclosure, the temperature rises 30% more due to the reflection and radiation of the walls.

The critical ignition point (flashover point) is 273 °C, until now only the aluminum structure would be affected. From here the so-called equivalent or normalized fire is developed, which is what all regulations and fire resistance of materials refer to, measured in minutes. Above 40 min of equivalent fire we are already talking about a very important fire with a true risk to human life.

To have a reference of how high temperatures affect materials, we will say that at 400 °C, the steel becomes ductile and at 600 °C, there is a sharp drop in its resistance [41].

3.4 Earthquake

It is defined as sudden and temporary shocks of the earth's crust due to the release of energy in the subsoil in the form of seismic waves, as a result of geological movements and displacements of the tectonic plates that make up the upper layers of the planet. An intense and prolonged earthquake can tear down buildings, shake the streets and tear them apart, and cause objects to collapse on us.

Types of earthquakes: tectonic, volcanic and collapse.

Earthquakes are measured based on a double scale, which records intensity on the one hand and magnitude on the other. These scales are:

Intensity: They measure the strength of the tremor based on the ravages caused. There are the Mercalli scale (12 points); the Medvédev-Sponheuer-Kárnik (12 points) and the Shindo scale (7 points).

Of magnitude: They measure the amount of tremor energy based on their reverberations. There are the Richter scale (7 points) and the seismological scale of magnitude of the moment [39, 42].

4 Evolutionary Relationship Over Time

There are different factors and parameters of both the extreme actions and the construction materials that must be taken into account in order to estimate the useful life of a building or even foresee its behaviour in the event of an extreme weather event. Knowing these parameters can also help design more resistant and durable structures.

As for the extreme action of a **strong wind or hurricane**, the location of a building, as well as the presence of other smaller buildings, should be taken into account, since they can contribute to accelerate the wind speed and cause turbulence that affects both the front section (windward walls) as the rear section of the building (leeward walls), with the consequent considerable increase in the basic wind pressure. Other factors, such as openings in the lower part of buildings, lead to an unusual increase in wind speed and turbulence in the rear of the building. The same goes for the gable roof buildings where the wind causes turbulence on the leeward roofs and on the side and rear walls. The pressure exerted by the wind on the structural system is a function of the dynamic part of Bernoulli's equation, known as basic pressure, which is modified by several factors:

- The roughness of the terrain affects wind speed and turbulence. The more irregular the surface, the lower the speed, but the greater the turbulence.
- The size and density of objects found on the surface, such as buildings and trees, affect the roughness of the terrain.
- The length of the roughness of the terrain indicates the magnitude of its influence on wind speed and longitudinal turbulence: the steeper the terrain, the greater the roughness and, consequently, the greater the friction effect that decreases the speed of the wind.

As the height increases, the wind speed also increases until it reaches a constant speed, called gradual velocity that is independent of the irregularity of the terrain. This variation in wind speed as a function of height can be predicted mathematically with a logarithmic equation. However, in practice a simpler model, the method of exponential law, is used to extrapolate the wind speed from one height to another.

The basic pressure accuses the effect of uncertainty due to the likelihood of wind hitting the structure from any direction. When determining the design pressure, this parameter, known as wind directionality, must be taken into account. Wind speed is the most important factor in determining the basic pressure.

The movement of the wind is turbulent and it is difficult to give a concise mathematical definition of turbulence. However, it is known that there is wind turbulence due to the low viscosity of the air compared to that of water. Any movement of air greater than 4 km/h is turbulent, that is to say that the air particles move erratically in all directions.

For structural engineering purposes, the wind speed can be considered to have two components: the average speed (whose value increases with height) and turbulence fluctuations.

The basic pressure, modified by the parameters indicated above, is known as the modified basic pressure, in accordance with ASCE-7 [43], which will vary according to the conditions of each region [44].

In this case study in which an isolated material is analyzed, it should be taken into account that a strong wind or hurricane will generate in this material a significant erosion due to the particles dragged at high speeds and within a turbulent flow. In turn, air and particles will exert a differential force at different points on the surface and in bursts of varying intensity and direction. In this case, the material with the greatest resistance to compressive stress is steel, followed by concrete, bricks and lime mortar, which have a very poor tensile and compressive strength.

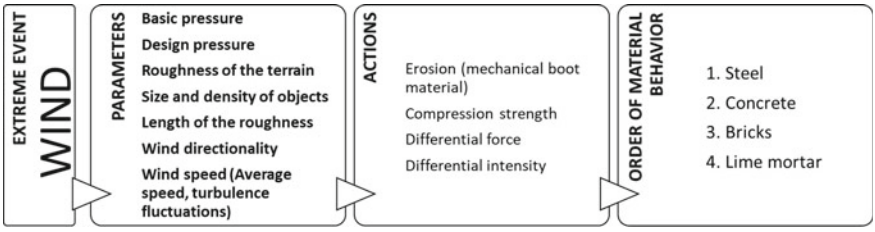

As for **earthquakes**, the horizontal component of seismic action (in some ways similar to that of wind) is much more important than vertical, be it the masonry, brick, concrete or steel structure. Although horizontal accelerations near gravity have been recorded in some large earthquakes, smaller movements can cause very serious damage to the vertical elements of the buildings (pillars, columns, walls, …), which are what more influence their stability, so a failure in them can cause the building to collapse.

If the elastic regime of some material is exceeded, it may deform without tending to recover its shape (plastic regime) or if it responds fragilely, break. From this point of view, the safest construction materials are elastic and coherent.

If the frequency of the seismic wave and the frequency of oscillation of the building coincide, the phenomenon of resonance occurs. This will probably cause the building to collapse.

The width of the streets can be a critical factor in favouring damage. In narrow streets, the fall of houses can affect the adjacent ones as if it were a house of cards. From a civil protection point of view, these types of streets can be collapsed, making access to aid and supplies very difficult.

The type of soil on which the buildings settle, their relief, the slope of the land, the surface and deep geology and in general the characteristics of the last tens of meters have a significant influence on the perception of the seismic movement and can be decisive in the damage caused. Soft soils amplify the movement; so many times the damage caused by an earthquake is not due to the poor quality of the construction, but to the low solidity of the soil.

Modern standards take into account in the structural design the concept of ductility or ability to deform a resistant element without breaking. In order to avoid human

losses, a building is designed so that before a major earthquake a certain element of the structure can be deformed (beam, support, knot, …) that, even if it makes it unusable for its use and had to be demolished later, however, do not collapse.

Regarding the distribution of masses in the building, care must be taken that they are arranged as uniformly as possible along the height. The rigidity must also be distributed gradually in height, and for the same plant, uniformity and symmetry are necessary. No structural element should change abruptly of rigidity, so, if diaphanous plants are placed together with other very compartmentalized plants, the difference of this characteristic should be taken into account. In general, elements of great rigidity should be placed on the outer perimeter of the plant and that general evacuation routes, such as stairs, will be provided with additional resistance and ductility to facilitate their use in case of an earthquake [45].

The most important parameters in an earthquake come from the seismic waves. These waves are classified as internal waves when they propagate through the interior of the earth, and superficial when the seismic energy polarizes and travels near the earth's surface. In turn, and depending on the type of elastic movement suffered by the particles in the environment, the internal waves are classified into two types: Primary (P) or compression and Secondary (S) or shear. With regard to surface waves, they are also classified into two other subtypes: Raleygh Waves (L_R) and Love Waves (L_Q) (Fig. 1).

Each type of wave travels at a different speed, called phase velocity, and depends fundamentally on the density of the material and its elastic modules (relationship between stress and strain suffered by the material). In general, and for internal waves the elastic modules that control the propagation speed are the compressibility (K) and the stiffness (μ). The compressibility module (K) measures the change in volume that a material undergoes when subjected to a hydrostatic stress (compressive and equal

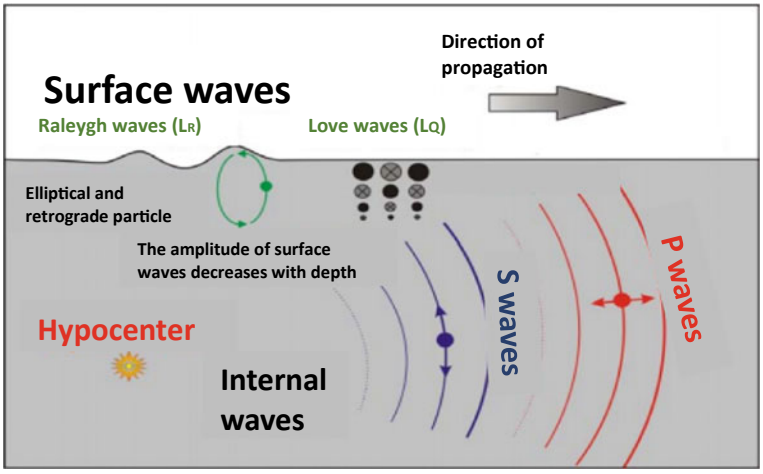

Fig. 1 Type of waves during an earthquake [46]

in all directions, P) and the stiffness (μ) measures the deformation that a material experiences when undergoes a tangential or shear effort [46].

The material that will best behave in this weather event will be the one with the greatest modulus of elasticity. In addition, the structures will be subjected to tensile and compressive stresses, so that the ideal material is steel, followed by concrete, lime mortar and bricks (these last two materials will be very similar).

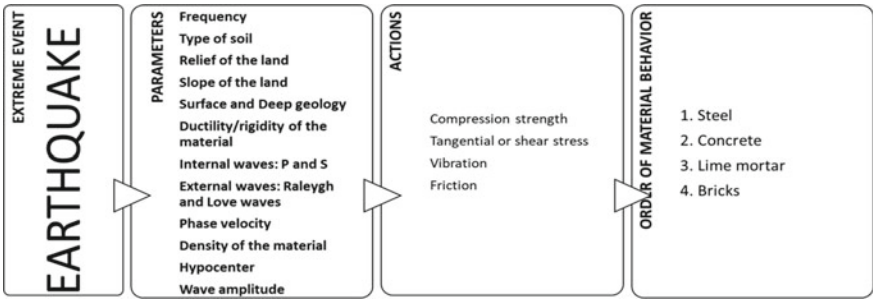

The first and most consubstantial **flood** damage is the waterlogging itself and its depth in normally dry areas, which entails soil wetting, with the consequent loss of bearing capacity of the land, and of the structures and buildings built on them, may affect its foundation and structural stability.

It is also important to consider the residence time of the water sheet, since prolonged exposures or waterlogging can aggravate these effects, breaking up the foundations, generating corrosion in the steel after a long period in contact with the water or generating chemical reactions in the concrete or when entering the pores of the bricks; while rapid drying can reduce damage significantly, since it also minimizes the deposit of materials in the bed. An effect of the flood that is likely to cause damage is the speed of the current, which can sometimes, by direct or indirect impact (undermining), tear down and drag material. Especially dangerous are the sudden changes in speed, such as those that occur in hydraulic ridges (regime changes in waterfalls and narrowings), in which the release of energy is enormous. During the floods, especially in torrential avenues, speeds can exceed even 4–6 m/s, values with which bulky and heavy objects are dragged, and even swirling and dangerous phenomena of air suction due to Venturi effect are created and Cavitation overpressures.

The force of the current can erode the bottom and the margins of the river, producing infrastructure undermining and instability of slopes, which triggers material movements (landslides, flows …). The solid charge carried by the water, whether suspended in the fluid, or as a bottom load (by jumping, rolling or dragging), can cause impact damage and abrasion to the buildings. These detritic materials (blocks, edges, gravels, sand, silt and clays) produce different hydraulic effects in the stream, such as increasing their density and viscosity (increasing their erosion capacity and transport of more materials, in a feedback effect) and decrease its speed, with the consequent increase in the height of the water sheet. In extreme cases, the high solid load can convert the current into an authentic mud river (mud flow) or debris (debris

flow), with high danger. In the same way, the transport of floating elements (such as plant fragments, hail or ice) makes it difficult to flow and pass through narrowings (bridges or sewer systems), prompting their collapse and breakage [47].

According to these parameters, the structures will be affected by strong differential hydraulic pressures and the dragging of sediments and materials will create erosion and tearing. In addition, exposure to water of certain building materials for long periods will generate chemical attack causing, for example, corrosion in the steel or arid-alkali reaction in the concrete. The material that best resists chemical attack in general, in addition to correctly supporting the effects of the weather, is lime mortar, which also has a very good plasticity and workability.

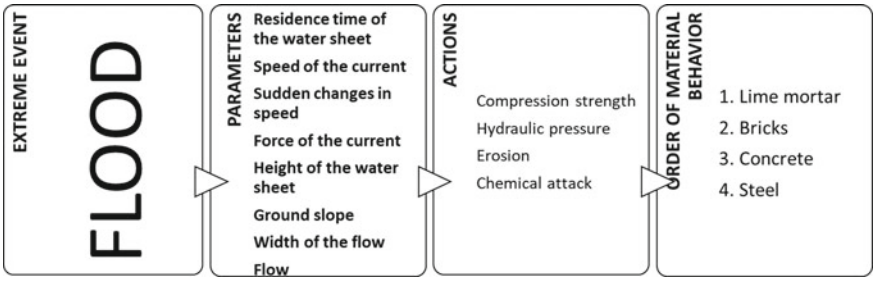

As for the extreme action of a **fire**, concrete loses less capacity at high temperatures than steel. In the case of prestressed steel, much more is accused: when the concrete suffers losses of 35%, we would be talking about the fact that prestressed steel loses 60–70% of its capacity. Normal concrete loose about 56% of their compressive strength after being exposed to 600 °C temperature in 150 min duration.

Concrete is very effective against fire due to its mineralogical composition, porous structure and low conductivity. Practically it will not be affected at temperatures below 300°, from them a strong loss of resistance begins that no longer recovers after the fire. Between 600 and 950 °C, the aggregates expand and the disintegration of the material arises and there is a loss of resistance between 60 and 90%.

When concrete is exposed to fire, the evaluations are more complex. In addition to the variables specific to each fire (fuel load, aeration, etc.), the variation in concrete results may be due to a series of intrinsic factors such as density, porosity, type of aggregate and vibration method during the execution.

At 400 °C steel becomes ductile and with levels close to 600 °C, so that the steel loses more than half of its resistance and reduces its elastic period producing permanent deformations. On the other hand, the high conductivity of steel, 42 W/m °C, causes it to transmit heat quickly to the rest of the structure.

As the bricks are manufactured in a fire oven, they are highly resistant to it. However, it is true that individual bricks are much more fire resistant than a brick wall. Depending on the construction and thickness of the wall, a brick wall can achieve a fire resistance rating of 1 to 4 h. The firing temperature of the clay bricks ranges between 800 and 1300 °C, depending on whether they are refractory, so that this material withstands the high temperatures quite well [48].

Lime mortar is classified as A1 of the European fire reaction classification system according to UNE-EN 13501-1 [49]. Products with this classification are expected to offer good fire behaviour.

Basically, the main effects of fire on reinforced concrete could be summarized as:

Adhesion damage: the existence of coke or weakening in the concrete section, allows high temperatures to pass through it and reach reinforcements very quickly. Steel is a good conductor, so the entire steel bar is heated but not the concrete. Steel tends to expand and concrete does not. This produces compressions and cracks. Then cooling and breakage occurs. The adhesion is damaged precisely by that thermal jump.

Effect of detachment: This process takes place quickly, at 100–150 °C, as a result of the thermal impact and the change of state of the interstitial water. As water becomes steam and due to the dense structure of concrete, steam cannot escape efficiently through its matrix and the pressure increases. When the pressure in the concrete is greater than its resistance, the detachment process begins. Inside a building, the part of the structure most exposed to fire and the most sensitive is the underside of the slabs. Here the tensions are of traction and fundamentally supported by the steel reinforcements. So if these are affected by high temperatures, the decrease in resistance results in the transmission of stress to concrete, already internally overstressed. It results in the fragile and sharp breakage of the concrete and the collapse of the slab due to the breakage at negative moments of the assembly [50].

Lime mortar, as an insulated material, has an excellent behaviour against fire, followed by brick, which withstands very high temperatures. The concrete has a medium behaviour and the steel has a bad behaviour in the face of high temperatures, although these last two joined materials (reinforced concrete) behave very well structurally against fire. As in this case each material is studied separately, in the following scheme the order of best to worst behaviour of each material can be observed.

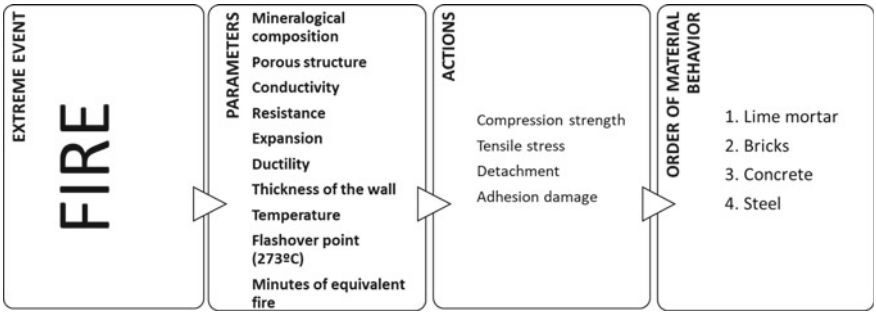

5 Conclusions

Climate change will produce extreme events more frequently in the future, so in this article each weather event has been related to the behaviour of different building materials, analysed individually.

Steel is the material that best reacts to earthquakes and strong winds due to its linearly elastic behaviour, with high tensile and compressive strength, which in both cases is the same. Faced with a long-term flood, it can generate corrosion in the material due to chemical reactions and its behaviour in the event of a fire is very bad due to its very high conductivity. Instead, it is suitable against hurricane winds and earthquakes.

The concrete has a good compressive strength and low tensile strength; it has an intermediate elastic modulus, which means that it is not a very rigid or very elastic material. This material behaves correctly in all adverse scenarios, although there are other much better materials against flooding and fire.

The bricks have a normal compressive strength, very similar to that of concrete, but with a much smaller elastic modulus. For this reason, bricks react well to the chemical attack and will correctly resist a flood or avenue. Due to its high cooking temperature, it is also a good fire resistant material.

Finally, the lime mortar, although usually used as a coating or joint bonding material, analysed exclusively as an independent material, has very low tensile and compressive strength and a modulus of elasticity similar to bricks. It behaves very well outdoors so it will resist the effects of floods and fires very well, giving worse results in earthquakes and hurricane winds.

Acknowledgements This project has been funded by the Spanish State Plan Project with reference RTI2018-101841-B-C22 entitled “Development of a decision support system based on intelligent management tools for the maintenance of existing buildings and the design of new buildings, in order to extend its working life to cope with climate change and extreme events. TAQ-I KISRA vision”, as well as the Research Project with reference 201660E054 entitled “Synthesis and evaluation of circadian materials for application in technical construction systems”.

References

1. Olcina, J.: Clima, cambio climático y riesgos climáticos en el litoral mediterráneo. Oportunidades para la geografía. Climate, climate change and climate risks in the Mediterranean litoral: Opportunities for geography. Universitat Autònoma de Barcelona. Departament de Geografia, Universidad de Alicante. Departamento de Análisis Geográfico Regional y Geografía Física (2020)
2. Gómez, M.: In the future there will be more extreme weather events. National Geographic Spain [online] (2020). https://www.nationalgeographic.com.es/. Accessed Jan 2020
3. Phillipson, M.C., Emmanuel, R., Baker, P.H.: The durability of building materials under a changing climate. WIREs Clim. Change **7**, 590–599 (2016)
4. Dalla Mora, T., Cappelletti, F., Peron, F., Romagnoni, P., Bauman, F.: Retrofit of an historical building toward NZEB. Energy Procedia **78**, 1359–1364 (2015)

5. Johns, J., Fedeski, M.: Adapting building construction to the effects of climate change. In: India, M.B., Bonillo, D.L. (eds.) Detecting and Modelling Regional Climate Change. Springer, Berlin Heidelberg Publisher, pp. 605–616 (2001)
6. Perez-Lombard, L., Ortiz, J., Pout, G.: A review on buildings energy consumption information. Energy Build. **40**, 394–398 (2008)
7. Rosso, F., Golasi, I., Castaldo, V.L., Piselli, C., Pisello, A.L., Salata, F., Ferrero, M., Cotana, F., de Lieto Vollaro, A.: On the impact of innovative materials on outdoor thermal comfort of pedestrians in historical urban canyons. Renew. Energy **118**, 825–839 (2018)
8. Bonazza, A., Messina, P., Sabbioni, C., Grossi, C.M., Brimblecombe, P.: Mapping the impact of climate change on surface recession of carbonate buildings in Europe. Sci. Total Environ. **407**(6), 2039–2050 (2009)
9. Erkal, A., D'Ayala, D., Sequeira, L.: Assessment of wind-driven rain impact, related surface erosion and surface strength reduction of historic building materials. Build. Environ. **57**, 336–348 (2012)
10. D'Ayala, D., Aktas, Y.D.: Moisture dynamics in the masonry fabric of historic buildings subjected to wind-driven rain and flooding. Build. Environ. **10**, 208–220 (2016)
11. Corvo, F., Reyes, J., Valdes, C., Villaseñor, F., Cuesta, O., Aguilar, D., Quintana, P.: Influence of air pollution and humidity on limestone materials degradation in historical buildings located in cities under tropical coastal climates. Water Air Soil Pollut. **205**, 359–375 (2010)
12. Cellura, M., Guarino, F., Longo, S., Tumminia, G.: Climate change and the building sector: modelling and energy implications to an office building in southern Europe. Energy Sust. Dev. **45**, 46–65 (2018)
13. Grossi, C.M., Brimblecombe, P., Harris, I.: Predicting long term freeze–thaw risks on Europe built heritage and archaeological sites in a changing climate. Sci. Total Environ. **377**, 273–281 (2007)
14. Masciotta, M.G., Roque, J.C.A., Ramos, L.F., Lourenço, P.B.: A multidisciplinary approach to assess the health state of heritage structures: the case study of the Church of Monastery of Jerónimos in Lisbon. Construct. Build. Mater. **116**, 169–187 (2016)
15. Berto, L., Doria, A., Faccio, P., Saetta, A., Talledo, D.: Vulnerability analysis of built cultural heritage: a multidisciplinary approach for studying the palladio's tempietto barbaro. Int. J. Architect. Herit. **11**(6), 773–790 (2017)
16. Betti, M., Orlando, M., Vignoli, A.: Static behaviour of an Italian Medieval Castle: damage assessment by numerical modelling. Comput. Struct. **89**(21–22), 1956–1970 (2011)
17. Ramaglia, G., Lignola, G.P., Prota, A.: Collapse analysis of slender masonry barrel vaults. Eng. Struct. **117**, 86–100 (2016)
18. Valente, M., Milani, G.: Seismic assessment of historical masonry towers by means of simplified approaches and standard (FEM). Construct. Build. Mater. **108**, 74–104 (2016)
19. Clementi, F., Pierdicca, A., Formisano, A., Catinari, F., Lenci, S.: Numerical model upgrading of a historical masonry building damaged during the 2016 Italian earthquakes: the case study of the Podestà palace in Montelupone (Italy). J. Civil Struct. Health Monitor. **7**(5), 703–717 (2017)
20. Clementi, F., Gazzani, V., Poiani, M., Mezzapelle, P.A., Lenci, S.: Seismic assessment of a monumental building through nonlinear analysis of a 3D solid model. J. Earthquake Eng. **22**(Sup1), 35–61 (2018)
21. Saisi, A., Gentile, C., Guidobaldi, M.: Post-earthquake continuous dynamic monitoring of the Gabbia Tower in Mantua, Italy. Constr. Build. Mater. **81**, 101–112 (2015)
22. Gentile, C., Guidobaldi, M., Saisi, A.: One-year dynamic monitoring of a historic tower: damage detection under changing environment. Meccanica **51**, 2873–2889 (2016)
23. Masciotta, M.G., Ramos, L.F., Lourenço, P.B.: The importance of structural monitoring as a diagnosis and control tool in the restoration process of heritage structures: a case study in Portugal. J. Cult. Herit. **27**, 36–47 (2017)
24. Concepto definición, Redacción: Definición de Acero "Definition of Steel" [online] (2019). https://conceptodefinicion.de/acero/. Accessed Nov 2019

25. Estudiantes metalografía: Diagrama hierro-Carbono, Universidad Tecnológica de Pereira [online] (2013). Disponible en http://blog.utp.edu.co/metalografia/5-diagrama-hierro-carbono/. noviembre 2019
26. Hernández, S.: Impacto Ambiental y Vida Útil de los Materiales más Comunes en la Industria de la Construcción [Environmental impact and useful life of the most common materials in the construction industry] (2008)
27. AISC, American Institute of Steel Construction: The Impact of Material Selection on Resilience of Buildings (2017)
28. Secretaría General Técnica: EHE Instrucción de hormigón Estructural, Capítulo 1, artículo 5: Requisitos. Ministerio de Fomento, Madrid (2008)
29. Mehta, P.K., Monteiro, P.J.M.: Concrete Microstructure, Properties, and Materials. McGraw Hill, New York (2006)
30. Bertolini, L., Elsener, B., Pedeferri, P., Polder, R.: Corrosion of Steel in Concrete. Wiley-VCH Verlag GmbH & Co, Weinheim (2004)
31. Hernández–Castañeda, O., Mendoza–Escobedo, C.J.: Durabilidad e infraestructura: retos e impacto socioeconómico. Ingeniería, Investigación y Tecnología [Durability and infrastructure: challenges and socio-economic impact. Eng. Res. Technol.] **7**(1) (2005) (México)
32. EHE-08, Instrucción de Hormigón Estructural, Real Decreto 1247/2008, Ministerio de la Presidencia, España
33. Kloeppel, J.: Smart bricks could monitor buildings, save lifes. Electrical and computer engineering [online] (2003). https://ece.illinois.edu/newsroom/article/168. Accessed Jan 2020
34. Rico, F.: Presidente de la Cámara Industrial Cerámica Roja, 2017. El ladrillo y su vida útil. The brick and its useful life, La Nación (2017)
35. Morton, T.: Earth Masonry Design and Construction Guidelines. Construction Research, Communications Limited, Berkshire (2008)
36. Van der Pluijm, R.: Non-linear behaviour of masonry under tension. Build. Construct. Res. **42**(1) (1997). ISSN 0046-7316
37. Institut de promoció cerámica, IPC: Guía de colocación de mortero de cal, Lime Mortar Placement Guide (n.p.)
38. Robador González, M.D.: Sostenibilidad de la luminosa cal en la arquitectura, Sustainability of the luminous lime in the architecture. Departamento de construcciones arquitectónicas (2015)
39. Uriarte, J.M.: Huracán, Hurricane [online] (2019). https://www.caracteristicas.co/huracan/. Accessed Nov 2019
40. Ministerio de Educación Superior: Glosario de términos que deben dominarse en la disciplina. Preparación para la Defensa, Glossary of terms that must be mastered in the discipline. Defense Preparation, Departamento de Enseñanza Militar [online] (2003). http://recursos.unica.cu/bibliografia/F.%20CulturaFisica/Preparacion%20para%20la%20defensa%20de%20la%20Facultad/materiales%20complementarios/nuevo%20glosariodoc(f).doc. Accessed Dec 2019
41. CEPREVEN: Curso Monográfico "Protección pasiva contra incendios", Monographic Course "Passive fire protection", Asociación de Investigación para la Seguridad de Vidas y Bienes. Madrid (2003)
42. Uriarte, J.M.: Huracán Patricia, Hurricane Patricia [online] (2019). https://www.caracteristicas.co/sismos/. Accessed Jan 2019
43. SEI/ASCE 7-05: Minimum Design Loads for Buildings and Other Structures
44. Comarazamy, D., Gibbs, T., Compañy, C., Vermeiren, J., Comarazamy, A., Sánchez, F.: Mitigación de Desastres en Instalaciones de Salud. Efectos del viento. Aspectos no estructurales, Disaster Mitigation in Health Facilities. Wind effects. Non-structural aspects. Organización Panamericana de la Salud (2005)
45. Estudio arquivolta: Terremotos ¿Cómo afecta el sismo a los edificios? How does the earthquake affect buildings? [online] (2016). https://estudioarquivolta.wordpress.com/2016/04/20/terremotos-como-afecta-el-sismo-a-los-edificios/. Accessed Nov 2019
46. Muñoz-Martín, A., de Vicente, G.: Análisis de esfuerzos tectónicos fallas y sismos, Analysis of tectonic stresses failures and earthquakes, Reduca (Geología). Serie Tectónica. **2**(6), 1–91. Universidad Complutense de Madrid UCM (2010)

47. Díez Herrero, A., Laín Huerta, L., Llorente Isidro, M.: Mapas de peligrosidad por avenidas e inundaciones, Hazard maps for floods and floods. Guía metodológica para su elaboración, Instituto Geológico y Minero de España IGME (2008)
48. McGrath, J.: Top 5 fire-resistant building materials [online] (2012). https://home.howstuffworks.com/home-improvement/construction/materials/5-fire-resistant-building-materials.htm. Accessed Jan 2020
49. UNE-EN 13501-1:2019, Clasificación en función del comportamiento frente al fuego de los productos de construcción y elementos para la edificación, Parte 1: Clasificación a partir de datos obtenidos en ensayos de reacción al fuego, Classification according to the fire behavior of construction products and building elements, Part 1: Classification from data obtained in reaction to fire test (2019)
50. Asefa: Efectos de incendios en estructuras de hormigón armado, Effects of fires on reinforced concrete structures [online] (2011). https://www.asefa.es/comunicacion/patologias/efectos-de-incendios-en-estructuras-de-hormigon-armado. Accessed Dec 2019

Green Cementitious Composites Made with PCM-Recycled Brick Aggregates: Thermal Energy Storage Characterization and Modelling

Christoph Mankel, Antonio Caggiano, Andreas Koenig, Diego Said Schicchi, Mona Nazari Sam, and Eddie Koenders

Abstract This work reports the results of an extensive experimental campaign aimed at investigating the Thermal Energy Storage (TES) behavior of PCM Recycled Brick Aggregate (RBA) mortars. Test specimens for TES measurements were produced following a new spherical-shaped technique, patented as "DKK test" by the Institute of Construction and Building Materials of TU-Darmstadt. DKK was used for characterizing the various test samples made of plain cement paste plus porous RBAs, these latter filled with paraffinic PCM waxes. Dynamic DSC tests and conductivity measurements were also done for thermally investigating both components and composites. Moreover, the study proposes a novel numerical approach for determining the energy storage capacity of the investigated systems, setting the experimental benchmarks for validation. Particularly, the experimental results have been finally employed for calibrating an enthalpy-based model, at both macro- and meso-scale level, to evaluate the temperature-based thermal parameters like specific heat, conductivity, or more in a general sense, the energy storage capacity of these systems under transient heat conduction conditions. The results show very promising possibilities for using RBAs as carriers in green concrete applications.

C. Mankel · A. Caggiano (✉) · D. Said Schicchi · M. N. Sam · E. Koenders
Institute of Construction and Building Materials, TU-Darmstadt, Darmstadt, Germany
e-mail: caggiano@wib.tu-darmstadt.de

C. Mankel
e-mail: mankel@wib.tu-darmstadt.de

M. N. Sam
e-mail: sam@wib.tu-darmstadt.de

E. Koenders
e-mail: koenders@wib.tu-darmstadt.de

A. Caggiano
Universidad de Buenos Aires, LMNI, INTECIN, CONICET, Buenos Aires, Argentina

A. Koenig
Department of Prosthodontics and Dental Materials Science, Leipzig University, Leipzig, Germany
e-mail: akoenig@uni-leipzig.de

E. B. Pereira et al. (eds.), *Proceedings of the 3rd RILEM Spring Convention and Conference (RSCC 2020)*, RILEM Bookseries 32,
https://doi.org/10.1007/978-3-030-76547-7_15

Keywords Recycled brick aggregates · Paraffin-based PCMs · Thermal energy storage · Enthalpy-based method · Meso-scale simulations

1 Introduction

The energy demand for heating and cooling the global building represents a huge share of the total energy consumption around the world (ca. 40%) [1]. It accounts for almost half its energy consumption in Europe [2]. To attenuate this number, improving the thermal efficiency of construction and building elements became one of the most important issues for energy savings of new and existing buildings [3].

Innovative solutions in this regard could include the potential of materials to store and release large amounts of thermal energy, which would be used to stabilize the inner thermal comfort of either residential or non-residential buildings. This can be achieved through an optimal use of Phase Change Materials (PCMs), which can help to minimize the additional need of primary energy for heating/cooling [4, 5]. Numerous studies on PCMs and in several fields of applications have been reported in literature. The experimental-based research on these deals with addressing the thermo-hydro-chemo-mechanical properties of cementitious materials with PCMs [6–8], where the investigated PCMs are characterized by melting temperatures that vary between 19 and 26 °C. This range corresponds to a standard temperature window for comfortable living [9].

On the other hand, numerical and/or theoretical approaches, available in scientific literature for modelling Thermal Energy Storage (TES) and heat accumulation/liberation of PCM-based applications, arose from the solution of the so-called Stefan problem [10]. Several authors, under simplified assumptions (i.e., 1D heat conduction), proposed analytical solutions [11]. Nonetheless, more complex models are needed for further evaluation of the classical Stefan problem: e.g., by introducing "mushy" zones for non-isothermal phase change conditions, 2D and 3D evaluations, etc. [12].

The solution methods of the Stefan problem and/or its extended formulations, can generally be subdivided into three different categories [13]: (i) Fixed grid method; (ii) Deformed grid method; and (iii) Hybrid methods. Most classical examples are those based on a further development of the fixed grid method, where the grid of spatial nodes, used for discretizing the problem, remains fixed during time, and the phase change is traced through auxiliary formulations and/or state functions. Particularly, the Enthalpy-based Approach (EA) [14], which mainly boils down into two alternative solutions (the Apparent Calorific Capacity Method (ACCM) [15] and (ii) the Heat Source Method (HSM) [16]), is the common way to solve the set of equations of the fixed grid method.

In this context, the present study investigates the TES of mortars made of RBAs containing PCMs. The results of an extensive experimental research are firstly presented for showing the TES performance of the various composites. Test data of a wide series of thermal tests [17] (in terms of Differential Scanning Calorimetry

(DSC) measurements, thermal conductivity and DKK tests [18]), carried out on PCM, aggregates, plain mortars and PCM-RBA mortars are shortly summarized. Then, a numerical procedure for simulating the effects of paraffin waxes on the thermal energy responses of these mortars produced with different amounts of PCM-RBAs is outlined.

2 Experimental Campaign

An experimental program was performed to characterize the TES response of PCM-RBA mortar mixtures and their components.

2.1 Components and Composites

Paraffin waxes [19], characterized by a high crystallinity and possess an excellent heat store capacity during the phase changes, were used as PCM (Fig. 1a). They have a melting temperature of 25 °C, a storage capacity of 230 kJ/kg approx., a latent heat capacity of almost 200 kJ/kg, a thermal conductivity of 0.20 W/(m K) and densities of 880 kg/m^3 and 770 kg/m^3 in liquid and solid states, respectively.

Six mixtures were prepared following an advanced technique, proposed and patented by the *Institut für Werkstoffe im Bauwesen* of TU-Darmstadt [20], having a w/c ratio of 0.5 and various amounts of PCM-RBA volume fractions (Table 1).

Fig. 1 **a** PCMs, **b** SB- and **c** PB-RBAs with grain groups 0.5–1 mm, 1–2 mm and 2–4 mm

Table 1 The investigated PCM-RBA mortars

Labels	REF-SB	SB-65	SB-80	REF-PB	PB-65	PB-80
Cement (kg/m^3)	701.5	694.2	692.9	700.2	691.7	691.7
Water (kg/m^3)	350.8	347.1	346.5	350.1	345.9	345.9
PCM-RBA (kg/m^3)	655.2	719.3	734.0	664.0	728.9	743.9
Air cont. (Vol%)	2.3	2.9	3.0	2.4	3.1	3.1
w/c ratio (–)	0.50					

All mixtures were prepared according to EN 196-1 [21]. Recycled bricks (labelled "SB", Fig. 1b) and High porosity Poroton® fired-clay blocks (labelled "PB", Fig. 1c) have been considered [22] as medium/coarse aggregates, and used as containers for storing predefined volume of PCM.

The complete description (materials, methods, results and discussion) of the experimental campaign is available in Mankel et al. [22].

2.2 DSC, Conductivity and DKK Tests

DSC tests, as shown in Fig. 2a, were done for each component of the investigated PCM-RBA mortar mixtures: i.e., surrounding cement paste, SB-, PB-RBAs and PCMs. Three samples per each component were analyzed under either heating or cooling, within the temperature range of 10–40 °C. A heating/cooling rate of 10 K $\times$ min^{-1} was employed for pastes and RBAs while the test procedure, conducted in accordance with the IEA DSC 4229 PCM Standard [23], was followed to determine the final heating/cooling rate for the considered PCMs which it was 0.25 K $\times$ min^{-1} on the final results.

The thermal conductivity of PCM-RBA mortar mixtures was then determined using the Hot-Disk transient plane source method (Fig. 2b). For this purpose, three samples of 150 mm $\times$ 150 mm $\times$ 80 mm cuboids were casted and investigated. Steady-state conditions with a temperature of 20 °C were considered.

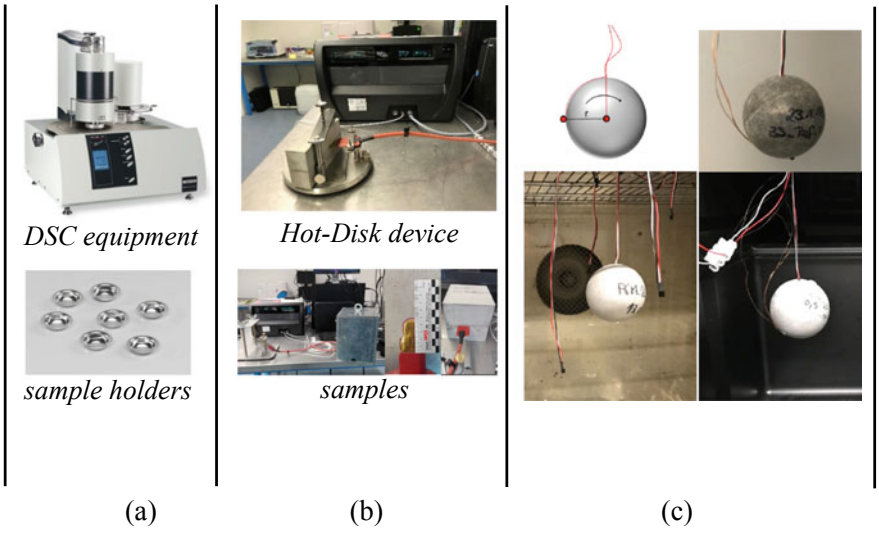

Fig. 2 **a** DSC tests (heat storage capacities of components), **b** hot-disk (conductivity of the composites) and **c** DKK tests (TES of the composites)

Finally, novel spherical-shaped specimens (Fig. 2c) were used to monitor the time-dependent TES of the PCM-RBA mortars. This non-conventional testing technique (adopted and patented under the name of *Dynamische Kugel Kalorimetrie*, DKK [18]) was followed by the authors for the thermal-energy identification of the composites. Three spherical samples were produced per each mortar. Heating tests were done by using an isothermal conditioned oven with a fixed temperature of ca. 49°, as well as cooling one were done with a climatic chamber fixing the temperature at ca. 9 °C.

3 Experimental Results

3.1 DSC Measurements: Aggregates, Paste and PCMs

DSC tests were done for each component used in the PCM-RBA mixtures. The heat storage capacity has been shown in terms of bulk density times the specific heat capacity. Three samples per each component were analyzed and the mean value presented. Particularly, both heating and cooling responses for cement pastes and for both SB- and PB-RBAs, have been shown in Fig. 3a. These tests were done within the temperature range of 10–40 °C and using a heating/cooling rate of 10 K × min^{-1}.

The DSC results of the used paraffin wax (namely, RT25HC) are shown in Fig. 3b. The adopted heating/cooling rate was 0.25 K × min^{-1}, fulfilling the IEA DSC 4229 procedure [23] for PCMs. DSC curves of the considered PCM, in Fig. 3b, deal with a pronounced latent peak in the region close to the temperature where the phase change occurs (i.e., T_m = 24.5 °C for heating and T_m = 22.95 °C for cooling).

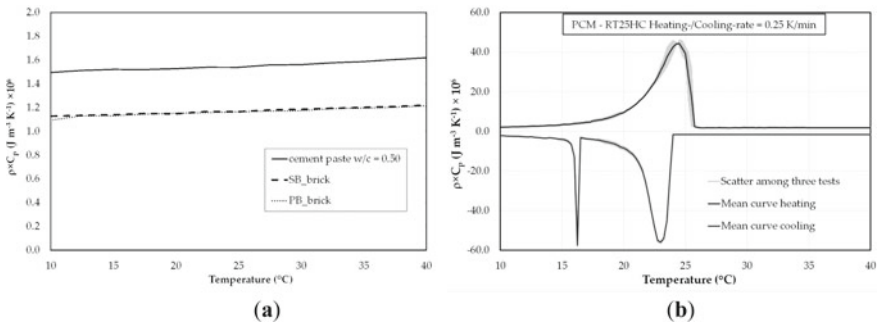

Fig. 3 DSC measurements of **a** cement paste, SB and PB RBAs and **b** Paraffin RT25HC

Table 2 Thermal conductivity of SB-RBA and PB-RBA mixtures

Parameter	REF-SB	SB-65	SB-80
λ (W/m K) (mean value)	0.846	0.768	0.768
Parameter	REF-PB	PB-65	PB-80
λ (W/m K) (mean value)	0.712	0.696	0.725

3.2 Thermal Conductivity of PCM-RBA Mortars

Thermal conductivities of the PCM-RBA mixtures were determined using the Hot-Disk transient plane source method. In Table 2, it can be observed that all mixtures have comparable λ, ranging between 0.696 W/mK (min.) and 0.846 W/mK (max. value).

3.3 "DKK" Test Data

DKK tests were used to evaluate the time-dependent temperature evolution of the spherical-shaped PCM-RBA mortar specimens. For each considered mixture, three spherical samples were tested.

The results plotted in Fig. 4 show the average results (from three spherical specimens) of the temperature evolution versus time. Both heating and cooling results are plotted. It can be seen that, for the mortar mixtures casted with either SB or PB bricks, a delay of the temperature development takes place when PCM-RBAs, with PCM filling degrees of 65 vol% and 80 vol%, are taken into consideration. The presence of PCM actually shifts the temperature curve into the right/down direction under heating response (Fig. 4a, c) and up/left for cooling (Fig. 4b, d).

4 Numerical Model and Results

4.1 Theoretical Assumption and Enthalpy-Based Model

The most classical equation for describing a heat conduction problem with phase change phenomena can be stated by following the so-called enthalpy-based approach

$$\frac{\partial H}{\partial t} = \nabla.(\lambda \nabla T) + \dot{q}_v \quad \forall \mathbf{x} \in \Omega \tag{1}$$

where H is the enthalpy of the system, t the time, $\lambda(T, \mathbf{x})$ the thermal conductivity of the material, which depends on the temperature T and position vector $\mathbf{x}$ (of the

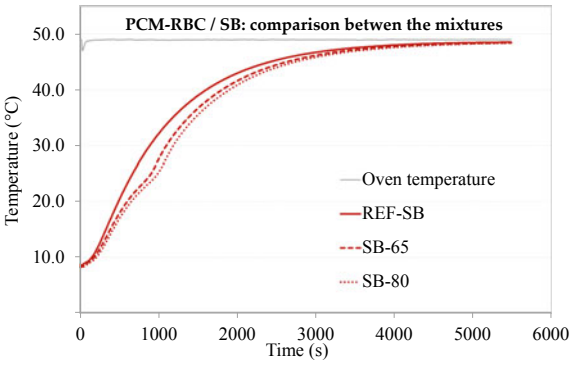

(a)

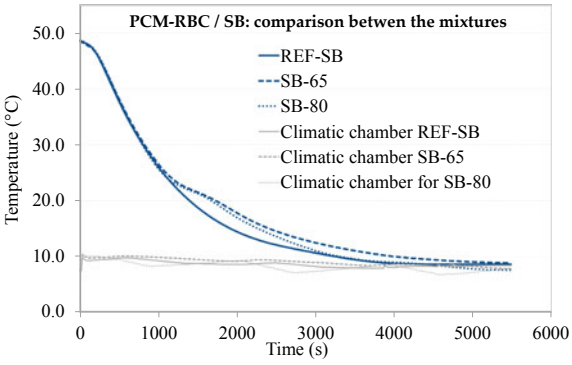

(b)

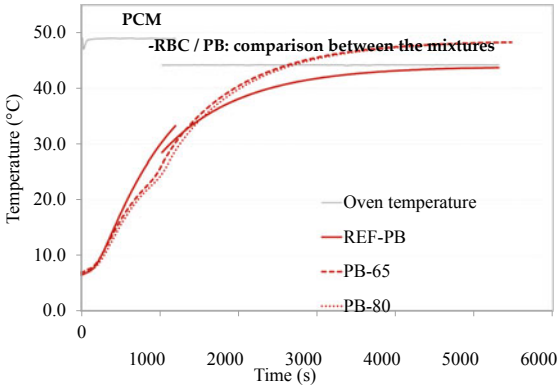

(c)

Fig. 4 Temperature evolutions of the DKK tests: **a** heating and **b** cooling of PCM-RBA mortars with SB bricks, **c** heating and **d** cooling of PCM-RBA mortars with PB bricks

Fig. 4 (continued)

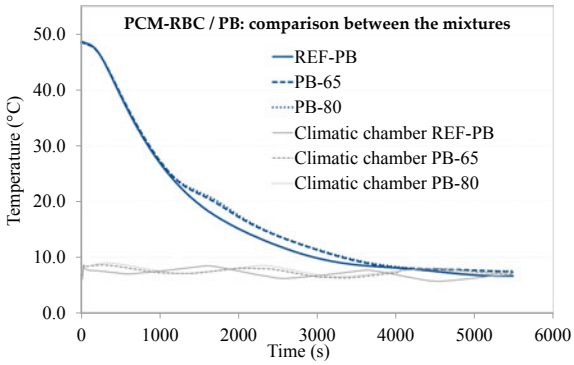

(d)

considered body Ω), $\dot{q}_v$ is the heat source term, while $\nabla.$ and ∇ are the divergence and gradient tensorial operators.

By applying the chain rule to $\frac{\partial H}{\partial t} = \frac{\partial H}{\partial T}\frac{\partial T}{\partial t}$ and introducing the concept of the Apparent Calorific Capacity Method (ACCM), the following temperature-dependent (apparent or effective) heat capacity expression can be written

$$\frac{\partial H}{\partial T} = \rho C_{eff}(T). \tag{2}$$

Thus, Eq. (1) modifies into the following heat transfer equation

$$\rho C_{eff}(T)\frac{dT}{dt} = \nabla.(\lambda \nabla T) + \dot{q}_v \quad \forall \mathbf{x} \in \Omega. \tag{3}$$

Finally, the description of the phase change problem is completed by introducing the Initial (IC) and Boundary Conditions (BCs) as for classical thermal problems.

A meso-scale based homogenization technique was employed for evaluating the effective heat storage capacity $(\rho C)_{eff}$ of the PCM-RBA mortars. It is based on adopting the volume percentages of each individual component as weighting parameter. More precisely, the model smears out the specific heat storage capacity of the RBA, cement paste and the apparent specific heat storage capacity of the PCM, through adopting the volume fraction of each component as the weighting factor.

The specific heat capacities of each component were experimentally determined with DSC measurements as summarized in Sect. 3.

The evaluation of the effective specific heat capacities was determined in two consecutive steps. At aggregate level, the following expression is employed

$$(\rho C)_{eff,PCM-RBA}(T) = \chi_{RBA} \times \rho_{RBA} C_{RBA}(T) + \chi_{PCM} \times \rho_{PCM} C_{app,PCM}(T) \tag{4}$$

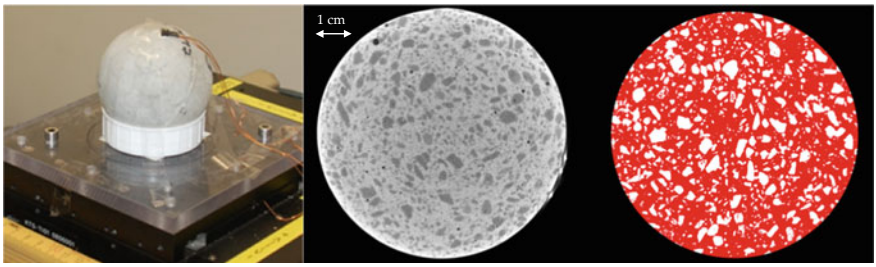

Fig. 5 μ3D-XCT-scans setup and images of the spherical specimens

where the PCM-RBAs were considered as lumped components of RBAs ($\rho_{RBA}C_{RBA}(T)$) plus PCM ($\rho_{PCM}C_{app,PCM}(T)$) and weighting their volume fractions χ_{RBA} and χ_{PCM}, the volume fraction of the recycled bricks and the filled PCMs, respectively.

At composite level (i.e., PCM-RBA mortar), the homogenized overall system of the effective heat storage capacity, $(\rho C)_{eff}$, can be determined as

$$(\rho C)_{eff}(T) = \psi_{paste} \times \rho_{paste}C_{paste}(T) + \psi_{PCM-RBA} \times \rho_{PCM-RBA}C_{eff,PCM-RBA}(T) \quad (5)$$

by weighting the heat storage capacities $\rho_{PCM\text{-}RBA}C_{eff,PCM\text{-}RBA}(T)$ and $\rho_{paste}C_{paste}(T)$ of the individual material components by their volume fractions ψ.

The exact volume fraction ratio between PCM-RBAs and cement paste, of the investigated mixtures, were investigated by performing *μ3D-XCT-scans* of the spherical specimens as shown in Fig. 5.

4.2 Simulations and Comparisons

By implementing the ACCM procedure and customizing it under spherical assumptions, the temperature evolutions of the DKK specimens were simulated and compared with the corresponding experimental data.

The spherical samples made of RBA mortars (with and without PCMs) were simulated with the proposed heat flow ACCM model. The input values were obtained from the conducted experimental measurements, as well as from the $\rho C_{eff}(T)$ described in the previous Sect. 4.1. The thermal conductivities were assumed as temperature-independent and measured through Hot-Disk tests, as outlined in Sect. 3.

For the numerical simulations, the number of Finite Difference space discretization was chosen as 100, while the number of time steps selected were 1000, in all simulations.

In Fig. 6, the 4 graphs show the temperature evolutions for the control mixtures (Fig. 6a, b), and for that one having the maximum PCM contents: i.e., SB-80 (Fig. 6c),

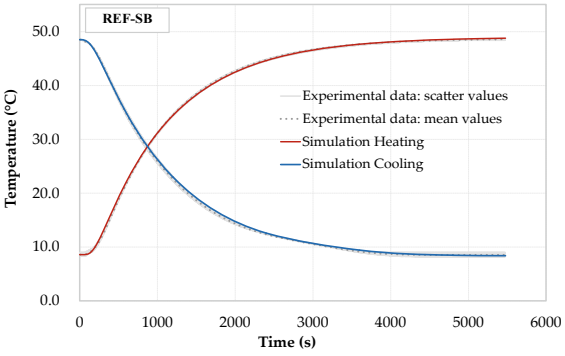

(a)

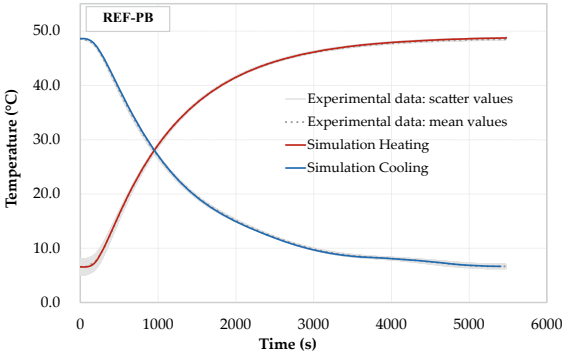

(b)

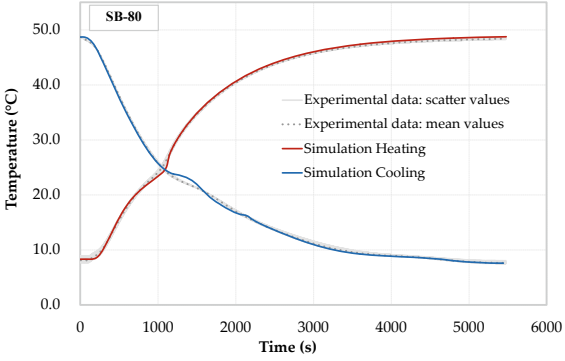

(c)

Fig. 6 Experimental "DKK" tests versus numerical results: **a**–**c** SB and **b**–**d** PB mixtures

Fig. 6 (continued)

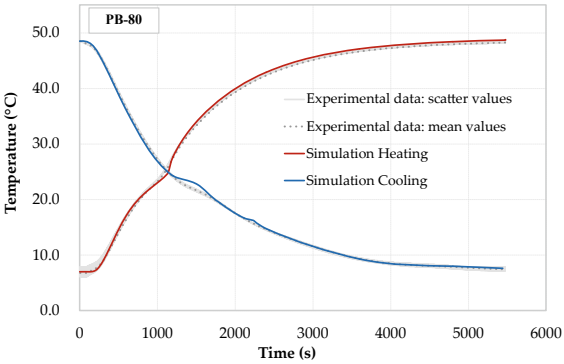

(d)

and PB-80 (Fig. 6d). It can be observed that the modeling approach was able to simulate the experimental temperature evolutions very accurately.

5 Conclusions

In this work, Thermal Energy Storage (TES) capacity of cementitious mortars made of Recycled Brick Aggregates (RBAs) are experimentally investigated and used as carriers for phase change materials (PCMs). Six mixtures were examined, all having a w/c ratio of 0.5 and various amounts of PCM-RBA fractions. Two different types of RBAs were employed, namely standard recycled bricks and high porosity Poroton® fired-clay blocks. Numerical simulations, which included a macroscopic enthalpy-based model, formulated for spherical coordinates and symmetry for predicting the TES in the tested specimens, were also done. The experimental results were employed as benchmark for calibrating and validating the numerical procedure. Input parameters were based on mesoscale observations taking into account the composite composition of the materials under study.

Acknowledgements The second author acknowledge the Alexander von Humboldt-Foundation (www.humboldt-foundation.de/) for funding his position at the WiB – TU Darmstadt under the research grant ITA-1185040-HFST-P (2CENERGY project). The support to networking activities provided by the PoroPCM Project (part of the EIG CONCERT-Japan funding, http://concert-japan.eu/) is also gratefully acknowledged.

References

1. Pérez-Lombard, L., Ortiz, J., Pout, C.: A review on buildings energy consumption information. Energy Build. **40**(3), 394–398 (2008)

2. https://ec.europa.eu/energy/en/topics/energy-efficiency/energy-performance-of-buildings
3. Voss, K., Musall, E., Lichtmeß, M.: From low-energy to net zero-energy buildings: status and perspectives. J. Green Build. **6**(1), 46–57 (2011)
4. Cabeza, L.F. (ed.): Advances in Thermal Energy Storage Systems: Methods and Applications. Woodhead Publishing Series I Energy: Number 66. Elsevier (2014)
5. Sukontasukkul, P., Uthaichotirat, P., Sangpet, T., Sisomphon, K., Newlands, M., Siripanichgorn, A., Chindaprasirt, P.: Thermal properties of lightweight concrete incorporating high contents of phase change materials. Constr. Build. Mater. **207**, 431–439 (2019)
6. Kenisarin, M., Mahkamov, K.: Passive thermal control in residential buildings using phase change materials. Renew. Sustain. Energy Rev. **55**, 371–398 (2016)
7. D'Alessandro, A., Pisello, A.L., Fabiani, C., Ubertini, F., Cabeza, L.F., Cotana, F.: Multifunctional smart concretes with novel phase change materials: mechanical and thermo-energy investigation. Appl. Energy **212**, 1448–1461 (2018)
8. Bahrar, M., Djamai, Z.I., Mankibi, M.E., Larbi, A.S., Salvia, M.: Numerical and experimental study on the use of microencapsulated phase change materials (PCMs) in textile reinforced concrete panels for energy storage. Sustain. Cities Soc. **41**, 455–468 (2018)
9. Silva, A.S., Ghisi, E., Lamberts, R.: Performance evaluation of long-term thermal comfort indices in building simulation according to Ashrae Std 55. Build. Environ. **102**, 95–115 (2016)
10. Rubinšteĭn, L.I.: The Stefan Problem, vol. 8. American Mathematical Soc. (2000)
11. Ceretani, A.N., Salva, N.N., Tarzia, D.A.: An exact solution to a Stefan problem with variable thermal conductivity and a Robin boundary condition. Nonlinear Anal.: Real World App. **40**, 243–259 (2018)
12. Mirzaei, P.A., Haghighat, F.: Modeling of phase change materials for applications in whole building simulation. Renew. Sustain Energy Rev. **16**(7), 5355–5362 (2012)
13. AL-Saadi, S.N., Zhai, Z.J.: Modeling phase change materials embedded in building enclosure: a review. Renew. Sustain. Energy Rev. **21**, 659–673 (2013)
14. Nedjar, B.: An enthalpy-based finite element method for nonlinear heat problems involving phase change. Comput. Struct. **80**(1), 9–21 (2002)
15. Šavija, B., Schlangen, E.: Use of phase change materials (PCMs) to mitigate early age thermal cracking in concrete: Theoret consider. Constr. Build. Mater. **126**, 332–344 (2016)
16. Fachinotti, V., Cardona, A., Huespe, A.: A fast convergent and accurate temperature model for phase-change heat conduction. Int. J. Numer. Methods Eng. **44**, 1863–1884 (1999)
17. Mankel, C., Caggiano, A., Ukrainczyk, N., Koenders, E.: Thermal energy storage characterization of cement-based systems containing microencapsulated-PCMs. Constr. Build. Mater. **199**, 307–320 (2019)
18. Koenders, E.A.B., Mankel, C., Caggiano, A.: Dynamische Kugel Kalorimetrie (DKK), German Patent N. 123-0069 AZ 2018/21 (am 18. Okt 2018 - DE Patentamt angemeldet)
19. RUBITHERM® RT, 'Datenblatt RT25HC, (09/2018)
20. Koenders, E.A.B., Mankel, C.: Patent DE 102016123739, "Wärmespeichergranulat aus rezyklierten Gesteinskörnungen" (2018)
21. EN 196-1: Methods of Testing Cement—Part 1: Determination of Strength (2005)
22. Mankel, C., Caggiano, A., Koenders, E.: Thermal energy storage characterization of cementitious composites made with recycled brick aggregates containing PCM. Energy Build. **202**, (2019)
23. Gschwander, S., Haussmann, T., Hagelstein, G., Sole, A., Diarce, G., Hohenauer, W., Lager, D., Rathgeber, C., Hennemann, P., Lazaro; A., Mehling, H.: Standard to determine the heat storage capacity of PCM using hf-DSC with constant heating/cooling rate (dynamic mode). A technical report of subtask A2.1 of IEA-SHC 42/ECES Annex 29 (2015)

Thermal Energy Storage Characterization of Environmental-Friendly Bio-Based PCMs as an Alternative to Petroleum-Based Paraffin Waxes

Mona Nazari Sam, Antonio Caggiano, Christoph Mankel, Frank Röser, and Eddie Koenders

Abstract Thermal-Energy Storage (TES) properties of organic phase change materials have been experimentally investigated and reported in this paper. Three paraffin-based PCMs and one bio-based one are considered with melting temperatures of 24 °C, 25 °C and 26 °C. Sensible heat storage capacities, melting characteristics and latent heat enthalpies are investigated through DSC measurements. Two alternative methods, namely the classical dynamic and the step-wise approach, are performed and compared with the aim to eliminate and/or overcome possible measurement DSC errors. The latters are due to the size of the samples and their representativity, heating/cooling rate effects and the low conductivity of the PCMs, which may affect the results and possibly cause a loss of objectivity of the measurements. Based on results achieved from this study, clear informations can be figured out on how to conduct and characterize paraffin and bio-based PCMs, and possible how to apply them in TES calculations for building applications and/or simulations.

Keywords Thermal-energy storage (TES) · Phase change materials (PCMs) · Latent enthalpy · Melting temperature · Differential scanning calorimetry · IEA method

M. N. Sam (✉) · A. Caggiano · C. Mankel · E. Koenders
Institut Für Werkstoffe Im Bauwesen, Technische Universität Darmstadt, Darmstadt, Germany
e-mail: sam@wib.tu-darmstadt.de

A. Caggiano
e-mail: caggiano@wib.tu-darmstadt.de

C. Mankel
e-mail: mankel@wib.tu-darmstadt.de

E. Koenders
e-mail: koenders@wib.tu-darmstadt.de

A. Caggiano
CONICET, LMNI, INTECIN, Universidad de Buenos Aires, Buenos Aires, Argentina

F. Röser
RIB RÖSER Ingenieurbeton, Neresheim-Dorfmerkingen, 73450 Neresheim, Germany
e-mail: Frank.Roeser@roeser-ingenieurbeton.de

E. B. Pereira et al. (eds.), *Proceedings of the 3rd RILEM Spring Convention and Conference (RSCC 2020)*, RILEM Bookseries 32,
https://doi.org/10.1007/978-3-030-76547-7_16

1 Introduction

The global challenge to strongly cut back the use of fossil fuels with the aim to implement renewable resources and to neutralize greenhouse gas emissions make the energy efficiency a key issue. According to the EU commission, heating and cooling in residential and non-residential sector account for half of the EU's energy consumption, while about the 84% it is still generated from fossil resources [1]. The development of new and smart energy storage solutions and technologies, with the aim to use environmental thermal energy more efficiently, and to balance out the daily heating/cooling demands, are worth investigation for building applications [2].

One promising technique available for Thermal Energy Storage (TES) applications is by implementing Phase Change Materials (PCMs) in construction and building composites [3]. PCMs are capable of storing large amounts of latent heat, at almost constant temperature, and are contributing to efficiently balance the thermal comfort of residential and non-residential buildings [4]. Then, designing large-scale practical applications, for passive latent thermal energy storage systems, requires in-depth knowledge on the thermal characteristics of a PCM before, during and after the phase change. Therefore, an accurate determination of the thermal properties of PCM systems is crucial to efficiently design composite systems that use latent TES [5].

Differential Scanning Calorimeter (DSC) is an effective method to characterize the thermal behavior of PCMs, and to determine their TES capacities, in terms of transition temperature, enthalpy, specific heat, and their stabilities throughout various melting and solidification cycles [6]. DSC method, despite its numerous positive features [7], has however some well-known limitations, which can complicate the analysis of the results and reduce the measurement accuracy and precision. Heating and cooling rates of DSC measurements are typically much faster than those in real applications, while the sample mass is also very small (less than 90 mg), which might lack representativity for real size applications [8, 9]. It follows that DSC measurements can be affected by changing the heating/cooling rate and sample mass. Both of them mainly influence the thermal equilibrium status, in the sample, thus producing a shifting of the phase change temperature and lead to non-realistic shapes of the heat capacity and/or enthalpy temperature responses [10]. Therefore, developing an appropriate and objective methodology, in this field, is essential to improve the accuracy of the PCM characterization test procedure and to make measurement errors negligible [11].

The main objective of this work is to investigate the thermo-physical properties and heat storage capacity of a representative organic (paraffinic and bio-based) PCMs, in terms of phase-change enthalpy, specific heat capacity and melting temperature, using different experimental setups. The influence of various parameters, involved in DSC measurements, are compared with results done on three comparable paraffin waxes. The measurements are carried out in accordance with the currently available standard of the International Energy Agency (IEA), i.e. under the Task 42 Annex

29, to characterize the thermal-energy properties of PCMs under discussion. Heat-flux DSC dynamic measurements and DSC step-wise procedures are considered and compared to scrutinize the aforementioned aims.

2 Materials and Methods

In this section, the employed materials, methods and experimental program, considered for analyzing the TES properties of the selected PCMs, are presented. Two types of organic phase change materials are analyzed, namely three paraffin waxes and one bio-based PCM, which have physical, kinetic, chemical and economic relevance for constructions and building application in civil engineering [12, 13].

2.1 Paraffin Waxes

Three commercial paraffin-based waxes (RT-series® by Rubitherm GmbH) are used as reference PCMs. These commercial products, having a melting temperature T_m that ranges between 22 °C and 26 °C (suitable for enhancing the thermal comfort in building applications) are selected for this study. More specifically, RT24, RT25 and RT26 are taken into consideration, which are characterized by a T_m of 24 °C, 25 °C and 26 °C, respectively.

2.2 Bio-Based PCM

One bio-based PCM has also been investigated in this work as an eco-friendly alternative to the aforementioned petroleum-based paraffin waxes. The bio-based material, viz. PureTemp25® by PureTemp LLC, made of natural oils with a T_m of 25 °C, is used, while its results can be directly compared to RT25. The thermal properties of the RTs and the bio-based PCM are listed in Table 1.

Table 1 Properties of RT24, 25, 26 [14] and PureTemp25 [15] as given by manufacturers

Properties	RT24	RT25	RT26	PureTemp25
Melting temperature [°C]	24	25	26	25
Specific heat [kJ/kg × K]	2	2	2	1.99–2.29*
Heat storage capacity [kJ/kg]	160 (16–31 °C)	170 (16–31 °C)	180 (19–34 °C)	187**

**Liquid–Solid **Measurement interval is not available in the datasheet*

2.3 Methods

This section reports the methods used to investigate the TES properties of the PCMs presented in Sects. 2.1 and 2.2. Two alterative heat-flux DSC methods (Fig. 1), namely the dynamic and step-wise methods, have been considered for this purpose. The German Standards DIN 51,005 [16] and DIN 51,007 [17] have been considered as a reference to perform these DSC tests (generally applied for this test method to any kind of material), while, the IEA standard procedure [18] is followed to determine the heat storage capacity of PCMs.

Characterizing the PCMs was done by measuring three cycles over three different temperature ranges: (i) solid phase (−20–10 °C), (ii) phase transition (melting and/or crystallization, 10 to 30 °C) and (iii) liquid phase (30–60 °C). It may be worth noticing that only for the dynamic DSC tests (according to IEA [18]), each sample measurement consisted of 3 (DSC) cycles over the pre-defined temperature range (−20–60 °C). Particularly, the first cycle was performed to eliminate previous thermal histories of the specimen; the second cycle was carried out to identify the TES characteristics; and finally, the third one was done mainly to check the reproducibility of the results and the possible appearance of (cyclic) chemical instability of the material.

3 Dynamic and Step-Wise DSC Method and Evaluation of TES Parameters

The most common way to operate DSC tests is by performing the experimental procedure with a constant heating/cooling rate. This is known as “dynamic DSC”, since the heat transfer (energy) is evolving without a necessary thermodynamic equilibrium inside the analyzed sample. This will result in significant errors in the temperature-dependent measurements, such that the heat supply/release, referred to

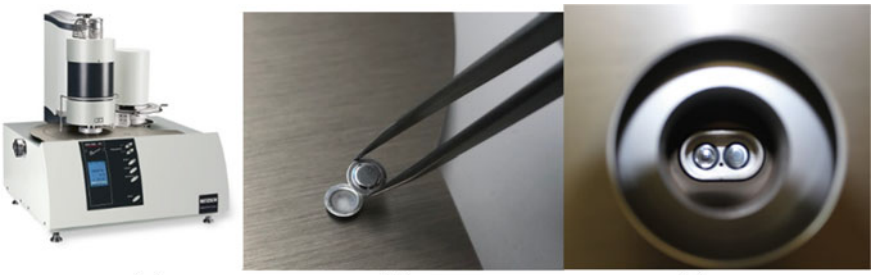

Fig. 1 **a** DSC equipment, **b** aluminum sample holders (maximum volume capacity of 40 μL) and **c** position into the DSC device

each temperature record, cannot be objectively attributed to the real TES values. For this reason, carrying out measurements with different heating rates and mass variations can provide good information about the influence of the measured variables and verifies the soundness of the measured data.

3.1 T(t) History Procedures

The results in the experimental tests showed that the selection of the "heating rate" and "sample mass" arises mainly from a compromise between accuracy of the measurements (e.g. enthalpy, specific heat capacities, melting point values and the mitigation of the data objectiveless due to heating rate effects). From the practical point of view, very low heating rates go along with huge signal noise. Contrarily, in low mass samples, thermal equilibrium can be reached more easily with higher heating rates. Experimentally, the most representative mass should be firstly found, followed by a proper "noiseless" heating rate. The procedure described in the IEA standard [18] gives some direction in this sense and it was used to control/solve the heating/cooling rates and sample mass issues in the melting range. For the measurements in the sensible range, following the DIN 51,007 [17], a heating rate of 10 K/min was adopted. In these measurements, issues related to temperature gradients are almost negligible and samples with large quantity can be tested without compromising a good device signal.

The enthalpy change (at both sensible and latent stage), *dH(T)*, of the sample, can be evaluated by integrating the heat flow registered during the DSC measurements. In general, changes in enthalpy (latent heat) or the specific heat capacity (sensible heat) of an examined sample are determined by recording the absorbed heat between two equilibrium states, assigned as baselines of the acquired measurement curves. It is worth noting that the baseline-construction due to the specific heat capacity measurements, outside its melting range, is determined by performing three measurements: 1. "empty", 2. "calibration", and 3. "real sample" measurement for each temperature range (more details are available in [17]). This is due to the correction of measurement results possible affected by asymmetries and to compensate device specific errors.

A step-wise method is used as an alternative for reducing the heating rate effect in the melting range that is affecting the measurements of dynamic DSC tests. In the step-wise procedure, the net heat applied in a certain temperature interval, is the same as the amount considered in the dynamic DSC tests. However, the whole interval is sub-divided into small sub-steps (see Fig. 2a). This will favor the accumulation time to reach the thermodynamic equilibrium, between each temperature step, and will improve the temperature resolution (indicated in Fig. 2b), which was assumed to be 1 K in this study. In this procedure, isothermal (equilibrium) states are always awaited between two subsequent temperature steps (i.e. 1 K). The waiting needed to reach this state of equilibrium mainly depends on the selected (temperature) step and can only be determined experimentally. The total specific heat, supplied over

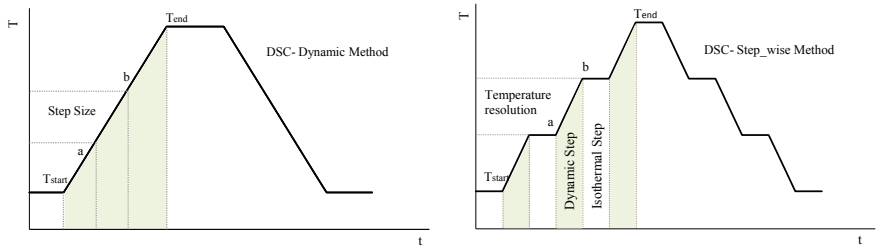

Fig. 2 $T(t)$ history for **a** dynamic DSC method and **b** step-wise DSC method

the individual intervals, is obtained by summarizing the heat increments supplied at each sub-step (by integrating the heat flow over time).

3.2 Experimental Program

For the measurement of each parameter pair (c_p, h), three samples per material (paraffin-based RT24, RT25, RT26 and bio-based PureTemp25, shown in Fig. 3) were taken into account.

Table 2 reports an overview of the full experimental program considered for the dynamic and step-wise method, respectively.

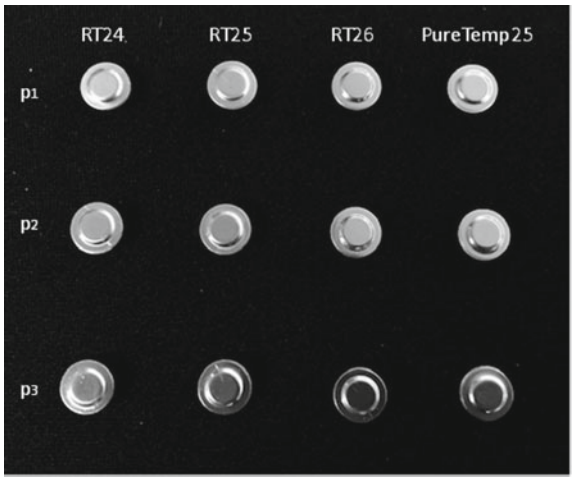

Fig. 3 DSC specimens for the measurement of specific heat capacity and enthalpy of PCMs following the dynamic and step-wise procedures

Table 2 Samples, heating rates, investigated parameters and DSC test-type applied in this study

Tests	Materials											
	RT24			RT25			RT26			PureTemp25		
	P1	P2	P3	P1	P2	P3	P1	P2	P3	P1	P2	P3
Dynamic - *h (T)* (R: 0.125 K/min)	✓ 13.3 mg	✓ 16.5 mg	✓ 16.9 mg	✓ 16.3 mg	✓ 18.4 mg	✓ 18 mg	✓ 17.7 mg	✓ 18.5 mg	✓ 16.1mg	✓ 18.9 mg	✓ 19 mg	✓ 17.7 mg
Dynamic - *cp (T)* (R: 10 K/min)	✓ 14.3 mg	✓ 16.0 mg	✓ 16.1mg	✓ 17.2 mg	✓ 18.4 mg	✓ 18 mg	✓ 16.4 mg	✓ 18.9 mg	✓ 12.4 mg	✓ 10.5 mg	✓ 18.9 mg	✓ 18 mg
Step-wise - *h (T)* (R: VAR)				✓ 16.3 mg						✓ 18.9 mg		

4 DSC Results

This section reports the results and the discussion of the TES data achieved from the experimental program on both the dynamic and step-wise DSC tests.

4.1 Specific Heat Capacities, Enthalpy and Melting Points Following the Dynamic DSC Procedure

For each PCM type, six samples were investigated through dynamic DSC tests. Three of them were used for the $c_p(T)$ characterization, and the remaining three for the $h(T)$. Before and after the non-isothermal phase change (melting), a heating rate of 10 K/min was adopted for all the tests to reduce the noise ratios [17]. While, in the latent zone, the considered heating rates were of 0.250 K/min for RT24 and RT26 and 0.125 K/min for RT25 and PureTemp 25, respectively. These assumptions were done following the IEA standard procedure [18] to mitigate the influence of the rate of heating in each compound. Figure 4 shows the results of dynamic DSC measurements done for paraffin wax RT24, RT25, RT26 and the bio-based PureTemp 25, for determining the c_p [J/g × K] versus T [°C] response, in both latent and sensible ranges. All DSC curves are characterized by an almost sensible behavior in the temperature range far from the melting points (i.e., in the solid range −20 °C–10 °C and the liquid one 30 °C–60 °C), while a non-isothermal latent behavior appears in the phase change region.

In the liquid sensible ranges (between 30 and 60 °C), the determined specific heat capacities varied between 2.1 and 2.3 J/g × K for RTs and PureTemp 25. Then, in the lower temperature ranges (solid sensible responses, between -20 and 10 °C), the c_p values varied between 1.7 and 2.0 J/g × K for RTs and PureTemp 25. In the latent response ranging between 10 °C and 30 °C, a pronounced peak took place, that represents the solid–liquid melting phase change of the various PCMs. The peak values of c_p, at which the melting happened (mean value of three specimens), were 48.5, 94.9, 70.6 and 60.0 J/g × K for RT24, RT25, RT26 and PureTemp 25, respectively. Furthermore, it can be also observed that the mentioned results showed

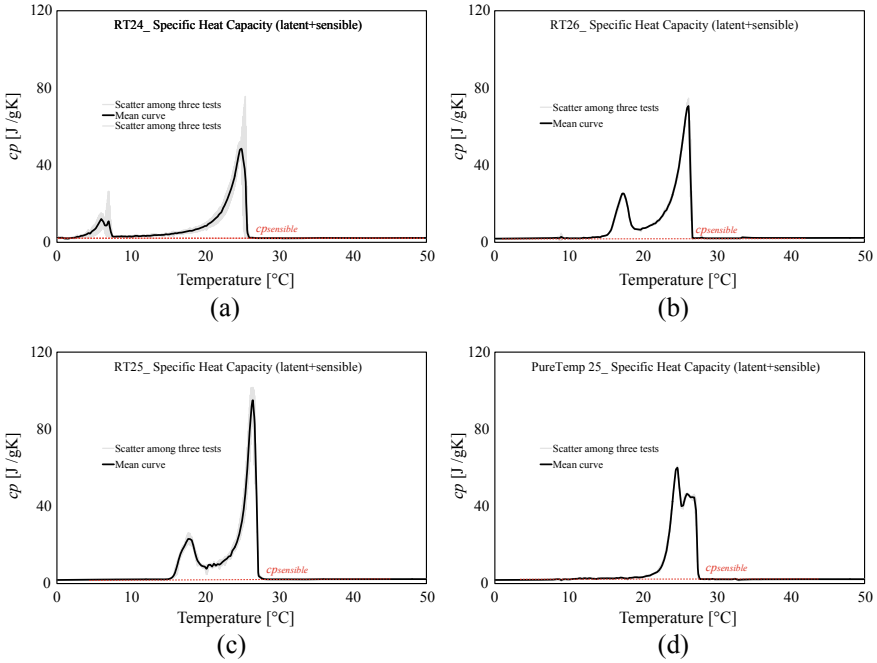

Fig. 4 Specific heat capacities following the dynamic DSC tests (between 0 °C and 50 °C): **a** RT24, **b** RT26, **c** RT25 and **d** PureTemp 25. *Note* the total specific heat capacities have been constructed by additively linking the sensible parts with the latent ones

a very little (almost negligible) scatter for all tests (indicated by the gray area in Fig. 4).

In Fig. 5, the resulting enthalpy curves (latent part only), during a phase change and measured with the dynamic DSC method, are shown for all materials. The plotted curves represent the mean values of the measurements done for three samples of each material.

It can be observed that the absorbed heat from 0 J/g to the total specific latent heat of each PCM (see Fig. 7a) is represented by a clear non-isothermal behavior. This becomes more clear by comparing the different mean curves of the *h(T)* responses, as shown in Fig. 6. This Figure shows the *h(T)* responses of RT24, RT25 and RT26 (Fig. 6a), and RT25 and PureTemp 25 (Fig. 6b), in comparison. It can be observed that PureTemp 25, compared to the RT25, is characterized by a faster acceleration of the *h(T)* response. It means that the phase change occurs in a narrower melting range, which is often more appreciated in practical passive building applications. As mentioned before, also these tests were characterized by a very low experimental scatter.

Finally, the melting temperature of all PCMs, defined as that point at which the maximum c_p was registered, have been showed in Fig. 7b. The presented values are the mean values of the melting temperatures of three specimens.

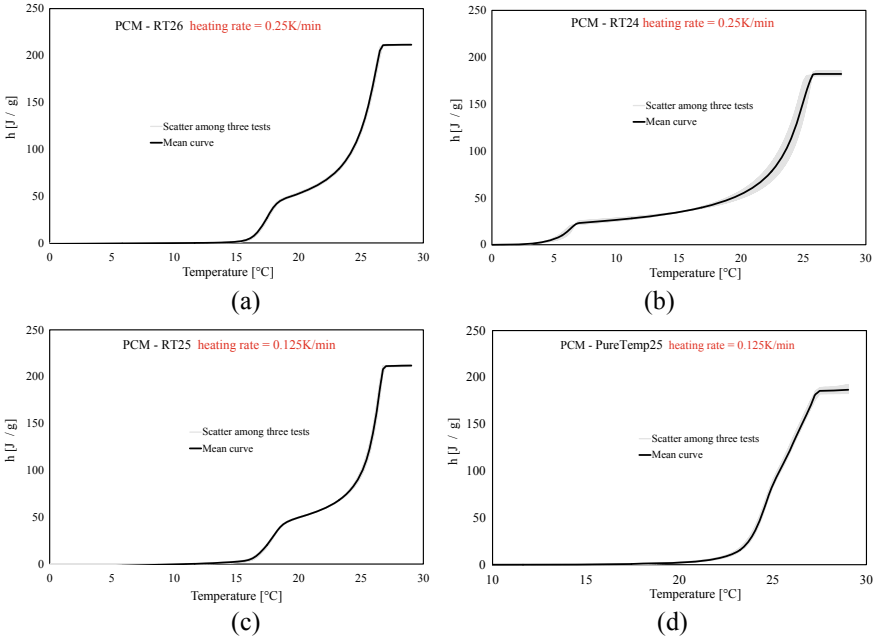

Fig. 5 Enthalpy (latent-only) measurements following the dynamic DSC tests: **a** RT24, **b** RT26, **c** RT25 and **d** PureTemp 25

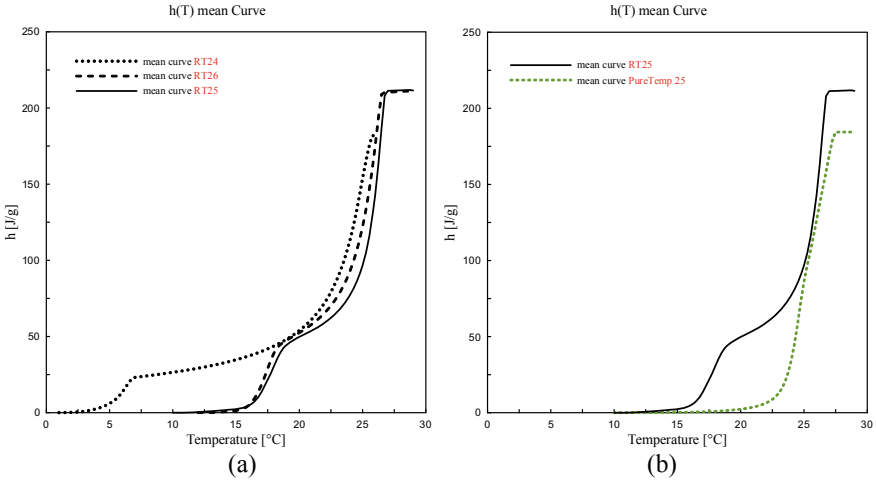

Fig. 6 Comparisons between the enthalpy mean curves, determined thorough dynamic DSC tests of **a** RT24, RT25 and RT26; **b** RT25 vs PureTemp 25

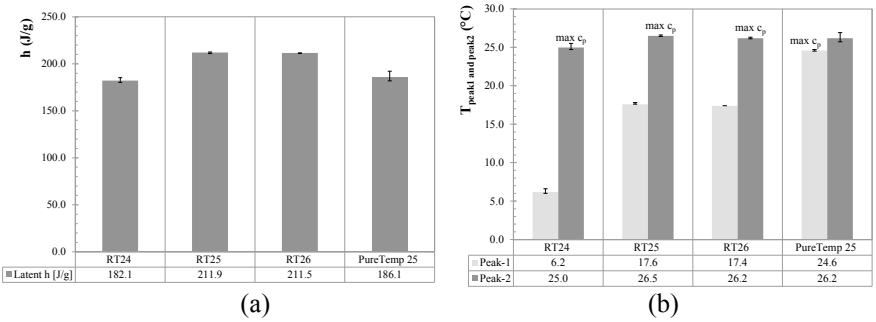

Fig. 7 **a** Latent h [J/g] following the dynamic DSC method of RTs and PureTemp. **b** Melting temperatures of all samples following the dynamic DSC method of RTs and PureTemp. The vertical scatter indicators represent the range between the minimum and the maximum values

4.2 Enthalpy and Phase Change Temperature: Step-Wise DSC Measurements

Tests with different heating rates (ranging from 2 to 0.125 K/min) have been performed for the step-wise DSC method. These activities were scheduled for RT25 and PureTemp 25 under temperatures ranging between 10 and 30 °C (range which is relevant for the phase transition). Results showed that by using the step-wise method the influence of the heating rate, which classically affects dynamic DSC measurements, is almost fully cleaned.

The enthalpy results and phase change temperatures (by adopting isothermal step-times of 10 min, at the beginning of the melting, and 25 min by reaching the melting peaks) are evaluated for both sensible and latent absorbed heat, in the range of 10 °C–30 °C. Figure 8a and b show the histograms of the stored heats, $\Delta q(T)$, between the temperature intervals, representing the temperature resolution of the acquired data, of 1 K, for the aforementioned tests.

From the results, it can be seen that the melting of RT25 mainly starts at 15 °C and ceases at 26 °C. A baseline construction was used to evaluate and separate the sensible part form the latent one. The sensible absorbed heat was evaluated at 2.10 J/g, which was in agreement with the value declared in the datasheet, (i.e. 2 J/g, see Table 1). The melting peaks as indicated in Fig. 8a can be appreciated in the range of 25–26 °C. Then the (latent) melting of the PureTemp 25 takes place in a smaller temperature interval (from 21 °C to 28 °C, see Fig. 8b). The absorbed sensible heat of PureTemp 25 was evaluated to 2.89 J/g while its melting point falls in the range of 25–26 °C.

The phase transition enthalpy (considering the latent part only), in the defined melting range of 15 °C–26 °C and constructing the baseline at 15 °C, was 207.21 J/g for RT25 (see Fig. 8a). This value is slightly different to that one measured through the dynamic DSC measurements (211.9 J/g reported in Fig. 7a). The total latent heat of PureTemp 25, evaluated in the temperature range between 21 °C and 28 °C, is 207.5 J/g (see Fig. 8b), which somehow deviates from the value measured using the

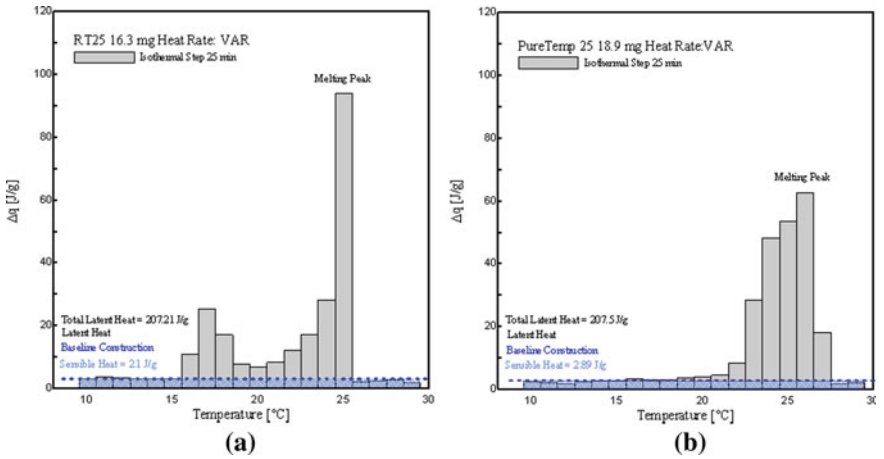

Fig. 8 **a** Histogram view of stored heat $\Delta q(T)$ for RT25; **b** histogram view of stored heat $\Delta q(T)$ for PureTemp 25, adopting a iso-thermal time step of 25 min by the melting peaks

dynamic DSC method (186.1 J/g, showed in the Fig. 7a). However, it may be worth to mention that the results obtained from dynamic DSC tests or the step-wise methods are highly depending on the baseline construction, which separates the sensible heat from the latent part. As the baseline-construction can be done more precisely for the dynamic DSC method, rather than for the step-wise one, the final results of the latent heat by using both the aforementioned methods might be significantly affected.

5 Conclusions

In this work, a detailed experimental program is reported for analyzing the Thermal Energy Storage (TES) capacity of paraffin-based and bio-based PCM, employable for construction and buildings applications. For this aim, three paraffin-based waxes (RT24, RT25 and RT26) and an eco-friendly bio-based PCM (PureTemp 25) were examined using DSC testing procedures. All selected PCMs have a melting temperature within the well-known comfort zone temperature for buildings, e.g. ranging between 19 and 26 °C. Heat storage capacities, melting responses and enthalpies, under both sensible (solid and liquid) and latent TES responses, were investigated through DSC tests. Two alternative methods were performed and compared, i.e. a dynamic DSC and a step-wise DSC method. Based on the results reported in this work, the following conclusions can be figured out:

- It can be stated that reliable and reproducible results can be achieved for characterizing the aforementioned (paraffin- and bio-based) PCMs by following the IEA standard procedure and adopting the dynamic DSC method.

- Main drawbacks of the step-wise method is related to its enormous time consuming character, imposed by the test procedure. The required length of the iso-thermal step is during melting relative high to achieve proper results.
- The temperature resolution of the stored heat is considerably higher, using the step-wise method, in comparison to the dynamic one. However, 1 K (maximum resolution employable in the step-wise method, at which the signal can be still detected) is not high enough to obtain the $c_p(T)$ curve of the material.
- The results obtained following both dynamic and step-wise methods are dependent on the baseline construction, which allows to separate the sensible from the latent heat part. In this regard, the baseline-construction can be more precisely built in the dynamic method than the step-wise one, because more valuable measurement data can be evaluated within very small temperature steps. For this reason, the step-wise method is more appropriate to measure the total enthalpy (both sensible and latent heat) in defined temperature steps and also validating the melting peak reached from the dynamic procedure, while the dynamic measurements can ascertain the stored latent heat much more quickly and precisely. Then using the IEA Standard, dynamic measurements are less time-consuming and also more precise to characterize the melting behavior of the material.

Further experimental characterizations of the TES capacity of several other types of bio-based PCM, to be employed as environmental-friendly substitute of petroleum-based PCM in cement-based systems, are currently under development. Main objective is to improve the current set-up and/or experimental procedure capable to completely remove (or significantly reduce) the side effects present in DSC methods (e.g., due to heating rate effects, non-thermal equilibriums or device inaccuracies).

References

1. European Commission.: https://ec.europa.eu/energy/en/topics/energy-efficiency/heating and cooling, last accessed 12 Dec 2019
2. Da Cunha, S.R.L., de Aguiar, J.L.B.: Phase change materials and energy efficiency of buildings: a review of knowledge. J. Energy Storage **27** (2020)
3. Cárdenas-Ramírez, C., Gómez, M., Jaramillo, F.: Characterization of a porous mineral as a promising support for shape-stabilized phase change materials. J. Energy Storage **26** (2019)
4. Goia, F., Perino, M., Serra, V.: Improving thermal comfort conditions by means of PCM glazing systems. Energy Build. **60**, 442–452 (2013)
5. Akeiber, H.J., et al.: Thermal performance and economic evaluation of a newly developed phase change material for effective building encapsulation. Energy Convers. Manag. **150**, 48–61(2017)
6. Mehling, H., Cabeza, L.F.: Heat and Cold Storage with PCM, vol. 308. Springer, Berlin (2008)
7. Thomas, L.C.: Modulated dsc® paper# 1 why modulated dsc®?; an overview and summary of advantages and disadvantages relative to traditional dsc, TA Instruments Technical Paper TP, vol. 6 (2005)
8. Castellón, C., Günther, E., Mehling, H., Hiebler, S., Cabeza, L.F.: Determination of the enthalpy of PCM as a function of temperature using a heat-flux DSC—A study of different measurement procedures and their accuracy. Int. J. Energy Res. **32**(13), 1258–1265 (2008)

9. Jin, X., Xu, X., Zhang, X., Yin, Y.: Determination of the PCM melting temperature range using DSC. Thermochim. Acta **595**, 17–21 (2014)
10. Barreneche, C., Solé, A., Miró, L., Martorell, I., Fernández, A.I., Cabeza, L.F.: Study on differential scanning calorimetry analysis with two operation modes and organic and inorganic phase change material (PCM). Thermochim. Acta **553**, 23–26 (2013)
11. Feng, G., Huang, K., Xie, H., Li, H., Liu, X., Liu, S., Cao, C.: DSC test error of phase change material (PCM) and its influence on the simulation of the PCM floor. Renew. Energy **87**, 1148–1153 (2016)
12. Abhat, A.: Low temperature latent heat thermal energy storage: heat storage materials. Sol. Energy **30**(4), 313–332 (1983)
13. Zhou, D., Zhao, C.Y., Tian, Y.: Review on thermal energy storage with phase change materials (PCMs) in building applications. Appl. Energy **92**, 593–605 (2012)
14. RUBITHERM-RT®.: Technical datasheets of RTs. https://www.rubitherm.eu. Last accessed 13 Dec 2019
15. PURETEMP 25 Technical Information.: http://www.puretemp.com. Last accessed 13 Dec 2019
16. DIN 51005.: Thermal analysis (TA)-Terms (2005)
17. DIN 51007.: Thermal analysis–differential thermal analysis (DTA) and differential scanning calorimetry (DSC)–general principles (2019)
18. IEA-SHC 42/ECES Annex 29.: Standard to determine the heat storage capacity of PCM using hf-DSC with constant heating/cooling rate (dynamic mode), a technical report of subtask A2.1 (2015)

Impact of the Accelerated Aging Protocols on the Hemp Concrete Durability

Kamilia Abahri, Alexandra Bourdot, Sylvain Langlois, and Ghaith Alhaik

Abstract Hemp concrete has been widely recommended as bio-based material to limit carbon emissions and energy consumption of buildings. This material presents interesting hygrothermal and acoustic performances. It is produced of hemp particles embedded in a natural cement that forms a very heterogeneous and porous component. Few works have studied the evolution of the properties of hemp and flax concrete, over time. This research aims to study the evolution of the compressive strength, the microstructure and porosity of hemp concrete over the time. Thus, three accelerated aging protocols were conducted on the formulated hemp concrete before undertaken properties tracking experimentations. Results shows that compressive strength increases up to 58 days for hemp concrete. The hemp shiv deformation depending on the accelerated aging in hemp concrete is calculated by 2D image analysis. Optical investigation was used for this experimentation. Microscopic results confirm the high degradation of such heterogeneous materials which is confirmed by the porosity results.

Keywords Immersion/drying · Microstructure · Porosity · Compressive strength

1 Introduction

Nowadays, the use of materials with a low environmental impact such as bio-based mortars, already recognized for their thermal and acoustic insulating qualities and their low environmental impact, is gaining more and more place in the construction sector. In addition, they present a renewable resource, derived from plant biomass, in comparison with other building materials. They also have a weak shot and are responsible for low CO_2 emissions, which respects the life cycle.

In fact, the hygrothermal properties of bio-based mortars and especially hemp concrete has been widely studied and demonstrated. From a hygric point of view,

K. Abahri · A. Bourdot (✉) · S. Langlois · G. Alhaik
LMT/ENS Paris-Saclay/CNRS/Université Paris-Saclay, 61 avenue du Président Wilson, 94230 Cachan, France
e-mail: alexandra.bourdot@ens-paris-saclay.fr

E. B. Pereira et al. (eds.), *Proceedings of the 3rd RILEM Spring Convention and Conference (RSCC 2020)*, RILEM Bookseries 32,
https://doi.org/10.1007/978-3-030-76547-7_17

hemp concrete has many advantages. It has an excellent moisture buffering capacity (MBV) to maintain the quality of indoor air [1, 2]. It's very porous structure, and its total porosity close to the open porosity, make it capable of absorbing significant quantities of water [3]. In addition, hemp concrete has a high permeability to water vapor, and the property of substantially moderating the relative humidity changes of the surrounding air [4]. In general, this material can reduce daily variations in indoor relative humidity by absorbing and returning moisture, reducing energy consumption, and maintaining hygrothermal comfort in the building [5].

Thermally, hemp shives present low thermal conductivity which makes them good insulating materials that are well adapted to be associate with binder [6, 7]. The porosity of hemp concrete ranges from 60 to 85% and for linseed concrete from 70 to 90% [7, 8].

Moreover, the use of these materials is hampered, in particular, by the unavailability of databases relating to their intrinsic properties and by lack of knowledge of their behavior over time (durability). This use requires taking into account several criteria that make them vulnerable; the problem of swelling-shrinkage at the cement-fiber plant interface and fungal growth are the most important criteria for assessing the degradation of these materials. Being hygroscopic materials, they are very sensitive to changes in relative humidity, which can cause dimensional variations, which in some cases lead to their deterioration. It is therefore essential to evaluate the behavior of these materials with regard to water demands.

Regarding literature, some researchers have studied the evolution of the hygrothermal properties [9, 10]. They use different aging protocol. The most reliable protocol for measuring the evolution of compressive strength over time is to age samples in situ. This kind of protocol can take several months, even several years. To answer this problem, different accelerated aging protocol, inspired by concrete, have been put in place.

That is why this study investigates the influence of accelerated aging on the properties of this material through a succession of immersion/drying cycles. Microscopic observations highlighted morphology changes of this bio-based material and porosity variations caused by the degradation has been performed. Indeed, a companion of compressive strength has been carried out for referenced samples and after aging. From these tests, crucial conclusions on the durability of this material are drawn.

2 Materials and Methods

This paper proposes different accelerated aging protocol for the study of the durability of hemp concrete. First, we will have to manufacture hemp concrete samples using literature formulations. Then evaluate the porosity, the microstructure and compressive strength at a young age. Next, we will quantify these properties after accelerated aging. Compressive strength has been done after 28 days of manufacturing and at the end of each accelerated aging protocol.

2.1 Hemp Concrete Formulation

The chosen formulation is based on the formulation of the hemp concrete samples already used by researcher in order to make relevant comparison [11]. The water/binder ration is W/B = 1.45, and the aggregate/binder ration is A/B = 0.42 In addition to concrete manufactured, samples of hemp concrete with the same formulation dating from April and May were given to us in order to characterize a more aged concrete. The concrete is placed in specimens of 10 × 10 × 40 cm. After 28 days we cut cubic samples of 5 × 5 × 5 cm. The binders used in the formulation of linseed concrete must ensure a desired cohesion between the different components and thus provide a certain rigidity and mechanical strength. The choice of binder used in the composition of the assembly must consider: ease of mixing while ensuring good coating of the constituents, facilitate implementation in the fresh state and finally guarantee the mechanical properties after hardening. The benchmark binder for applications involving linseed concrete is Tradical PF70 lime, a mixture of air lime, hydraulic lime and pozzolan [12]. This hydraulic lime is characterized by a hydraulic price declaring between 3 and 5 h depending on the mixing rate. It has many physical, chemical and plastic qualities. Also, it easily adheres to different supports; It promotes water exchange, air permeability and impermeability to liquid water [9]. It is a mixture This binder consists of 75% aerated lime, 15% hydraulic binders and 10% pozzolanic binders. Its density is of 500 kg/m^3.

First of all, we prepared the necessary quantities of each component (linen, binder, water); Mixed the water and the binder until the lime swells, which corresponds to the appearance of air bubbles (estimated time between 2 and 3 min); Gradually add the flax shives while mixing. The mixture is judged close as soon as a homogeneous paste is obtained; Stop the mixer and empty the concrete into the wheelbarrow (mixing speed is 90 rpm); Start directly to fill the test pieces with a light compaction so as to have a homogeneous sample.

Rectangular samples of 40 × 10 × 10 cm were obtained after manufacturing the different sizes (medium, large, bulk) which will then be stored in a macroscopic room (50% of relative humidity and 23 °C) until the age of 28 days.

In this study, the retained application is a wall application. It is developed from the professional rules of implementation of hemp concrete structures and corresponds to a composition of materials used on construction sites. The mass dosages of shiv, lime and water are recapitulated in Table 1.

Table 1 Composition of the studied materials

Shiv (kg)	10
Lime (kg)	25
Water (kg)	35
Water/Lime (–)	1.4
Lime/Shiv (–)	2.5

2.2 Methods

This paper proposes several accelerated aging protocols for the study of the durability hemp concrete. This step required the analysis of hemp samples porosity and microstructure and young age to perform comparison with the same samples which have been aging.

First, the NF P 18-459 standard was adopted for the water porosity measurement on a minimum of three cubic hemp concrete samples. Measuring this porosity involves determining by weighing the: apparent mass in water after immersion in water (hydrostatic weighing) of a concrete test body previously impregnated with water under vacuum; dry samples masses. The standard required to put samples in desiccators under vacuum at a constant pressure of 25 mbar (±5 mbar) during 4 h and then gradually inject water inside the desiccator ensuring that samples are covered by a minimum of 20 mm of water level during 48 h. Hydrostatic whetting at 0.01% were carried out (M_w) accompanied with air weighing (M_a). Finally, the mass after drying (M_d) (at 100 °C) was determined for all samples and when the mass becomes stable (no variation up then 0.05% between two successive weighing in an interval of 24 h) we calculate the porosity according Eq. (1):

$$\varepsilon = \frac{M_a - M_d}{M_a - M_w} \cdot 100 \tag{1}$$

Further, a microscopic characterization was done using scanning electron microscopy (SEM) to identify the hemp shiv structure and the interface between the fibers and the binders inside hemp concrete. The Keyence VHX-2000 microscope at LMT Laboratory was used to quantify the hemp concrete swelling/shrinkage and their variation through time for all samples before and after aging: at 58 days for samples stocked in normal conditions of temperature and relative humidity (50% RH and 23 °C) and also for the same samples after 30 days of accelerated aging. This comparison needs to conserve the same samples position before and after observations under the microscope.

2.3 Mechanical Tests

At the end of each protocol of aging, mechanical tests have been done on 3 samples of each formulation. The compressive strength was determined by crushing three cubes of 5 × 5 × 5 cm.

For this, the INSTRON (Fig. 1) is used with a loading speed of 5 mm/min. Before mechanical tests, microscopic observations are performed on each formulation and for each protocol. These observations focus on the evolution of space between the aggregate and the binder, also the proliferation of molds.

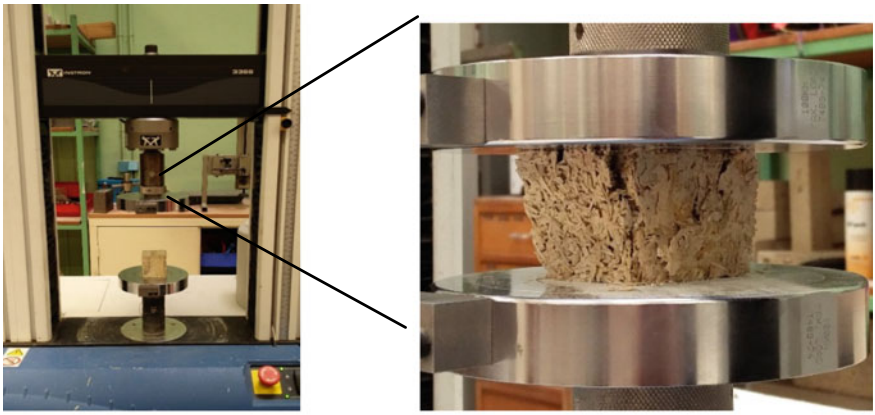

Fig. 1 INSTRON dispositive for mechanical tests: compressive strength

2.4 Accelerated Aging Protocols

The accelerated aging protocols were inspired from conventional protocols applied on concrete. To quantify the evolution of compressive strength over time three accelerated aging protocols were conducted in parallel on 3 specimens of each formulation as presented on the Fig. 2.

Fig. 2 Hemp concrete sample conditioned in the oven for drying (left) and immersed in water (right)

Table 2 Description of used aging protocols

Protocol	Description
Immersion/drying	This test consists of a series of immersion cycles of the sample in water for 48 h, followed by drying in an oven at 50 °C for 72 h [9, 11]
Immersion/freeze/drying	The first protocol is retained by adding a gel step between immersion and drying at −10 °C for 24 h. This protocol permits the flaking of the sample
Climatic chamber	The relative humidity is varied between 33 and 85% at a constant temperature T = 30 °C. The duration of a complete cycle is 10 days. 5 days for wetting (RH = 85%) and 5 days for drying (RH = 33%). This protocol favors the apparition of mold [11]

The immersion/drying test [9, 11], the immersion/freeze test, and the climatic chamber protocol [11]. These protocols make it possible both to make aggressive accelerated aging tests, and less-aggressive with aging in the climatic chamber. The description of used aging protocols in this study was presented in Table 2.

3 Results and Discussion

As expected in literature, hemp concrete offers a high porosity [1, 7, 8]. Concerning the studied formulation, the results are indicated in Table 3. These results obtained from 5 hemp concrete samples. This step made it possible to verify the repeatability of the tests for the different samples from the same formulation.

Microscopic observations were investigated function of the hemp concrete age. By the same as porosity, various samples were observed to guaranty the repeatability of the results. The aims of this part are to study the dimensional variation caused by the aging at microscopic scale.

During the 119 days of accelerated aging, the eventual presence of microorganisms has been detected on hemp and flax concrete. The development of mold has been observed on all formulation and for the immersion/drying and immersion/freeze protocols. Several types of mold are visible with the optic microscope. They can take the form of white "mushroom" and black/gray spots. They are visible on Fig. 3.

By the same the microscopic degradation was analyzed for different ages. Images from Fig. 4 show the morphology evolution from samples conditioned at 58 days in normal conditions of temperature and relative humidity and for the same sample after aging: 30 days of immersion. The corresponding dimensional variation were quantified the graphs of Fig. 5.

Table 3 Hemp concrete porosity

Porosity (%)	Deviation (%)	Variation coefficient (%)
77.41	0.7	0.91

Fungi appears at 119 days only for immersion protocols

Fungi appears at 60 days and visible for all protocols

Fig. 3 Fungi degradation of hemp concrete

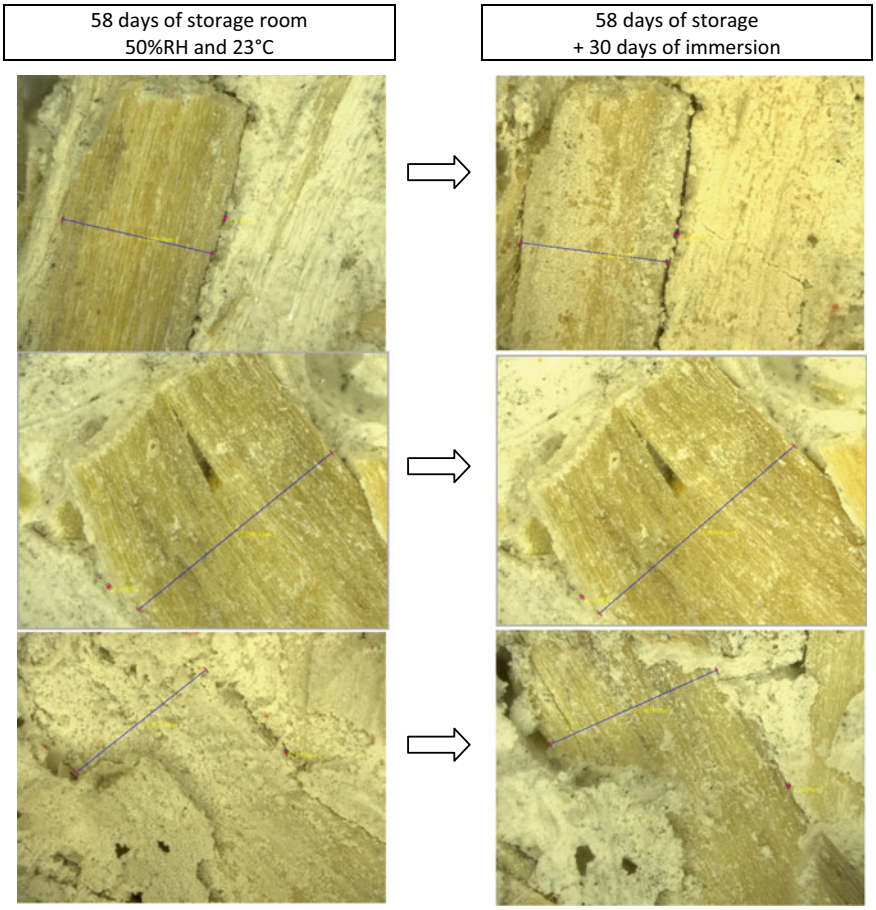

Fig. 4 Microstructural deformations before and after degradation

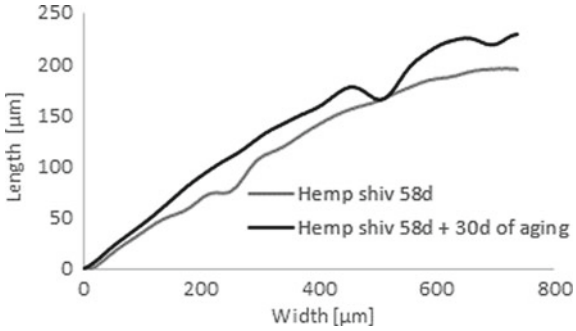

Fig. 5 Dimensional variation of hemp shiv after 58 days of hydrothermal aging

Figure 5 shows the microstructural variability of granulates profiles after 58 days of normal conditioning of temperature and relative humidity. The same position of the samples was again observed by the microscopic after 30 days of aging (without immersion) to performed correctly comparison.

From these curves we can clearly notice a difference of the hemp shiv dimension before and after aging. After aging the specimen swell and shrink representing more distance between the wooden fibers and the cementitious interface.

By the same Fig. 6 indicates the hemp shiv evolution, this time, after 30 days of immersion and drying from the 58 days of aging. The comparison has been done her for hemp shiv conserved at 58 days of normal conditioning and the same hemp shiv after 30 days of accolated ageing by immersion and drying.

The difference between the two cases can easily observed. For the 58 days of normal conditioning, the hemp aggregates present shrink and swelling zoon. When following this test by immersion and drying cycle the distance between the shives widens and becomes more regular because it is in the limit of the cementitious binder.

Compressive strength results

Before every test all samples are weight and the density is measured. During the experiments, the samples usually break in the direction parallel to the loading. The mean compression stresses are shown on Fig. 7 for each formulation and for each

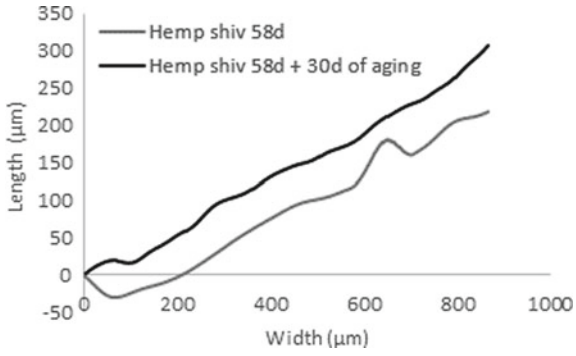

Fig. 6 Dimensional variation of hemp shives after 58 days of immersion and drying

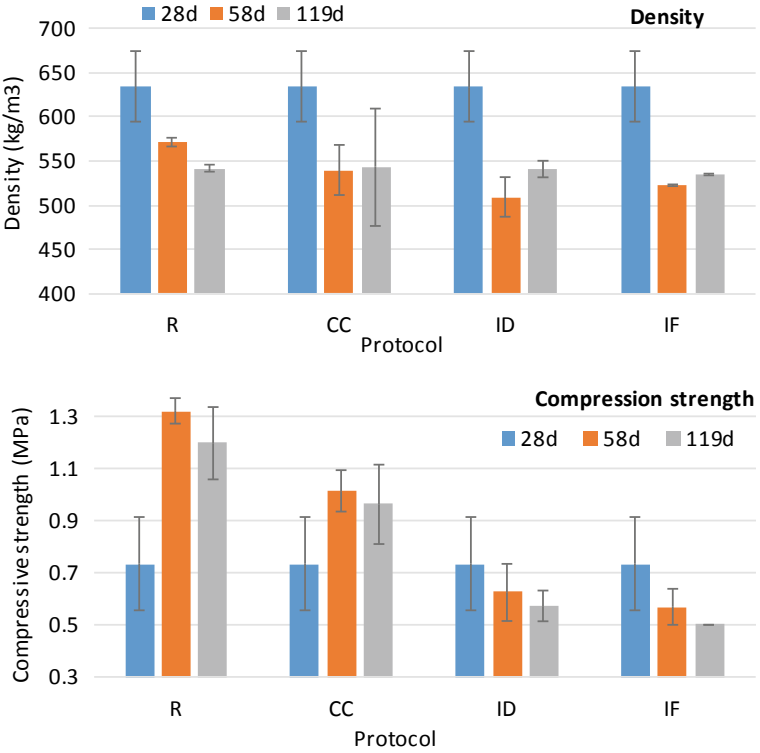

Fig. 7 Compressive strength of tested specimens over time according to accelerated protocols

aging protocol.

Literature indicate that the compressive strength of hemp concrete ranges from 0.1 to 0.7 MPa [10].

Based on results presented this figure, hemp concrete has the higher compressive strength at 28 days. Up to 58 days, compressive strength increases for all mix except for hemp concrete for the immersion/drying and immersion/freeze protocol. Up to 119 days, the strength continues to increase for flax concrete.

4 Conclusion

In this report, we have attempted to provide new information on mechanical and microstructural properties of hemp concrete under aging. The monitoring of the evolution of these properties following accelerated ageing type stresses has been attentively presented in this paper.

The microstructure of the concretes has been observed by optic microscopy. These observations show the porosity of both hemp and flax concrete, as well as the quality

of the granulate-binder interface. A good cohesion is observed for hemp and flax concrete no matter their formulation.

The less aggressive accelerated aging protocol was the climatic chamber, which lead to compressive strength just under the reference one (aging in storage room). Immersion/drying and immersion-freeze lead to close value in term of compressive strength for both hemp and flax concrete.

In this article, we observed that bio-based concretes reach their maximum resistance after 28 days. Hemp concrete has a significant gain of 44% in in situ aging in compressive strength between 28 days and 58 days. Among all types of concrete seems to be the one that resists best after accelerated aging, regardless of the type of stress. Finally, it would have been interesting to consider the compaction direction. We observe that compaction of hemp concrete induces an orthotropy in the material which can cause the material to crash and not crack under a load.

This study provides the literature and the future works with promising results, especially concerning the evolution of the hemp concrete mechanical and morphological properties where the material age should be carefully considered. These parameters are used as input parameters in the simulation models of coupled heat and mass transfer.

References

1. Bennai, F., Issaadi, N., Abahri, K., Belarbi, R., Tahakourt, A.: Experimental characterization of thermal and hygric properties of hemp concrete with consideration of the material age evolution. Heat Mass Transf. **54**, 1189–1197 (2018)
2. Collet, F., Pretot, S.: Experimental investigation of moisture buffering capacity of sprayed hemp concrete. Constr. Build. Mater. **36**, 58–65 (2012)
3. Tran Le, A.D., Maalouf, C., Mai, T.H., Wurtz, E., Collet, F.: Transient hygrothermal behaviour of a hemp concrete building envelope. Energy Build. **42**, 1797–1806 (2010)
4. Bennai, F., El Hachem, C., Abahri, K., Belarbi, R.: Microscopic hydric characterization of hemp concrete by X-ray microtomography and digital volume correlation. Constr. Build. Mater. **188**, 983–994 (2018)
5. Shea, A., Lawrence, M., Walker, P.: Hygrothermal performance of an experimental hemp–lime building. Constr. Build. Mater. **36**, 270–275 (2012)
6. de Bruijn, P., Johansson, P.: Moisture fixation and thermal properties of lime–hemp concrete. Constr. Build. Mater. **47**, 1235–1242 (2013)
7. Collet, F., Pretot, S.: Thermal conductivity of hemp concretes: variation with formulation, density and water content. Constr. Build. Mater. **65**, 612–619 (2014)
8. Rahim, M., Douzane, O., Tran Le, A.D., Promis, G., Laidoudi, B., Crigny, A., Dupre, B., Langlet, T.: Characterization of flax lime and hemp lime concretes: hygric properties and moisture buffer capacity. Energy Build. **88**, 91–99 (2015)
9. Marceau, S., Glé, P., Guéguen-Minerbe, M., Gourlay, E., Moscardelli, S., Nour, I., Amziane, S.: Influence of accelerated aging on the properties of hemp concretes. Constr. Build. Mater. **139**, 524–530 (2017)
10. Page, J., Sonebi, M., Amziane, S.: Design and multi-physical properties of a new hybrid hemp-flax composite material. Constr. Build. Mater. (2016)

11. Sentenac, C., Sonebi, M., Amziane, S.: Investigation on the performance and durability of treated hemp concrete with water repellent. In: Conference Proceedings of 2nd ICBBM 119 RILEM SarlAt Clermont-Ferrand, vol. 1 (2017)
12. Chamoin, J.: Optimisation des propriétés (physiques, hydriques et mécaniques) de bétons de chanvre par la maîtrise de la formulation. Ph.D. thesis, INSA Rennes (2013)

Behaviour of Poorly Indurated Clay/Concrete Interface Due to Lateral Stress: Application for the Disposal of Radioactive Waste

T. Lamouchi, F. Agostini, N. Gay, F. Skoczylas, S. Ben Hadj Hassine, and S. Levasseur

Abstract In the framework of studies for the disposal of radioactive waste, ONDRAF/NIRAS, the Belgian National Agency for Radioactive Waste and enriched Fissile Materials investigates the option of a geological repository. In a geological repository, the waste is sidelined within a deep and stable geological layer, named host rock, behind a whole series of artificial barriers. Together, natural and artificial barriers ensure the isolation of waste, their confinement and the delay and spread of release of radioactive substances. The interaction of the host rock and the concrete support of disposal galleries is investigated to analyse the long-term sustainability of the structure. The host rock considered in this study is a poorly indurated clay present in the northern part of the Belgium, the Boom Clay. The behaviour of the interface between the Boom Clay and the concrete of the galleries is studied experimentally from both mechanical and gas transfer perspectives. Samples have been prepared consisting of two half cylinders, one made of concrete and the other one of Boom Clay to obtain an interface. A dedicated device has been designed using an HOEK type cell, which allow applying confining pressure to simulate lithostatic loading, injecting gas to measure transfer properties and generating relative displacement of both sides of the interface. Mechanical behaviour of the interface under short loading has first been studied. One originality of this study consists in using gas injection and Poiseuille's law to monitor and quantify the opening and closure of the interface during mechanical loading. A partial irreversible closure of the interface and effects of long term loading have been observed. By increasing the confinement, the opening of the interface (clay-concrete) gradually decreases (initially 38 μm for 1.2 MPa of confining pressure) until it reaches 5 μm for 4.5 MPa. There is moderate expected irreversibility during unloading (19 μm at 1.7 MPa). The objective is to identify the main parameters allowing predicting the properties of the interface, such as initial roughness of the interface, water content, applied stress and time. The second part

T. Lamouchi (✉) · F. Agostini · N. Gay · F. Skoczylas
University of Lille, CNRS, Centrale Lille, LaMcube CNRS UMR 9013, Lille, France
e-mail: takoua.lamouchi@centralelille.fr

S. Ben Hadj Hassine · S. Levasseur
ONDRAF/NIRAS, Brussels, Belgium

E. B. Pereira et al. (eds.), *Proceedings of the 3rd RILEM Spring Convention and Conference (RSCC 2020)*, RILEM Bookseries 32,
https://doi.org/10.1007/978-3-030-76547-7_18

of the work consists in studying transfer properties at the interface. The aim is to identify paths available for gas produced during waste storage.

Keywords Interfaces · Poorly indurated clay · Concrete · Transfer properties · Shearing

1 Introduction

The management of radioactive waste requires specific solutions to prevent radioactivity from harming people and environment. The objective of a repository is the long-term containment of radioactivity in order to keep radionuclides isolated from humans and the environment for as long as necessary and then avoid any impact on health or environment. With that perspective, repository has to isolate the waste from the biosphere before its radioactivity level has returned to a level lower than the natural one. One solution proposed by the ONDRAF/NIRAS, the Belgian organism in charge of the management of radioactive waste, is to set radioactive waste in a deep geological formation [1]. Several potential host formation are under study in Belgium, one of these is the Boom Clay.

The excavation of disposal galleries induces a significant redistribution of the stresses around the structure, potentially accompanied with fractures, generating what is called an excavation damaged zone (EDZ). In the EDZ, despite efficient self-sealing in the Boom Clay, the redistribution of stress around galleries may still alter on the long-term the transport and flow properties and therefore the performance of the host formation as the last containment barrier. Water venues in the storage lead to the corrosion of metallic components of the waste and of the disposal system leading to hydrogen production. In this context, it is necessary to identify potential pathways for the flow of hydrogen from the waste to the self-sealed clay barrier as well as to the interface between the disposal galleries and the surrounding host rock. The objectives of this study are then to identify the main parameters allowing predicting the hydromechanical behavior of the interface, such as initial roughness of the clay, water content, applied stress and time. The second part of the work consists in studying transfer properties at the interface.

2 Experimental Campaign and Methodology

In in situ conditions, the interface is mechanically loaded due to lithostatic pressure and water saturation can vary from low values during digging to reach 100% at the long term. An experimental campaign has been designed to reproduce in situ conditions and to evaluate the effect of mechanical loading on the interface behavior. In order to analyse the experimental results on the interface, it is first necessary to identify the properties of the two materials constituting the interface, i.e. concrete and

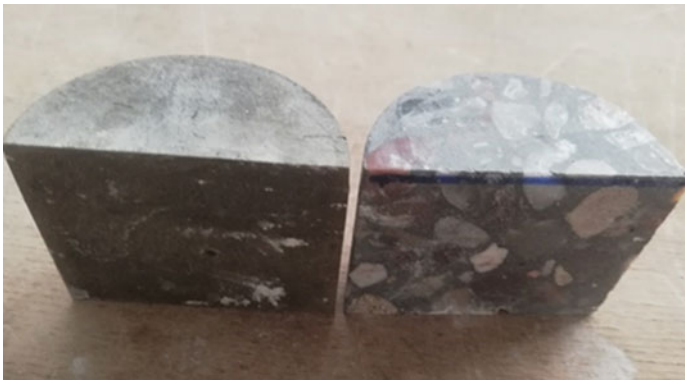

Fig. 1 Boom Clay and concrete samples

Boom Clay. Realistic interfaces have been prepared consisting of two half cylinders, one made of concrete and the other one of Boom Clay (see Fig. 1).

2.1 Boom Clay

Cored samples of Boom Clay have been provided by EURIDICE for the ONDRAF/NIRAS. Samples come from HADES URF (R72-73 W). This clay is characterized by a high porosity (~35%) and a bulk density of about 2000 kg m^{-3} and a grain density of 2650 kg m^{-3}. It is composed of 22–66% of quartz, 0–4.6 of calcite, 6.8–37% of smectite and illite-smectite, 0.5–4% of chlorite and finally the typical water content of Boom water is thus about 20%. This is consistent with the water content weight range from 19 to 24% reported by the literature [1].

2.2 Concrete

Concrete samples have been provided by EURIDICE for ONDRAF/NIRAS. This concrete is the one used for the lining of the Connecting Gallery of the HADES URF. Its formulation is described in Table 1.

Table 1 Concrete's formulation

Water (kg/m^3)	Cement CEM II/B-V (kg/m^3)	Fly ash (kg/m^3)	Coarse agg. (kg/m^3)	Fine agg. (kg/m^3)
135	335	115	1252	540

The average porosity (after oven drying at 65 °C) reaches 11.9%. Expected uniaxial compressive strength after 28 days is equal to 49.5 MPa.

2.3 Interface Concrete-Boom Clay

The design of interfaces has been done in order to meet the different objectives of this study (which is wider than what is presented in this article). Indeed, it was necessary to be able to control the mechanical stress applied on the interface with a simple geometry, to perform gas and water permeability tests and to generate a relative displacement of both sides of the interface.

Samples of Boom Clay and concrete have been cored and mechanically sawed in half (see Fig. 1). Interfaces are obtained by putting together half cylinders of both materials. The diameter of the reconstituted interface is 65 mm with a height of 70 mm.

2.4 Interface Qualification Throw Poiseuille's Law and the Hoek's Cell

A dedicated device has been designed based on an HOEK type cell. A schematic view of the device is presented in Fig. 2. It allows applying confining pressure to simulate lithostatic loading, injecting gas to measure transfer properties and generating relative displacement of both sides of the interface (this last point will not been presented here).

To measure the transfer properties of the interface, it was first necessary to measure transfer properties of the two materials constituting the interface. In in situ conditions, the main concern is to identify flow path of H_2 generated by the corrosion of wastes. For practical and safety reasons we have chosen to use Argon instead of Di-Hydrogen.

Control of confining pressure is ensured by an automatic pump (Gilson®), it allows to simulate mechanical loading due to lithostatic pressure. The cell is connected to a gas permeability measurement apparatus designed in the laboratory. It allows to apply a pressure gradient and to measure gas flow rates. The injection pressure is noted P_i and the drainage pressure P_o. When steady state flow is reached, downstream gas flow rate allows to calculate gas permeability (K_g) according to Darcy's law [2] for compressible fluid given by (Eq. 1):

$$Kg = \frac{\mu * Q0 * 2 * L * P}{A * \left(Pi^2 - P0^2\right)} \tag{1}$$

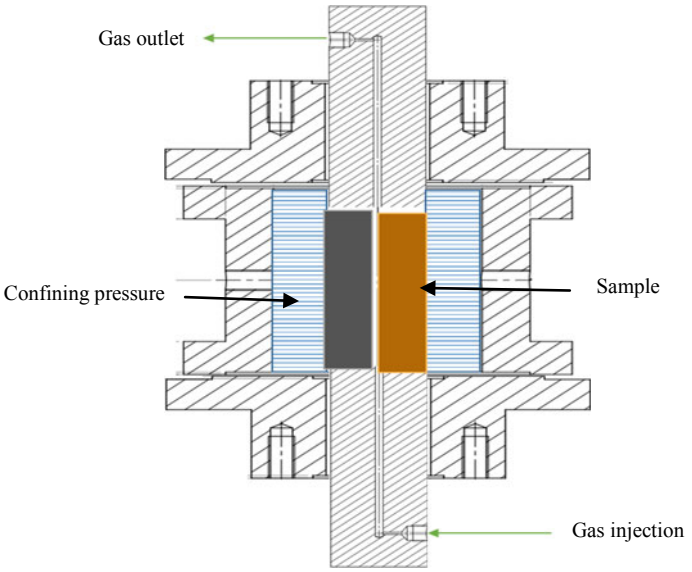

Fig. 2 HOEK's cell

where μ is the dynamic viscosity of the gas (2.2×10^{-5} Pa s for Argon), A is the section (m^2) and L the length of the sample (m). K_g is in m^2 and *Q0* is the flow (m^3/s).

For concrete, gas permeability was measured after drying. After oven drying at 65 °C, average dry permeability for concrete reaches 1.3×10^{-16} m^2 with a standard deviation of 2.8×10^{-17} m^2 and a median value of 1.27×10^{-16} m^2,we tasted eight samples for concrete permeability.

Drying of Boom Clay is likely to produce significant macro cracking. Gas permeability of dried Boom Clay would then not be representative of the sound material. Water permeability was then measured. For a full understanding of transfer mechanism, it is still necessary to study effective gas permeability of the Boom Clay (i.e. determining the relationship between gas permeability and water saturation). This is part of the experimental plan of this study and will be performed in a close future. The test procedure is close to the one for gas permeability. The injection device is replaced by an Isco® pump allowing a very precise monitoring of the injected water volumes with a resolution of a few micro liters. The water injected is water reconstituted according to [3]. The water flow rate Q is measured at the sample inlet and it makes it possible to obtain the water permeability K_w using Darcy's law for uncompressible fluids (Eq. 2):

$$Kw = \frac{\mu * Q * L * P}{A * (Pi - P0)} \tag{2}$$

where μ is the dynamic viscosity of water (10^{-3} Pa s at 20 °C).

Water permeability has been measured under two effective Terzaghi average stresses of 2.25 and 4.5 MPa. We have chosen a water injection pressure of 1.5 MPa giving an average pressure (linear profile) of 0.75 MPa. Confining pressures have then been fixed to 3 and 5.25 MPa. Boom Clay is not isotropic but stratified, the effect of strata orientation has then been considered by measuring the permeability of samples carrotated in the direction of the strata and in the perpendicular direction.

Measured water permeability ranges between 1 and 8×10^{-19} m^2. The effect of effective Terzaghi stress was small, and flow along the plan of strata is about two times higher than the one measured perpendicularly to the plan of strata.

Those results will then allow determining if gas flow on reconstituted interfaces can be considered as mainly controlled by interface aperture or if we have to consider Darcy's flow across the two half samples of concrete and Boom Clay.

3 Influence of the Confining Pressure on the Interface

The objective is to study the behavior of the interface (opening/closing) following mechanical loading and unloading (confining pressure). A preliminary test has been conducted to measure gas flow rate on reconstituted interface. When compared to the flow rate due to Darcy's flow [4, 5], it appeared that it was 3 orders of magnitude higher. We can then consider that gas is mainly flowing in the interface and we will then neglect the part of gas flow across the two half samples. Darcy's law is no longer applicable and we will then use Poiseuille's law (Eq. 3) in the case of a flow of a compressible fluid between two planes to analyse experiments. Injection and drainage pressure being known measuring the gas flow rate allows estimating the average hydraulic opening of the interface. This is how the behavior of the interface under mechanical loading will be monitored in this study.

$$qx = \int_{-a/2}^{a/2} vx(z)dz = \frac{-\omega a^3 \Delta P}{12\mu \Delta x} \tag{3}$$

q: is the Poiseuille's flow, a: is the value of the opening/closing.

Four experiments have been conducted, on four different samples, aiming four different maximum confining pressures (17, 22.5, 30 and 45 bars). To observe the behavior of the interface, the confining pressure was gradually increased by stages to reach the targeted pressure, before decreasing confining pressure. It can be seen on a similar behavior of the interface.

The interface is gradually closed following the increase of confining pressure. Unloading led to a partial re-opening of the interface. For example, for the third test (Fig. 3c), interface opening gradually decreases from 28.03 μm at the start under 9 bars of confining pressure until 5.54 μm under 30 bars. Unloading at 19 bars leads

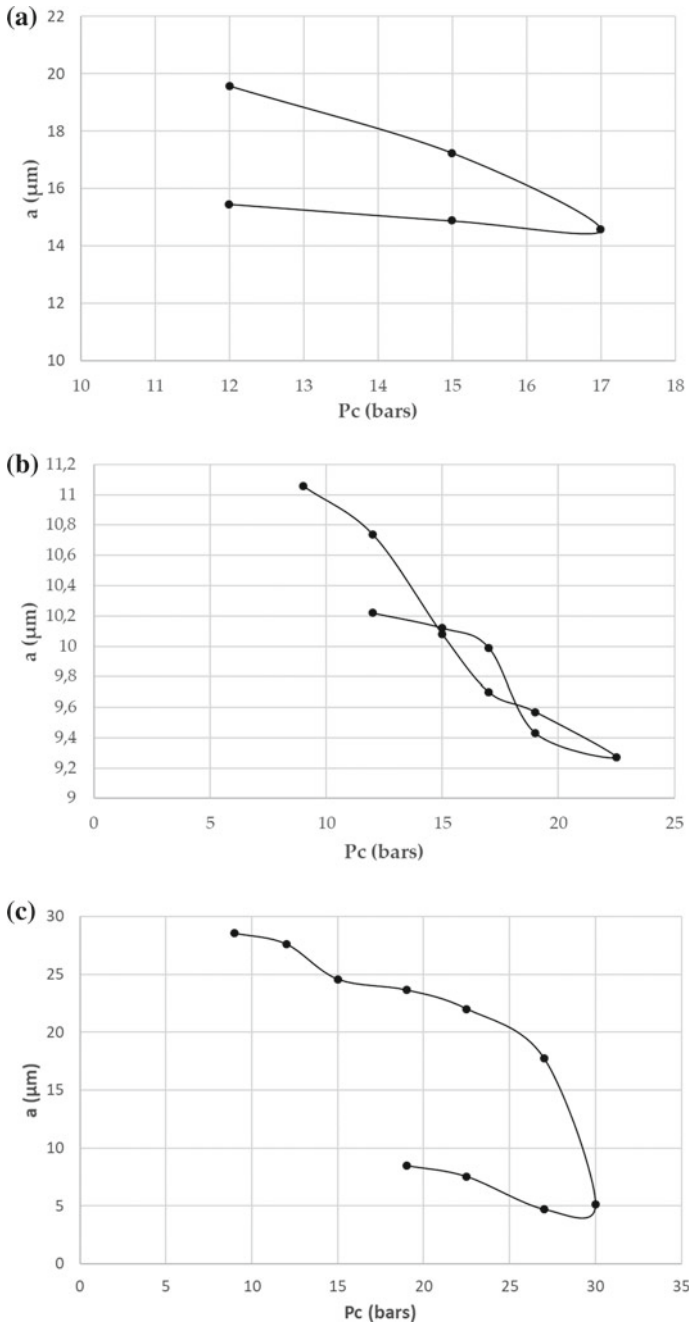

Fig. 3 Opening and closing of the interface in function of Pc **a** Pc = 17 bars, **b** Pc = 22.5 bars, **c** Pc = 30 bars, **d** Pc = 45 bars

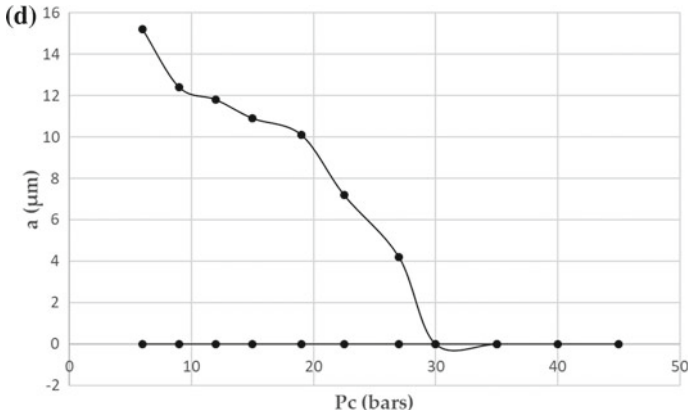

Fig. 3 (continued)

to a moderate reopening, showing the irreversibility of the mechanism (under 19 bars crack opening was measured was estimated at 23 µm and reached 8.5 µm after unloading).

Despite similar manufacturing processes of the four reconstituted interfaces, the four samples are all different, and this lead to different initial opening values. This can be attributed to geometrical imperfections or roughness difference. In order to compare the different tests that will be conducted in this study it is crucial to identify pertinent indicators of the interface in the initial state.

Using initial opening did not appear to be a good indicator. Indeed, analysis of the fours tests shows, for example, that there is no correlation between initial opening and stress sensitivity. This is illustrated in Fig. 4. A normalized opening has been

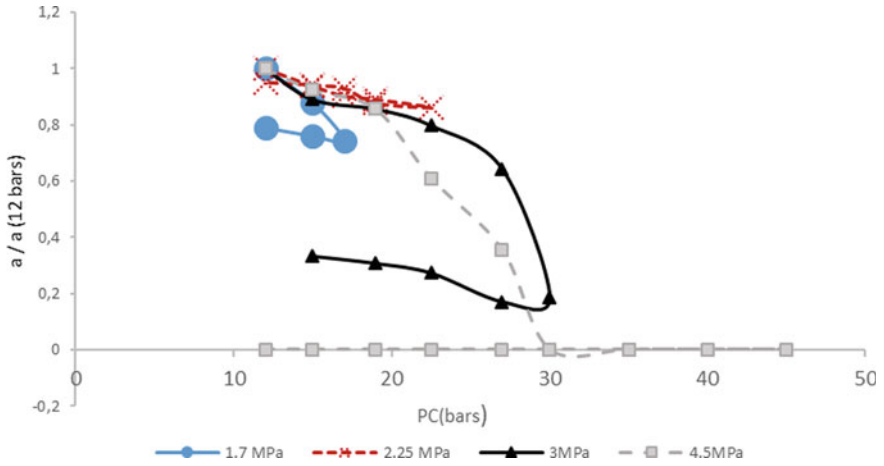

Fig. 4 The interface opening at Pc = 12

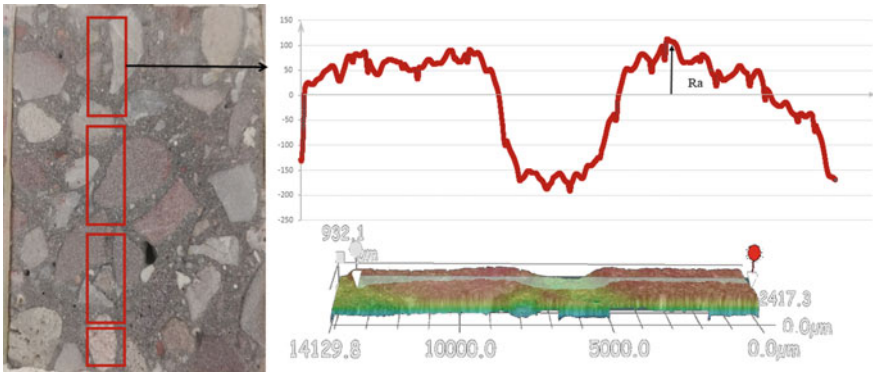

Fig. 5 Picture of concrete interface (left), recomposed profile obtained using Keyence optical microscope (right)

plotted dividing the opening for different confining pressures by the opening under 12 bars of confining pressure for an easier comparison of the results.

In order to characterize the initial state of the interface, we have decided to evaluate its roughness. Furthermore, using initial roughness and interface closure, it would be possible to estimate the contact surface between the two sides of the interface which will be an important parameter to analyse long term behavior of the interface.

A Keyence® optical microscope has been used to estimate the average arithmetic roughness. Figure 5 shows the results of this test on a sanded concrete sample.

Roughness has been evaluated by calculating R_a, which is the arithmetic mean height. It corresponds to the mean of the absolute values over the base length and is calculated according to the formula below:

$$Ra = 1/L \int_0^L |z(x)| dx \tag{4}$$

Different profiles and roughness calculation have been performed in order to estimate the suitability of this interface characterization procedure. Due to the size of the observation window, several profiles have to be considered in order to obtain an average roughness value. On this sanded concrete sample, average roughness has been evaluated to 425 µm. R_z (which is calculated as $R_z = \max(|z(x|))$ reaches 765 µm. During the next steps of the experimental plan, the link between roughness and interface behaviour will be investigated.

It has to be underlined that a good agreement between average opening of interface and roughness measurement is not expected. Indeed, hypothesis on the evaluation of interface opening using Poiseuille's law assume a flow between two parallel plans which is obviously far from the real shape of the interface. Nevertheless, using Poiseuille's law remain an efficient tool to monitor the closure of the interface which cannot be performed directly.

4 Conclusion and Perspectives

This paper presents the first results on mechanical behavior of Boom Clay-concrete interfaces. Poiseuille's law has been used to monitor the opening and closure of the interface according to confining pressure. This methodology has allowed to measure the variation of interface opening and the irreversibility of the mechanism during unloading. Due to hypothesis on the shape of the interface to use Poiseuille's law, measured openings are not absolute values. Nevertheless, the variation of this opening remains usable. It appeared that a good characterization of the initial state of the interface was necessary to analyze the results. We have chosen to measure the roughness of the sides of the interface as an indicator.

This work is part of a larger experimental study in the framework of the geological radioactive waste disposal, in collaboration with the ONDRAF/NIRAS. It aims at investigating the mechanical behavior of the interface between the Boom Clay and the concrete lining of galleries under instantaneous or long term mechanical loading. The effect of this mechanical loading upon transfer properties (i.e. gas permeability, gas diffusion or breakthrough pressure) will also be studied.

References

1. ONDRAF/NIRAS.: Research, Development and Demonstration (RD&D) Plan for the geological disposal of high-level and/or long-lived radioactive waste including irradiated fuel of considered as waste, State-of-the-art report as of December 2012. ONDRAF/NIRAS, Rep. NIROND-TR 2013-12 E, no. December 2012, p. 413 (2013)
2. M'jahad, S.: Impact de la fissuration sur les propriétés de rétention d'eau et de transport de gaz des géomatériaux: Application au stockage géologique des déchets radioactifs
3. S. C. K. C. E. N. Blg.: Geochemistry of Boom Clay pore water at the Mol site Status 2004 (2004)
4. M'Jahad, S., Davy, C.A., Skoczylas, F., Talandier, J.: Characterization of transport and water retention properties of damaged Callovo-Oxfordian claystone. Geol. Soc. Lond. **443**, 159–177 (2017). https://doi.org/10.1144/SP443.23
5. Liu, J.F., Song, Y., Skoczylas, F., Liu, J.: Gas migration through water-saturated bentonite–sand mixtures, COx argillite, and their interfaces. Can. Geotech. J. **53**(1), 60–71 (2016). https://doi.org/10.1139/cgj-2014-0412

Experimental Study for Making Easily to Recovery of RC Piers Damaged by Earthquakes

Hisako Kobayashi, Kaoru Kobayashi, and Takeshi Yamamoto

Abstract Many reinforced concrete (RC) piers have cut-offs where the number of rebars in the longitudinal direction are reduced according to the cross-sectional force. When such piers, the cover concrete in the intermediate section of RC piers can fall off in large earthquakes. Usually RC piers receive damage at their bases when large earthquakes lateral force act. Thus, for RC piers set in a river or those with deep-set bases, it can be that recovery work after earthquakes would require huge temporary construction facilities and result in large expenses and work time (Fig. 1). If damage can be made occur above the water surface and the ground level where recovery work can be easily done, more reasonable aseismic design of RC pier structure including recoverability can be achieved. In this research, we carried out cyclic loading tests using 3 specimens having cut-offs. We studied which position of piers will yield and failure occurred based on the cyclic loading tests. We set a flexural performance ratio (ratio of bending moment to flexural yield strength) at the rebar cut-off point. This ratio is the quantitative value that controls damage in the intermediate section of the frame. As a result, the difference in yield position and bending fracture due to difference in a flexural performance ratio, and difference in position of between yield and flexural fracture due to reinforce the inner spiral rebar of the cut-off point were clarified.

Keywords Cut-off point · Cyclic loading test · Flexural damage

H. Kobayashi (✉) · T. Yamamoto
East Japan Railway Company, 2-479, Nisshin-cho, Saitama-shi 331-8513, Japan
e-mail: hisako-kobayashi@jreast.co.jp

K. Kobayashi
JR East Consultants Company, 1-1-1, Nishi-Shinagawa, Shinagawa-ku 141-0033, Japan

E. B. Pereira et al. (eds.), *Proceedings of the 3rd RILEM Spring Convention and Conference (RSCC 2020)*, RILEM Bookseries 32,
https://doi.org/10.1007/978-3-030-76547-7_19

1 Introduction

On October 23, 2004, the Niigataken-chuetsu earthquake, with a magnitude of Mj = 6.8, occurred in Japan (Fig. 1). Figure 2 shows the cover concrete can spall in the Niigataken-chuetsu earthquake. This damage were showed in the Higashi-nihon-taiheiyo-oki earthquake on March 11, 2011.

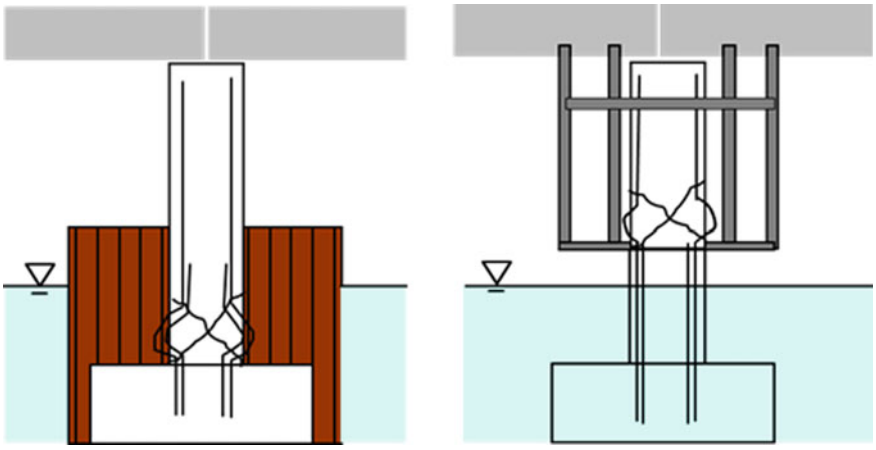

Fig. 1 Images of RC piers repairing

Fig. 2 Damage of RC piers after the earthquake

With a design that prevents damage at cut-offs, however, damage can occur at the pier bases, making it difficult to find damage of RC piers that are set in rivers or underground.

We have been studying a structure that can make flexural damage occur at the cut-off point of RC piers excellent in elastoplastic energy absorptivity. The aim of intentionally allowing damage in the intermediate section of a pier frame is to facilitate easier checking and detection of damage and thus earlier recovery.

In this study, we examined the difference in the damage form of the specimens due to the difference in the flexural performance ratio at the cut-off point, and the difference in the damage form when the inner spiral rebar was set into the specimen.

2 Experimental Programs

2.1 Outline

Table 1 shows the specimen specifications used in the experiment (a: sheer span, co: height of cut-off point from the base).

Table 2 is a material specifications, and Fig. 3 shows a shape and reinforcement arrangement of specimens (Myb: Yield bending capacity at the base, Myc: Yield bending capacity at the cut-off point, Mxyc: bending moment at the cut-off point, Myc/Mxyc: racio of bending moment at the cut-off point to yield bending capacity at the cut-off point).

Assuming RC piers of common railway structures, we used model specimens of one-third scale. The axial rebar had cut-offs, the rebar diameter was D10, and the thickness of the cover concrete was 35 mm. In this experiment, with the expectation of sufficient deformation performance of the intermediate hinge, an inner spiral was placed in No. 3 at a height of 550 mm with 1D (350 mm) + upper and lower ends 10φ (100 mm) around the cut-off point. And the other 2 specimens have no inner spiral reinforcement, but have hoop ties at the over the entire height (Fig. 3).

As shown in Fig. 3, the length of the area provided with inner spiral reinforcement was 1D (350 mm) + 100 mm above and below that (550 mm total), with the cut-off at the middle. In order to more clearly identify the effect of inner spiral reinforcement, we used easily removable D6 tie hoops of right-angled hooks at Upper and lower ends of that area.

Figure 4 shows the loading status of the specimen. The loading method is described in Chap. 2.2.

Table 3 shows calculated result of specimens. The ratio of calculated shear capacity to flexural capacity of the specimens is between 3.06 and 3.43 under the rebar cut-off point and between 2.48 and 3.68 above the rebar cut-off point. We avoided remarkable shear damage, based on the past studies [1, 2]. The flexural performance ratio at the rebar cut-off point at the bending yield is between 1.05 and 1.09.

Table 1 Specimen specifications

Specimen No.	B*H, mm	a (sheer span), mm	d (effective-depth), mm	co (height of cut-off), mm	Axial rebar arrangement		Inner spiral reinforcement			Axial force, Mpa
					cut-off	base	φ	pitch mm	number	
1	1050*350	2200	315	1280	D10*10	D10*18*2 layers	–	–	–	0.60
2	1050*350	2200	315	1200	D10*16	D10*228*2 layers	–	–	–	0.50
3	1050*350	2200	315	1280	D10*16	D10*18*2 layers	9	20	4	0.60

Table 2 Material specifications

Specimen No.	Pier concrete strength (Mpa)	Footing concrete strength (Mpa)	Axial rebar yield strength (Mpa)	Spiral rebar yield strength (Mpa)	Horizontal rebar yield strength (Mpa)	Myb (kN m)	Myc (kN m)	Mxyc[*1] (kN m)	Myc/Mxyc
1	22.1	26.1	386	–	381	278.12	121.72	116.30	1.05
2	26.9	31.7	390	–	404	330.75	164.44	150.34	1.09
3	22.9	27.8	388	336	409	280.57	122.70	117.33	1.05

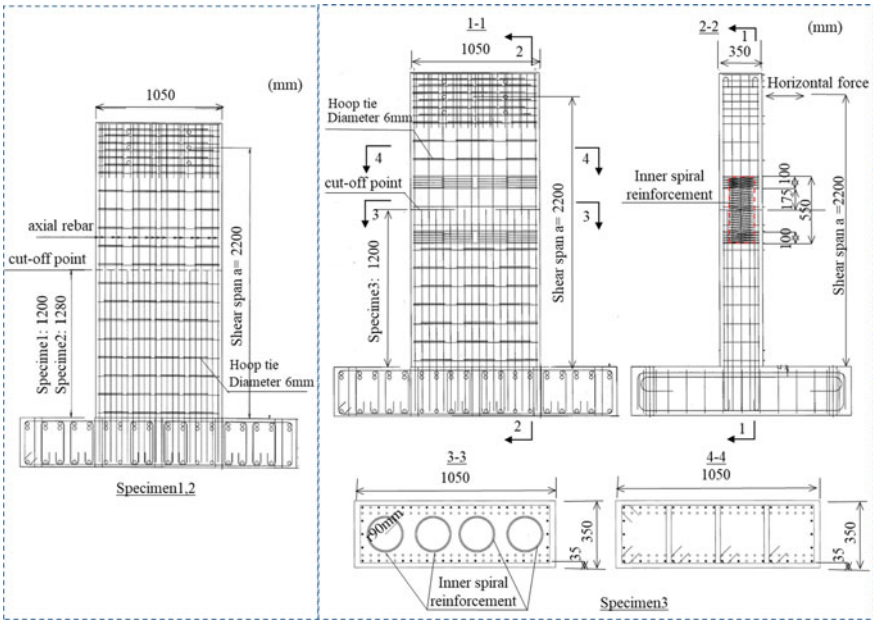

Fig. 3 A shape and reinforcement arrangement of specimens

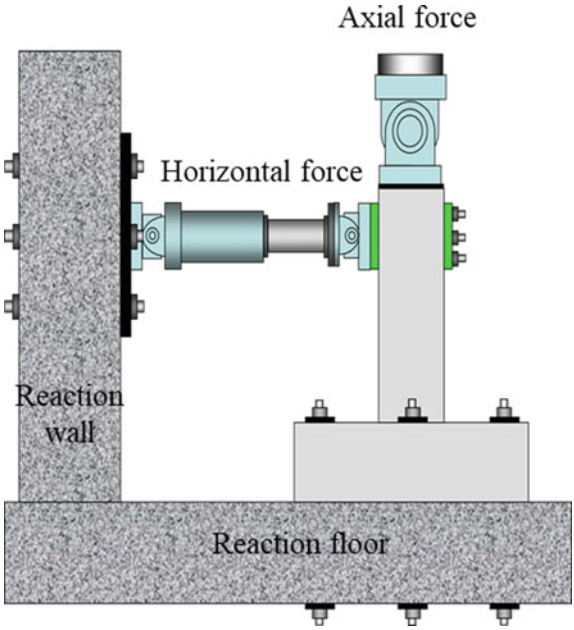

Fig. 4 Loating status of the specimen

Table 3 Calculated result of specimens

Specimen No	Vmyb[a] (kN)	Vmyc[b] (kN)	Vyc[c] (kN)	Vyb[d]/Vmyb	Vyc/Vmyc	Myb (kN*m)	Myc (kN*m)	Myc/Mxyc[5]
1	126	95	350	3.25	3.68	278.12	121.72	1.05
2	150	137	396	3.06	2.89	330.75	164.44	1.09
3	128	96	238	3.43	2.48	280.57	122.70	1.05

[a]Vmyb = Myba
[b]Vmyc = Myc/(a-co), Myc: Yield bearing capacity at cut-off point
[c]Vyc: Yield sheer strength at cut-off point
[d]Vyb: Yield sheer strength at base
[e]Mxyc = Myb*(a-co)/a

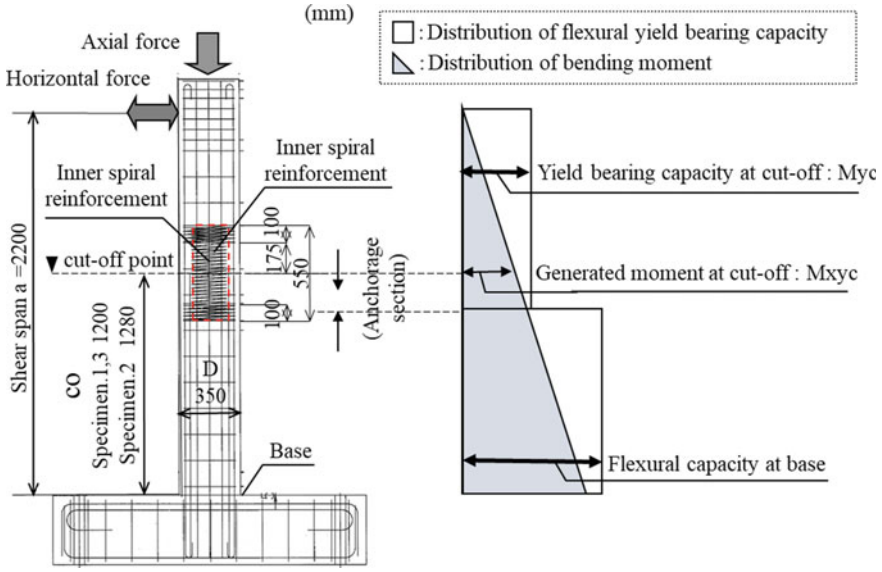

Fig. 5 Specimen overview

2.2 Loading Method

As shown in Fig. 5, the cyclic loading point was set at 2,200 mm from base. We carried out positive and negative loading once each while applying axial force to each specimen.

In the cyclic loading test, we defined as "yield displacement δy" the horizontal displacement of the load point at the point when the strain of the main reinforcement of the specimen base on the outermost edge in the loading direction reached the yield strain. We applied loads, sequentially increasing the displacement amplitude by the integral multiple of horizontal displacement n*δy (n = 1,2,3…,10 δy).

3 Experimental Results

3.1 Failure Properties at Yield Load and Maximum Load

Figure 6 shows the strain distribution when the axial rebar yields.

The pink line shows non cut rebar and the blue line shows cut-off rebar.

Specimen 1 axial rebar yielded at the cut-off point slightly earlier yield than at base. Specimen 2 with flexural performance ratio 1.09(larger than Specimen 1) yielded at base. In addition, Specimen 3 with the same flexural performance ratio as Specimen 1 has an inner spiral rebar near cut-off point, yielded at base.

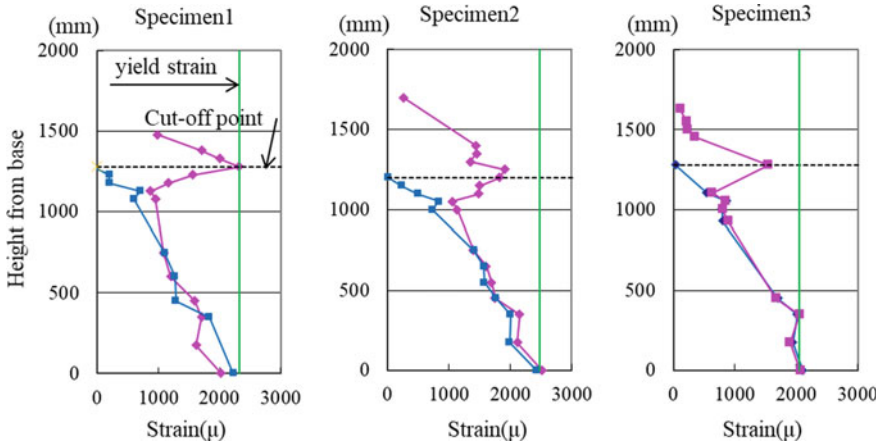

Fig. 6 Strain distribution when the axial rebar yields

Focus on the strain distribution of the axial rebar and the cut-off rebar overlaps.

It can be seen that Specimen 3 with an inner spiral rebar near the cut-off point have longer overlapping areas between the non-cut rebar and the cut-off rebar than another specimens. From the strain distribution, it can be seen that the cut-off rebar of specimen 3 has less the bond deterioration at yield point.

Figure 7 shows the strain distribution of the axial rebar at the maximum load. Only specimen 3 with the inner spiral rebar placed near the cut-off point shows that the strain is very small at the cut-off position.

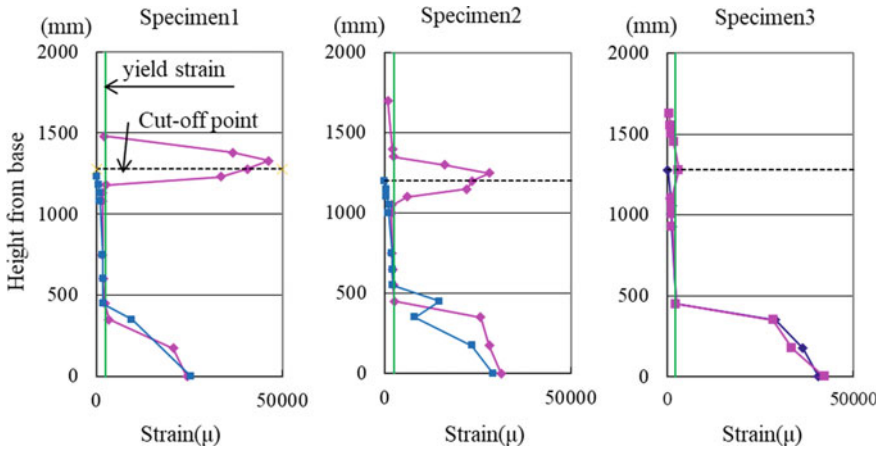

Fig. 7 Strain distribution at maximum load

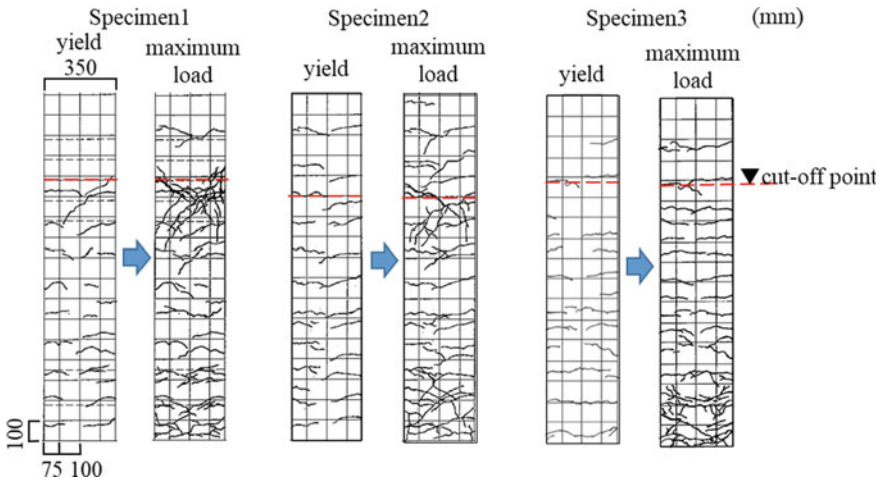

Fig. 8 Crack diagrams at yield and maximum load

Specimen 1 with a flexural performance ratio of 1.05 had the largest strain at the cut-off point. Specimen 2 with a flexural performance ratio of 1.09 had almost the same strain at the cut-off point and the base.

Figure 8 shows crack diagrams at yield and maximum load.

Focus on the crack diagram at the maximum load.

Specimen 1 crack had many oblique cracks near the cutoff point, forming a plastic hinge. The cracks of specimen 2 developed at both the base and the cut-off point, but the damage near the cut-off point is smaller than that of specimen 1.

Specimen 3 had many cracks at the base and flexural cracks were dispersed throughout.

The strain distribution of specimen 3 developed only near the base, and it can be seen from the crack diagram that there was little damage near the cutoff point.

3.2 Failure Properties at the Load Drop After the Maximum Load

Figure 8 shows load-displacement relationship when the yield load (Py) of each specimen is set to 1.0 (Fig. 9). And Fig. 10 shows damage of specimen after the load dropped to the under yield load.

Specimen 1 and 2 broke near the cut-off point, and specimen 3 broke at the base.

Displacement at the loading point that started to decrease, specimen 1 was 6δy, specimen 2 was 6δy, and specimen 3 was 7δy. The displacement at the horizontal load lower than the yield load was set as δu. Then calculated δu/δy, specimen 1 was 7.14, specimen 2 was 7.04, and specimen 3 was 7.83.

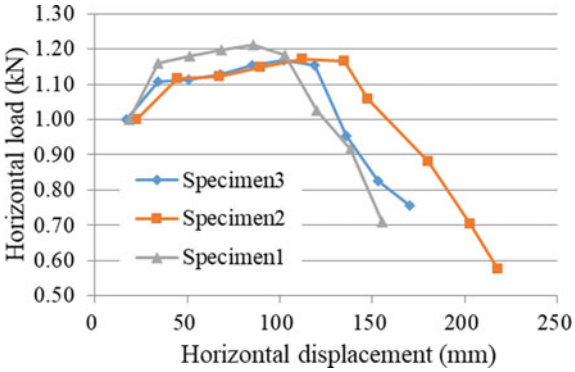

Fig. 9 Load-displacement relationships

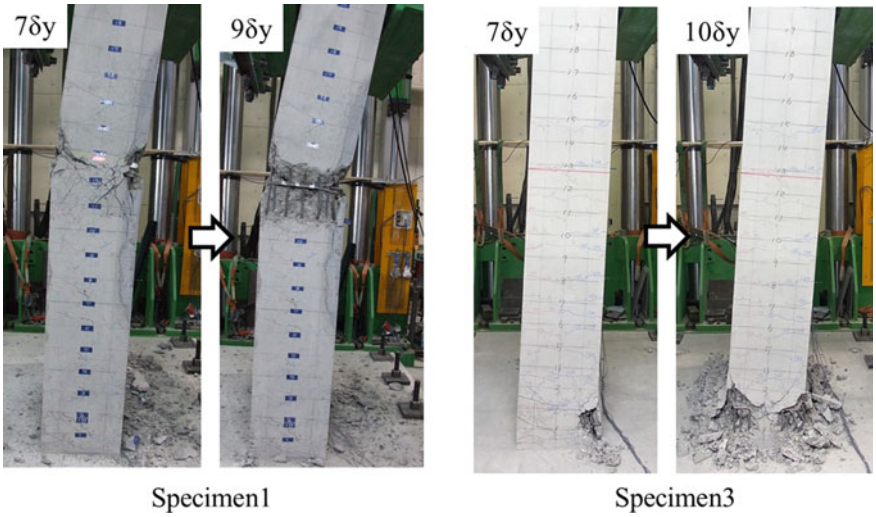

Fig. 10 Damage of specimen after the maximum load

4 Conclusions

The following results were obtained from the cyclic loading test of three specimens having cut-off points.

- Specimen 1 with a flexural performance ratio of 1.05 yielded at the cut-off point and then flexural failure occurred around the cut-off point. And a flexural performance ratio of 1.05 is bigger to failure occurred at the cut-off point, it need to smaller at the cut-off point.
- Specimen 3 with a flexural performance ratio of 1.05 which have the inner spiral rebar around the cutoff point, yielded at the base and the flexural failure occurred

at the base. Even at the same flexural performance ratio, it was found that the yield and failure positions could be controlled by inserting a spiral reinforcing bar inner the cut-off point position.

- Specimen 2, whose flexural performance ratio was increased to 1.09, yielded at base and flexural failure occured at cut-off point. The reason why yield of the rebars first occurred at the base and damage then shifted to the rebar cut-off point was that expansion of the area of rebar yield at the base shifted the generated bending moment. As the generated bending moment near the rebar cut-off point increased, damage consequently shifted from the base to the rebar cut-off point.
- The yield strain of the longitudinal rebar and the cut-off rebar of specimen 3 was smallest of the bond deterioration at the cut-off point than other specimens. We believe that the inner spiral rebar restrains the core concrete of pier at cut-off point position, and suppressed the deformation at cut-off point, thereby reducing the bond deterioration of the cut-off rebar.
- $\delta u/\delta y$ (dividing the displacement:δu when the load had get smaller than the yield load by the yield displacement:δy) was the highest value in specimen 3 with 7.83. Specimen 1 was 7.14 and specimen 2 was 7.04, almost the same value.

References

1. Ishibashi, T., Tsuyoshi, T., Kobayashi, K., Kobayashi, M.: An experimental study on damage levels and repairing effects of reinforced concrete columns subjected to reversal cyclic loading with large deformation. Japan Soc. Civil Eng. J. Mater. Concrete Struct. Pavements **47**(648), 55–69 (2000)
2. Railway Technical Research Institute, comp. Railway Bureau, Ministry of Land Infrastructure, Transport and Tourism edit., Design Standards for Railway Structures and Commentary (Concrete Structure), Maruzen Company Limited (2004)

Resilience Strategy After 2016 Central Italy Earthquake in Historical Centres: Seismic Vulnerability Assessment Method of Traditional Masonry Buildings

L. Bernabei, R. Gulli, G. Mochi, and G. Predari

Abstract The experience of the 2016 earthquake in central Italy shows that the approach to the post-seismic phase is still based on an emergency approach, while the prevention and the reduction of seismic risk are proving difficult. In the particular context of rural and mountainous area, the seismic shock produced the depopulation of several minor historical centres and the scattering of urban communities. This kind of damage had dramatic impacts on the possibility of both preservation and restoration of traditional architectures, due to the specificity of the peculiar material used and construction techniques. In order to reverse the trend, the goal of future interventions must be to provide a reconstruction strategy, with the aim of defining the problems to be solved as a priority in the post-seismic phase and, at the same time, to provide risk prevention measures also within ordinary planning. The starting point of the current research is the impact of the earthquake on the historical centre of Caldarola to evaluate the damage state through three types of analyses: at the urban scale to identify the performance deficits that caused the loss of functionality of the whole urban system; at the building scale, through an expeditious assessment method to identify the vulnerability of the building façade in relation to the usability of the emergency routes; in addition, the vulnerability of the building aggregates have been examined to verify the correspondence between the real damage occurred post-earthquake. The analysis results highlight a strong link between the development of an empirical vulnerability assessment and the more effective strategies of damage mitigation.

Keywords Seismic vulnerability · Expeditious assessment method · Historical centres · Built environment resilience · 2016 Central Italy earthquake

R. Gulli · G. Predari
Department of Architecture, University of Bologna, Bologna, BO, Italy

L. Bernabei · G. Mochi (✉)
Department of Civil and Environmental Engineering, University of Perugia, Perugia, PG, Italy
e-mail: giovanni.mochi@unipg.it

E. B. Pereira et al. (eds.), *Proceedings of the 3rd RILEM Spring Convention and Conference (RSCC 2020)*, RILEM Bookseries 32,
https://doi.org/10.1007/978-3-030-76547-7_20

1 Introduction

The recent disaster events occurred in Italy have resulted in a renewed interest on safety issues in many at-risk areas.

The 2016 Central Italy earthquake hit 138 municipalities that are divided into four regions, spanning 8,000 km^2 [1]. There were three main seismic events:

- On the 24th of August 2016, Mw 6.0 epicenter in Accumoli (RI), Amatrice (RI), Arquata del Tronto (AP);
- On the 26th od October 2016, Mw 5.9, ore 21:18, Castelsantangelo sul Nera (MC), Visso (MC), Ussita (MC) and Preci (PG);
- On the 30th of October 2016, Mw 6.5, ore 07:40, Norcia (PG), Castelsantangelo sul Nera (MC) and Preci (PG).

The first one caused the destruction of the entire villages and serious human losses. The last two caused damage only on the building stock because the majority of villages had been evacuated. The most affected region was the Marche region: widespread damage in 85 municipalities forced the 22.6% of regional residents to abandon their homes and carry on living in a different place. In the immediate aftermath of the earthquake, the first step was to count the damage on the building stock in the urban settlement. Moreover, from a social point of view, human settlement faced a progressive loss of identification, which considerably undermined economic and social life leading to an impoverishment [2]. The disproportion between the potential destructiveness of earthquakes, expressed through their magnitude, and the devastating impacts can be ascribed to several factors, including the high exposure of the population, the obsolescence of many buildings, the high seismic vulnerability of the historical centres and of the huge Italian cultural heritage and monuments. At the same time, seismic risk mitigation policies require a different and parallel approach to be pursued, including the knowledge improvement, the reduction of the vulnerability and exposure, the mitigation of the effects [3].

Starting from the 2009, the Italian Government launched a National Plan for Seismic Risk Prevention dedicated to the establishment of safe public buildings and to the allocation of funds for evaluating local seismic hazard, aiming at defining an exhaustive seismic classification of the entire territory. In order to integrate the seismic risk mitigation at the municipal scale, the Italian Government introduced the so-called Limit Condition for the Emergency (LCE) [4]. The aim of this tool is to examine the efficiency of the emergency management systems by considering some buildings and routes as strategic elements and infrastructures, which must be preserved after a seismic event, as well as their internal connection and their access routes from the external territorial context.

However, seismic prevention remains a difficult goal to be fully achieved; the relevance of this type of indirect action, such as LCE, is a new vision of urban settlement as a system that can respond to disasters by its fundamental elements. Moreover, it is necessary to support investigation about the buildings vulnerability

to identify both the strategic elements and the significant critical condition in order to avoid envisaged damage scenario.

Buildings evaluation requires historical surveys and inspection that would take time. Due to this reason, the purpose of this research is the definition of vulnerability assessment measures to identify the buildings that need to be restored first and avoid envisaged risk condition. Defining the vulnerability conditions of buildings before a seismic event is the key factor to enhance seismic risk reduction strategies in order to improve the resilience of building heritage in historical centres and to create safer urban settlement.

The challenge of this kind of tools for the disaster risk reduction is to change government's approach, starting from the emergency planning to the application of prevention strategies by designing ordinaries urban transformations. Consequently, short and long-term strategies could effectively permit communities to live in safely and protect their cultural heritage and socio-economic assets.

In this particular framework of the reconstruction phase in Central Italy, an increased public awareness of seismic hazards highlights the requirement of preventive measures to preserve the architectural heritage and to boost the resilience of at risk or already affected territories and communities.

Moving from these suggestions, the aim of current research is to show strategies and planning tools to be applied in post-disaster reconstruction program as an opportunity to introduce prevention measures in the ordinary urban management and to implement a strategic plan for the regeneration of the affected areas. The following evaluating tool allows to reduce the seismic risk in advance intervening directly in vulnerability and exposure, instead of restricting the intervention to the aftermath of earthquake.

With the purpose to reaching the real effectiveness of the following research during the reconstruction phase, this paper is part of the PRIN 2017 research project, funded by MIUR (Ministry of Education, University and Scientific Research of the Italian Government), entitled "*BE S2ECURe - (make) Built Environment Safer in Slow and Emergency Conditions through behavioUral assessed/designed Resilient solutions*".

2 Methodological Approach and Phases

The academic discussion concerning seismic risk during last decade has shown a growing awareness of the need to reduce disaster risk in urban areas by adopting a wider perspective, not only focused on the single building but also on the urban and territorial system as a whole. In fact, urban centres are complex systems that cannot be reduced to individual elements, but they include the interaction between buildings and the functional organization.

When dealing with earthquakes, it is currently impossible to predict when they will occur and how intense the shock will be; however, the risk and the impact on the built environment can be mitigated by reducing vulnerability and exposure in the site.

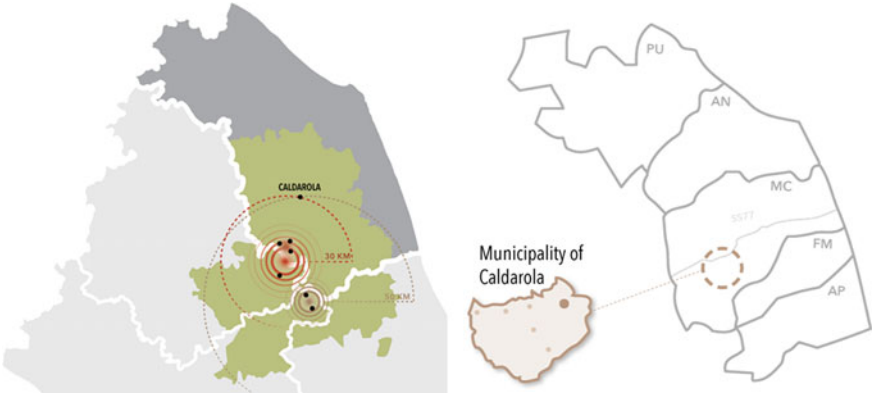

Fig. 1 Areas affected by the 2016 central Italy earthquake and the case study

The urban settlement risk evaluation requires an integrated approach for vulnerability assessment that takes into account urban aspects and specific structural building conditions [5]. From an urban point of view, vulnerability is affected by the morphological asset of historical centres, because narrow and winding streets and the lack of open spaces do not guarantee safety. On the other hand, the building vulnerability is increased by a large presence of un-reinforced masonry buildings and by their specific structural evolution resulting from an old aggregation process, such as unmanaged stratifications and lack of maintenance.

These types of situations are widespread in the whole area of central Italy affected by the earthquake in 2016. In this context, the current survey proposes a case study in the Marche region, the historical centre of Caldarola (Fig. 1), with the aim of assessing the response to the earthquake of the urban system and the vulnerability and damage scenarios of the built environment.

The study methodology is developed in the following three sections, carried out first on urban scale and then on buildings.

2.1 Urban Vulnerability: The Emergency Response of the Urban System in the Post-earthquake Framework

The starting point was the need to solve the problems of a real case, since the dramatic impact of an earthquake provides certain and immediate answers to the question "which parts of city cause the disruption of activities and put human life at risk?". In order to investigate the emergency response of an urban system to an earthquake, the recognition of damages assists in finding prompt and consistent solutions which otherwise would be difficult to determine in ordinary conditions. Therefore, it is important to start the analysis from the current urban asset to identify the performance

deficits of the system and then find all the necessary actions to achieve a future urban safety condition.

Emergency management is partially included in the current National Seismic Prevention Program, promoted by the Italian Department of Civil Protection (DCP). In fact, the DCP adopted the Limit Condition for Emergency (LCE) by introducing a planning concept that depends on the performance-based seismic design. The LCE is based on the Urban Limit States and identifies the necessary emergency routes to access areas and buildings having strategic functions in the post-earthquake framework. Assuming that urban vulnerability could involve different sub-systems by affecting their functionality, the LCE guarantees strategic functions for the emergency management, even if urban functions are gradually interrupted. The main limit of this tool is that it does not have a forward-looking approach because it only controls the state of emergency and does not help the urban system recovery.

In order to preserve the urban system after the shocks, the Umbria region introduced the concept of *minimum urban structure* in the urban-planning regulation, with the so-called SUM tool (*struttura urbana minima* in Italian, *minimal urban structure* in English) [6]. The SUM identifies parts of an earthquakes-resistant urban system, so that they remain functional even during the emergency and reconstruction phase, aiming at guaranteeing the preservation of urban life and becoming the driving force behind the recovery. The SUM determines several urban sub-systems where the strategic functions, their internal connection and the access routes from the territorial context are preserved anyway. Moreover, it represents a suitable planning tool for historical centres for the vulnerability assessment of the urban fabrics, both on an architectural scale and on an urban scale. Unfortunately, nowadays we have very few application examples [7] of SUM because it is required only in Umbria region and its methodology has been the major reference in Italy overtime.

In the current case study, our steps follow this approach to identify which urban sub-system caused the collapse of the historical centre of Caldarola on the 30th October of 2016. The main problem occurred in the mobility system because the main road was occupied by debris that blocked the access to emergency services and the connection with the other municipalities in the territorial context. Moreover, after the security checks, 90% of the buildings were declared unsuitable for use and the whole centre was closed for over two years.

2.2 Expeditious Vulnerability Assessment for Façades Facing the Public Areas and Rescue Routes

Depending on the observations of the damage scenarios after an earthquake, we can identify all the parts of the settlement that have been collapsed, that have interfered with the evacuation and that have affected the safety of the fleeing people and rescuers. This shows that urban vulnerability is strictly related to the possible overturning mechanisms of the walls facing the street. Therefore, the emergency

response of an urban system is more effective if a number of routes are safe and free from debris or fallen obstacles. So, these rescue routes should be preventively identified by considering the accessibility and damage scenarios. This type of action planning could improve performance against catastrophic events by strengthening urban elements and enhancing the interaction between them.

Moving from these suggestions, we identified a critical urban context and two masonry building aggregates in order to determine the causes of the debris and to assess the seismic vulnerability of the façade facing the main road (that was scattered from debris after the shock) through an expeditious assessment method that calculates the tendency of the façade to overturn. This type of analysis, if carried out throughout the whole historical centre, provides a risk map of serious vulnerabilities which represent the essential background knowledge for the reconstruction plan aimed at improving the overall resilience of the settlement and providing seismic preventive actions. Therefore, the assessment method allows identifying the strategic buildings included in the LCE that must withstand the earthquake without collapsing to ensure the functionality of the paths connecting the emergency routes and nodes.

2.3 The Comparison Between Buildings Vulnerability and the Damage Suffered After Earthquake

An index-based method for masonry building aggregates [8] has been also applied in order to identify buildings that have a natural propensity to collapse than others; it is necessary to establish priorities interventions for them, to reduce their vulnerability. In addition, a damage index was calculated by an assessment method, in according to the EMS98 scale for masonry structures, numerically expressing the severity of the damage level. At the end of the analysis, we compiled a comparative ranking for the buildings, which showed a strong link between the empirical vulnerability assessment and the damage state, demonstrating the reliability of the applied methodology. Defining the vulnerability conditions of the buildings before a seismic event is a key factor in assessing the type of buildings that must be restored first.

3 The Application of Seismic Vulnerability Assessment Method on the Historical Centre of Caldarola

The historical centre of Caldarola, an Italian village located in the province of Macerata was chosen as particular case study. Caldarola is well-known for the historical significance of its architecture and for the natural scenery. The urban system demonstrated an inefficient reaction against the shock on the 30th October 2016, which led it to isolation because the access road was blocked from debris. The historical centre was closed for two years due to security investigation on buildings.

The earthquake had dramatic impacts on both protection and restoration of traditional architectures, due to the specificity of the peculiar material used and construction techniques. Moreover, from a social point of view, human settlement faced a progressive loss of identification, which considerably undermined economic and social life leading to an impoverishment.

Investigating the emergency response of the urban system to the earthquake highlights all the performance deficit in the settlement and which urban sub-system has failed (Fig. 2). In our specific case study, mobility was the major critical issue to be solved. In fact, there is only one main road (Via Roma) to access into the historical centre and the internal paths are insufficient to guarantee a safety evacuation. Moving from this analysis, we could identify a critical urban context coinciding with the built-up area at the entrance of the historical centre, aiming at assessing the vulnerability of the two building aggregates facing the main road (Via Roma). It could be possible to identify the overturning of three façade that interfered with the evacuation by analysing the pre and post shock photographs (Fig. 3).

The vulnerability assessment method, used for the following building aggregate evaluating, was carried out by Prof. Mochi and Prof. Predari within the Department of Architecture of the University of Bologna and had been adopted in different case studies affected by the Aquila earthquake in 2009 and Emilia Romagna earthquake in 2012 [9]. It is based on the determination of synthetic indicators providing a prior estimate of possible earthquake damages and identifying the fragilities of masonry buildings by considering their possible collapse mechanisms (I mode in-plane and II mode out-of-plane), such as the overturning of the façades.

The starting point of this approach was represented by the studies of Antonino Giuffrè, who already pointed out: "the earthquake does not disintegrate houses, but it

Fig. 2 Urban response of the historic centre of Caldarola

Fig. 3 Critical urban context: the damage state of three structural units of building aggregates

selects the structural parts and the weakest technological solutions, causing damage and collapse through mechanisms that can be defined in advance" [10].

First of all, the identification of the transformation phases constitutes the initial point of the calculation protocol, which leads to the current situation through the comprehension of the layout extensions, super-elevations, demolitions and reconstructions. So that, the synthetic vulnerability indicators require An exhaustive knowledge phase to be acquired, including a preliminary bibliographical research and an on-site survey in order to outline the evolutionary processes suffered by each aggregate in its planimetric and elevation development and to detect all the construction factors (based on techniques and design concepts used in the local area) which directly influence the seismic behaviour of the masonry buildings. On the other hand, the elements that positively influence the seismic response (such as the presence of anti-seismic devices and the good quality of the construction technique) are considered. Sometimes, the survey from outside of the building façades and from accessible courtyards is quite enough to collect all information for the application of the vulnerability assessment. The purpose of this methodology is to provide useful information to achieve a greater awareness in building interventions. Therefore, we used two different procedure to assess the vulnerability: the expeditious method was applied on the façade of the two building aggregates facing the main road and the analytic method was calculated on the 10 SUs (structural units) composing the building aggregate n.1. The first method requires only the ground floor plan and a

photogrammetric survey of the façades to identify the vulnerability indicators. The second is more detailed and requires an in-depth investigation.

The following Eqs. (1, 2) show how calculate building vulnerability through numeric index on a scale of values from 0 to 100: VGS index (global expeditious vulnerability) for the first methodology, and the VGA index (global analytic vulnerability) for the second one. They are calculated as the sum of partial indices, each multiplied by its own weight (whose total is 100), which is a sort of quantification of the relevance of each indicator within the overall building seismic performance.

These partial indicators are obtained from a critical evaluation of buildings technological solutions that can be identified the propensity to damage due to the construction lacks. They are based on the assumption that the out of plane mechanism is triggered from the loss of stability of individual components, which are seen as rigid blocks moving due to the ground acceleration [10].

They summarize the following collapse mechanism (Fig. 4):

- RF index: out-of-plane collapse of the façades;
- RT index: out-of-plane collapse of the tympanums;
- FP index: cracks due to the rafters;
- DM index (disconnection of wall): it derives essentially from the historic transformation processes of buildings and allows to define the portions of façades that can be subjected to out-of-plane collapse, and the width of the fronts to be considered effective for the shear mechanism;
- MSS/MCA index: hammering due to constructive irregularities (as the presence of buildings having a reinforced concrete structure inside the aggregate);
- VT index (weak shear strength): due to insufficient width of the masonry walls.

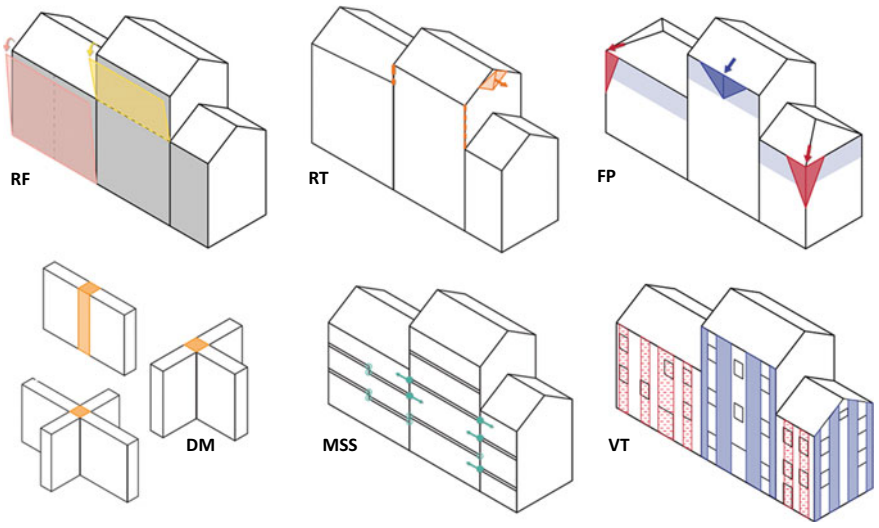

Fig. 4 Indicators for seismic vulnerability assessment

$$\begin{aligned} VGS \;=\; & TA \cdot P_{TA} + TP \cdot P_{TP} + FP \cdot P_{FP} + \; MSS \cdot P_{MSS} \\ & + MCA \cdot P_{MCA} + VT \cdot P_{VT} \end{aligned} \tag{1}$$

$$\begin{aligned} VGA \;=\; & RF \cdot P_{RF} + RT \cdot P_{RT} + FP \cdot P_{FP} + \; DM \cdot P_{DM} \\ & + MSS \cdot P_{MSS} + MCA \cdot P_{MCA} + \; VT \cdot P_{VT} \end{aligned} \tag{2}$$

The final result, represented by the global index, demonstrate the causal relationship with the damage describing the global aggregate seismic behaviour.

The focus point of the methodology is to identify, before the earthquake occurs, the situations of greatest fragility and the potential damage to parts of the buildings with the aim of providing the best intervention solutions and removing specific situation that put human safety at risk.

4 Results and Further Development of the Research

The widespread application to the façades of the building aggregates in the whole historical centre of Caldarola could represent a clear improvement in the preparation of emergency plans and in the development of preventive seismic actions at the urban scale. Moving from these suggestions, we estimate the total cost of the procedure by considering the required time for site inspections through the use of a portable photogrammetry tool. This survey procedure provides an exhaustive geometric description of the buildings that are investigated by the seismic vulnerability assessment and guarantees an economic evaluation of the whole urban settlement, as a result of the assumption of a small financial amount (lower than the direct economic losses due to the cost of the building restoration after earthquake) and 3–4 months required to complete the work.

Moreover, the expeditious assessment method highlights the major vulnerability of the building aggregate n.1; this result has caused by the RT index of the SU n.7 outlined in orange (see Fig. 5) representing the out-of-plane collapse of the tympanums that actually occurred after the 30th October seismic shock (Fig. 6).

On the other hand, the application of analytic assessment method to the 10 SUs (structural units) of the building aggregate n.1 allowed to verify how the vulnerability assessment method can identify in advance the damage occurred after seismic shocks.

Fig. 5 Facades of building aggregate (BA) 1 and 2

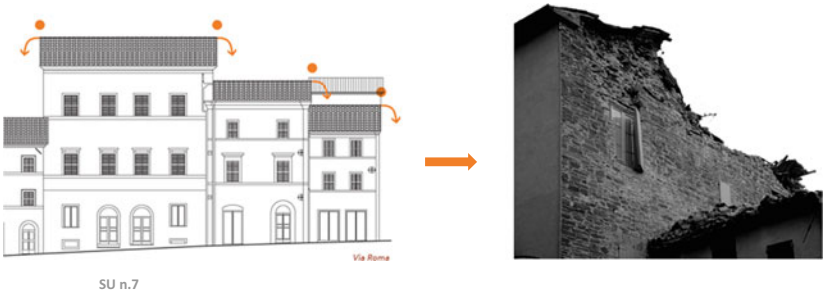

Fig. 6 Vulnerability and damage state of SU n.7

In order to obtain the best result according to the SoA (State of Art) of the building aggregate, it was necessary introduce a new indicator, the so-called CR_{QM} (*coefficiente riduttivo della qualità muraria* in Italian, *reducing coefficient of masonry quality* in English), shown in the Eq. 3, which describes the good quality of the masonry construction technique, that certainly influence the seismic response of the building. This parameter was calculated as a percentage of the initial VGA index (see Eq. 4) following a quality classification which includes: Italian normative reference about masonry classification (NTC 2018), the common construction models of masonry walls in the specific local area [11], theoretical descriptions of the potential behaviour of masonry walls responding seismic shock.

$$CR_{QM} = \% \cdot VGA_{ij} \tag{3}$$

$$VGA_{QM} = VGA_{ij} - CR_{QM} \tag{4}$$

In conclusion, the final VGA index was calculated on 10 SUs, obtaining a ranking to be compared with the post-earthquake damage scenario. The histograms in Fig. 7 highlight that a high percentage (90%) of the vulnerability ranking (VGA_{12}) matches with the damage ranking (see ID); in fact, only the SU n. 10 doesn't take the correct place in the vulnerability ranking corresponding with its damage state, probably due to the structural configuration that could influence the seismic response.

The results show the reliability of the proposed protocol and the strong link between the development of an empirical vulnerability assessment and the most effective damage mitigation strategies.

5 Conclusions

The overall analysis that have been carried out allow us to understand that the post-earthquake reconstruction requires a deep and complex reflection. This action is difficult to be carried out in ordinary conditions of urban management and planning.

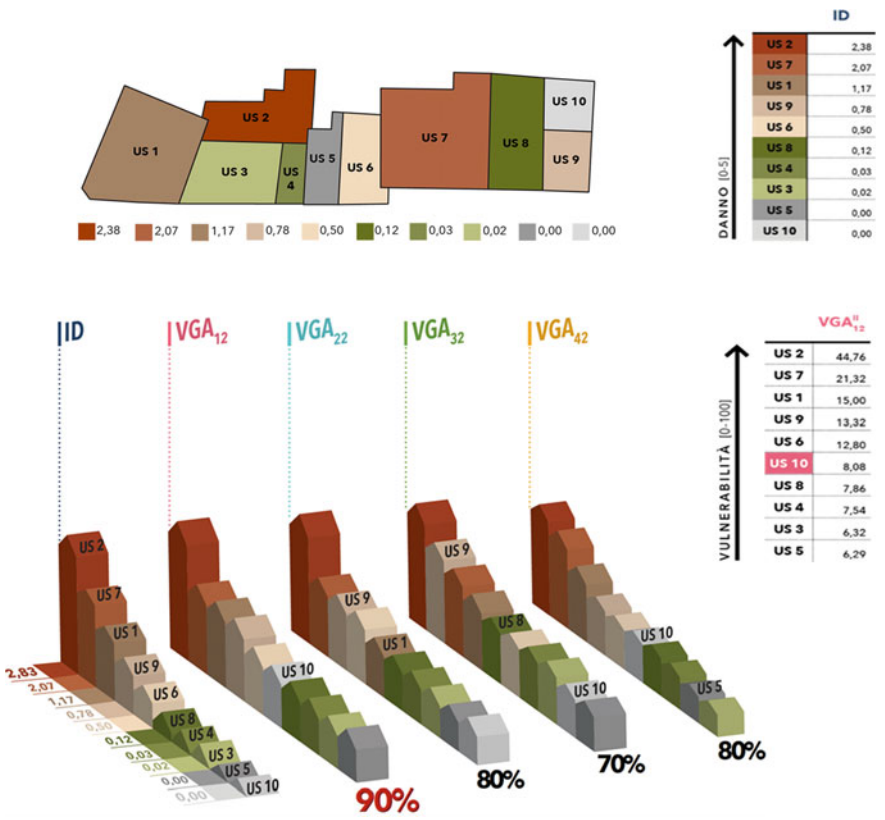

Fig. 7 Distribution of damage in BA n.1 and comparison between damage (ID) and vulnerability ranking (four hypotheses of calculation: VGA_{12}, VGA_{22}, VGA_{32}, VGA_{42}) of the 10 SUs

Therefore, the urban analysis was indispensable to understand the importance and effectiveness of the prevention policies and the usefulness of cooperation between seismic skills and technical knowledge, to adopt innovative tools in order to reduce and mitigate the seismic risk.

The reconstruction phase must not be limited to the improvement of the seismic behavior of buildings but must be finalized to the reduction of the urban vulnerability of the entire built-up area, through in-depth analyses. Indeed, our methodology approach has many beneficial and effective applications on both urban and buildings scale. The widespread application of the seismic vulnerability assessment to the urban scale is essential to provide a framework of the risk conditions in an urban settlement. On the one hand, it helps to increase the public safety through the safe areas and escape routes; on the other hand, it provides a specific rehabilitation program in the post-seismic phase in order to speed up the recovery of the compromised urban areas.

In conclusion, this research is a methodological and real contribution, which allows us to rethink the concept of the reconstruction phase as an opportunity to introduce seismic prevention actions within ordinary urban planning and to ensure a new strategic development of the affected territories. The urban planning tool that can summarize these two purposes is the SUM, which plays a significant role in the seismic vulnerability assessment to improve urban resilience to shocks, life safety and the protection of architectural heritage. This issue especially involves the Italian territory, especially in historical contexts characterized by settlement complexity, historical fabrics made up of building aggregates, which represent a significant part of the national architectural heritage. Moreover, the implementation of these latter strategies in Italian historical centres will hopefully lead public administrations to enhance preventive planning and reduce the seismic risk of the urban fabric.

The introduction of this type of strategies in the current reconstruction phase is a difficult but virtuous challenge in order to ensure a future of these territories, to achieve a public awareness of the seismic risk and to develop a resilient attitude against catastrophic disaster.

References

1. Dipartimento della Protezione Civile: Relazione di aggiornamento numeri del sisma nel Centro Italia (2018)
2. Virgili, V.: Patrimonio culturale resiliente: il contributo della ricerca e dell'innovazione. In: Carrocci Editore, Building Back Better: idee e percorsi per la costruzione di comunità resilienti, Roma (2017)
3. Dolce, M.: The Italian national seismic prevention program. In: 15th World Conference on Earthquake Engineering (15 WCEE), Lisbon (2012)
4. Bramerini, F., Castenetto, S.: Manuale per l'analisi della Condizione Limite per l'Emergenza (CLE) dell'insediamento urbano, BetMultimedia, Roma (2014)
5. Galderisi, A.: Città e terremoti. Metodi e tecniche per la mitigazione del rischio sismico, Gangemi Editore, Roma (2004)
6. Fabietti, V.: Dalla CLE alla SUM: i contenuti urbanistici della protezione dai rischi. In: Urbanistica Dossier, INU Edizioni, Roma (2013)
7. Di Salvo, G., Giuffré, M., Pellegrino, P., Pizzo, B.: Prevenzione e ricostruzione per la riduzione del rischio sismico. In: Atti della XV Conferenza Nazionale SIU – Società Italiana degli Urbanisti, Pescara (2012)
8. Gulli, R., Mochi, G., Predari, G.: An expeditious methodology for the seismic vulnerability assessment of building aggregates. In: TEMA: Technologies Engineering Materials Architecture, vol. 4, no. 2. Ar.Tec. Onlus (2018)
9. Mochi, G., Predari, G.: La vulnerabilità sismica degli aggregati edilizi. Una proposta per il costruito storico. Edicom Edizioni, Monfalcone (2016)
10. Predari, G., Bartolomei, C., Morganti, C., Mochi, G., Gulli, R.: Expeditious methods of urban survey for seismic vulnerability assessments. In: The International Archives of the Photogrammetry, Remote Sensing and Spatial Information Sciences, 6th International Workshop LowCost 3D—Sensors, Algorithms, Strasbourg (2019)
11. Guerrieri, F.: Manuale per la riabilitazione e la ricostruzione postsismica degli edifici. Regione Umbria, Editore DEI, Roma (1999)

Crack Analysis of Tensile and Bending RC Members

Gintaris Kaklauskas and Aleksandr Sokolov

Abstract The authors have recently proposed a new concept of crack analysis based on the assumed reinforcement strain profile between the adjacent cracks. Mean crack spacing is obtained from the equality of mean strains of the tensile reinforcement assessed from the strain profile and the mean value calculated by EC2. The current study considers mean crack spacing for both tensile and bending RC members. For bending members, mean spacing is established separately for primary and secondary cracks. The current paper quantifies constitutive parameters of the model for the cases mentioned above. The model is validated against independent test data. A comparative analysis has demonstrated that the predictions of mean crack distance by the proposed model agree well with the tests of RC elements.

Keywords Crack spacing · Tensile and flexural elements · Reinforcement strain profile · Mean strain · Primary and secondary cracks · Reinforced concrete · Stress-transfer approach

1 Introduction

Cracking is arguably the most complicated phenomenon of the behaviour of reinforced concrete. A large number of models have been proposed to predict cracking characteristics, but most rely on empiricism. Much has been learned already about crack width and spacing, but a completely rational and general method is still unavailable.

Cracking models can be generally divided into two main groups. The first group covers the models based on the bond stress-slip approach proposed by Saliger [1].

G. Kaklauskas (✉)
Department of Reinforced Concrete Structures and Geotechnical Engineering, Vilnius Gediminas Technical University, Vilnius, Lithuania
e-mail: gintaris.kaklauskas@vgtu.lt

A. Sokolov
Research Institute of Innovative Building and Bridge Structures, Vilnius Gediminas Technical University, Vilnius, Lithuania

E. B. Pereira et al. (eds.), *Proceedings of the 3rd RILEM Spring Convention and Conference (RSCC 2020)*, RILEM Bookseries 32,
https://doi.org/10.1007/978-3-030-76547-7_21

This approach represents the *classical bond theory* stating that crack spacing and crack width are governed by the ratio of reinforcement bar diameter and effective reinforcement ratio d_s/ρ_{ef}. The second group covers the models unified by an alternative theory suggested by Broms [2] who claimed that a single most important parameter controlling crack spacing is concrete cover. Until now there is a heated discussion which of the approaches is valid [3].

Recently the authors have suggested a new concept of crack analysis of RC members [4]. The philosophy behind the proposed methodology is to define the mean crack spacing at the stage of stabilized cracking through compatibility of the stress-transfer and mean deformation approaches, which, respectively, represent the discrete and smeared cracking concepts. The proposed approach was applied for two cases of analysis: (1) Mean spacing between primary cracks of bending RC members; (2) Mean crack spacing of tensile RC members. The first of the above techniques is an analytical one, whereas the second is performed iteratively.

The current study suggests new analytical mean crack spacing models for both tensile and bending RC members that are developed on the basis of the above approach. For bending members, mean spacing is established separately for primary and secondary cracks. The current paper quantifies constitutive parameters of the model for the cases mentioned above. The model is validated against independent test data. A comparative analysis has demonstrated that the predictions of mean crack spacing by the proposed model agree well with the tests of RC elements.

2 Assumptions and Fundamental Concepts

2.1 Assumptions

1. The stage of stabilized cracking is considered.
2. Tension softening stresses in the cracked sections are neglected.
3. Deformations of a single RC block having the length of mean crack spacing represent the averaged behaviour of the cracked member.

2.2 Crack Patterns

The crack patterns for tensile and bending members RC members are shown in Fig. 1. Only the cracks penetrating to the surface of the member are considered, thus the internal cracks (also called the Goto cracks [5]) are not taken into account. The crack pattern for tensile members is shown in Fig. 1a assuming that all cracks penetrate through the whole section. These cracks can be categorized as primary cracks. Cracking of bending members can be of different nature with the crack pattern being dependent on the section height of the member [6]. For the RC members with a relatively small section (generally $h < 300$ mm) only primary cracks appear within

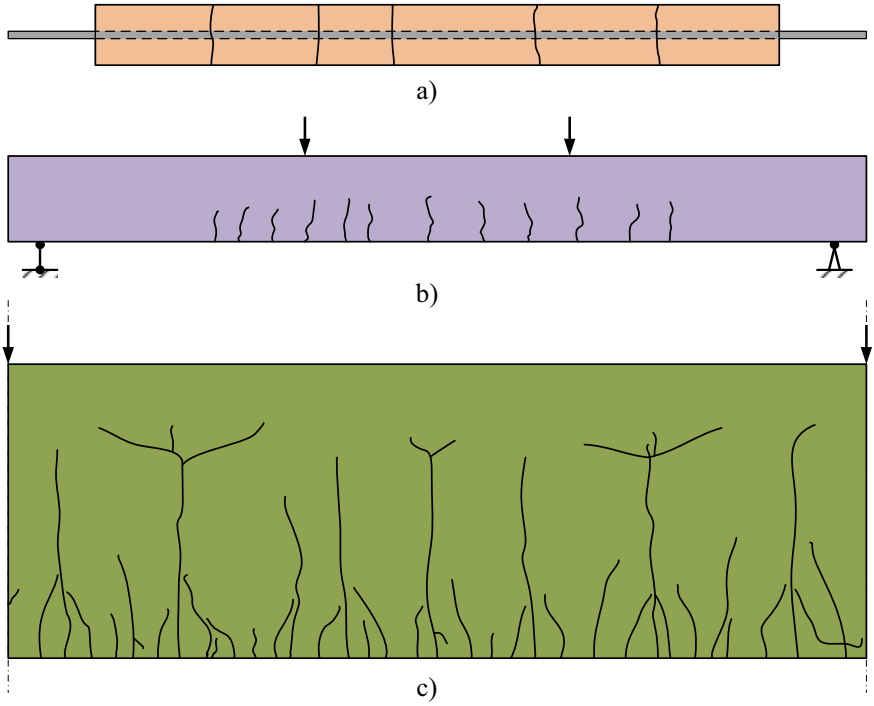

Fig. 1 The crack patterns of: **a** a tensile member, **b** a bending member having a small section and **c** a bending member having a high section

the tensile zone (Fig. 1b). However, as can be seen in Fig. 1c, both primary and secondary cracks might form in the members having a higher section ($h > 300$ mm). The process of cracking of such members is well described by [7–9]. With increasing load, the first cracks to appear are called primary: they spontaneously extend up to the height just below the neutral axis. When the primary crack pattern stabilizes, secondary cracks (also called as cover-controled cracks) form between the primary cracks. The internal cracks, typically occurring at the reinforcement ribs [5], tend to penetrate less deeply in the concrete and exist in the vicinity of the reinforcement bars.

2.3 Reinforcement Strain Profile: The Concept of Strain Compliance

Mean crack spacing is established through the compatibility of the stress-transfer and mean strain techniques by equating mean strains in the reinforcement assessed by the two approaches. The stress-transfer approach governs the strain distribution of

the reinforcement between adjacent cracks, whereas the mean strain approach quantifies the mean crack spacing, thus full advantage of both approaches is exploited. The compatibility (or *strain compliance*) principle is illustrated in Fig. 2. Figure 2a shows the assumed reinforcement strain profile between adjacent cracks as originally introduced in [4]. It consists of three different zones having different bond characteristics: (1) the *debonding zone* with the length l_d. It is assumed that bond between the concrete and reinforcement bar is fully damaged due to the local effects in the concrete surrounding the reinforcement bar; thus bond stress is taken zero; (2) the *central zone* with length l_c is another zone with zero bond stress; (3) the *effective zone* with the length l_{ef} represents the only interval within the crack spacing where bond stresses are equal to zero.

The extremities of the reinforcement strain profile indicate the location of the adjacent cracks. Strain ε_{sm} represents mean reinforcement strain that can be easily calculated by known techniques, i.e. the one presented in [10]. As noted, mean crack spacing is obtained from the equality of ε_{sm} and mean strain obtained from the reinforcement strain profile (Fig. 2b).

The reinforcement strain variation within the effective zone is assumed by this linear relation:

$$\varepsilon_s(x) = \varepsilon_{si} - Ax \tag{1}$$

where ε_{si} is the reinforcement strain at the crack; A is the slope of the linear strain function:

$$A = \frac{4\tau}{E_s d_s} \tag{2}$$

where E_s and d_s are the modulus of elasticity and diameter of reinforcement, respectively.

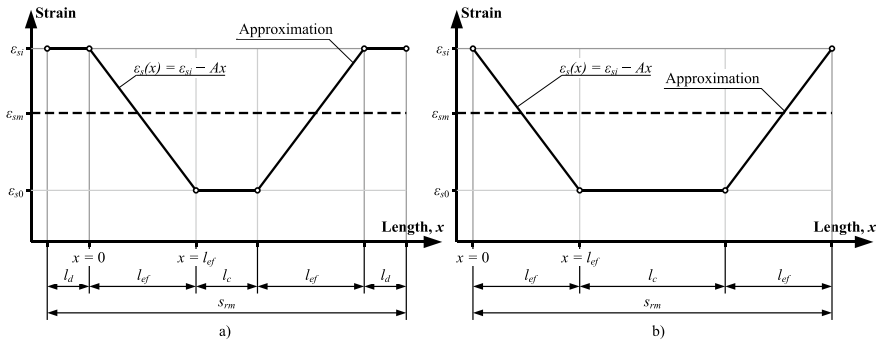

Fig. 2 Strain profiles of tensile reinforcement: **a** the originally proposed [4], **b** the one assumed in the current study with the excluded debonding zones

The current study assumes $\tau = 2f_{ct}$ where f_{ct} is the tensile strength of concrete. The effective zone length can be expressed as:

$$l_{ef} = \frac{(\varepsilon_{si} - \varepsilon_{s0})}{A} \tag{3}$$

where ε_{s0} is the minimum strain in the reinforcement (see Fig. 2).

In order to reduce the number of constitutive parameters included into the analysis and, thus, to simplify the approach, the current study removes the debonding zone parameter l_d as shown in Fig. 2b. By this, the zones with zero bond stress, that is the debonding zone and the central zone are merged and represented by the central zone alone. The expression of the length of the *central zone* will be presented further.

3 Prediction of Mean Crack Spacing

Mean crack spacing is expressed as the sum of zone lengths of the reinforcement strain profile shown in Fig. 2b:

$$s_{rm} = l_c + 2l_{ef} \tag{4}$$

The condition of equality of mean strains (displacements) defined by the mean strain approach and the adopted shape function can be written as follows (see Fig. 2b):

$$\varepsilon_{s0} l_c + 2\left(\varepsilon_{si} - 0.5Al_{ef}\right)l_{ef} = \varepsilon_{sm}\left(l_c + 2l_{ef}\right) \tag{5}$$

Equation (5) can be expressed as a second order equation:

$$Al_{ef}^2 + (2\varepsilon_{sm} + l_c A - 2\varepsilon_{si})l_{ef} + (l_c\varepsilon_{sm} - l_c\varepsilon_{si}) = 0 \tag{6}$$

or:

$$Al_{ef}^2 + Bl_{ef} + C = 0 \tag{7}$$

where

$$B = l_c A - 2(\varepsilon_{si} - \varepsilon_{sm}) \tag{8}$$

$$C = -(\varepsilon_{si} - \varepsilon_{sm})l_c \tag{9}$$

Then the effective zone length is calculated as:

$$l_{ef} = \frac{-B + \sqrt{B^2 - 4AC}}{2A} \tag{10}$$

Reinforcement strain in the cracked section ε_{si} is obtained from these well-known equations:

$$\varepsilon_{si} = \frac{P_{ref}}{E_c A_{tr}} \text{(for tensile members)} \tag{11}$$

$$\varepsilon_{si} = \kappa(d - y_0) = \frac{M_{ref}(d - y_0)}{E_c I_{tr}} \text{(for bending members)} \tag{12}$$

where E_c is the modulus of elasticity of concrete; A_{tr} is the of area of the transformed section; I_{tr} is the second moment of area of the transformed section; d is the effective depth of the section; y_0 is the depth of the compressive zone in the cracked section assessed by the standard elastic theory.

Mean crack spacing is assessed at the reference load level related to the cracking load:

$$P_{ref} = 3P_{cr} = 3A_c f_{ct} \text{(for tensile members)} \tag{13}$$

$$M_{ref} = 3M_{cr} = 3f_{ct}\frac{bh^2}{6} \text{(for bending members)} \tag{14}$$

where P_{cr} and M_{cr} are the cracking force and bending moment, respectively.

The mean strain of the tensile reinforcement, ε_{sm}, is calculated by the [10] technique. Minimal strain, ε_{s0}, can be expressed through strain ε_{si} using Eq. (3). The constitutive parameter l_c will be described in the next section.

Mean crack width can be assessed by this classical formula:

$$w_m = \varepsilon_{sm} s_{rm} \tag{15}$$

where ε_{sm} is the mean strain in reinforcement.

The current approach has some advantages in regard to other cracking models. Unlike the Eurocode 2 [10] and Model Code [11] techniques, it does not require the knowledge of the effective area of the tensile zone. In addition, the current concept aims at harmonizing the serviceability analysis. In the theory and design of RC structures, cracking and deformations are considered as the two most important and highly related aspects of the serviceability limit states. However, the codes [10, 11] do not make the emphasis on the coherence of the deformation and crack analysis. In the above codes, the mean reinforcement strain calculation that could relate these two issues is performed using different formulas. On the contrary, in the proposed approach the same formula for the mean deformations of reinforcement taken from [10, 11] is used both for deformation and crack analysis.

4 Establishing Constitutive Parameter l_c

Central length l_c is calculated taking mean spacing from the test ($s_{rm} = s_{rm,exp}$):

$$l_c = s_{rm,exp} - 2l_{ef} \tag{16}$$

The equation of mean strains Eq. (5) is expressed in a slightly different shape:

$$\varepsilon_{s0} l_c + 2\left(\varepsilon_{si} l_{ef} - 0.5 A l_{ef}^2\right) = \varepsilon_{sm} s_{rm,exp} \tag{17}$$

After simplification, the latter equation gets this form:

$$0.25 A l_c^2 + \varepsilon_{si} s_{rm,exp} - 0.25 A s_{rm,exp}^2 = \varepsilon_{sm} s_{rm,exp} \tag{18}$$

Then l_c can be expressed as:

$$l_c = \frac{2\sqrt{A\left(\varepsilon_{sm} s_{rm,exp} - \varepsilon_{si} s_{rm,exp} + 0.25 A s_{rm,exp}^2\right)}}{A} \tag{19}$$

The above technique was further applied to obtain l_c for tensile and bending members. For bending members, different expressions of l_c were derived for the cases of primary cracks and secondary cracks. The central zone lengths l_c defined on the basis of limited experimental data are given below:

$$l_c = 2.73 d_s - 0.0049[\text{m}](\text{for tensile members}) \tag{20}$$

$$l_c = 0.44(d - y_0)(\text{for bending members: primary cracks}) \tag{21}$$

$$l_c = 1.06c + 0.046[\text{m}](\text{for bending members: secondary cracks}) \tag{22}$$

where c is the concrete cover.

5 Comparison of Predicted Mean Crack Spacings to the Test Data

In order to examine the predictive capability of the proposed model, experimental data of mean crack spacing s_{rm} was collected by the authors. Main characteristics of the RC ties and RC beams/slabs) are presented in Tables 1 and 2, respectively. The test data covers a wide range of reinforcement ratio, bar diameter and concrete compressive strength. The bending members, in addition, also had a high range in

Table 1 Main characteristics of RC ties

Authors	Number	$h \times b$ (mm)	d_s (mm)	ρ (%)	f_{cyl} (MPa)
B. Farra and J. P. Jaccoud [12]	1–32	100 × 100	10–20	0.79–3.14	29.9–87.1
M. Lorrain et al. [13]	33–57				42.0–101.0
M. H. Q. Wu [14]	58–61		12–16	1.13–2.01	21.6–24.7
G. Danielius [15]	62–69		10–14	0.79–1.54	53.1
A. Rimkus [16]	70–88	150 × 150	5–14	1.40–2.68	39.5–59.6

Table 2 Main characteristics of RC beams and slabs

Authors	Number	h (mm)	b (mm)	d_s (mm)	ρ (%)	f_{cyl} (MPa)
H. Rüsch and G. Rehm [17]	1–30	0.625–1.200	0.300–0.450	10–32	0.46–1.22	13.1–43.0
B. E. Calderón [18]	31–44	0.500	0.250	10–25	0.34–2.34	21.9–28.2
V. Gribniak et al. [19]	45–50	0.299–0.303	0.271–0.284	8–22	0.61–1.03	43.0–49.7
R. I. Gilbert and S. Nejadi [8]	51–62	0.161–0.348	0.250–0.400	12–16	0.54–0.65	36.5–38.8
M. H. Q. Wu [14]	63–68	0.140–0.400	0.200–0.800	12–16	0.50–0.88	26.0–40.0
J. Frosch [20]	69–78	0.203	0.914	16	0.28–0.84	44.0–47.0
E. Hognestad [21]	79–83	0.406	0.203	13–25	1.34–1.44	17.9–39.0
G. D. Base et al. [22]	84–111	0.391	0.178	19	0.93	21.5–27.0
A. Clark [23]	112–165	0.152–0.584	0.152–0.381	10–35	0.35–2.56	22.1–31.0
A. Caldentey [3]	166–177	0.450	0.350	12–25	0.30–1.53	26.9

section height and depth. In Tables 1 and 2, h and b are the height and width of the section, respectively; ρ is the reinforcement ratio, f_{cyl} is the mean compressive strength of 150 × 300 mm concrete cylinder at the age of testing.

The prediction results are described in terms of normalized mean crack spacing ($\overline{s}_{rm} = s_{rm,th}/s_{rm,exp}$). Mean values of $\overline{s}_{rm}$ and coefficients of variation CV were obtained for four cases of test data regarding the type of loading (tension or bending) and crack pattern (primary or primary + secondary):

(1) Primary cracks in tensile RC members (Fig. 3a); $\overline{s}_{rm} = 1.02$ and CV = 18% (88 data points).
(2) Primary cracks of bending RC members (Fig. 3b); $\overline{s}_{rm} = 0.99$ and CV = 19% (122 data points).
(3) All cracks (primary and secondary) of bending RC members (Fig. 3c); $\overline{s}_{rm} = 1.04$ and CV = 18% (180 data points).
(4) Combined data of (1) and (3) (Fig. 3d); $\overline{s}_{rm} = 1.02$ and CV = 19% (268 data points).

It can be seen that the mean values of $\overline{s}_{rm}$ for the above cases were close to unity and ranged within the small interval of 0.99–1.04. The scattering results were also

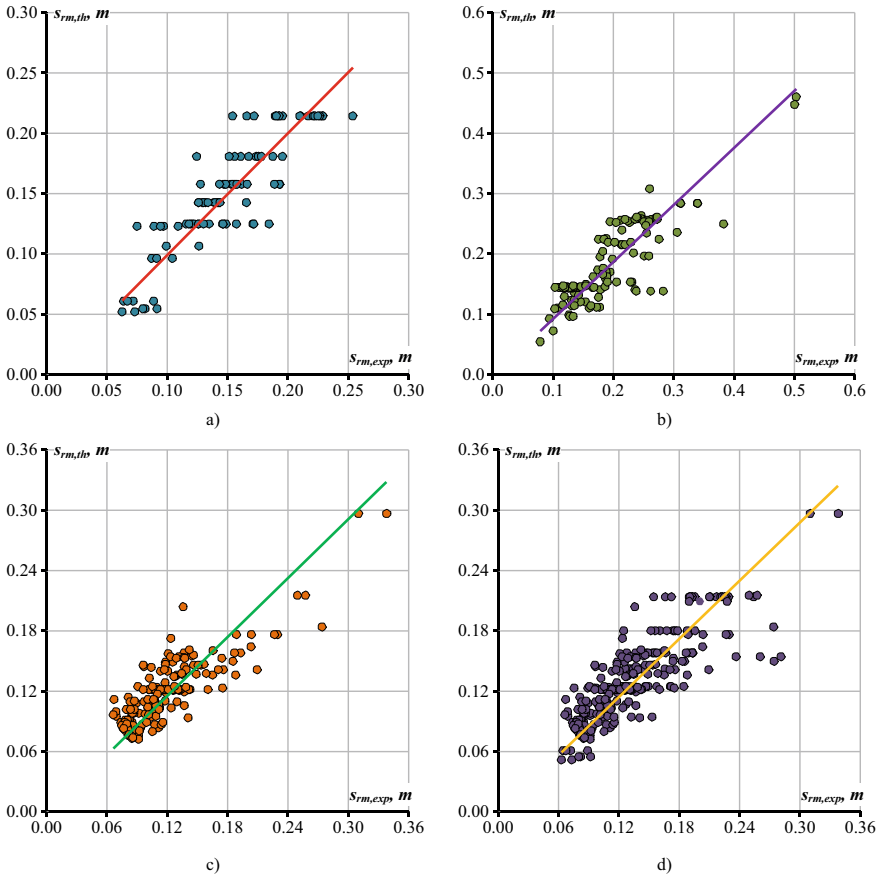

Fig. 3 The predicted versus test results of mean crack spacing: **a** primary cracks in tensile RC members, **b** primary cracks in bending RC members, **c** all cracks (primary and secondary) of bending RC members and **d** combined data of (a) and (c) cases

very close with the coefficient of variation not exceeding 19%. The predicted versus test results of mean crack spacing for the four cases are also depicted graphically in Fig. 3.

Further studies will be dedicated to width analysis of primary and secondary cracks in both tensile and bending RC members. It will include both theoretical and experimental investigations.

6 Concluding Remarks

It was shown that a novel approach for predicting crack spacing recently proposed by the authors can be applied both for tensile and bending members as well as for the cases of primary and secondary cracks. Mean crack spacing is obtained based on the principle of equality of mean strains of the tensile reinforcement assessed from the strain profile and the mean value calculated by Eurocode 2. In order to minimise the number of constitutive parameters, the debonding zone was removed from the reinforcement strain profile. As a result, the mean crack spacing model is limited to two empirical constitutive parameters, namely, the mean bond stress (in the effective zone) and the length of the central zone l_c of the reinforcement strain profile. Different expressions were suggested for l_c in order to cover the cases of tension versus bending and primary/versus primary and secondary cracking. A significant advantage of the proposed approach is that it does not require the knowledge of the effective area of the tensile zone.

A predictive capability of the proposed model has been investigated for the above cases of test data sets. The statistical analysis has resulted in adequate predictions regarding the mean value and variation. Further studies will be dedicated to width analysis of primary and secondary cracks in both tensile and bending RC members.

Acknowledgements The authors gratefully acknowledge the financial support provided by the European Social Fund under grant agreement with the Research Council of Lithuania (LMTLT) for the project No. 09.3.3-LMT-K-712-01-0145.

References

1. Saliger, R.: High grade steel in reinforced concrete. In: 2nd Congress of International Association for Bridge and Structural Engineering, vol. 2, pp. 293–315. IABSE Publications, Berlin (1936)
2. Broms, B.B.: Crack width and crack spacing in reinforced concrete members. ACI J. **62**(10), 1237–1256 (1965)
3. Pérez, A., Peiretti, C.H., Iribarren, J.P., Soto, G.A.: Cracking of RC members revisited: influence of cover, $\varphi/\rho_{s,ef}$ and stirrup spacing: an experimental and theoretical study. Struct. Concr. **14**(1), 69–78 (2013)
4. Kaklauskas, G.: Crack model for RC members based on compatibility of stress-transfer and mean-strain approaches. J. Struct. Eng. **143** (2017)
5. Goto, Y.: Cracks formed in concrete around deformed tension bars. ACI J. **68**(4), 244–251 (1971)
6. Rasmussen, A.B.: Modelling of reinforced concrete in the serviceability limit state: a study of cracking, stiffness and deflection in flexural members. Ph.D. Thesis, Aarhus University, Aarhus, Denmark (2019)
7. Beeby, A.W.: An investigation of cracking in slabs spanning one way. Technical Report No. TRA 433, Cement and Concrete Association, London (1970)
8. Gilbert, R.I., Nejadi, S.: An Experimental Study of Flexural Cracking in Reinforced Concrete Members Under Short Term Loads. Univ. of New South Wales, School of Civil and Environmental Engineering, Sydney, Australia (2004)

9. Rasmussen, A.B., Fisker, J., Hagsten, L.G.: Cracking in flexural reinforced concrete members. Procedia Eng. **172**(2017), 922–929 (2017)
10. EN 1992-1-1. Eurocode 2: design of concrete structures: part 1-1: general rules and rules for buildings. CEN European Committee for Standardization, Brussels, Belgium (2004)
11. *fib* (International Federation for Structural Concrete): Model code for concrete structures 2010, p. 434. Wiley, Berlin (2013)
12. Farra, B., Jaccoud, J.P.: Bond behaviour, tension stiffening and crack prediction of high strength concrete. In: Proceedings of International Symposium 'Bond in Concrete' (1992)
13. Lorrain, M., Maurel, O., Seffo, M.: Cracking behavior of reinforced high-strength concrete tension ties. ACI Struct. J. **95**(5), 626–635 (1998)
14. Wu, H.Q., Gilbert, R.: An experimental study of tension stiffening in reinforced concrete members under short-term and long-term loads. UNICIV Report No. R-44, The University of New South Wales (2008)
15. Danielius, G.: Experimental and theoretical investigation of tension stiffening in tensile reinforced concrete members. Master Thesis, Vilnius Gediminas Technical University, Vilnius, Lithuania (2014)
16. Rimkus, A.: Effects of bar reinforcement arrangement on deformations and cracking of concrete elements. Ph.D. Thesis, Vilnius Gediminas Technical University, Vilnius, Lithuania (2017)
17. Rüsch, H., Rehm, G.: Versuche mit Betonformstahlen, Deutscher Ausschuss fur Stahlbcton. Berlin (1964)
18. Calderón, B.E.: Estudio experimental de la fisuración en piezas de hormigón armado sometidas a flexión pura. Ph.D. Thesis, Universidad Politécnica de Madrid, Madrid, Spain (2008)
19. Gribniak, V., Pérez Caldentey, A., Kaklauskas, G., Rimkus, A., Sokolov, A.: Effect of arrangement of tensile reinforcement on flexural stiffness and cracking. Eng. Struct. **124**(1), 418–428 (2016)
20. Frosch, R.J.: Investigation of bridge deck cracking in various bridge superstructure systems. Final Report FHWA/IN/JTRP-2002/25, School of Civil Engineering, Purdue University (2003)
21. Hognestad, E.: High strength bars as concrete reinforcement, part 2: control of flexural cracking. J. PCA. Res. Dev. Lab. **4**(1), 46–63 (1962)
22. Base, G.D., Read, J.B., Beeby, A., Taylor, H.: An investigation of the crack control characteristics of various types of bar in reinforced concrete beams. Research Report 18, Cement and Concrete Association (1966)
23. Clark, A.P.: Cracking in reinforced concrete flexural members. J. Proc. **52**(4), 851 (1956)

Using Data Analysis to Extract Structural Deterioration Information from the US National Bridge Inventory Database

Filippos Alogdianakis, Dimos C. Charmpis, and Ioannis Balafas

Abstract Various infrastructure information is gathered nowadays in databases, which have become rather large after years of development and data collection. For thorough search and broad exploitation of the available information, even beyond its original scope, advanced data analysis approaches need to be employed. The present work is concerned with the exploitation of the data in the US National Bridge Inventory (NBI) maintained by the Federal Highway Administration (FHWA), which includes information for over 500,000 bridges. The information provided in NBI was analyzed in combination with additional data from other sources (for climatic conditions, earthquake hazard, etc.). Where needed, data were converted to correspond to bridge locations using spatial interpolation techniques. Then, Exploratory Data Analysis (EDA), Analysis of Variance (ANOVA) and regression analysis methods were utilized to study the causes of bridge deterioration. These statistical methods yield quantitative results and allow the identification, ranking and measurement of intensity of factors contributing to the decrease of the structural condition of bridges with time.

Keywords Deterioration · Spatial interpolation · Exploratory data analysis · Analysis of variance · Regression analysis

F. Alogdianakis · D. C. Charmpis (✉) · I. Balafas
Department of Civil and Environmental Engineering, University of Cyprus, Nicosia, Cyprus
e-mail: charmpis@ucy.ac.cy

F. Alogdianakis
e-mail: alogdianakis.filippos@ucy.ac.cy

I. Balafas
e-mail: ibalafas@ucy.ac.cy

E. B. Pereira et al. (eds.), *Proceedings of the 3rd RILEM Spring Convention and Conference (RSCC 2020)*, RILEM Bookseries 32,
https://doi.org/10.1007/978-3-030-76547-7_22

1 Introduction

Today's society relies on data collected from multiple sources, which are combined and processed to produce information that assists decision making at various levels, ranging from everyday life to very specialized cases. All these processes can be included in the broad term of 'Data Analysis', which refers to various tools, such as data visualization, hypothesis testing and other statistical methods, that are employed to handle samples and select the most appropriate variables for modelling reality.

Infrastructures, and more specifically bridges, are exposed to various factors that could worsen their structural condition. When reliable data are available, a data analysis process can confirm or challenge building practices and design processes already applied, but also assist in modelling deterioration by identifying factors affecting it.

In many countries, inspections are performed on bridges to monitor the infrastructure's stock condition. The US Federal Highway Administration maintains an up-to-date National Bridge Inventory (NBI), which includes over 500,000 bridges in US territory. The NBI contains a considerable amount of information; this includes 116 coded items to describe each bridge, its characteristics, its condition, etc. [1]. An updated NBI is published annually, as each bridge must be inspected visually biennially. Bridge condition ratings are recorded on a scale 0–9, with 9 representing 'excellent' and 0 'failed' conditions. Inspections are carried out by qualified personnel complying with standard procedures set out in National Bridge Inspection Standards (NBIS) [1].

The NBI has been used by several researchers to investigate structural deterioration and material performance for bridges. In the various statistical methods utilized for this task, the explanatory variables have been usually selected by expert judgement [2, 3]. Such approaches may derive erroneous models due to the neglect of other variables, which may be affecting structural deterioration more. Another common practice usually employed is the utilization of bridge data for only one individual State of the US and inclusion in the assessment of additional explanatory variables, such as weather data and other data available from GIS [4]. In these cases, although maintenance policies and acquired data can be considered uniform, the limited variation of exposure factors can lead to modelling errors. On the other hand, when utilizing the whole US bridge sample, many exposures have to be taken to account and not including them in the analysis may also lead to misleading results due to unjustified averaging. Furthermore, questions arise regarding the effect of typical factors suggested by experts, which have already been taken to account during the design process. Thus, a process is needed to formally select the variables, which should be incorporated in modelling structural deterioration. Recently, some data analysis procedures have started to be utilized, in order to select among factors affecting deterioration. Relevant efforts either include limiting assumptions for the factors considered [5] or study an individual State and consider only NBI factors [3].

In this paper, NBI data for the conterminous US States are utilized to study the factors affecting the superstructure condition of bridges. To enable this, it is assumed

that hazard-driven maintenance and rehabilitation policies are predominant and that the effect of potential State policies can be neglected. Additional reliable sources were used, such as National Oceanic and Atmospheric Administration (NOAA) for climatic data [6] and United States Geological Survey (USGS) for earthquake hazard data [7]. These were combined with NBI data using spatial interpolation methods. Data analysis procedures were utilized to explore the data and attain an appropriate model for the combined dataset, whose main purpose is to reveal predominant factors affecting structural condition.

2 The Data Analysis Process

Data analysis is a broad term used to describe a set of procedures utilized to process data, comprehend and quantify their important relationships and finally generate models that aim to describe reality. The data analysis process followed herein is graphically summarized in Fig. 1. Initially, various relevant data collections (from NBI, NOAA, USGS) are utilized to attain the necessary information. From each dataset, a number of variables are selected and filtered to exclude unwanted information (i.e. bad records, outliers, etc.), a process performed with the aid of Exploratory Data Analysis (EDA), whose tools are mainly graphical and assist the analyst in identifying problematic/unexpected features [8]. The filtering process is repetitive

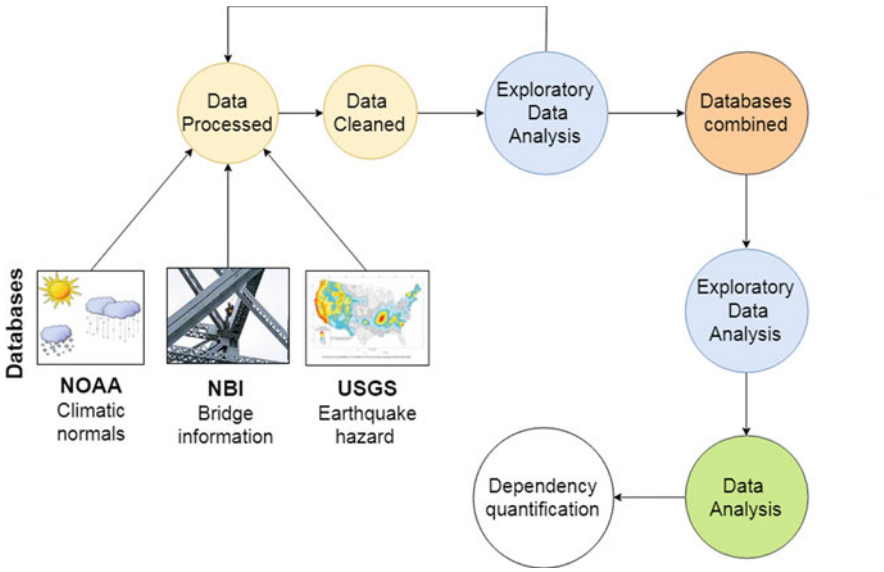

Fig. 1 The data analysis process

and ends when the datasets are clear from outliers or errors, which could affect the actual data analysis that follows.

The cleaned datasets are then combined and EDA is once again performed to show variable distributions and intercorrelations, as well as to assist the analyst in selecting the appropriate data analysis methods to utilize [8]. The data analysis performed herein employs statistical modelling tools, such as Analysis of Variance (ANOVA) and regression analysis, which unveil and quantify relationships between the variables considered. Only parts of the conducted data analysis are presented. Specifically, initial variable selection, its filtering and the process of combining the different datasets are briefly discussed. Then, main EDA results are given, followed by the most important findings of ANOVA and indicative results of the regression analysis.

3 Formation of the Analyzed Dataset

Structural deterioration of bridges is linked to corrosion, which depends on various factors, such as temperature, aggressive chemicals (i.e. deicing salts, sea chlorides), freeze–thaw cycles, wet-dry cycles, among others [9]. Furthermore, accidental factors, such as earthquake hazard/action, are also important, as they dictate the implemented design standards and may add sudden induced damage to gradual/continuous deterioration. In this paper, to investigate deterioration, bridge characteristics, properties and current structural condition were extracted from the NBI, while climatic and earthquake attributes at bridge locations were obtained from NOAA and USGS, respectively.

The set of variables considered are presented in Fig. 2. The variables are grouped based on the database they were extracted from and the variable type. Hence, the dependent variable is actually the product of evaluation (i.e. structural condition rating), while the independent variables offer information regarding bridges and potential deterioration factors. Further categorization was performed in numerical or categorical variables according to the form of information contained. Moreover, categorical variables were grouped in ordinal and nominal ones.

3.1 NBI Variable Selection and Filtering

A total of 25 variables (Fig. 2) were selected from the NBI database regarding bridge superstructure condition, age, clearances, geometry, traffic (numerical variables), as well as ownership, water presence under the bridge, traffic type over and under the bridge (categorical variables). Of the total 614,387 structures included in the NBI database, not all were of interest in this study, therefore certain criteria were used to exclude e.g. culverts or bridges made of timber or stone. The exclusions performed regarded 166,750 structures, leaving a remaining population of interest

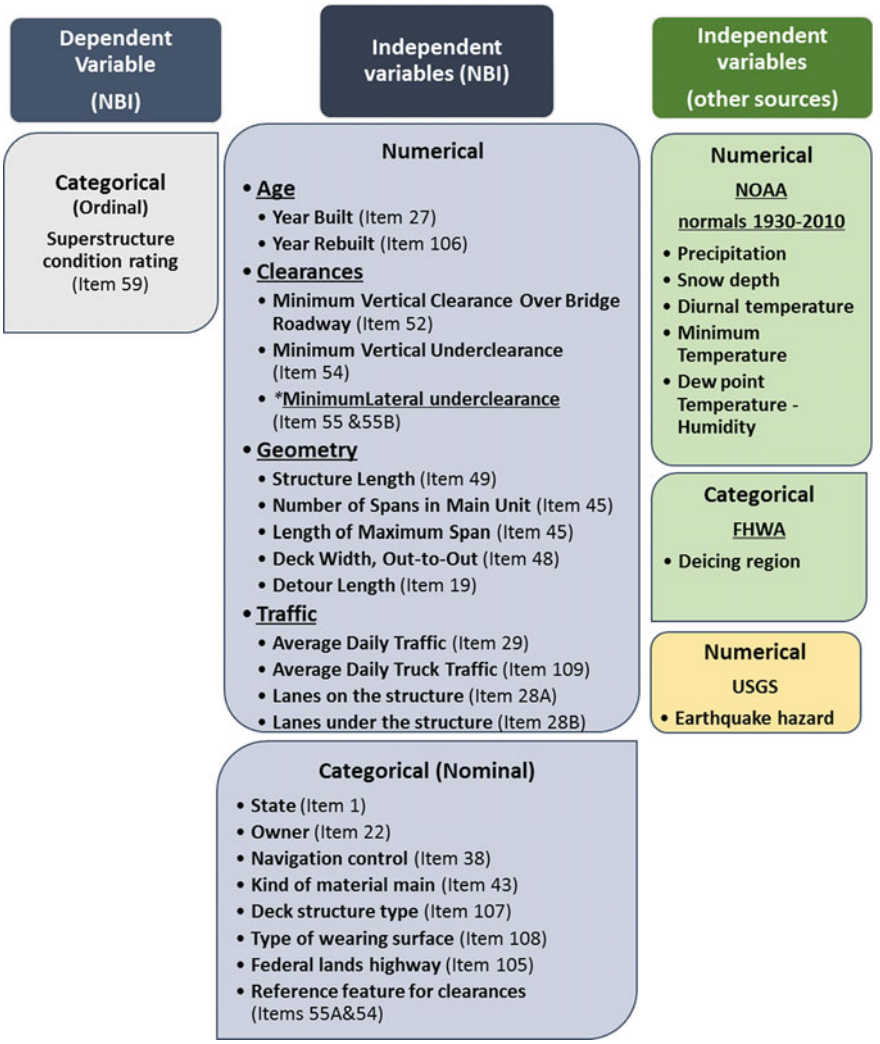

Fig. 2 Variables considered in the data analysis

of 447,637 bridges with year of construction after 1900 and specific utilized materials (reinforced/prestressed concrete, structural steel).

3.2 Climatic Data

Structures are affected in the long term by local weather conditions, therefore the most appropriate respective data to take into account are the'climatic normals'. NOAA

manages and maintains a relatively dense network of weather stations all over the US and sustains a large collection of climatic and weather data. The US climatic normals are average values of climatological variables over a 30-year period (1981–2010) characterizing the conditions at each location [6]. The climatic normals utilized herein were: annual precipitation/rainfall, days of snow depth above 1 inch in a year, monthly average minimum temperature, monthly diurnal temperature range, hourly dew point temperature. The data were filtered for errors and processed to transform monthly and hourly data to annual ones. Furthermore, calculations were performed to attain values for annual average temperature and humidity.

3.3 Deicing Region Limits

Climatic data affect also the users of a bridge, inducing interventions to prevent accidents that may accelerate corrosion. Such is the case of deicing salts spread on the road surface to prevent frost. Deicing salts can be effective if snow depth is less than few centimeters. Thus, the FHWA map of US regions, where deicing is allowed, was copied as an image [10] and, using Google Earth, the coordinates of deicing region limits were identified, to be included in the analysis as complimentary data to the climatic variable of snow depth above 1 inch.

3.4 Earthquake Hazard Data

Earthquake resistance is a crucial attribute for a structure's service life in a seismic region. Seismic damage to bridges results usually from complex effects by various contributing variables that interact together. Peak ground acceleration (PGA), usually measured in terms of the acceleration of gravity (g), is the main variable typically used to represent the intensity of ground motion [11], although the seismic effect can be magnified by other factors. Seismic hazard maps are a product of analysis that considers past faults and earthquakes, behavior of seismic waves travelling the crust and near-surface site conditions [7]. Such maps are available from USGS, as derived from analyzing data from the whole US network. The seismic hazard expressed as the PGA with 2% probability of exceedance in 50 years was chosen to be incorporated in the analysis process. Relevant data were downloaded from USGS [7] for the conterminous US in the form of PGA values at gridded data-points (every 6 km) that formed a dense network of calculated hazard locations.

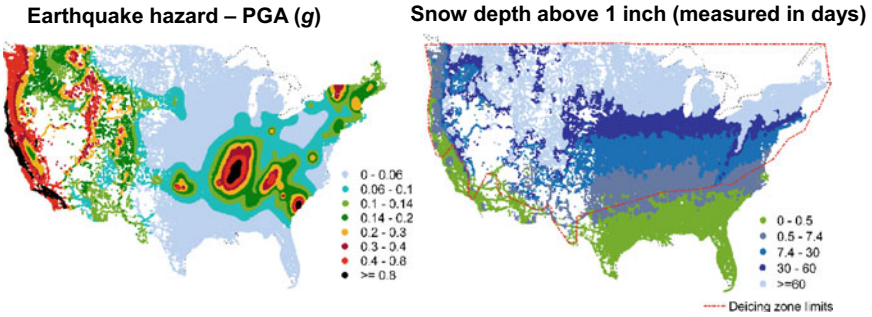

Fig. 3 Maps of interpolated values regarding snow depth (kriging interpolation) and earthquake hazard (linear interpolation) at bridge locations

3.5 Combining the Datasets

The aforementioned non-NBI databases offered information at locations, where data had been collected (weather stations) or calculated (grid of PGA values). To assign the corresponding climatic and earthquake hazard values to bridge locations, two different interpolation methods were utilized. Specifically, ordinary kriging interpolation was used for climatic data, as it is preferred for climatic and weather information [12]; linear interpolation for the densely gridded data of USGS was selected among the suggested methods by USGS. Results for two characteristic cases are presented in Fig. 3.

4 Exploratory Data Analysis (EDA)

The EDA conducted for the whole sample included histograms and charts to visualize and explore distributions and frequencies of all selected variables. Additionally, correlograms were utilized to investigate the existence of statistical dependences among the variables.

Correlation is a statistical measure that shows whether and how strongly pairs of variables are statistically related. In particular, the Pearson correlation coefficient, which takes absolute values between 0 (no correlation) and 1 (full correlation), reveals how close two variables are to having a linear relationship with each other. Weak correlations are usually associated with absolute values in the range 0–0.65, moderate in the range 0.65–0.75, while strong correlations correspond to coefficients taking values higher than 0.75. A negative correlation value indicates that the two variables are negatively correlated. In Fig. 4, correlation results are represented circles of appropriate size and color intensity. Specifically, larger circles with intense colors reveal stronger correlations, while small circles with faded colors weaker correlations. The

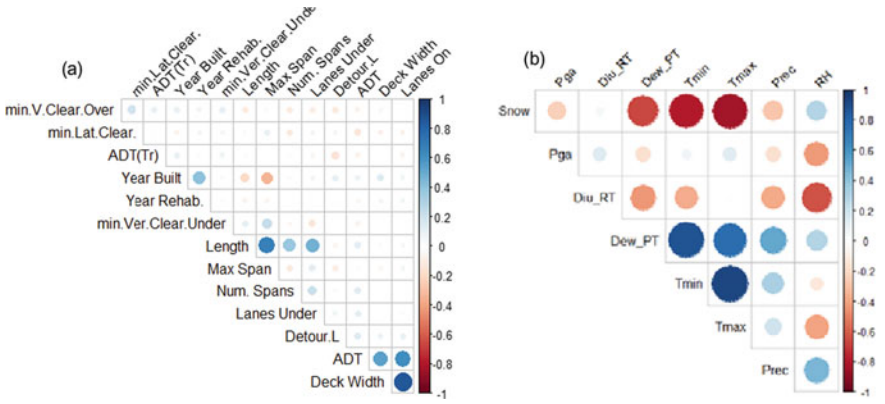

Fig. 4 **a** Correlogram of independent NBI variables (min vertical clearance over bridge, min lateral clearance, average daily truck traffic, year built, year rehabilitated, min vertical under clearance, length, max span, number of spans, lanes under bridge, detour length, average daily traffic, deck width, lanes on bridge). **b** Correlogram of independent climatic (non-NBI) variables (snow depth above 1 inch, PGA—earthquake hazard, diurnal range temperature, dew point temperature, min temperature, max temperature, precipitation rainfall, relative humidity)

color map given allows negative or positive correlations to be distinguished. The reported correlation results were calculated only for numerical variables.

The correlation analysis was conducted separately for NBI-based independent variables (regarding bridge characteristics and properties) and for independent climatic and earthquake hazard variables. The results for NBI independent variables (Fig. 4a) showed that there are mostly weak correlations among them. Exceptions were geometric variables measuring similar properties (deck width and lanes on a structure; length and maximum spans). On the other hand, independent climatic and earthquake hazard variables (Fig. 4b) showed strong correlations among the different temperatures and days of snow depth above 1 inch.

5 ANOVA

ANOVA is a technique that, in its simplest form, provides a statistical test of whether or not the population means of a number of samples are equal. It is usually employed to analyze categorical independent variables (herein, deterioration factors) for their effect on the dependent variable (superstructure condition). In the present study, all numerical variables were transformed to categorical variables by utilizing their distributions to form meaningful groups of values. To assess the importance of the differences found for each variable's groups, ANOVA results were visualized using multiple comparisons Tukey–Kramer method [13]. Certain cases were selected to be presented herein that show important patterns found among groups of the variables studied.

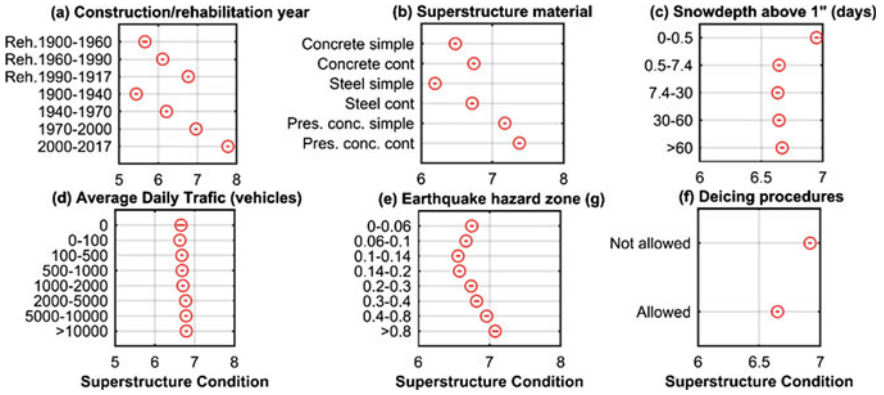

Fig. 5 ANOVA results for selected bridge deterioration factors displayed using multiple comparisons

The multiple comparisons presented in Fig. 5 show the effect of each variable's groups to superstructure condition. For each group of values, an average value of the superstructure condition is represented by a circle. The magnitude of the error of the average estimate is indicated with a line in the center of each circle; actually, dots indicate small errors, while lines larger ones. Furthermore, increased difference between a variable's group means indicate the higher importance of the variable to superstructure deterioration.

Figure 5a demonstrates the high importance of year of construction or rehabilitation in the structural condition of bridge superstructures. It is also clear from the same figure that differences in superstructure condition between rehabilitated bridges (upper part of Fig. 5a) and non-rehabilitated bridges (lower part of Fig. 5a) exist. On the other hand, as regards Average Daily Traffic, only minor differences are observed between group means (Fig. 5d).

The structural materials utilized in superstructures also appear to have increased differences between their group means (Fig. 5b). Simple-span superstructures made of structural steel seem to be in the worst condition, while prestressed concrete superstructures with continuous span are on average in the best condition.

Regarding the earthquake hazard variable, Fig. 5e shows that up to a certain group (PGA 0.14–0.2 *g*), bridges tend to have decreasing mean condition for increasing PGA level. This effect is reversed for the means of the higher PGA groups, which could be attributed to the more demanding design standards for bridges built to withstand higher seismic actions in locations with increased earthquake hazard.

Figure 5f shows that, as expected, the use of deicing salt negatively affects the mean condition of superstructures. According to Fig. 5c, the days of snow depth above 1 inch do not have an effect on the mean superstructure condition, with the exception of the first group (0–0.5 days). However, as can be seen in Fig. 3, the first group roughly coincides with the non-deicing region, where the use of deicing salts is not allowed, which explains the better mean superstructure condition for this group.

As regards the other groups exhibiting practically the same mean condition, it seems that superstructures are affected by the presence of deicing salts, irrespective of the snow volume on the deck surface.

6 Regression Analysis

Regression analysis is a statistical process for modelling and analyzing the relationship of a dependent variable with one or more independent variables. It is commonly used for prediction and forecasting, but it has also been utilized for achieving a better understanding of the relative importance of each independent variable in modelling the dependent variable.

In the negative binomial regression analysis performed herein, the initial number of variables studied were reduced based on the obtained results from correlation analysis and ANOVA. The independent variables included in the analysis are shown in Table 1. For these variables, an additive, generalized linear model fit was calculated using MASS library in R [14]. An initial regression was performed to fit a model using all independent variables. Then, a stepwise regression process was utilized, according to which independent variables were added (forward regression) or removed (backward regression) and the so-called Akaike Information Criterion was employed to indicate whether a better model was achieved. By comparing the results of successive regression models, conclusions on omitting unnecessary variables were reached.

In the regression function obtained, the logarithm of the superstructure condition rating is equated to an intercept term and the added independent variables multiplied by each variable's coefficient:

$$\begin{aligned} \ln(\text{Superstructure Condition}) = {} & \text{Intercept} + C1 * \text{Length} + C2 * \text{Deck width} \\ & + C3 * \text{Year of construction} + C4 * \text{Detour Length} \\ & + C5 * \text{ADT} + C6 * \text{PGA} + C7 * \text{Precipitation} \\ & + C8 * \text{Snow depth} + C9 * \text{Deicing} + C10 * \text{Material} \\ & + C11 * \text{Water underneath} \end{aligned} \quad (1)$$

The intercept term is a grand average of the dependent variable, while the effect of the various independent variables is indicated by the estimated coefficients provided in Table 1. The categorical independent variables included in this table are handled through binary dummy variables (one dummy variable is introduced for each group of a categorical variable). These dummy variables can take only the values of 1 (to activate the coefficient for the specific group) or 0 (to deactivate it). For example, as regards superstructure material, there is no coefficient for 'concrete continuous', thus C10 is deactivated (the dummy variables for all other groups take the value 0), i.e. Equation (1) is by default calibrated for the particular material. If another material is used, then Eq. (1) needs a 'correction' to shift its result, which is achieved by activating the C10-value (with a dummy variable value equal to 1) of the corresponding

Table 1 Regression analysis results for superstructure condition rating

Variable		Coefficient estimate
–		Intercept = −5.3E + 00
Length (m)		C1 = −4.8E-05
Maximum span (m)		Omitted
Deck width (m)		C2 = 7.1E-04
Year constructed (date/year)		C3 = 3.6E-03
Detour length (km)		C4 = 1.4E-04
Average Daily Traffic - ADT (vehicles)		C5 = 2.7E-08
Truck traffic (% ADT)		Omitted
Earthquake hazard - PGA (*g*)		C6 = 4.9E-02
Precipitation (inches)		C7 = −5.6E-04
Snow depth above 1 inch (days)		C8 = 1.6E-04
Deicing	Not allowed	–
	Allowed	C9 = −2.5E-02
Material	Concrete continuous	–
	Concrete simple	C10 = −9.6E-03
	Prestressed concrete continuous	C10 = 2.1E-02
	Prestressed concrete simple	C10 = 1.8E-02
	Steel continuous	C10 = 9.8E-04
	Steel simple	C10 = −4.6E-02
Water underneath	No	–
	Yes	C11 = −7.3E-03

group of Table 1. Clearly, only one group of a categorical variable and its coefficient value can be active and have a dummy variable value equal to 1 at any time (all other dummy variable values for the remaining groups of the categorical variable are equal to 0 to deactivate the corresponding regression coefficients).

The increase of the value of each independent variable causes either increase or decrease of the value of superstructure condition, depending on the sign of the respective regression coefficient. The regression analysis results reveal the most influencing factor, which is the year of bridge construction, as well as the least influencing ones, which are the bridges' geometric characteristics. The traffic characteristics appear to have a small effect on the superstructure condition. Indeed, the results for ADT are in agreement with the corresponding results obtained with ANOVA in the previous section. The same applies for earthquake hazard, with increase of the PGA value having a positive effect on superstructure condition. Increased annual precipitation and days of snowfall above 1 inch cause a decrease in superstructure condition. The

same applies for bridges, which are located in deicing regions or have water underneath. Furthermore, the structural materials used in superstructures appear to have effects similar to the ones observed with ANOVA.

7 Conclusions

In this paper, factors affecting the superstructure condition of bridges were studied using data from existing bridges located in the US. To perform this task, recorded inspection data for more than 600,000 bridges included in the NBI database were utilized. Since the US territory contains a large variety of environmental exposures, the databases of NOAA and USGS were used to introduce additional (non-NBI) variables regarding climate and earthquake hazard. To estimate data values for each bridge location, spatial interpolation methods were implemented. The combined dataset including NBI and non-NBI data was then analyzed using data analysis procedures, to determine which variables affect the structural condition of bridges.

The exploratory data analysis performed showed that there are low correlations among the selected NBI variables in contrast to climate variables, which were moderately to highly intercorrelated. ANOVA and multiple comparisons revealed useful patterns, which indicated the effect of each variable to structural condition rating. Moreover, the analysis showed the existence of certain thresholds, after which variables have a different effect to the condition ratings, such as the deicing policy implemented and the days of snow depth above 1 inch: although the deicing region coincides with the region of more than 0.5 days of snowfall above 1 inch, further increase in days of snowfall do not affect superstructure condition rating.

The regression analysis confirmed that superstructure condition is mostly affected by:

1. year of construction,
2. materials of superstructure,
3. earthquake hazard,
4. deicing practices region,
5. precipitation and
6. water underneath.

Less important factors for the superstructure condition were:

1. average daily traffic,
2. truck traffic,
3. detour length and
4. geometric characteristics.

References

1. Federal Highway Administration (FHWA), Recording and coding guide for the structure inventory and appraisal of the nation's bridges. US Department of Transportation, Washington DC (1995)
2. Mauch, M., Madanat, S.: Semiparametric hazard rate models of reinforced concrete bridge deck deterioration. ASCE J. Infrastruct. Syst. **7**(2), 49–57 (2001)
3. Chang, M., Maguire, M., Sun, Y.: Framework for mitigating human bias in selection of explanatory variables for bridge deterioration modeling. ASCE J. Infrastruct. Syst. **23**(3), 04017002 (2017)
4. Kim Y.J., Yoon, D.K.: Identifying critical sources of bridge deterioration in cold regions through the constructed bridges in North Dakota. ASCE J. Bridg. Eng. **15**(5), 542–552 (2010)
5. Radovic, M., Ghonima, O., Schumacher, T.: Data mining of bridge concrete deck parameters in the national bridge inventory by two-step cluster analysis. ASCE-ASME J. Risk Uncertain. Eng. Syst., Part A: Civ. Eng. **3**(2), F4016004 (2017)
6. National Oceanic and Atmospheric Administration (NOAA).: www.noaa.gov. Last accessed 5 Mar 2017
7. United States Geological Survey (USGS).: www.usgs.gov. Last accessed 20 Mar 2017
8. Tukey, J.W.: Exploratory data analysis. Addison-Wesley Longman, Inc., Reading, Massachusetts, USA (1977)
9. Neville, A.: Chloride attack on reinforced concrete: an overview. Mater. Struct. **28**(1), 63–70 (1995)
10. Federal Highway Administration (FHWA), Road weather management program.: https://ops.fhwa.dot.gov/weather/weather_events/snow_ice.htm. Last accessed 5 Feb 2017
11. Chen, W.-F., Duan, L.: Bridge engineering handbook: seismic design, 2nd edn. CRC Press, Boca Raton Florida (2014)
12. Mair, A., Fares, A.: Comparison of rainfall interpolation methods in a mountainous region of a tropical island. J. Hydrol. Eng. **16**(4), 371–383 (2011)
13. Wilcox, R.R.: Basic statistics (understanding conventional methods). Oxford University Press, Oxford, New York (2009)
14. R Development Core Team, R: A language and environment for statistical computing. Austria: R Foundation for Statistical Computing, Vienna (2008)

Towards the Understanding the Role of the Mix Design Method in the Mechanical Behaviour of Recycled Aggregate Concrete at Early Ages

Jeonghyun Kim, Miguel Azenha, and Łukasz Sadowski

Abstract The aim of this paper is to provide an original, systematic and critical review of existing mix design methods for recycled aggregate concrete (RAC), with identification of research gaps. These design methods were compared to the design methods used for natural aggregate concrete (NAC). Also a short literature survey showing the effect of the design methods on the properties of RAC and NAC was conducted. Special emphasis was placed on the critical analysis of literature results to show the existing relations between the individual mechanical properties of RAC. Also, a critical comparison was made with existing relations for NAC that can be found in the literature. Based on the analysed research results, hypotheses related to the possible behaviour of RAC at early ages were formulated towards the understanding the role of the mix design method in the mechanical behaviour of RAC at early ages.

Keywords Recycled aggregate concrete · Concrete mix design · Equivalent mortar volume method · Early age properties of concrete

1 Introduction

Many studies on the mechanical properties of recycled aggregate concrete (RAC) have shown that its mechanical properties are different from those of natural aggregate concrete (NAC) [1, 2]. In particular, when only the type of aggregate is different and the remaining mixing conditions, such as the amount of materials and mixing methods, are the same, the RAC has been found to have worse mechanical properties compared to NAC from very early ages, and this tendency extends towards later ages [3, 4]. These shortcomings can be overcome to attain similar properties to those of

J. Kim (✉) · Ł. Sadowski
Wrocław University of Science and Technology, Wybrzeże Wyspiańskiego 27, 50-370 Wrocław, Poland
e-mail: jeonghyun.kim@pwr.edu.pl

M. Azenha
University of Minho, 4800-058 Guimarães, Portugal

E. B. Pereira et al. (eds.), *Proceedings of the 3rd RILEM Spring Convention and Conference (RSCC 2020)*, RILEM Bookseries 32,
https://doi.org/10.1007/978-3-030-76547-7_23

NAC in terms of elastic modulus and compressive strength by the use of appropriate mix design methods, such as the equivalent mortar volume (EMV) method [5] and its modifications [6, 7], which treat residual mortar attached to recycled aggregate (RA) as new mortar. Most of these studies, however, focused on mechanical properties at later ages (e.g. mechanical strength and elastic modulus at 7, 14, 28 days), and hence lacked information on the early ages, before 7 days. Rapid paces of evolution of properties are known to occur in such initial time frame (regardless of being NAC or RAC). Therefore, measurements on early age properties should be performed at early ages to better understand the early behaviour of RAC designed with proper mix designs such as EMV method, which can be of great importance in many applications (e.g. to decide formwork/propping removal dates in slabs). The aim of this paper is to initially give an overview of existing mix design methods for RAC, and compare them with those used for NAC. Also a short literature survey showing the effect of the design methods on the properties of RAC and NAC will be conducted. Special emphasis will be placed on the critical analysis of literature results to show the existing relations between the individual mechanical properties of EMV-designed RAC. Also, a critical comparison will be made with existing relations for NAC that can be found in the literature. Based on the analysed research results, hypotheses related to the possible behaviour of EMV-designed RAC at early ages will be formulated towards the understanding the role of the mix design method in the mechanical behaviour of RAC at early ages.

2 Overview of Concrete Mix Design Methods for NAC and RAC

2.1 Conventional Mix Design (CMD)

Each country or organization has their own concrete specifications, such as American Concrete Institute (ACI 211.1-91) [8], European Standard (EN 206-1) [9]. These conventional mix design (CMD) methods are based on the use of natural aggregates (NA) (Fig. 1a). However, when RA is used together with these CMD standards, due to the attached mortar, the volume of total mortar constituting concrete is larger than that of NAC as shown in Fig. 1b. In particular, the increase of the total mortar fraction in concrete has been pointed out as one of the factors that explain RAC properties being lower than those of NAC in general [5, 10].

2.2 Equivalent Mortar Volume (EMV) Mix Design Method

Fathifazl et al. [5] state that the lower physical properties of RAC designed with existing mix design methods (CMD) can be improved by adopting proper mix design

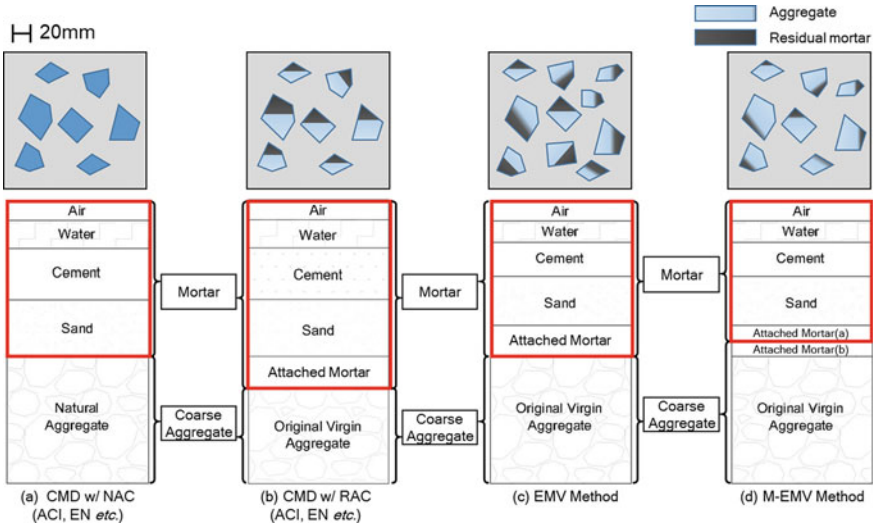

Fig. 1 Comparison of concrete mix design methods

methods. Therefore, the EMV method has been proposed, which treats the attached mortar as new mortar to be added, unlike CMD which considers the attached mortar as aggregate (Fig. 1c). The EMV method is characterized in that more RA are required compared to the CMD method in order to equalize the total volume of NA in NAC and original virgin aggregate in RAC with EMV. Therefore, the amount of newly added materials such as cement, sand, and water is decreased by the volume amount of the attached mortar.

2.3 Modified Equivalent Mortar Volume (M-EMV) Mix Design Method

In case of RA with high attached mortar content or high replacement rates of RA, several problems have been observed in the resulting RAC designed with EMV method: poor performance in fresh state; and not being able to fully cover aggregates. These problems have been traced back to the insufficiency of cement [10, 11], hence, the modified equivalent mortar volume (M-EMV) method has been proposed, which regulates the effective attached mortar content (Fig. 1d) [6, 7].

3 Overview of Properties of RAC Designed with CMD

3.1 Early Age Properties of RAC Designed with CMD

In general, if RAC is manufactured in the same manner as NAC, its mechanical properties, such as compressive strength and elastic modulus at 28 days curing are well-known to decrease as a function of RA replacement ratio. In practice, lower properties of RAC are observed from the beginning of concrete casting [12]. When the amount of admixture is kept the same, slump and density tend to decrease with increasing RA ratio, and water absorption capacity increases [13]. Figure 2 shows the compressive strength development of RAC and NAC under the same mix design conditions. The lower physical properties of RAC compared to NAC appear in the measurement of compressive strength on the 1st day after casting, and this trend continues until the later age [14]. Velay-Lizancos et al. [4] performed continuous measurement of elastic property of RAC at early ages through the Elastic Modulus Measurement through Ambient Response Method (EMM-ARM) proposed by Azenha et al. [15]. The results showed an inverse relation between replacement rate of RA and elastic modulus, and the gaps of elastic modulus of RAC with different percentages of replacement occured within 24 h after casting. This tendency is also observed in drying shrinkage [16] and ultrasonic pulse velocity (UPV) testing [12].

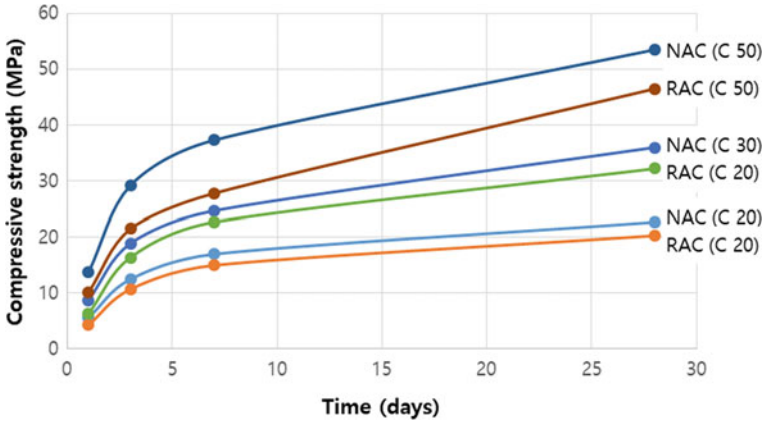

Fig. 2 Comparison of typical compressive strength development of NAC and RAC (data from [14])

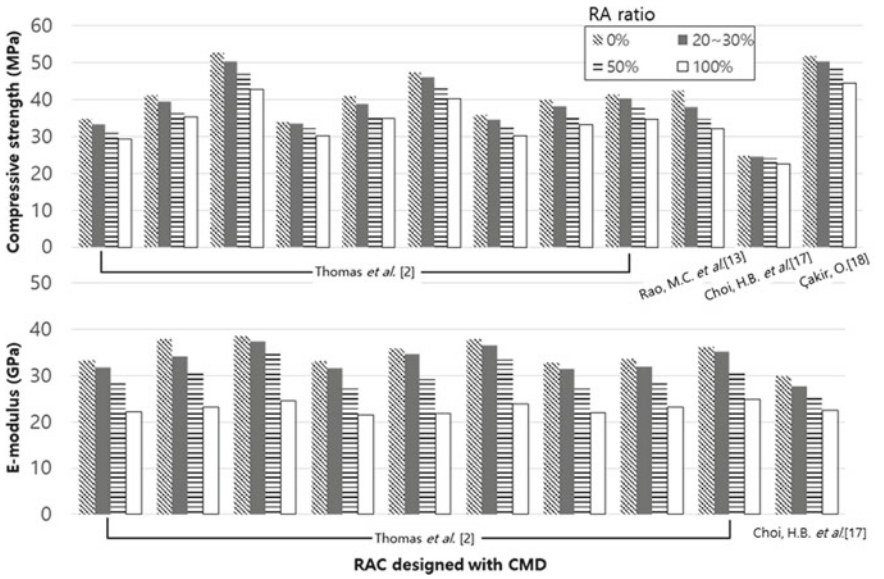

Fig. 3 Correlation between mechanical properties of RAC designed with CMD and RA replacement ratio (data from [2, 13, 17, 18])

3.2 Mechanical Strength of RAC Designed with CMD

As mentioned in the previous section, the gaps of property development that occurred from the early ages continue to later ages. Figure 3 shows the difference in compressive strength and elastic modulus as a function of the RA replacement rate 0, 25–30, 50, 100%, in case of the amount of cement and water used for mixing is the same. It can be observed that: as the replacement rate is increased, the mechanical properties are significantly lowered.

4 Overview of Properties of Recycled Aggregate Concrete Designed with EMV and M-EMV Method

The original EMV mix design method has been studied since it was first proposed in 2009 by Fathifazl et al. [5], and it has been modified by other researchers to improve its performance [10, 11]. Figure 4 shows the compressive strength and modulus of elasticity as a function of the replacement rate of RAC designed with EMV/M-EMV. In some mixtures, as in the case of the compressive strength of study [19], a decrease in properties is observed, but no particular trend that occurs as RA increases. Figure 5 shows the effects of CMD and EMV/M-EMV mix design on RAC made from the

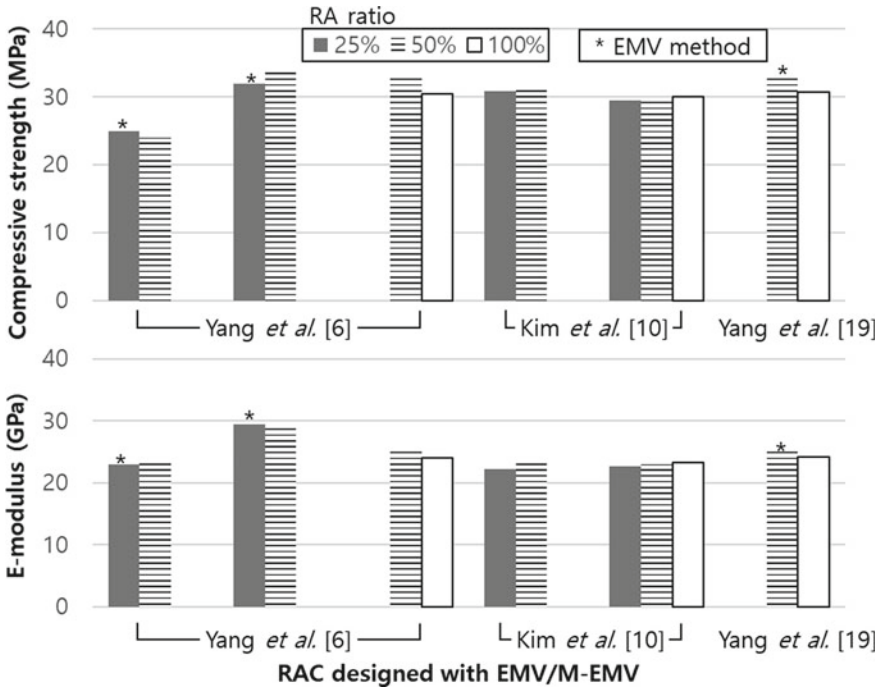

Fig. 4 Correlation between mechanical properties of RAC designed EMV/M-EMV mix design methods and RA replacement ratio (data from [6, 10, 19])

same RA. In the case of using the same replacement ratio and mixing with EMV/M-EMV, the compressive strength and elastic modulus values ranged from −8.9 to 9.5% and −1.69 to 10.8%, respectively, compared to CMD concrete. The results indicate that strength can be improved while reducing the use of cement and sand, and increasing the use of RA. However, as mentioned in the author's previous paper [20], the effectiveness of EMV and M-EMV has been demonstrated, but accumulated research data are insufficient, and most of the research conducted are focused on the mechanical properties at later ages (Table 1).

5 Research Gaps and Perspectives

The use of EMV/M-EMV mix design can be comparable to the conventional mix design with NAC with respect to the mechanical strength. As shown in the Table 1, most of studies related to EMV/M-EMV methods, however, focused on the mechanical properties at later ages (e.g. mechanical strength and elastic modulus at 7, 14, 28 days). In study [22], compressive strength and elastic modulus of EMV-designed concrete were measured the day after casting. However, it was a one-time

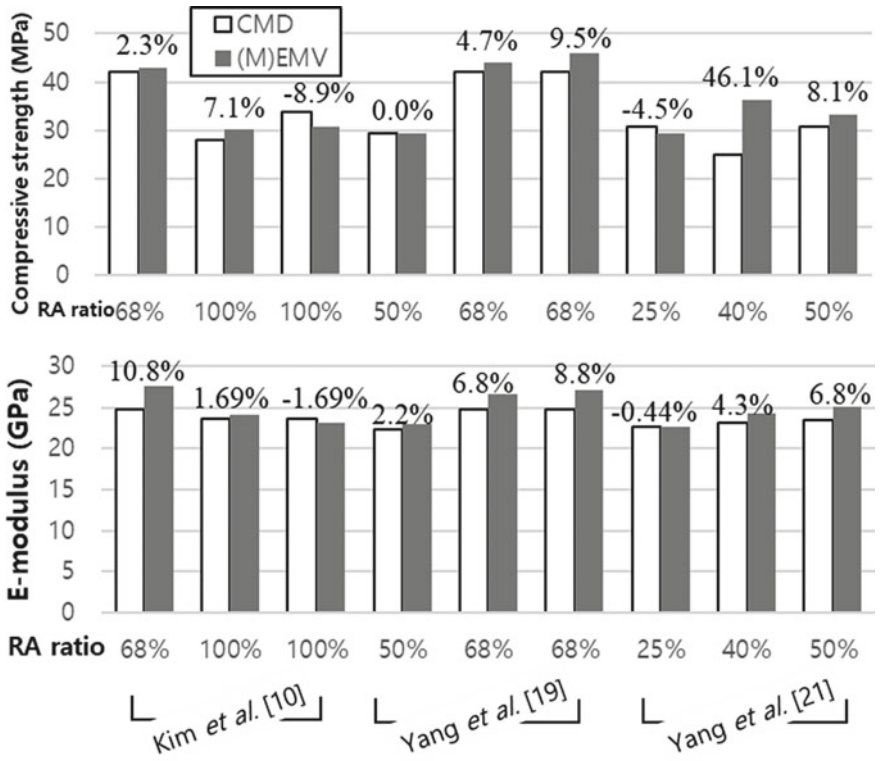

Fig. 5 Comparison of experiment results of RAC designed with CMD and M-EMV (data from [10, 19, 21])

test, not a continuous measurement, and strength development at early ages was not investigated. Considering the fact that the rapid change of the strength development of concrete including RAC ends before the seventh day of age, measurements on early age properties need to be performed earlier as to better grasp impacts (Fig. 6). Figure 6a shows typical strength development trends of CMD-designed RAC based on the experimental results in [4], whereas the continuous measurements of mechanical properties of EMV-designed RAC at early ages were not performed (Fig. 6b).

Taking into account the fact that EMV-designed concrete is a mixture of a small amount of fresh mortar and a greater amount of hardened mortar compared to CMD-designed concrete, the early age properties are expected to be different from those of NAC. Therefore, a study of EMV-designed concrete at early ages is considered of high importance in terms of that it can accelerate construction works.

Table 1 Investigated tests from the selected studies on EMV/M-EMV

	[5, 6, 10, 25]	[7]	[19]	[21]	[22]	[23]	[24]	[26]	[27]
fc (~7d)	–	–	–	–	+	–	–	–	–
fc (7d~)	+	+	+	+	+	+	–	–	+
ff (~7d)	–	–	–	–	–	–	–	–	–
ff (7d~)	–	–	–	–	+	+	–	–	–
ft (~7d)	–	–	+	–	+	–	–	–	–
ft (7d~)	–	+	–	–	–	+	–	–	–
Ec (~7d)	–	–	–	–	–	–	–	–	–
Ec (7d~)	+	+	+	+	–	+	–	–	–
Freeze–Thaw	–	–	–	–	–	–	+	+	–
D-shrinkage	–	–	+	+	–	+	+	–	–
Cl-penetration	–	–	–	–	–	–	–	+	+
carbonation	–	–	–	–	–	–	–	+	–

*~*7d* before 7 days of casting; *7d~* after 7 days of casting; *fc* compressive strength; *ff* flexural strength; *ft* tensile strength; *Ec* elastic modulus; *D-shrinkage* drying shrinkage; *Cl-penetration* chloride ion penetration

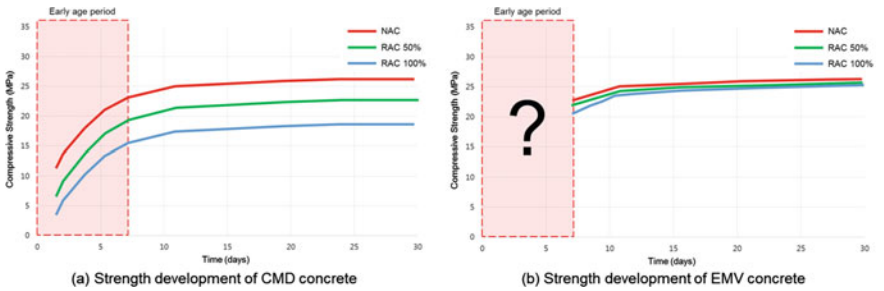

Fig. 6 Strength development of concrete with CMD (L) [4], EMV (R)

6 Conclusions

The conclusions and suggestions for future research are as follows:

– Physical properties of CMD-designed RAC show lower values as a function of replacement rate of RA, whereas RAC designed with proper mix design methods such as EMV/M-EMV can be comparable to NAC with respect to the mechanical strength properties.
– In a study on EMV-designed RAC, compressive strength and elastic modulus at early age (at 1 day after casting) were measured. However, since the test was a non-continuous and one-time measurement, the strength development at early ages was not studied.

– Since the total volume amount of mortar in RAC is adjusted, EMV-designed RAC are expected to have different early age properties. Therefore, direct and continuous measurements of the mechanical behaviour of EMV-designed RAC at early ages need to be investigated using appropriate techniques, such as EMM-ARM method, which can measure the early age properties of cementitious material since casting.

Acknowledgements Funding provided by the Portuguese Foundation for Science and Technology (FCT) and FEDER (COMPETE2020) to the Research Project IntegraCrete (PTDC/ECM-EST/1056/2014 - POCI-01-0145-FEDER-016841) is acknowledged. This work was was also financially supported by UID/ECI/04029/2019—ISISE—Institute for Sustainability and Innovation in Structural Engineering, funded by national funds through the FCT/MCTES (PIDDAC).

References

1. de Juan, M.S., Gutiérrez, P.A.: Study on the influence of attached mortar content on the properties of recycled concrete aggregate. Constr. Build. Mater. **23**(2), 872–877 (2009)
2. Thomas, J., Thaickavil, N.N., Wilson, P.M.: Strength and durability of concrete containing recycled concrete aggregates. J. Build. Eng. **19**, 349–365 (2018)
3. Hanif, A., Kim, Y., Lu, Z., Park, C.: Early-age behavior of recycled aggregate concrete under steam curing regime. J. Clean. Prod. **152**, 103–114 (2017)
4. Velay-Lizancos, M., Martinez-Lage, I., Azenha, M., Granja, J., Vazquez-Burgo, P.: Concrete with fine and coarse recycled aggregates: E-modulus evolution, compressive strength and non-destructive testing at early ages. Constr. Build. Mater. **193**, 323–331 (2018)
5. Fathifazl, G., Abbas, A., Razaqpur, A.G., Isgor, O.B., Fournier, B., Foo, S.: New mixture proportioning method for concrete made with coarse recycled concrete aggregate. J. Mater. Civ. Eng. **21**(10), 601–611 (2009)
6. Yang, S., Lee, H.: Mechanical properties of recycled aggregate concrete proportioned with modified equivalent mortar volume method for paving applications. Constr. Build. Mater. **136**, 9–17 (2017)
7. Hayles, M., Sanchez, L.F.M., Noël, M.: Eco-efficient low cement recycled concrete aggregate mixtures for structural applications. Constr. Build. Mater. **169**, 724–732 (2018)
8. Commite, A.C.I.: 211, Standard Practice for Selecting Proportions for Normal, Heavy weight and Mass Concrete (ACI 211.1–91). ACI Manual of Concrete Practice, Detroit (2002)
9. EN, BS. 206-1: 2000. Concrete, Specification, Performance, Production and Conformity (2001)
10. Kim, N., Kim, J., Yang, S.: Mechanical strength properties of RCA concrete made by a modified EMV method. Sustainability **8**(9), 1–15 (2016)
11. Surya, M., Rao, V.V.L.K., Lakshmy, P.: Mechanical, durability, and time-dependent properties of recycled aggregate concrete with fly ash. ACI Mater. J. **112**(5), 653–661 (2015)
12. Latif Al-Mufti, R., Fried, A.N.: The early age non-destructive testing of concrete made with recycled concrete aggregate. Constr. Build. Mater. **37**, 379–386 (2012)
13. Chakradhara Rao, M., Bhattacharyya, S.K., Barai, S.V.: Influence of field recycled coarse aggregate on properties of concrete. Mater. Struct. **44**(1), 205–220 (2011)
14. Rahal, K.: Mechanical properties of concrete with recycled coarse aggregate. Build. Environ. **42**(1), 407–415 (2007)
15. Azenha, M., Magalhães, F., Faria, R., Cunha, Á.: Measurement of concrete E-modulus evolution since casting: a novel method based on ambient vibration. Cement Concr. Res. **40**(7), 1096–1105 (2010)

16. Kou, S.C., Poon, C.S.: Enhancing the durability properties of concrete prepared with coarse recycled aggregate. Constr. Build. Mater. **35**, 69–76 (2012)
17. Choi, H.B., Yi, C.K., Cho, H.H., Kang, K.I.: Experimental study on the shear strength of recycled aggregate concrete beams. Mag. Concr. Res. **62**(2), 103–114 (2010)
18. Çakir, O.: Experimental analysis of properties of recycled coarse aggregate (RCA) concrete with mineral additives. Constr. Build. Mater. **68**, 17–25 (2014)
19. Yang, S., Lee, H.: Structural performance of reinforced RCA concrete beams made by a modified EMV method. Sustainability **9**(1), 1–13 (2017)
20. Kim, J., Sadowski, L.: The equivalent mortar volume method in the manufacturing of recycled aggregate concrete. Czasopismo Techniczne **11**, 123–140 (2019)
21. Yang, S., Lim, Y.: Mechanical strength and drying shrinkage properties of RCA concretes produced from old railway concrete sleepers using by a modified EMV method. Constr. Build. Mater. **185**, 499–507 (2018)
22. Rajhans, P., Chand, G., Kisku, N., Panda, S.K., Nayak, S.: Proposed mix design meth od for producing sustainable self compacting heat cured recycled aggregate concrete and its microstructural investigation. Constr. Build. Mater. **218**, 568–581 (2019)
23. Yang, S.: Effect of different types of recycled concrete aggregates on equivalent concrete strength and drying shrinkage properties. Appl. Sci. **10**(11) (2018)
24. Yang, S., Lee, H.: Freeze–Thaw resistance and drying shrinkage of recycled aggregate concrete proportioned by the modified equivalent mortar volume method. Int. J. Concr. Struct. Mater. **11**(4), 617–626 (2017)
25. Knaack, A.M., Kurama, Y.C.: Design of concrete mixtures with recycled concrete aggregates. ACI Mater. J. **110**(5), 483–493 (2013)
26. Abbas, A., Fathifazl, G., Isgor, O.B., Razaqpur, A.G., Fournier, B., Foo, S.: Durability of recycled aggregate concrete designed with equivalent mortar volume method. Cem. Concr. Compos. **31**(8), 555–563 (2009)
27. Rajhans, P., Gupta, P.K., Ranjan, R.K., Panda, S.K., Nayak, S.: EMV mix design method for preparing sustainable self compacting recycled aggregate concrete subjected to chloride environment. Constr. Build. Mater. **199**, 705–716 (2019)

Finite Element Modelling of Concentrated Anchorage Load in Early Age Concrete

Massoud Sofi, Lino Maia, Elisa Lumantarna, Aocheng Zhong, and Priyan Mendis

Abstract Analyses of end-block and beam-end specimens have been undertaken based on the finite element models. The purpose of the analyses is to investigate the effects of concrete early age properties on the response behaviour of the anchorage zone. Time dependent strains and stresses in the anchorage zone are evaluated. The mechanical concentrated load represents the anchorage in post-tensioning of slab or beam during construction where the load is transferred typically at 1 and 4-days ages. The analyses incorporate thermal, creep and shrinkage effects. The double power law (DPL) is adopted to represent the creep effects. The ACI 209 and the CEB-FIP shrinkage models in FE TNO DIANA were also adopted to account for shrinkage. The models are validated based on experiments. Results indicate that early ages concrete effects need to be considered for design of sensitive elements in particular such as anchorage zones of post-tensioned elements.

Keywords Early age concrete · Post-tensioning · Anchorage · Load transfer

1 Introduction

During the early ages, concrete experiences a significant amount of volume change, primarily due to the cementitious materials' hydration reaction (chemical shrinkage), available moisture (autogenous shrinkage) and temperature evolution (thermal deformations). These volume changes generate compressive and tensile stresses when the

M. Sofi · E. Lumantarna · P. Mendis
Infrastructure Engineering Department, Melbourne University, Parkville, Australia
e-mail: massoud@unimelb.edu.au

L. Maia (✉)
Faculty of Engineering (FEUP), CONSTRUCT-LABEST, University of Porto, Porto, Portugal
e-mail: linomaia@fe.up.pt

Faculty of Exact Sciences and Engineering, University of Madeira, Campus Universitário da Penteada, 9020-105 Funchal, Portugal

A. Zhong
Melbourne University, Parkville, Australia

E. B. Pereira et al. (eds.), *Proceedings of the 3rd RILEM Spring Convention and Conference (RSCC 2020)*, RILEM Bookseries 32,
https://doi.org/10.1007/978-3-030-76547-7_24

concrete member is restrained. These stresses are intensified with the higher rate of creep at early ages. Heavy reinforcements and adjoining structural members can act as internal and external restraints, respectively. Stresses associated with effects of early age concrete simultaneously occur at the time when the concrete is developing strength.

Early age dilatations and the associated stresses become significant during construction when post-tensioning loads are transferred to the element. To account for the early age stresses, a conservative design approach is normally adopted for the anchorage zone concrete.

In post-tensioning applications, the tendon forces are transferred to the concrete using an anchorage device that are often proprietary. They are supplied with special bearing plates that have a complex geometry and rely on local confinement reinforcements to resist higher bearing pressures than normally imposed on concrete. Post-tensioning load transfer is completed within a space of 7 days after the concrete pour. Therefore an accurate characterisation of the state of concrete during this time is essential. Current design standards intrinsic thermal stresses.

This paper reports on the finite element modelling of anchorage zone concrete behaviour taking into consideration the early age concrete effects. Finite element models of two different types of specimens are described, where in addition to simulation of early age properties as first part of the analysis, an external mechanical load is applied in the second part. The first type of specimen "end-block" model is validated on published literature. The more complex type "beam-end" model includes the dead-end anchor and considered detailing of the geometry of an anchor. The beam-end specimen model is validated by comparisons with the experimental results.

2 Review of Literature

In 1953, Guyon presented a solution based on the theory of elasticity to the problem of determining the bursting force in a concentrically loaded rectangular member [1]. Guyon's approach to the determination of stresses in the anchorage zone has been widely used to date and can be found in most textbooks covering design of concrete structures [2, 3].

The transverse stresses in the anchorage zone are well elaborated in Warner et al. [2]. In considering the transverse stresses set up in an end-block, it is important to keep in mind that the stress field is essentially three-dimensional. The anchorage applies a compressive force to the concrete in the longitudinal direction (x-direction). This fans out in the lead length and, in doing so, it sets up transverse stresses in both the vertical direction and the lateral direction. These stresses are radial, but for design purposes they are resolved into 2 dimensions (Fig. 1).

According to Breen et al. [4], the objectives of the anchorage zone design are to assure the safe introduction of the tendon force into the structure and to control crack width under service load. Transverse tensile stresses and some concrete cracking in the anchorage zone, particularly along the tendon path is expected.

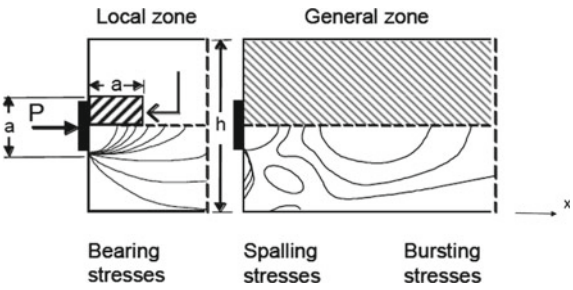

Fig. 1 Local and general anchorage zones [4]

The problem associated with introducing a concentrated load into a pseudo-elastic structural member (such as concrete) has existed as long as the concept of post-tensioning has been around over a century ago. Different approaches have been adopted towards a solution to the problem. Initially, the problem was treated based on linear elastic theory and the equilibrium method of analysis. Although, this approach forms the basis of analysis recommended by the standard code of practice to date and is deemed to be safe [4], it ignores the fact that cracking of the structure introduces significant stress redistributions. In practice, one added problem for concrete properties during the construction is that the concrete is not fully cured and it is at the same time subjected to early age effects.

3 FE Model Description of Anchorage Specimens

Non-linear finite element code DIANA has been used to simulate the structural response of anchorage in concrete. Program TNO DIANA has been used to simulate the anchorage zone behaviour. The FE model of a push-in specimen (end-block) according to the Zielinski and Rowe [5] experiments are presented first. The second model (beam-end) is a more elaborate version of a dead-end anchor. The FE model of beam-end specimen is validated by experimental results. As for early age properties, it is assumed that concrete is fully restrained in both cases.

For this study adopted the modified Newton-Raphson iteration. In the modified Newton-Raphson iteration, the stiffness matrix is calculated at each time-step.

3.1 End-Block Model

The current model presented by the Australian Standards to estimate the bursting stresses is a modified version of the equation proposed by Zielinski and Rowe [5]. In order to consider the concrete early age effects, it was deemed important to study a model that is a replica of the end-block specimen experimentally tested [5]. The

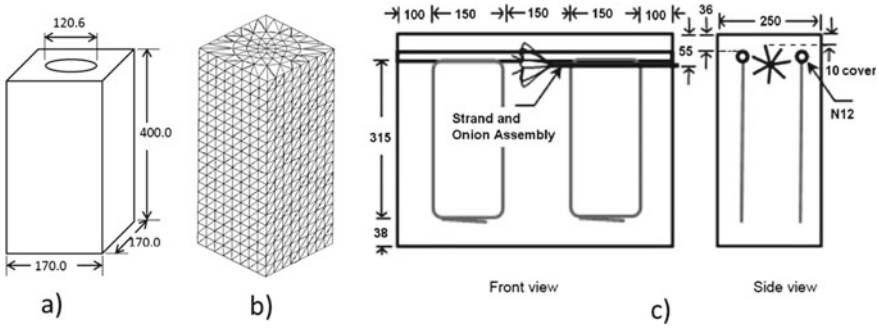

Fig. 2 **a** End-block; **b** FE model end-block; **c** beam-end geometry

FE model consists of an end-block with a circular loading anchorage surface (type CIII, no embedded anchorages, no Ductubes), as shown in Fig. 2a.

3.2 Beam-End Model

In order to consider the early age properties of concrete and to study the effect of these on the anchorage zone, a robust beam-end analytical model is presented in this section. The model can simulate both the early age effects and the mechanical action due to the application of the anchorage pullout load. The model is conveniently presented such that it can simulate: (a) the early age properties, including the concrete hydration associated thermal and time-dependent effects in view of the thermal boundary conditions and external conditions (heat flow analysis); and (b) the mechanical action due to the application of pullout load on the anchor (structural analysis). The purpose of this model was to simulate the interaction of an actual dead-end anchor within the concrete. The model can simulate (a) and (b) as these two are exclusively independent analyses, or alternatively, combine the two effects and simulate the thermal analysis of concrete while the mechanical load is imposed simultaneously.

The embedded anchorage "onion" has a $90 \times 90 \times 90$ mm dimensions. One of the most complicated features of the beam-end model is the onion. The location of the onion is set next to the 'exposed' concrete surface. The connection between the steel elements (strand and wire) and the surrounding concrete is done via the interface elements. The truss lines representing the wires are made of very small lines, all interconnected. This is to provide flexibility of displacement when the specimen is subjected to the pullout load. The lines representing the wires are joined together on the left and the right sides. On the right side, the lines are joined again with the line representing the strand. The wire and the strand is made up of truss elements connected to the concrete blocks surrounding it, via the interface elements. The

lines representing the 7 mm wires and the 12.7 mm strands are each given a cross-sectional dimension representative of their actual diameters. A detailed description of the experimental work and FEM approach is reported in Ref. [6].

3.3 Temperature Development in Hydrating Concrete: Theoretical Background

The temperature development in hardening concrete due to hydration may be described by the Fourier differential equation for heat conduction in a homogeneous and isotropic body.

$$div(q) + \rho c\dot{T} = Q \tag{1}$$

$$q = -K\nabla T \tag{2}$$

where q is the heat flux, T is the temperature, $\dot{T}$ is the rate of temperature rise, ∇T is the temperature gradient, ρ is the mass density, c is the specific heat, Q is the rate of internal heat generation per unit volume, and K is the conduction coefficient.

Convection refers to the heat transfer that occurs between the concrete surface and a moving fluid (usually air) when a temperature gradient is installed between both materials. According to Newton's cooling law, the convective heat transfer can be expressed as shown in Eq. (3) [7]:

$$q \cdot n = h(T_f - T) \tag{3}$$

where q is the convective heat flux per unit area, n is the vector pointing outwards normal to the boundary, h is the heat transfer coefficient, T is the boundary temperature, and T_f is the temperature of the surroundings.

3.4 Material Properties

A 32 MPa commercial concrete specially designed for post-tensioning of slabs in multi-story building is considered for this work. In the experimental work, 16 mm plywood was used as the formwork for curing the concrete (Fig. 3a) (Table 1).

The adiabatic temperature rise of the mix is presented in Fig. 4.

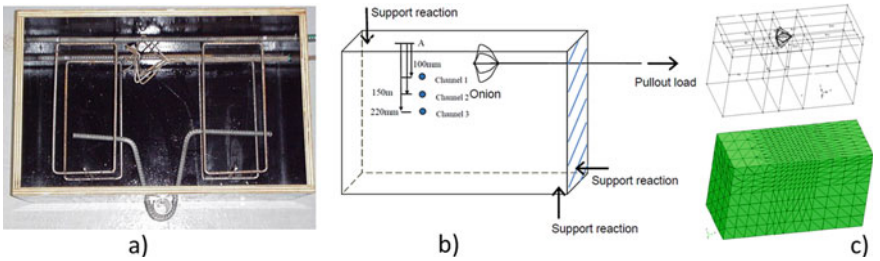

Fig. 3 **a** Beam-end mould, reinforcements and the anchor; **b** beam-end support reactions and the location of thermal sensors (Channel 1–3); **c** beam-end FE model

Table 1 Thermal properties of concrete and the boundary conditions

Parameter	Value
Concrete thermal conductivity (W/m °C)	2
Concrete volumetric heat specific capacity (J/m^3 °C)	4.6×10^6
Convection-radiation coefficient between concrete and air (W/m^2 °C)	7.5
Plywood thermal conductivity W/(m °C)	0.1154
Heat transfer coefficient concrete-air W/(m^2 K)	10
Equivalent convection-radiation coefficient between concrete and formwork (W/m^2 °C)	6
Arrhenius constant Ea/R	4000

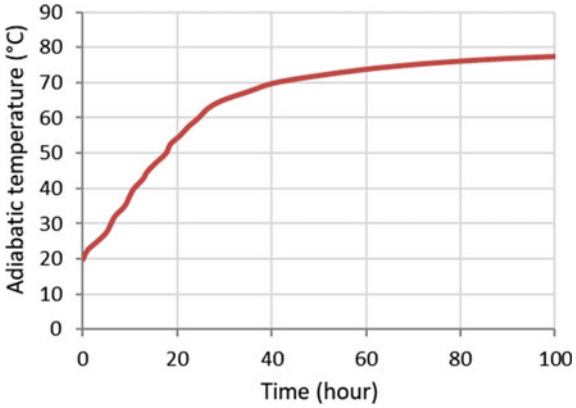

Fig. 4 Adiabatic temperature of the concrete mix

4 Model Validation and Results

Figure 5 presents a comparison between the recorded temperature profile and that simulated from FE model. Only one temperature location in the concrete block is pretend. The model was shown to be in good agreement with the experimental results. Temperature profiles recorded from the experiment and the analyses were found to be very similar, with a maximum temperature difference of about 2 °C. It is noted that the values of the input parameters were found to vary quite significantly in the literature.

The thermal stresses and the cracking tendency of cast in situ concrete at early ages under restrained condition is a concern. The interim findings of a research program that is aimed to investigate the in situ thermal stresses at early ages. The intrinsic thermal stresses including the effects of creep and shrinkage associated with early age concrete have been investigated. A degree of reaction approach is adopted to account the evolution of material properties of concrete [8].

4.1 Material Properties Anchorage Zone Strains in Early Age Concrete

The beam end model presented in (Fig. 3) has been shown to be able to simulate the anchor-concrete interaction with a reasonable accuracy. This highly complex model involves the anchorage assembly, which consists of the wires and the strands, the concrete volumes which surrounds the anchorage, and the interface elements representing the connection between the steel elements and the surrounding concrete. Investigation of early age concrete include extensive number of parameters associated with early age properties on strains and stresses that occur on the concrete surface as a result of mechanical actions. To bring the computation time to a manageable level, the simpler end block model is chosen for the parametric studies presented.

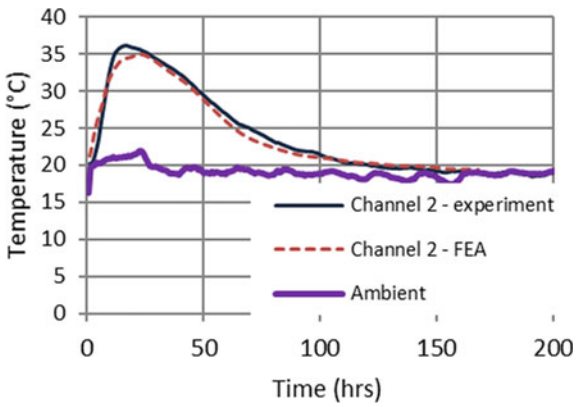

Fig. 5 Comparison of temperatures between the FEM and experimental results

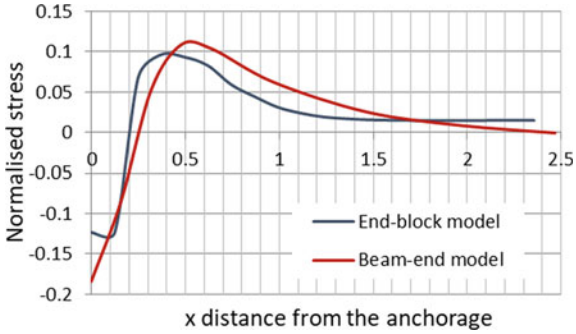

Fig. 6 Comparison of stress distributions between end block and beam end models

The end block model has been used by numerous researchers to investigate the development of bursting stresses under post tension load [1, 5]. The model was validated against experimental data in order to ascertain that the end-block model can simulate the response behaviour of the more sophisticated beam-end model, the stress distributions in the transverse direction were compared. As the helical and transverse reinforcements in the local and general anchorage zone, respectively, are designed to prevent the occurrence of cracks, finite element analyses were conducted on both models assuming linear elastic behaviour. Figure 6 presents the stress distributions along the central line on the face of end block (z direction) and beam (y direction) models.

The stress values normalised with respect to the imposed stress were plotted against the distance (x) from the location of the plate normalised with respect to the width of the specimen (h). The stress values on the end block and beam end models are shown to be similar (Fig. 6). Given the complexity of the analysis, the smaller end-block model is considered adequate for the analysis of the anchorage zone behaviour.

Further, in order to adjust the size effects between the beam-end and the end-block models, the thermal properties of the FE models can be adjusted such that the temperature development and degree of hydration obtained from the model are similar to that from the beam-end model. Comparison of the temperature development and degree of hydration values between the end-block and beam-end models is presented in Fig. 7. The results of Fig. 7 are based on the ambient temperatures presented in Fig. 5.

The compressive forces imposed on the end-blocks were determined based on common tendon unit types supplied by VSL, with a breaking load of 184 kN for a 12.7 mm wire strand. The post-tensioning load is applied up to 80% of the breaking load of the strands in accordance with AS3600 (2009).

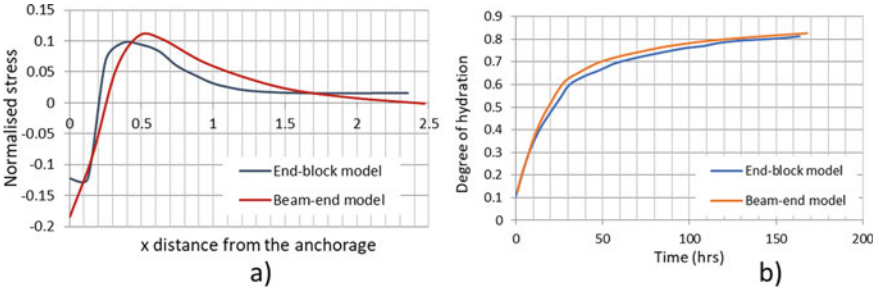

Fig. 7 Comparison of: **a** temperature development; and, **b** degree of hydration between end block and beam end model

4.2 Strain Increment Due to a 2 Stage Post-tensioning Load

The push-in stress imposed on the end-block was determined based on common tendon unit types supplied by VSL Australia Pty Ltd, with a breaking load of 184 kN for a 12.7 mm wire strand. The post-tensioning load is applied up to 80% of the breaking load of the strands in accordance with AS3600 (2009). Depending on the strength gain of concrete, it is also a requirement that the post-tensioning load be introduced in two stages: 25% of the post-tensioning load imposed 1–2 days after casting the concrete member; and the remaining 75% applied 4 to 7 days after.

It is postulated that strain levels in the highly stressed zone of concrete increase significantly during the time when the load is first introduced to the second stage of loading. Therefore, it is important to investigate whether the strain levels in the anchorage zone increase between the two stages of the loading process. For simplicity, it is assumed that the post-tensioning load is applied at 1 and 4-days age. The stress values corresponding to an anchorage plate areas 11,500 mm^2 is calculated to be 10 and 38.5 MPa for 1 and 4-days age concrete. The strain and stress values were calculated for a duration of 7 days.

To investigate the effects of creep, shrinkage and temperature development in concrete on its response behavior in the anchorage zone, the variation in ambient temperature is initially excluded. The concrete end-block is subject to a constant temperature of 20 °C. The preliminary analysis was undertaken using ACI 209 models to describe the effects of creep and shrinkage.

Figure 8 presents the strain development in the concrete when shrinkage is ignored. Instantaneous increase in tensile strain observed at 1 and 4-days age represents the instantaneous increase in loads applied when concrete is at 1 and 4-days age. The total strain value decreases between 1 day and 4-days, but increases from 4-days onwards Fig. 8a. The total strain consists of thermal and creep strains, as presented in Fig. 8b. The reduction in the strain values between 1 to 4-days is as a result of rapid reduction in the thermal strain in the concrete block from 1 to 4 days. The high rate of reduction in the thermal strain is expected as the in situ temperature of the concrete block decreases rapidly from 1 to 4-days.

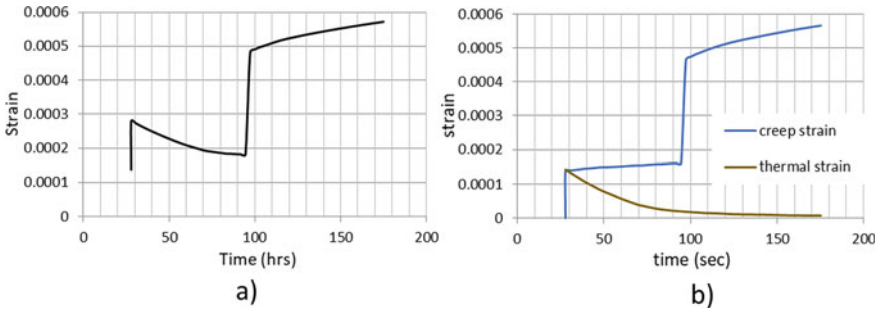

Fig. 8 Strain results based on ACI 209 creep model (ignoring shrinkage): **a** total strain; and, **b** creep strain and thermal strain

The analyses show that the rate of reduction in compressive strain due to temperature is higher than the increase in tensile strain due to creep between 1 and 4 days. Therefore, the concrete experiences a reduction in total tensile strain. On the other hand, the effects of temperature on the concrete block of 4-days age onwards are not significant due to a much less pronounced decrease in the temperature after 4 days. The increase in the tensile strain due to creep is higher than the decrease in the thermal strain. As a result, an increase in the total tensile strain was observed in the concrete block at 4 days onwards. It was also observed from the analyses that initial strain exists at 1 day, prior to the application of the load. The initial strain was contributed to by the thermal strain developed as the temperature increases to a peak value at around 1 day.

5 Concluding Remarks

Finite element approach for two different specimens representing anchorage zone of concrete at early ages is presented. It is shown that the simpler model "end-block" model yields similar results to that of beam-end specimen which takes into consideration all detailing of a typical anchorage zone concrete. Therefore, to conduct parametric studies looking into the effects of early age concrete, it is end-block model is preferred as it will take less run time.

The end-block model is then used to simulate the two stage post-tensioning load application at 1 and 4-days age. The tensile strain at the anchorage zone is then plotted against time (representing duration of the time since the load is applied).

Acknowledgements This research is financially supported by the Melbourne Research Scholarship offered by the University of Melbourne and the Australian Research Council's Discovery Early Career Researcher Grant (DE170100165, DE 2017 R1). This work is financially supported by: Base Funding—UIDB/04708/2020 of the CONSTRUCT—Instituto de I&D em Estruturas e Construções—funded by national funds through the FCT/MCTES (PIDDAC). This work is funded

by national funds through FCT—Fundação para a Ciência e a Tecnologia, I.P., under the Scientific Employment Stimulus—Institutional Call—CEECINST/00049/2018.

References

1. Guyon, Y.: Prestressed Concrete. Parsons, London (1953)
2. Warner, R.F., Rangan, B.V., Hall, A.S., Faulkes, K.A.: Concrete Structures. Longman, Melbourne (1998)
3. Loo, Y.C., Chowdhury, S.H.: Reinforced and Prestressed Concrete, Analysis and Design with Emphasis on Application of AS 3600–2009. Cambridge University Press, Melbourne, Australia (2010)
4. Breen, J.E., Burdet, O., Roberts, C., Sanders, D.H., Wollmann, G.: Anchorage Zone Reinforcement for Post-Tensioned Concrete Girders, NCHRP 356. The University of Texas, Washington, D.C. (1994)
5. Zieliński, J., Rowe, R.E.: An investigation of the stress distribution in the anchorage zone of post-tensioned concrete members. Research Report No. 9, Cement and Concrete Association, London (1960)
6. Sofi, M., Mendis, P., Baweja, D., Mak, S.: Influence of ambient temperature on early age concrete behaviour of anchorage zones. Constr. Build. Mater. **53**, 1–12 (2014)
7. Faria, R., Azenha, M., Figueiras, J.A.: Modelling of concrete at early ages: application to an externally restrained slab. Cement Concr. Compos. **28**(6), 572–85 (2006)
8. Sofi, M., Lumantarna, E., Mendis, P., Zhong, A.: Thermal stresses of concrete at early ages. J. Mater. Civ. Eng. **31**(6), 04019056 (2019)

Analysis of the Interfacial Debonding Behaviour of NSM CFRP Laminates with Cement-Based Adhesive Using Digital Image Correlation Technique

R. Mohammadi Firouz, L. M. P. Matos, Eduardo B. Pereira, and Joaquim A. O. Barros

Abstract The superb performance of carbon fiber reinforced polymer (CFRP) composites as near surface mounted (NSM) reinforcement in strengthening solutions for structures is already well recognized. Due to their deficiencies in fire conditions, cement-based adhesives as an alternative to polymeric matrices are recently suggested as a solution in these systems. However, the interface between the CFRP laminate and cement-based adhesives should have good stress transferring capacity. Thus, it is of great importance the research on improving this interface to increase the bonding capacity of CFRP/cement-based adhesive system. For that purpose, pull-out tests were conducted to examine the interfacial debonding process of two types of CFRP laminates: conventional smooth surface laminates and sand surface treated laminates. Digital image correlation (DIC) technique was used to verify the potentiality of the proposed sand treating approach. Therefore, the interlocking mechanism of sand treated laminates with the developed cement-based adhesive is assessed and the results are compared to those with non-treated smooth surface laminates. Furthermore, the bond-slip behaviour from pull-out tests is compared to obtained data through the DIC technique. The results verified the effectiveness of sand treatment approach applied to NSM CFRP reinforcements. Moreover, the DIC technique has revealed capable of providing qualitative and quantitative information in this regard.

Keywords FRP · NSM · Cement adhesive · Sand treatment · DIC

1 Introduction

During the past decades, strengthening of concrete structures by means of Carbon Fibre Reinforced Polymers (CFRP) has been vastly investigated and is now a widely accepted method to rehabilitate deficient or deteriorating structures. These materials

R. Mohammadi Firouz (✉) · L. M. P. Matos · E. B. Pereira · J. A. O. Barros
Department of Civil Engineering, ISISE, Institute for Sustainability and Innovation in Structural Engineering, University of Minho, Guimarães, Portugal
e-mail: rezamf@civil.uminho.pt

E. B. Pereira et al. (eds.), *Proceedings of the 3rd RILEM Spring Convention and Conference (RSCC 2020)*, RILEM Bookseries 32,
https://doi.org/10.1007/978-3-030-76547-7_25

are very appealing due to their high tensile capacity, lightweight, corrosion resistance and relatively ease of installation. Near Surface Mounted (NSM) technique is one of the most adopted approaches in the application of FRP-based strengthening to enhance structural performance. This approach consists in cutting grooves in the cover of reinforced concrete (RC) element and embedding the CFRP strip or bars within an adhesive medium pre-introduced into the grooves. Some of the advantages of this methodology include the elimination of surface preparation, increased protection from environmental effects and vandalism acts, and preventing premature debonding, compared to externally bonded reinforcement (EBR) technique [1]. In recent years, many researchers have proven the efficiency of such NSM technique in increasing flexural [2], shear [3], torsional [4], and punching [5] capacity of reinforced concrete (RC) elements.

In the NSM technique, the bonding capacity of the adhesive material plays an essential role in the performance of the rehabilitated element, and often constitutes a cut off factor in the expected structural performance [6]. Typically, epoxy-based materials are used to ensure the stress transferring mechanism between the CFRP and the concrete substrate. However, fire resistance of such materials is one major drawback due to their low glass transition temperature (Tg). When subjected to high temperatures, their bonding capacity is severely affected, which compromises the structural performance of the strengthening intervention. In an attempt of surpassing this limitation, some researchers suggested the use of cementitious-based materials as bonding agent between the CFRP and the concrete substrate [7–9]. In this research, a cement-based material is used as an adhesive for NSM CFRP strengthening technique.

Digital Image Correlation (DIC) is a computer image-based measurement technique that consists in monitoring the undergoing deformations of materials by tracking a regular grid of points on the surface of the specimen over subsequent digital images [10]. The captured images are divided in sets of pixels called “facets”, which are tracked throughout the process by means of the greyscale values of the pixels that compose the facet. Thus, the uniqueness of each facet is of utmost importance since this will aid the algorithm to monitor the facet throughout the process [11]. Moreover, smaller facet sizes will lead to higher resolution in the obtained results. However, the computation time significantly increases and can result in the inability of the algorithm to correlate the facet position since there is a smaller number of “features”, or in other words, the uniqueness of each facet decreases [12]. Some materials have enough features on the surface to allow the application of DIC technique, i.e. concrete or stone. In order to decrease the measurement error and ensure results over the entire imaged area, a stochastic speckle pattern is applied onto the surface of the specimen for granting the uniqueness of the facets. This methodology presents several advantages since it is a non-destructive/non-contact technique and allows the monitoring of the entire surface of interest, whereas more conventional approaches are restricted to a discrete number of points. Furthermore, in case of concrete structures, DIC is capable of detecting crack formation and propagation at a much earlier stage, eliminating the necessity of pausing the test to photograph and mark the specimen throughout the experimental study [13]. Several researchers

have been exploring the potential of DIC technique to measure deflection and crack widths in concrete beams [14], the fatigue behaviour of strengthened RC beams [13], analysing the bond-slip behaviour of FRP to concrete elements [15, 16] and monitor crack patterns [17].

The current research is focused on the bond-slip response of CFRP laminates attached to the concrete substrate by cementitious-based adhesive. The interaction between the CFRP laminates and the adhesive was evaluated using the DIC technique.

2 Experimental Work

The experimental program consists of pull-out tests of NSM CFRP strips, in order to investigate the bond stress-slip behaviour between the cement-based adhesive and laminates with smooth and sand treated surfaces.

The experimental study consists of two series of pull-out tests, considering two types of CFRP laminates, namely, untreated (UT) smooth surface laminates and fine sand treated (FS) laminates. Fine sand with the particle size in the range of 0.6–0.85 mm was used to cover these surfaces with S&P® 55 epoxy resin, as the bonding agent. Figure 1 shows a typical FS and UT laminate.

2.1 Specimen and Mixture Description

The specimens consist of 3 normal strength concrete blocks (class of C20/25 according to the Eurocode 2) with 200 × 200 × 100 mm dimensions. On each prism, two grooves were cut to introduce CFRP laminates. A bonding length of 125 mm was selected for all samples. In Fig. 2 a schematic representation of the specimens is presented. In order to perform NSM strengthening, S&P® CFRP laminates supplied by Clever Reinforcement with a cross section of 1.4 × 10 mm^2 and average tensile strength and modulus of elasticity of 1909 MPa and 171 GPa, respectively, were used in this work. The laminates were inserted and centred into the grooves that were pre-filled with cement adhesive.

Fig. 1 Sand treated (top) and smooth (bottom) surface CFRP laminates

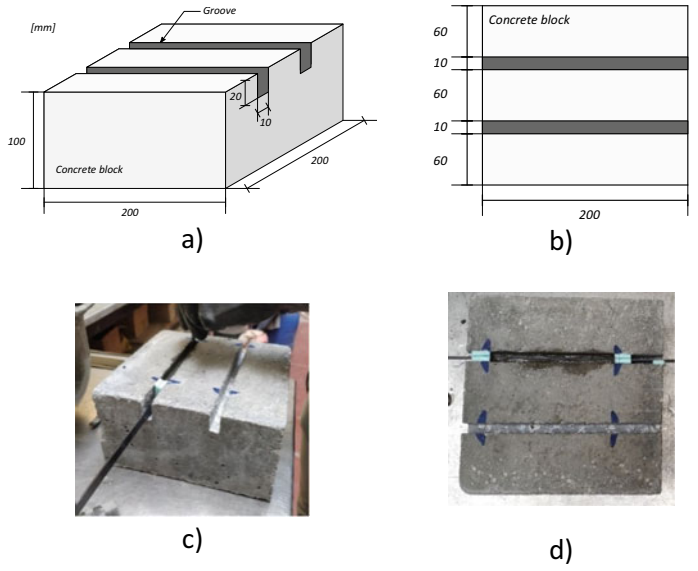

Fig. 2 Schematic representation of the specimen in **a** perspective and **b** plan view; **c** placement of CFRP laminate inside the groove, and **d** Strengthened prism (all dimensions are in mm)

In order to capture the evolution of the sliding between laminate and surrounding adhesive, the top surface of the laminate was cleared from adhesive so that a better view of the laminate's bonding zone could be obtained. Hence, only the lateral and bottom faces of the CFRP laminates were embedded in the adhesive material. Nonetheless, bonding performance was not significantly affected since the top face only corresponds to 6.5% of the total bonding area and has no attachments to the concrete substrate.

A schematic representation as well as photographs of the specimens are presented in Figs. 3 and 4.

The description of the mixture composition used for cement-based adhesive, herein designated as CBA, is presented in Table 1.

2.2 Test Setup

A pull-out test configuration is presented in Fig. 3. Linear variable differential transformers (LVDT) were used to record both loaded-end and free-end slip of CFRP laminates. In addition, a DIC system was applied to monitor the displacement and strain fields on the surface of the specimens. The DIC and LVDT results were compared as well as the performance of the two types of CFRP laminates, when embedded in cement-based adhesives. The pull-out tests were conducted using a

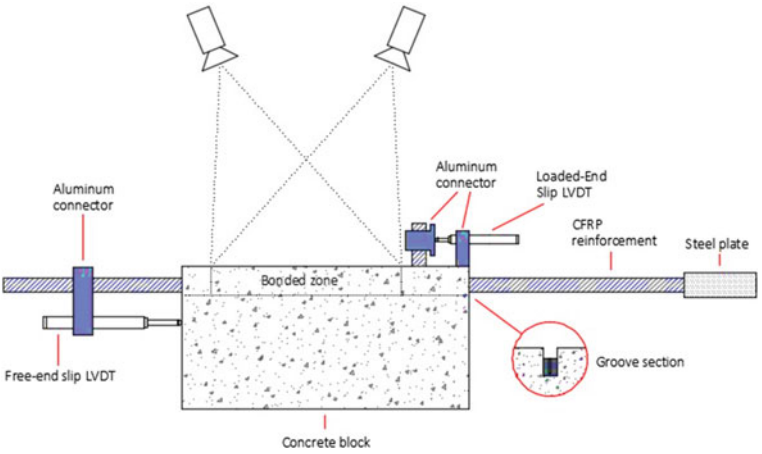

Fig. 3 Schematic representation of the pull-out test setup schematic of the LVDT placement and DIC system cameras

Fig. 4 Setup configuration of the DIC Q-400 system

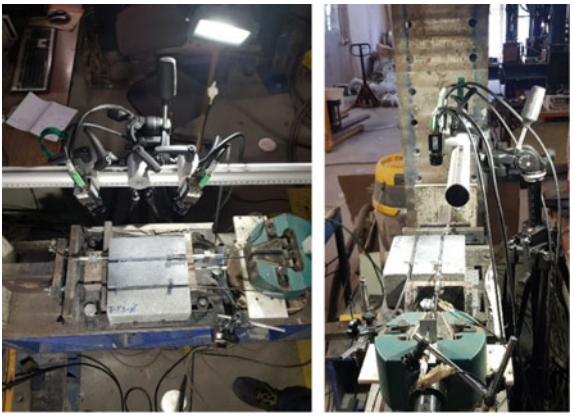

Table 1 Mixture and properties of cement-based adhesive

Cement type	Silica fume	Water/binder	Super plasticizer	Shrinkage reducing agent	Fine sand/Binder	Compressive strength	Modulus of elasticity
CEM I 52.5R (grey)	15% of binder (vol)	20% (mass)	2% of binder (mass)	2% of binder (mass)	50% (mass)	78.6 MPa	29.6 GPa

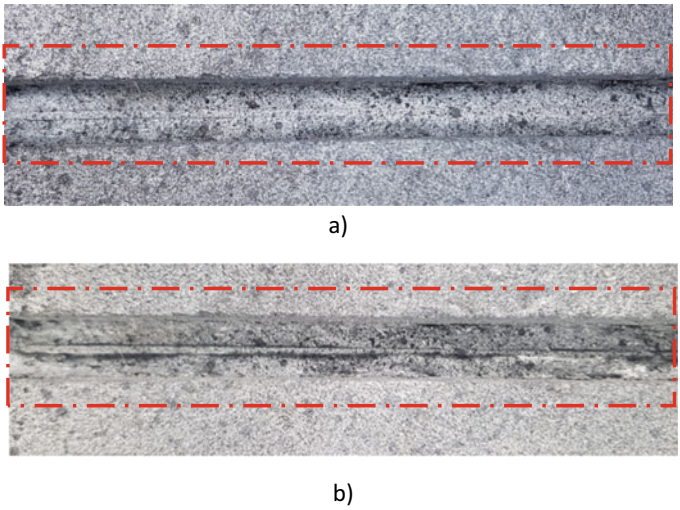

Fig. 5 Speckle pattern applied onto the region of interest; **a** sand treated NSM CFRP, **b** un-treated NSM CFRP

displacement control protocol by imposing a displacement rate of 2 μm/s and the force was monitored by means of a 50 kN load cell.

The Q-400 3D DIC system from Dantec Dynamics was used in this study. This system is composed by 2 cameras with 2.5 MP resolution, two light lamps, a support frame and a tripod. The system was connected to a laptop computer and the image capturing procedure was controlled in the ISTRA 4D software. The image acquisition rate was set to 1 Hz continuously throughout the loading procedure. The setup configuration of the DIC system is depicted in Fig. 4.

In order to apply the DIC technique, a speckle pattern was applied onto the surface of the specimens and inside the NSM grooves. The pattern was applied in two phases, firstly the surface of the specimen was sprayed with a thin layer of white, and subsequently the region of interest was sprayed with black ink in a dynamic manner in order to create a random speckle pattern. The obtained speckle pattern within the NSM groove is presented in Fig. 5.

3 Results and Discussion

In total, 6 samples were tested. Three of them were strengthened using untreated laminates, while in other three sand treated CFRP reinforcements were used. The summary of the obtained results from direct pull-out tests is presented in Table 2. The contribution of the sand treatment of CFRP's surfaces to increase the maximum pull-out force was observed, in agreement with the results obtained in previous researches [9, 18]. The FS-CA samples reached up to 5.38 MPa of average bonding stress during

Table 2 Pull-out test results

Label	Maximum pull-out force (KN)	Load-end slip at max force (mm)	Free-end slip at max force (mm)	Avg. bond strength (MPa)
P-NT-CA	1.87	0.054	0.003	0.66
	1.75*	0.107	0.006	0.61
	1.67	0.046	0.009	0.59
P-FS-CA	15.32	0.488	0.043	5.38
	13.52*	0.451	0.053	4.74
	10.49	0.599	0.037	3.68

P Pull-out test, *NT* no treatment, *FS* fine sand treatment, *CA* cement adhesive, * DIC

pull-out, while this value was 0.66 MPa for NT-CA samples. The average maximum pull-out force for the samples strengthened with sand treated laminates (FS-CA) was 12.91 KN, which was about 7 times higher than for the NT-CA samples, with an average maximum pull-out force of 1.77 KN. The coefficient of variation (COV) for these results were 18.7% and 5.7%, respectively.

Results showed the effectiveness of the sand treating approach in terms of improving the bond between CFRP reinforcements and cement-based adhesive. The adopted technique increased the roughness of the CFRP laminate surfaces, and consequently the interlock resisting mechanisms between this type of laminate and the used adhesive. In order to study this mechanism, DIC technique was used to observe the interaction between laminate and adhesive with the evolution of pull-out force during the test.

Figure 6 shows the strain fields (in the direction of load, X) obtained with the DIC procedure after processing the images taken from the exposed surface of the specimens, as illustrated in Fig. 5 (marked with red line). The results reveal the interaction between the un-treated or the sand treated CFRP laminates and cement-based

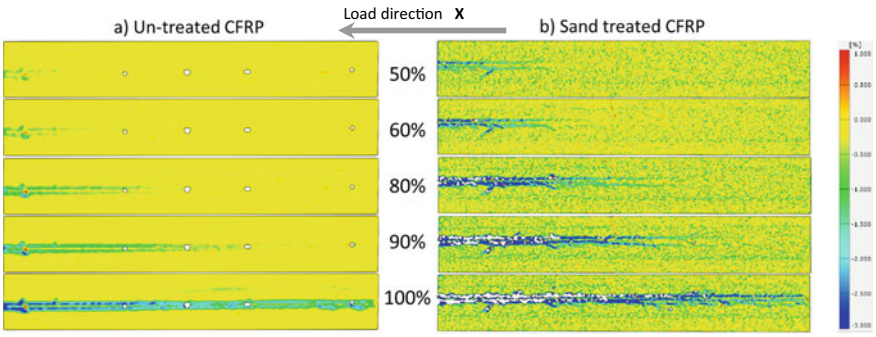

Fig. 6 Strain field in X direction at the top surface of the specimen for **a** un-treated and **b** sand treated CFRP laminates and cement-based adhesive, at different stages of the pull-out test before the peak load was reached, for increasing ratios of the maximum pull-out force varying between 50 and 100%

adhesive, at different stages of the loading procedure with respect to the maximum pull-out force. The negative value is due to the X direction (load direction) and the positive values are considered as error in DIC evaluation. The hollow spaces, visible as white colour are zones in which the software could not follow the facets due to the debilities in stochastic pattern or due to large displacements undermining the face tracking algorithm. The aforementioned interlocking mechanism between the laminate's sand treatment layer and adhesive is revealed by the strain contours in Fig. 6, as the pull-out force increases. The thickness of adhesive which is involved in the process of pull-out force resisting mechanism seems to be considerably larger, as well as the magnitude of the strain increments observed. In contrast, the sample strengthened with untreated CFRP laminate showed a significantly milder interaction, up to the maximum bonding capacity of the strengthened system.

In Fig. 7, the pull-out force versus loaded-end and free-end slip responses obtained from the tests are shown for (a) untreated, and (b) sand treated NSM CFRP reinforcements. The slip in both cases was also obtained using the DIC technique, up to the peak load, by tracing the displacement of the laminate in one point at the loaded end, and in one point at the free end. After the peak load it was not possible to trace the displacements using DIC. This was due to the brittle behaviour of the cement-based adhesive, which caused a sudden pull-out force drop and an abrupt displacement in the laminate and the inability of the DIC algorithm to subsequently follow the facets. The load vs slip experimental responses obtained when considering both the LVDT and the DIC displacements are shown in Fig. 7. The curves obtained from DIC are in relatively good agreement with the ones obtained using the displacements measured with the LVDTs for the ascending branch of pull-out force/slip relationship. However, in case of the sand treated NSM CFRP laminates, there is a difference between the experimental data and DIC results for pull-out force/free-end slip curve, perhaps due to the slight movement of the reaction supports.

4 Conclusion

In the present work a preliminary analysis of the bonding performance of NSM CFRP with cement-based adhesive by using digital image correlation technique was performed. Two different types of CFRP reinforcements were used in the strengthening process: (1) plain untreated, and (2) sand treated CFRP reinforcements. The laminates were installed on the surface, and the bonding region was monitored during the test and later analysed using the DIC technique.

While using a cement-based adhesive, the average pull-out force for untreated and sand treated NSM CFRP strengthened samples was 1.77 (CoV = 6%) and 12.91 (CoV = 19%), respectively. Hence, the adopted treatment strategy contributed to significantly increase the average maximum pull-out force about 7 times, compared to those strengthened with untreated NSM CFRP reinforcements.

It was also possible to document the resisting mechanisms established between CFRP reinforcement and cement-based adhesive along the bonding length during the

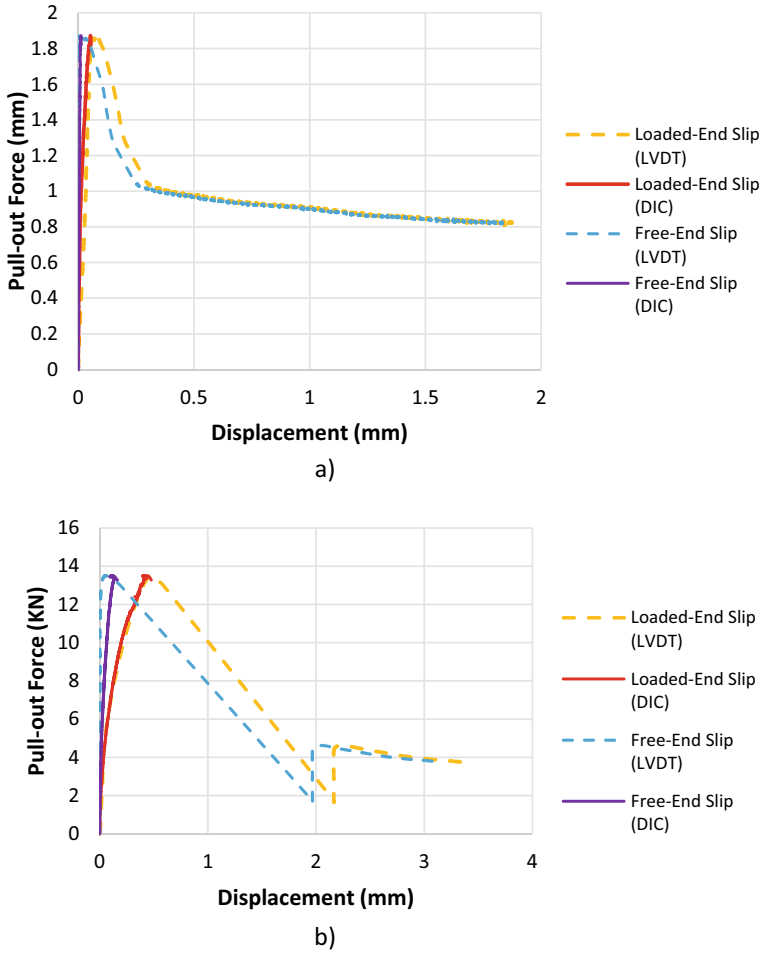

Fig. 7 Pull-out force versus slip curve for **a** un-treated NSM CFRP, **b** sand treated NSM CFRP reinforcements

pull-out test. While comparing the samples with the two different CFRP reinforcement types, the adhesive region involved in the pull-out force resisting mechanisms seems thicker and subjected to higher strain gradients at the interface of sand treated CFRP/adhesive, when compared to the one with untreated laminate. The DIC analysis showed the effectiveness of the interlocking mechanism at the interface of the CFRP laminate/adhesive, produced by the sand layer.

Based on the results obtained from the conducted monotonic pull-out tests, the extracted data from DIC analysis for samples with untreated and sand treated CFRP laminates were used also to derive the load/slip responses. DIC analysis showed a good agreement with experimental results for the ascending branch of pull-out force/slip when LVDTs were used. However, only the experimental response before

the peak load was reached was captured, due to brittle failure of the samples and consequent abrupt slip gradient that made it impossible to follow the facets during the image analysis. Nonetheless, the DIC approach provides the possibility to observe the crack formation throughout the bond zone and follow its propagation, prior to the sudden pull-out load drop of the FS treated laminate.

Acknowledgements The Authors acknowledge the support provided by FCT through the PTDC/ECM-EST/1882/2014 FIRECOMPOSITE project. The collaboration of Sika and Clever reinforcement Iberica is also acknowledged.

References

1. De Lorenzis, L., Teng, J.G.: Near-surface mounted FRP reinforcement: an emerging technique for strengthening structures. Compos. B Eng. **38**(2), 119–143 (2007)
2. Dalfré, G.M., Barros, J.A.O.: NSM technique to increase the load carrying capacity of continuous RC slabs. Eng. Struct. **56**, 137–153 (2013)
3. Dias, S.J.E., Barros, J.A.O.: NSM shear strengthening technique with CFRP laminates applied in high T cross section RC beams. Compos. B Eng. **114**, 256–267 (2017)
4. Gowda, C.C., Barros, J.A.O., Guadagnini, M.: Experimental study of torsional strengthening on thin walled tubular reinforced concrete structures using NSM-CFRP laminates. Compos. Struct. **208**, 585–599 (2019)
5. Barros, J.A.O., et al.: Simultaneous flexural and punching strengthening of RC slabs according to a new hybrid technique using U-shape CFRP laminates. Compos. Struct. **159**, 600–614 (2017)
6. Lorenzis, L.D., Nanni, A., Bond between near-surface mounted fiber-reinforced polymer rods and concrete in structural strengthening. ACI Struct. J. **99**(2) (2002)
7. Hashemi, S., Al-Mahaidi, R.: Investigation of bond strength and flexural behaviour of FRP-strengthened reinforced concrete beams using cement-based adhesives. Aust. J. Struct. Eng. **11**(2), 129–139 (2010)
8. Täljsten, B., Blanksvärd, T.: Mineral-based bonding of carbon FRP to strengthen concrete structures. J. Compos. Constr. **11**(2), 120–128 (2007)
9. Firouz, R.M., Pereira, E.N.B., Barros, J.A.O.: Cementitious adhesives for NSM carbon laminate strengthening system with treated surfaces. In: IABSE Symposium, Guimaraes 2019: Towards a Resilient Built Environment Risk and Asset Management—Report (2019)
10. Sutton, M.A., et al.: Advances in two-dimensional and three-dimensional computer vision. In: Rastogi, P.K. (Ed.) Photomechanics. Springer Berlin Heidelberg, Berlin, Heidelberg. pp. 323–372 (2000)
11. Crammond, G., Boyd, S.W., Dulieu-Barton, J.M.: Speckle pattern quality assessment for digital image correlation. Opt. Lasers Eng. **51**(12), 1368–1378 (2013)
12. Triconnet, K., et al.: Parameter choice for optimized digital image correlation. Opt. Lasers Eng. **47**(6), 728–737 (2009)
13. Mahal, M., et al.: Using digital image correlation to evaluate fatigue behavior of strengthened reinforced concrete beams. Eng. Struct. **105**, 277–288 (2015)
14. Destrebecq, J.-F., Toussaint, E., Ferrier, E.: Analysis of cracks and deformations in a full scale reinforced concrete beam using a digital image correlation technique. Exp. Mech. **51**(6), 879–890 (2011)
15. Zhu, H., et al.: Digital image correlation measurement of the bond–slip relationship between fiber-reinforced polymer sheets and concrete substrate. J. Reinf. Plast. Compos. **33**(17), 1590–1603 (2014)

16. Corr, D., et al.: Digital image correlation analysis of interfacial debonding properties and fracture behavior in concrete. Eng. Fract. Mech. **74**(1–2), 109–121 (2007)
17. Yu, K.-Q., et al.: Development of ultra-high performance engineered cementitious composites using polyethylene (PE) fibers. Constr. Build. Mater. **158**, 217–227 (2018)
18. MohammadiFirouz, R., Pereira, E., Barros, J.: Bond performance of NSM–CFRP laminates using different surface treatments and cementitious adhesives. Fiber Reinforced Polymer for Reinforced Concrete Structures (FRPRCS) 14, pp. 1–4. Belfast, Northern Ireland (2019)

Inverse Analysis of Three-Point Bending Tests for 3D Printed Fibre Reinforced Mortars

Behzad Zahabizadeh, João Pereira, Claúdia Gonçalves, and Vítor M. C. F. Cunha

Abstract The 3D concrete printing has been developed as one of the digitized technologies for the construction industry aiming to cope with some drawbacks of conventional construction methods. One of the main particularities of 3D printed cement based materials is its anisotropic/orthotropic behaviour, which is related to the layer wised approach of these addictive manufacturing processes. In this work, a cement based composition reinforced with polyvinyl alcohol fibre was used to evaluate the post-cracking behaviour of printed specimens in two different loading directions related to the layers' orientation. Three-point bending tests were used to indirectly obtain the tensile behaviour (i.e. stress–crack width relationship) through an inverse analysis procedure. The results of inverse analysis showed that tri-linear relationship was able to accurately model the post-cracking behaviour of PVA-FRC specimens. No significant differences were observed on the tensile behaviour of 3D printed and mould cast specimens.

Keywords Inverse analysis · FEM · 3D concrete printing · PVA fibres · Stress–crack width law

1 Introduction

The 3D concrete printing (3DCP) is an additive manufacturing (AM) based technique specially developed/adapted to be used in construction industry [1–3]. Wet-extrusion [4–8] and powder-based [9, 10] are two of the 3DCP main techniques. Nonetheless,

B. Zahabizadeh (✉) · J. Pereira · C. Gonçalves · V. M. C. F. Cunha
Department of Civil Engineering, ISISE, Institute of Science and Innovation for Bio-Sustainability (IB-S), University of Minho, 4800-058 Guimarães, Portugal
e-mail: b.zahabizadeh@civil.uminho.pt

J. Pereira
Innovation Point, Rua de Pitancinhos – Palmeira, 4700-727 Braga, Portugal

C. Gonçalves
DST Group, Rua de Pitancinhos – Palmeira, 4700-727 Braga, Portugal

E. B. Pereira et al. (eds.), *Proceedings of the 3rd RILEM Spring Convention and Conference (RSCC 2020)*, RILEM Bookseries 32,
https://doi.org/10.1007/978-3-030-76547-7_26

wet-extrusion 3DCP processes are the most commonly used in AM techniques for cement based materials [11], which consists of extruding a fresh mixture with specific rheological properties. One of the main challenges while using wet-extrusion 3DCP technology is achieving a balance between the rheological and mechanical properties of the material [11–13], together with the printer's technology, in order that the material may be simultaneously printable and buildable [11].

Regarding the mechanical properties of the cement based 3D printed elements, assessing its potential anisotropic/orthotropic behaviour is of paramount importance. This type of behaviour in 3D printed elements arises intrinsically due to the printing process, i.e. layer wised approach [11, 14]. The bond behaviour between filaments/layers is one of the factors that can have a significant impact on the mechanical properties of printed elements [14, 15]. Moreover, fresh properties of mixture composition [11], printing parameters such as printing speed, time gap between printed layers [14], and the geometrical shape/dimension of layers [12] have also a significant influence on the mechanical properties of 3D printed elements. Distinct test methods such as compressive, flexural and tensile tests were used in the literature, e.g. [7, 14, 16, 17], in order to evaluate the mechanical properties of 3D printed specimens based on different loading directions regarding to the layers' orientation.

The three-point bending test (3PBT) is commonly used to evaluate the flexural behaviour of cement based materials. Moreover, 3PBT may also be used as an indirect tensile test methodology in order to determine the stress–crack width relationship (σ–w). In this case, the σ–w relationship can be determined through performing an inverse analysis (IA) of the experimental 3PBT results by using an optimization procedure [18, 19]. The determination of the σ–w relationship makes it possible to assess the fracture energy of a certain cement based material [18]. This method can be used for both plain and fibre reinforced cement based materials. Even though the shape of σ–w curves in unreinforced matrices is somehow independent of the strength class [18, 20], in FRC this shape can be completely different based on the type, content, distribution and orientation profile of fibres within the matrix [18]. Therefore, the post-cracking tensile behaviour of an unreinforced matrix can be accurately estimated through a bilinear σ–w relationship [18]. On the other hand, a tri-linear or multi-linear relationship is more appropriate for FRCs [20–22].

In this study, 3PBTs were performed to indirectly assess the σ–w relationship of cement based printed specimens reinforced with polyvinyl alcohol fibres (PVA-FRC). The printed specimens were tested along two different loading directions, i.e. loaded perpendicular and parallel to the layers' printing orientation. Additionally, mould cast specimens were also tested as reference. An IA procedure under the finite element method framework was carried out in order to determine the parameters that define the uniaxial tensile σ–w law of the 3D printed material.

2 Materials and Methods

2.1 3D Concrete Printing Technology

In this study, the printing process was executed using a small 3D concrete printer with a maximum printable volume near to $0.4 \times 0.4 \times 0.4\ m^3$. This printer comprises a main aluminium frame, which supports the printing head, a stainless steel funnel and an auger inside it. Moreover, stepper motors are used in order to control the movements of the printing system along X, Y, and Z directions, as well the rotation of the auger inside the funnel. Figure 1 shows a general view of the developed 3D concrete printer.

In each printing process, three steps were followed in order to print the final specimens. First, the fresh mortar mixture was placed into the funnel. Second, the G-code file was sent to the equipment. Finally, the extrusion process was started to create the required specimens in a layer-wised approach. The geometrical dimensions of the specimens/layers and the printing parameters such as speed of printing and flow rate of material were defined in the G-code file.

The rotation of the auger inside the funnel and self-weight of the fresh material both cause the movement of material inside the funnel when the printing process is

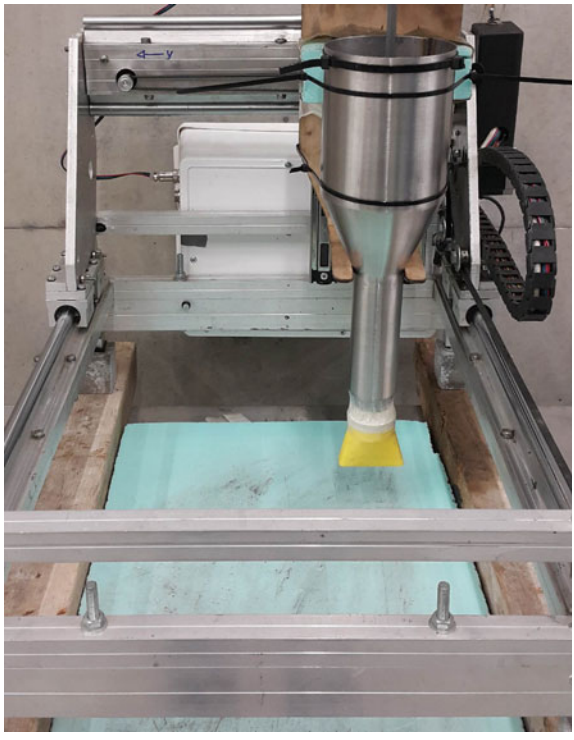

Fig. 1 General view of 3D concrete printer

Table 1 FRC Mortar mixture compositions

Material	Sand	Cement	Fly ash	Silica fume	water	Superplasticizer	Retarder	Fibre
(kg/m^3)	1054	271	468	74	252	8	3	19.5

Table 2 Physical properties of PVA fibre

Length (mm)	Diameter (μm)	Aspect ratio (–)	Tensile strength (MPa)	Elasticity modulus (GPa)	Density (g/cm^3)
8	40	200	1600	41	1.30

in progress. Finally, during the printing process, the fresh material passes through a customized nozzle to create the final specimen based on the desired geometry, layer upon the layer.

2.2 Mortar Composition

The mortar mixture, used in this study, was selected after performing rheological tests on several distinct PVA-FRC mixtures. The workability of the mixtures was evaluated through the flow table test. Moreover, the printability and buildability of each mixture were previously assessed using the 3D concrete printer. The selected PVA-FRC mixture showed a workability of 121 and 198 mm before and after strike of the flow table, respectively. These values of workability were in agreement with the requirements established to print unreinforced matrices with this 3D printer [23, 24]. The PVA-FRC mixture also complied the requirements regarding the printability and buildability of material based on the used 3D printing technology. These requirements and the flow table test methodology for checking the desired rheological behaviour are described elsewhere [23]. Tables 1 and 2 include the FRC mixture and the physical properties of PVA fibres, respectively.

2.3 Specimen's Geometry and Preparation

Mould cast and printed specimens with the dimensions of 40 × 40 × 160 mm were prepared for 3PBT. The printed specimens were cut from larger printed prismatic elements (Fig. 2). The larger prismatic elements all printed using a customized rectangular nozzle with a width of 50 mm and a thickness of 12 mm. In order to eliminate printing of several filaments in each layer, a 50 mm width for nozzle was adopted. In this case, the effect of interfaces between the filaments of a same layer was removed and just the influence of one interface between printed layers is considered.

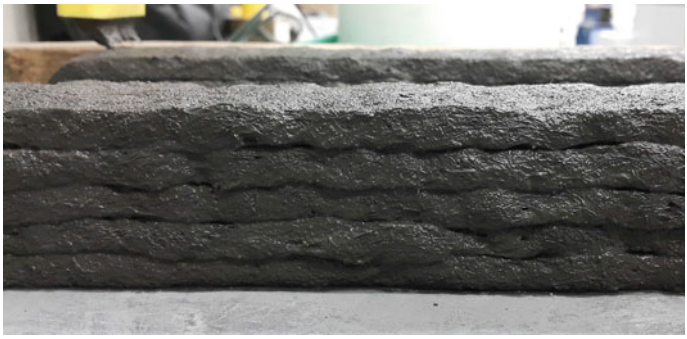

Fig. 2 Printed prismatic elements

A 10 mm depth notch with the width of 2 mm was created on all the mould cast and printed specimens at their middle length on the opposite surface to loading surface. This notch was created to localize the cracking process during the 3PBT. Regarding the printed specimens, two loading directions relative to the layers' printing orientation were considered, namely loading perpendicular (series LZ) and loading parallel (series LY) to the layers' orientation, respectively (see Fig. 3a, b). For each series, i.e. mould cast (MC) and printed (LZ and LY), four specimens were prepared and tested. A plastic sheet was wrapped around specimens and all of them kept at the room temperature up to the required age of testing.

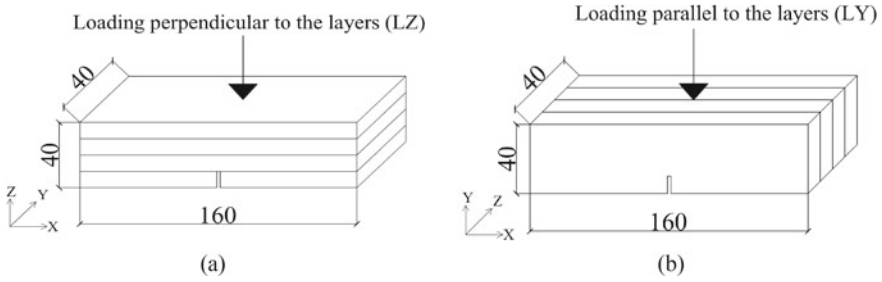

Fig. 3 Schematic view of the cut and preparation of printed specimens from reference 3D printed prismatic elements for three-point bending test, **a** loading perpendicular and **b** loading parallel to the layers' orientation. Units: mm

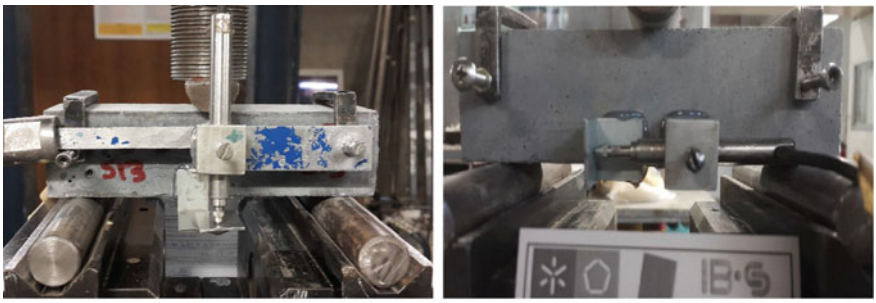

(a) (b)

Fig. 4 Three-point bending test setup for measuring **a** flexural strength and **b** CMOD

3 Determination of the Stress–Crack Width Relationship by Inverse Analysis

3.1 Three-Point Bending Tests

The 3PBT was used to assess the tensile behaviour of specimens under flexure. In general, regardless of the specimens' size, the recommendations of [25] were followed to perform the test. For measuring the deflection and crack mouth opening displacement (CMOD), two LVDTs with a displacement range of ±2.5 mm were used in the vertical and horizontal positions, respectively (Fig. 4a, b). The 3PBT was done under closed-loop control at displacement rate of 0.002 mm/s.

3.2 Finite Element Model

The finite element analysis were performed assuming a plane stress state due to the specimen's geometry, support and loading conditions [18]. Due to symmetry conditions, just one-half of the prismatic specimens was modelled to reduce the number of elements and hence the computational time. Two types of elements were used in the modelling process. At the symmetry axis of specimen, 2D line interface elements were placed along the specimen's height to model nonlinear behaviour of the crack initiation and propagation process. On the other hand, eight-node Serendipity elements with linear elastic behaviour were used to model the specimen's geometry. Figure 5 shows the mesh configuration and the boundary conditions used in the simulations. One support restraining the vertical displacement was placed near the bottom left corner of the mesh, while the others restraining the horizontal displacement were placed at the nodes along the symmetry axis. A Gauss–Lobatto integration scheme with three integration points (IP) was used for the 2D line interface elements. On the

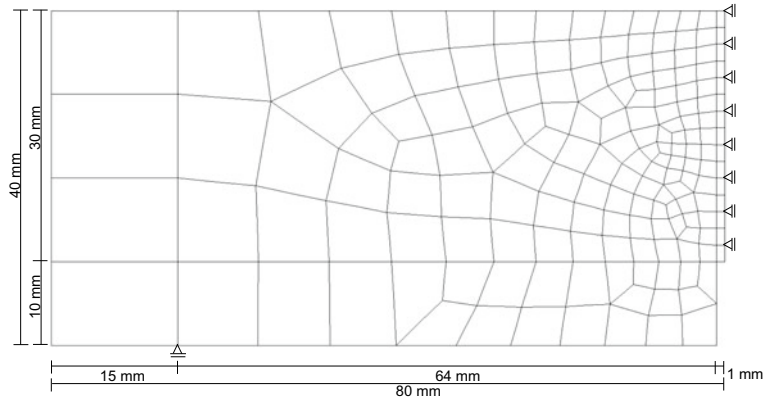

Fig. 5 Finite element mesh used in the inverse analysis of the three-point bending tests

Table 3 Material properties for simulation of three-point bending test

Property	Series	
	LZ and LY	MC
Density	$\rho = 2.4 \times 10^{-6}$ N/mm^3	
Poisson's ratio	$\nu_c = 0.20$	
Elasticity modulus	45,000 N/mm^2	48,000 N/mm^2
Tensile strength	Inverse analysis	
Tri-linear softening parameters	Inverse analysis	

other hand, a Gauss–Legendre integration scheme with 2 × 2 IP was used for the eight-node elements. Table 3 includes the material properties used in the analyses.

A comprehensive search method was used to carry out the inverse analysis (IA), further details can be found in [20]. The IA was performed for the three series, i.e. printed ones (series LZ and LY) and mould cast (series MC). For each series, the average and envelope (minimum and maximum) experimental curves were simulated and the parameters of the σ–*w* relationship that lead to the optimal fit between numerical and experimental curves were obtained.

3.3 Determination of the α–W Relationship by Inverse Analysis

Figure 6a, b, and c depict both the average experimental and numerical load–deflection curves for the series LZ, LY, and MC, respectively. A very good fitting between the average experimental and numerical curves can be observed for all of the three

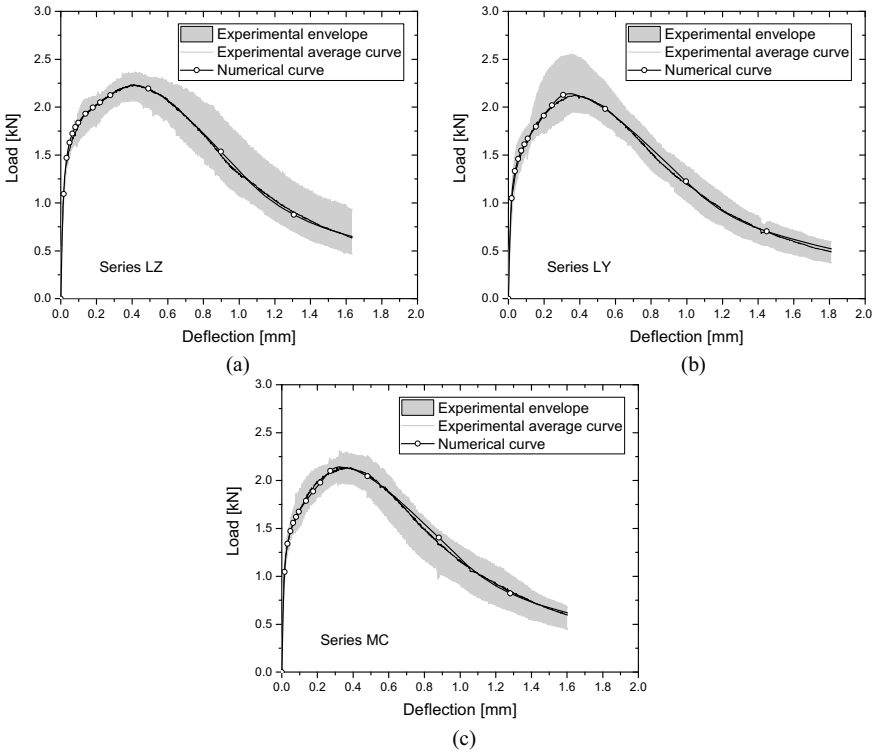

Fig. 6 Numerical simulation of the three-point bending test for series **a** LZ, **b** LY, and **c** MC

series. The grade of adjustment corroborates also the suitability of the tri-linear σ–*w* relationship in modelling the tensile post-cracking behaviour of 3D printed fibre reinforced composites.

Regarding the pre-peak branch of the curves, the comparison between the simulations of all the series revealed a very good adjustment. Nonetheless, a slightly better agreement of numerical curve was found for the series LZ (Fig. 6a) than series LY and MC in the pre-peak stage (Fig. 6b, c).

Table 4 includes the parameters of the σ–*w* relationship obtained from the IA for the maximum, average, and minimum experimental curves of each series, and the correspondent fitting errors (e) obtained in each simulation process. The results of the σ–*w* relationships, for the average experimental curves, showed 20% higher f_{ct} for series LZ than series LY and MC. Regarding the results obtained for the upper boundary of the experimental envelope curve, herein defined as Max experimental curve, the f_{ct} of LZ is 3% higher than series LY and MC. On the other hand, for the lower boundary of the experimental envelope curve, herein designated by Min experimental curve, the f_{ct} was 15% and 18% lower for series LY and MC than LZ series, respectively. In the case of the post-cracking parameters, there were not

Table 4 Parameters of σ–*w* relationship obtained through IA for series LZ, LY and MC

Series		f_{ct} (MPa)	σ_1 (MPa)	σ_2 (MPa)	w_1 (mm)	w_2 (mm)	w_u (mm)	G_f (N/mm^2)	e (%)
LZ	Max	3.7	4.59	0.52	0.14	0.55	4.0	2.52	1.2
	Avg	3.6	4.39	0.36	0.14	0.46		1.96	0.8
	Min	3.4	4.18	0.31	0.14	0.42		1.71	1.3
LY	Max	3.6	5.00	0.36	0.09	0.45	4.0	1.99	2.4
	Avg	3.0	4.38	0.36	0.10	0.46		1.86	1.1
	Min	2.9	4.09	0.26	0.13	0.40		1.51	1.3
MC	Max	3.6	4.43	0.50	0.12	0.47	4.0	2.23	1.0
	Avg	3.0	4.23	0.39	0.10	0.45		1.86	0.9
	Min	2.8	3.84	0.25	0.11	0.39		1.39	1.2

Note The σ-*w* relationship is defined based on the following points: (f_{ct}, 0), (σ_1, w_1), (σ_2, w_2) and (0, w_u)

very significant difference on the parameters that define the first and second post-peak points. Regarding the fracture energy (G_f) of the average experimental curves, obtained from IA, the result for series LZ was 5% higher than series LY and MC. The parameters of the σ–*w* law obtained from IA of the average experimental curves for all the series up to the crack opening width of 4 mm and 0.6 mm are depicted in Fig. 7a and b, respectively. In general, the shape of the σ–*w* law obtained from average experimental curves through IA were similar for all the series.

As it can be observed in Fig. 6, the experimental curves stop at a deformation level in which the residual load is still considerable. In order to accurately determine the G_f, the value of the ultimate crack width (w_u) will be important, however the deformational level, and consequently the residual load should be sufficiently low

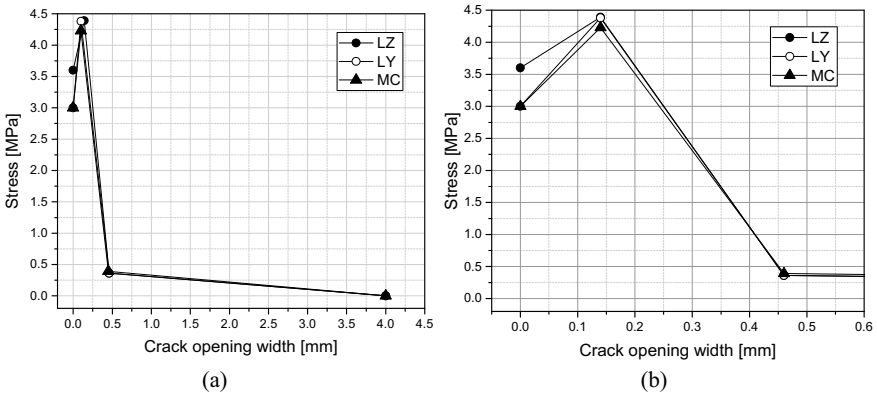

Fig. 7 The σ–*w* relationships obtained through IA from average experimental curves for series LZ, LY and MC up to crack opening width of **a** 4 mm and **b** 0.6 mm

in order to accurately determine w_u through IA [20]. Therefore, in this work, the ultimate crack width for all the series was estimated based on the theoretical average embedded length of the fibres (4 mm) [20].

Figure 8 shows the envelope of σ–*w* law's parameters obtained by IA of the Max and Min experimental curves, as well as the σ–*w* obtained from the average curve. Since the main differences were observed in the initial stage of the response, Fig. 8 represents the σ–*w* relationships up to a 0.6 mm crack opening width. Generally, the shape of the laws is also similar for the envelopes. Moreover, even though that all the series showed deflection-hardening, a sharper increase was observed in the first post-cracking branch of series LY and MC. On the other hand, for series LZ there is higher scatter on the softening of the second post-cracking branch. For the series LY and MC, the higher scatter can be observed during the deflection–hardening branch up to a nearby crack width of 0.1 mm.

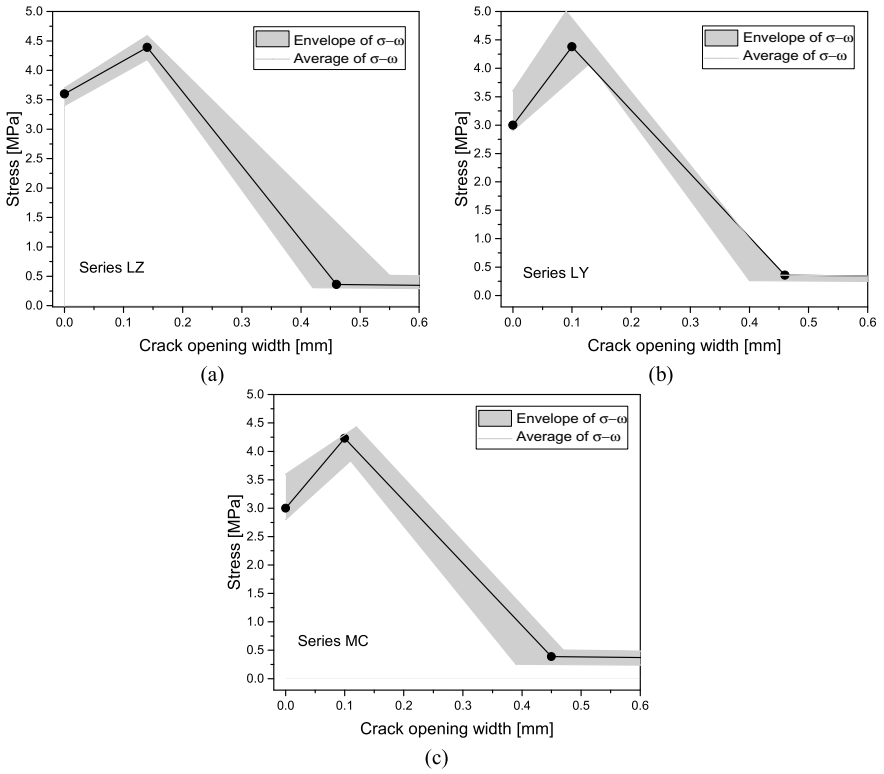

Fig. 8 The σ–*w* relationships obtained through IA for maximum, average, and minimum experimental curves of series **a** LZ, **b** LY and **c** MC up to crack opening width of 0.6 mm

4 Conclusions

In this work the tensile post-cracking behaviour of 3D printed and mould cast specimens was investigated through performing an inverse analysis (IA) of experimental curves obtained from three-point bending tests. Regarding the printed specimens, two loading directions were considered, i.e. perpendicular and parallel relative to the layers' printing orientation. All the specimens were made of fibre reinforced mortars (PVA-FRC) with specific rheological properties compatible with the developed 3D concrete printing technology. The results of the IA analyses corroborated the ability of tri-linear σ–*w* relationship to model accurately the flexural response of the PVA-FRC specimens even in the case of 3D printed elements, regardless of the loading directions. No significant differences were observed on the stress–crack width relationships obtained for printed and mould cast specimens, which may indicate that the extrusion process did not influence the fibre orientation profile when compared to the cast ones. The σ–*w* law's parameters obtained by IA showed that f_{ct} was slightly higher for series LZ than series LY and MC. Series LY showed a higher scatter on the first post-cracking branch of the σ–*w* law, while for LZ the scatter was higher for the second post-cracking branch.

Acknowledgements The authors acknowledge the support of dst group for funding the project Chair dst/IB-S: Smart Systems for Construction. The first author would like to thank FCT (Fundação para a Ciência e a Tecnologia) for the scholarship with the reference number SFRH/BD/143636/2019. Moreover, the authors appreciate the support of following companies that gratuitously provided the material for the experimental campaign: SECIL; Sika; Elkem Microsilica and Unibetão.

References

1. Lim, S., Buswell, R.A., Le, T.T., Austin, S.A., Gibb, A.G.F., Thorpe, T.: Developments in construction-scale additive manufacturing processes. Autom. Constr. **21**, 262–268 (2012). https://doi.org/10.1016/j.autcon.2011.06.010
2. Perrot, A., Rangeard, D., Pierre, A.: Structural built-up of cement-based materials used for 3D-printing extrusion techniques. Mater. Struct. **49**, 1213–1220 (2016). https://doi.org/10.1617/s11527-015-0571-0
3. Weng, Y., Lu, B., Tan, M.J., Qian, S.: Rheology and printability of engineered cementitious composites-a literature review. In: Proceedings of the 2nd International Conference on Progress in Additive Manufacturing (Pro-AM 2016) (2016)
4. Khoshnevis, B.: Automated construction by contour crafting—related robotics and information technologies. Autom. Constr. **13**, 5–19 (2004). https://doi.org/10.1016/j.autcon.2003.08.012
5. Lim, S., Buswell, R., Le, T., Wackrow, R., Austin, S.A., Gibb, A., Thorpe, T.: Development of a viable concrete printing process. In: 28th International Symposium on Automation and Robotics in Construction (ISARC2011). pp. 665–670. Seoul, South Korea (2011)
6. Bos, F., Wolfs, R., Ahmed, Z., Salet, T.: Additive manufacturing of concrete in construction: potentials and challenges of 3D concrete printing. Virtual Phys. Prototyp. **11**, 209–225 (2016). https://doi.org/10.1080/17452759.2016.1209867

7. Nerella, V.N., Krause, M., Näther, M., Mechtecherine, V.: Studying printability of fresh concrete for formwork free Concrete on-site 3D Printing technology (CONPrint3D). Presented at the 25th Conference on Rheology of Building Materials, Regensburg, Germany (2016)
8. Zhang, X., Li, M., Lim, J.H., Weng, Y., Tay, Y.W.D., Pham, H., Pham, Q.-C.: Large-scale 3D printing by a team of mobile robots. Autom. Constr. **95**, 98–106 (2018). https://doi.org/10.1016/j.autcon.2018.08.004
9. Cesaretti, G., Dini, E., De Kestelier, X., Colla, V., Pambaguian, L.: Building components for an outpost on the Lunar soil by means of a novel 3D printing technology. Acta Astronaut. **93**, 430–450 (2014). https://doi.org/10.1016/j.actaastro.2013.07.034
10. Delgado Camacho, D., Clayton, P., O'Brien, W.J., Seepersad, C., Juenger, M., Ferron, R., Salamone, S.: Applications of additive manufacturing in the construction industry—a forward-looking review. Autom. Constr. **89**, 110–119 (2018). https://doi.org/10.1016/j.autcon.2017.12.031
11. Ngo, T.D., Kashani, A., Imbalzano, G., Nguyen, K.T.Q., Hui, D.: Additive manufacturing (3D printing): a review of materials, methods, applications and challenges. Compos. Part B Eng. **143**, 172–196 (2018). https://doi.org/10.1016/j.compositesb.2018.02.012
12. Paul, S.C., Tay, Y.W.D., Panda, B., Tan, M.J.: Fresh and hardened properties of 3D printable cementitious materials for building and construction. Arch. Civ. Mech. Eng. **18**, 311–319 (2018). https://doi.org/10.1016/j.acme.2017.02.008
13. Buswell, R.A., Leal de Silva, W.R., Jones, S.Z., Dirrenberger, J.: 3D printing using concrete extrusion: a roadmap for research. Cem. Concr. Res. **112**, 37–49 (2018). https://doi.org/10.1016/j.cemconres.2018.05.006
14. Sanjayan, J.G., Nematollahi, B., Xia, M., Marchment, T.: Effect of surface moisture on inter-layer strength of 3D printed concrete. Constr. Build. Mater. **172**, 468–475 (2018). https://doi.org/10.1016/j.conbuildmat.2018.03.232
15. Panda, B., Chandra Paul, S., Jen Tan, M.: Anisotropic mechanical performance of 3D printed fiber reinforced sustainable construction material. Mater. Lett. **209**, 146–149 (2017). https://doi.org/10.1016/j.matlet.2017.07.123
16. Ogura, H., Nerella, V.N., Mechtcherine, V.: Developing and testing of strain-hardening cement-based composites (SHCC) in the context of 3D-Printing. Mater. Basel Switz. 11 (2018). https://doi.org/10.3390/ma11081375
17. Bao, Y., Xu, M., Soltan, D., Xia, T., Shih, A., Clack, H.L., Li, V.C.: Three-dimensional printing multifunctional Engineered Cementitious Composites (ECC) for structural elements. In: Wangler, T., Flatt, R.J. (eds.) First RILEM International Conference on Concrete and Digital Fabrication—Digital Concrete 2018, pp. 115–128. Springer International Publishing, Cham (2019)
18. Cunha, V.M.C.F., Barros, J.A.O., Sena-Cruz, J.M.: Numerical simulation of three-point bending tests: two distinct approaches. In: Barros, J., et al. (eds.) BEFIB2012—Fibre Reinforced Concrete. UM, Guimarães (2012)
19. Roelfstra, P.E., Wittmann, F.H.: Numerical method to link strain softening with failure of concrete. In: Fracture Toughness and Fracture Energy, pp. 163–175. Elsevier, Amsterdam (1986)
20. Cunha, V.M.C.F.: Steel fibre reinforced self-compacting concrete (from micromechanics to composite behavior), Doctoral thesis, University of Minho, Guimarães, Portugal (2010)
21. Barros, J.A.O., Cunha, V.M.C.F., Ribeiro, A.F., Antunes, J.A.B.: Post-cracking behaviour of steel fibre reinforced concrete. Mater. Struct. **38**, 47–56 (2004). https://doi.org/10.1617/14058
22. Cominoli, L., Meda, A., Plizzari, G.A.: Fracture properties of high-strength hybrid fiber-reinforced concrete. In: Grosse, C.U. (ed.) Advances in Construction Materials 2007, pp. 139–146. Springer Berlin Heidelberg, Berlin, Heidelberg (2007)
23. Zahabizadeh, B., Pereira, J., Gonçalves, C., Cunha, V.M.C.F.: Development of cement-based mortars for 3D printing through wet extrusion. In: IABSE Symposium 2019 Guimarães: Towards a Resilient Built Environment—Risk and Asset Management. Guimarães, Portugal (2019)

24. Zahabizadeh, B., Pereira, J., Gonçalves, C., Cunha, V.M.C.F.: The effect of loading direction on the compressive behaviour of a 3D printed cement-based material. In: IABSE Symposium 2019 Guimarães: Towards a Resilient Built Environment—Risk and Asset Management. Guimarães, Portugal (2019)
25. BS EN 14651:2005+A1:2007: Test method for metallic fibre concrete. Measuring the flexural tensile strength (limit of proportionality (LOP), residual) (2005)

Mechanical Properties of Fibre Reinforced Concrete Incorporating Recycled Tyre Steel Fibres and Industrial by-Products as Aggregates

Ana Neves, Eduardo B. Pereira, Vítor Cunha, Tiago Miranda, Mafalda Rodrigues, and José Costa

Abstract The main objective of this work is to investigate the properties of a Fibre Reinforced Concrete (FRC) at fresh and hardened states, obtained by a partial substitution of coarse and fine natural aggregates with Electric Arc Furnace Slag (EAFS) and Fly Ash (FA). Recycled Tyre Steel Fibres (RTSF) were incorporated in the developed concrete in order to maximize and reuse wastes that were not biodegradable. The design of the FRC mixture with EAFS was based on a reference concrete by using the modified Andreasen and Andersen particle-packing model. The composition was optimized to achieve maximum packing density. Workability, compressive and tensile splitting strength, modulus of elasticity and post-cracking behaviour were evaluated for the different concrete mixtures developed and compared to the ones of the reference mixture. The selected concrete composition, with an EAFS and FA maximum content of 70% and 10%, respectively, has shown good workability and suitable elasticity modulus according to the specified requirements. The latter mixture revealed a lower compressive and tensile splitting strength, comparatively with the reference mixture (w/o fibres), which was compensated by the improved ductility and energy absorption capacity under compressive loading.

Keywords Recycled materials · Industrial by-products · Electric arc furnace slag · Fly ash · Recycled tyre steel fibres · Particle-packing model

1 Introduction

Construction is one of the largest and most active sectors of the European industry. However, it is also responsible for a significant parcel of the industrial negative environmental impact. This is due to the constant exploitation of raw materials and

A. Neves (✉) · E. B. Pereira · V. Cunha · T. Miranda
Department of Civil Engineering, ISISE, Institute of Science and Innovation for Bio-Sustainability (IB-S), University of Minho, 4800-058 Guimarães, Portugal
e-mail: id6951@alunos.uminho.pt

M. Rodrigues · J. Costa
Domingos da Silva Teixeira & Filhos Lda. (DST), 4711-911 Braga, Portugal

E. B. Pereira et al. (eds.), *Proceedings of the 3rd RILEM Spring Convention and Conference (RSCC 2020)*, RILEM Bookseries 32,
https://doi.org/10.1007/978-3-030-76547-7_27

the high energy consumption involved [1–3]. Climate change and greenhouse gas emissions, as well as the depletion of resources, raise concerns about the sustainability of societies and call for new development paradigms.

The use of natural aggregates for the concrete production results in an excessive consumption of natural resources and is increasingly one of the reasons for environmental concern worldwide. Thus, alternative methods of production are being revised, in order to establish as one of the fundamental objectives not only the functional and economic aspects, but also the reduction of the environmental impact in the production of structural concrete [1, 3]. In order to pursue the sustainability of structural concrete, it is inevitable to change its traditional composition. As such, in recent years, the production of concrete based on wastes or recycled materials either as aggregates, binder or as fibers has been studied. Industrial wastes or by-products, such as fly ash, vegetable ash, municipal solid waste ash, pulverized fuel ash, blast furnace or electric furnace slag, silica fume, glass, glycerol, cooking oil, plastics, textiles, ceramics, quarrying, construction and demolition residues, recycled tyre fibres, tyre rubber, among others, are currently considered in the development of alternative compositions for structural concrete incorporating significant percentages of recycled materials [4–9]. Many of these studies have found quite satisfactory results; nevertheless, these compositions are still not being used by the construction industry because of the uncertainty and insecurity about their functionality, as well as the stability and durability of their properties in the long-term.

This work intends to design concrete mixtures that will primarily employ electric arc furnace slag (EAFS), fly ash (FA) and recycled tyre steel fibres (RTSF) rewarding recycling environmental benefits. Electric arc furnace slag (EAFS) is a dense by-product material obtained from the electric arc furnace steelmaking process, where different types of recycled steel scrap are melted. The latter may also be used as binder or as aggregates [4, 7]. Even so, detailed studies are still needed to properly characterize this material as a replacement of certain components in concrete. Fly ash is a fine mineral powder and is generated from the coal used in thermoelectric power plants and is, therefore, characterized as an industrial by-product that can be used in the concrete to correct fine particles granulometry and/or partially replace the Portland cement [10, 11]. Recycled tyre steel fibres (RTSF) are obtained from tyre recycling that are no longer suitable for use on vehicles due to wear or irreversible damage. The tyre wastes can be applied in different markets include tire-derived fuel (TDF), ground rubber applications/rubberized asphalt and civil engineering applications [12]. In this case the tyre waste will be applied as a reinforcement in concrete mixtures to perform a fibre reinforced concrete (FRC) in order to achieve better mechanical characteristics. Generally, the use of RTSF as a concrete reinforcement leads to good mechanical performances such as the increase in concrete's residual strength, ductility and toughness, having high energy-absorption capacity, which makes it ideal for high-impact and explosive loading, or for extended durability. Studies demonstrated that the behaviour of concrete reinforced with these fibres can be comparable to that of concrete reinforced with industrial steel fibres [13–15].

2 Experimental Program

2.1 Materials and Mix Composition

For this study, a conventional structural concrete, designated as MR_N, was selected as a reference mixture to develop novel mixtures comprising industrial by-products and recycled fibres. The reference structural concrete MR_N was considered to have a strength class of C25/C30 and a slump class of S4 (≈200 mm). This reference concrete, MR_N, consisted of Portland cement CEM II/A-L 42.5 R, fly ash (FA), fine sand (0–2 mm) and medium sand (0–4 mm), natural aggregate with different grain size fractions (6–14 and 14–20 mm), superplasticizer (SP) and plasticizer (PL). The water/cement (*w/c*) ratio and the water/powder (*w/p*) ratio were equal to 0.75 and 0.35 (in weight), respectively.

Table 1 lists the main physical properties of natural materials and Table 2 lists the quantities of the mixture constituents of MR_N. Figure 1a shows the curves of the particle size distribution of the natural aggregates.

The used electric arc furnace slag came from the steel industry in Porto (Portugal) and was divided in two different grain sizes of 0–4 and 0–20 mm. The concrete compositions developed with EAFS as an aggregate considered also the use of natural sand with a grain size of 0–2 mm. Recycled tyre steel fibres (RTSF) came from pneumatic industry in Sines (Portugal) and were incorporated in the EAFS concrete without any preliminary treatment or preparation. Usually, this kind of residues are subjected to treatments in order to confer them better mechanical properties. Figure 2a shows the aspect of RTSF that were characterized by different diameters, lengths and shapes of steel fibres, synthetic fibres and tyre rubber, because they were not previously treated.

Table 1 Specific density of the materials used in the concrete compositions

Component	Apparent particle density, ρ_a (Mg/m^3)	Particle density on an oven-dried basis, ρ_{rd} (Mg/m^3)	Particle density on a saturated-dried basis, ρ_{ssd} (Mg/m^3)	Water absorption, WA_{24} (%)
FA		2.35		
Sand 0–2		2.62		
Sand 0–4		2.61		
Natural aggregate 6–14		2.65		
Natural aggregate 14–20		2.65		
EAFS 0–4	3.58	3.49	3.51	0.7
EAFS 0–20	3.42	3.25	3.29	1.55

Table 2 Materials quantities of the reference mixture MR_N and the designed EAFS and FRC_EAFS mixtures [kg/m^3 or L/m^3]

	MR_N	EAFS 8D1	0.5FRC_EAFS 8D1
CEM II/AL 42.5R	205	209.22	205.84
FA	115	243.97	249.53
Sand 0–2	350	279.52	288.51
Sand 0–4	530		
Natural aggregate 6–14	388		
Natural aggregate 14–20	580		
EAFS 0–4		979.87	995.39
EAFS 0–20		764.08	776.44
SP	1.6	1.63	1.61
PL	1.6	1.63	1.61
Water	154.1	165.53	181.33
RTSF			39.25
w/p	0.35	0.35	0.38
w/c	0.75	0.79	0.88
% EAFS		70.4	70.4
% FA	9.5	9.9	9.9

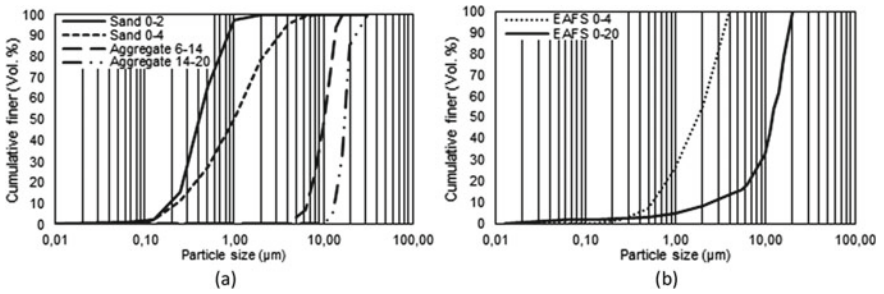

Fig. 1 Particle size distribution of the used materials: **a** natural materials; **b** EAFS materials

The main physical properties of the industrial by-products, electric arc furnace slag (EAFS) and fly ash (FA), are listed in Table 1. Figure 1b shows the curves of EAFS aggregates particle size distribution with a grain size between 0–4 mm (EAFS 0–4) and 0–20 mm (EAFS 0-20).

The fibre reinforced concrete with electric arc furnace slag (FRC_EAFS) composition was defined using the modified Andreasen and Andersen particle-packing method [16, 17]. The latter considers a minimum particle size to maximize the packing of the granular solid materials and a distribution module, q, that is used to determine the proportion between the fine and coarse particles in the mix, which

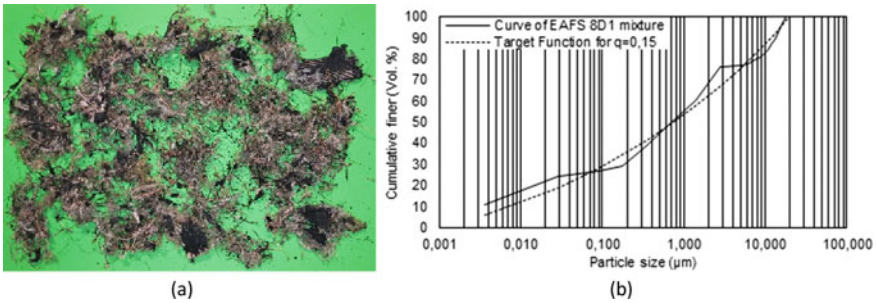

Fig. 2 **a** Representative samples of recycled tyre steel fibres; **b** particle size distribution of the target curve and the resulting grading curve of the EAFS mixture for $q = 0.15$

according to Husken [18] may vary between the values of 0.1 (fluid concretes) and 0.9 (dense concretes). Studies suggest that a q value of 0.23 should be adopted for UHPC (Ultra-High Performance Concrete), UHPFRC (Ultra-High Performance Fibre Reinforced Concrete) and UHPHFRC (Ultra-High Performance Hybrid Fibre Reinforced Concrete) [5, 19–21]. Hence, in this study, considering the high density of EAFS aggregates, the value of q was decreased to 0.15. With the aim of optimizing concrete compositions, this research used an optimized algorithm developed by Husken [18] based on the modified equation of Andreasen and Andersen.

Initially, an EAFS mixture without fibres was developed based on reference mixture MR_N by applying the optimized particle-packing model, designated as EAFS 8D1. In a second stage, 0.5% (in vol.) of RTSF were added to this mixture, which was designated as 0.5FRC_EAFS 8D1. Table 2 includes the composition of both mixtures, whereas the resulting grading curve of the EAFS mixture are shown in Fig. 2b.

2.2 Casting, Curing and Testing Procedures

Specimen preparation. The workability of the mixtures was assessed with the Abrams cone, indirectly evaluating the shear stress and the viscosity of the mixtures in the fresh state. These tests were carried out according to the European Standard EN 12350-2 [22]. Subsequently to the fresh properties determination, the respective specimens were cast and then vibrated in the shaking table, in order to reduce the air entrapped in the mixture. The entire vibration and casting process was performed according to EN 12390 [23]. After 24 h of curing, the specimens were demolded and placed in a climatic room that guarantees constant curing conditions with a temperature of 20 ± 2 °C and 60% of relative humidity until testing.

The characterization of the compressive behaviour of the developed mixtures was carried out at 7, 28 and 90 days. The elasticity modulus and compressive strength were assessed according to the standard EN 12390 [23]. For each mixture twelve

cylindrical specimens (four specimens per testing age) with a diameter of 150 mm and a height of 300 mm were cast [23], to evaluate the mechanical properties of the concrete. On the other hand, the tensile splitting tests were carried out at 28 days and only three cylindrical specimens with a diameter of 150 mm and a height of 300 mm for MR_N and 0.5FRC_EAFS 8D1 mixtures were cast. Each cylinder was divided into 6 parts of 50 mm thickness and just the two cores cut from the middle were tested. This test was performed aconding to the EN 12390 [23].

Testing set-ups. In terms of the compressive behaviour, the adopted procedure consisted on determining initially the compressive strength in one specimen, at each age, in order to obtain an estimation of the compressive strength to define the loading procedure for the determination of the elasticity modulus. After determining the modulus of elasticity for each of the three remaining specimens, the uniaxial compression test was performed until failure to obtain the stress–strain relationship. The uniaxial compression tests were carried out under closed-loop displacement control, with a displacement rate of 0.005 mm/s. An actuator with a 1600 kN load cell was used. The tests were performed using four LVDTs (Linear Variable Differential Transducers), three internal LVDTs, located between plates in the sample, and one external LVDT (Fig. 3a). The compressive stress–strain curves were determined from the mean value of the displacements of the three internal LVDTs. The external LVDT was just used for validation purposes.

Tensile splitting tests were carried out using a displacement rate of 0.002 mm/s. An actuator with a 100 kN load cell was used. In these tests, an external LVDT was positioned on the actuator to control the vertical deformation of the specimen. Additionally, four LVDTs were installed at opposite surfaces of each core to measure the crack width along the fracture surface (Fig. 3b). One LVDT was mounted on the front face and the other three on the rear face of the specimen, which corresponded to the top and bottom faces of the cast cylinders, respectively.

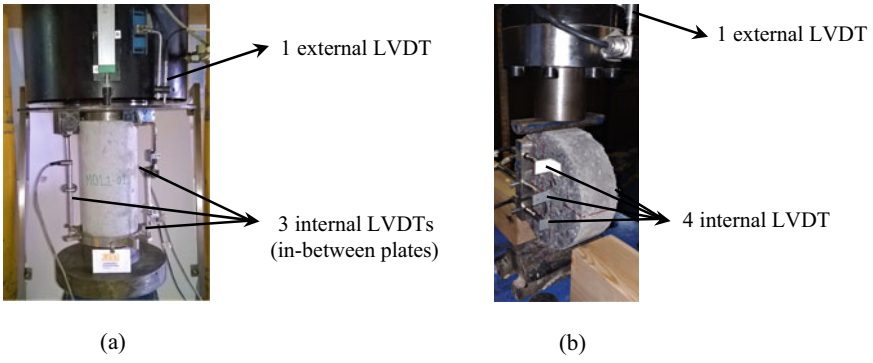

Fig. 3 Experimental set-up: **a** uniaxial compression test; **b** tensile splitting test

Table 3 Results of the rheological properties obtained for the reference mixtures MR_N and for the concrete designer mixtures developed with EAFS and RTSF

Mixtures	Curing age (days)	Slump (mm)	Slump class
MR_N	7, 28 and 90	160	S4
EAFS 8D1	7, 28 and 90	160	S4
0.5FRC_EAFS 8D1	7, 28 and 90	0	S1

3 Results and Discussion

3.1 Fresh Properties

The fresh state behaviour of the mixtures was characterized through slump tests with the Abrams cone. Table 3 shows the results obtained for the EAFS mixtures, with and without RTSF, as well for the reference mixture MR_N.

The use of a distribution module, $q = 0.15$, in the Andreasen and Andersen model, proved to be adequate, since the mixture EAFS 8D1 has shown a good fresh behaviour in similitude to the reference mixture MR_N. Moreover, as expected the addition of fibres to fresh concrete resulted in a loss of workability being this type of FRC characterized as a dense concrete, since its slump was equal to zero.

3.2 Hardened Properties

Compressive behaviour. Table 4 shows the results of the uniaxial compression tests, including the average and characteristic compressive strengths, f_{cm} and f_{ck}, respectively, as well the elasticity modulus, E_{cm} at 7, 28 and 90 days. The characteristic compressive strengths were obtained according to NP EN 206-1 [24]. The coefficients of variation obtained for the parameters analysed were quite low, varying between the range of 0.02–0.05 and 0.02–0.07 for the average compressive strengths and elasticity modulus, respectively.

Table 4 Results of the mechanical properties obtained for the reference mixture MR_N and for the concrete designed mixtures developed with EAFS and RTSF

Mixtures	f_{cm} (MPa)			f_{ck} (MPa)	Strength class	E_{cm} (GPa)		
	7 days	28 days	90 days			7 days	28 days	90 days
MR_N	18.40	27.37	35.85	24.10	C20/25	24.58	27.01	30.14
EAFS 8D1	15.40	29.22	36.82	25.22	C25/30	29.70	36.04	36.82
0.5FRC_EAFS 8D1	13.60	25.09	31.64	21.09	C20/25	30.07	37.37	36.74

Table 5 Results of the residual mechanical properties obtained for the reference mixture MR_N and for the concrete designed mixtures developed with EAFS and RTSF

Mixtures	$f_{cm,res}$ (MPa)			$\varepsilon_{cm,res}$ (‰)		
	7 days	28 days	90 days	7 days	28 days	90 days
MR_N	6.07	9.00	11.67	6.40	5.74	5.25
EAFS 8D1	5.06	9.58	12.18	6.54	6.11	5.06
0.5FRC_EAFS 8D1	4.18	8.26	10.44	14.83	11.74	9.58

Table 5 shows the results for average residual compressive strengths and strains, $f_{cm,res}$ and $\varepsilon_{c,res}$, respectively. The average residual compressive strengths were defined for 1/3 of the peak strength in the post peak phase and the average residual strains were obtained for the correspondent residual strengths.

The reference mixture, MR_N, strength class was C25/30 and a S4 slump class. Although MR_N strength class proved to be below expectations, this could be explained by the distinct conditions in which the concrete batches were produced at the Laboratory of Structures at University of Minho (LEST). Nonetheless, it should be highlighted that the designed compositions were compared using a common set of mixing and testing conditions.

As shown in Table 4, mixture EAFS 8D1 complied with the reference mixture in terms of strength capacity, being the strength class C25/30. Analysing the elasticity modulus at 28 days of EAFS 8D1 (Table 4), it was verified that it was higher than the average elasticity modulus defined by Eurocode 2 [25], i.e. 31 GPa for a C25/30 strength class. Thus, according to the characteristics so far analysed, the EAFS 8D1 mixture accomplished the requirements predefined for the reference mixture MR_N.

As shown in Table 4, the reinforced mixture (0.5FRC_EAFS 8D1) reached a lower compressive strength than the non-reinforced concrete mixtures, i.e. EAFS 8D1 and MR_N. In fact, when compared to EAFS 8D1 mixture the compressive strength class dropped from C25/30 to C20/25, as a result of the reduction in its characteristic compressive strength at 28 days of 4 MPa. The elasticity modulus remained practically similar for all ages analysed when both mixtures are compared (Table 4). The decrease on the compressive strength can be justified by the significant amount of tyre rubber present in the recycled fibres used, which have a significant lower stiffness and higher Poisson coefficient than the cement paste and aggregates and consequently contributes to the decrease of the compressive strength. In contrast, Fig. 4 demonstrates the increased ductility in compression of the mixture 0.5FRC_EAFS 8D1. In fact, the reinforced EAFS mixture exhibited a mean residual strain value 2 times greater than the non-reinforced mixtures EAFS 8D1 and MR_N at 7, 28 and 90 days. At 7 days the increase of the average residual strains of 0.5FRC_EAFS 8D1 mixture compared to EAFS 8D1 mixture was 127%, at 28 days was 92% and at 90 days was 89%. Comparing the 0.5FRC_EAFS 8D1 mixture to the reference mixture MR_N the increase of the average residual strains at 7, 28 and 90 days was, correspondingly, of 132, 105 and 82% greater (Table 5). Although the fibre-reinforced mixture

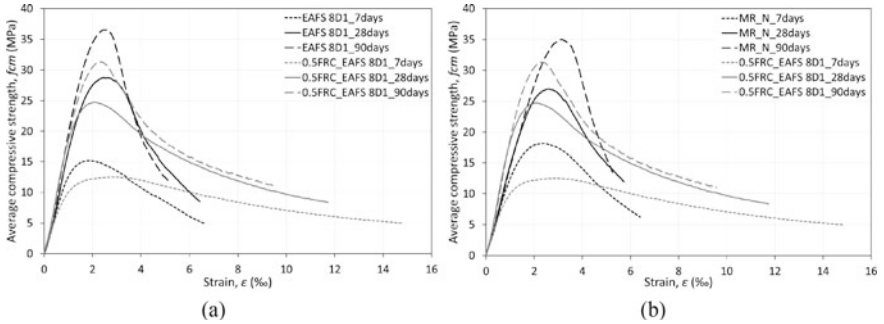

Fig. 4 Comparison of the average compressive strength curves for each curing age: **a** comparison of mixtures EAFS 8D1 with 0.5FRC_EAFS 8D1; **b** comparison of mixtures MR_N with 0.5FRC_EAFS 8D1

showed lower compressive strength, the incorporation of RTSF increased the ductile behaviour.

Tensile splitting strength and post-cracking behaviour. The tensile splitting test was performed for the reinforced concrete and for the reference mixture MR_N. Table 6 shows the tensile splitting tests' results for each specimen, namely, the average tensile splitting strength, f_{ctm}, the average displacement for maximum tensile splitting stress, $\delta_{fctm,max}$ and the average crack width for maximum tensile splitting stress, $w_{fctm,max}$. For each specimen, two cores extracted from the central region of the cylinder (see Sect. 2.2) were tested. The coefficients of variation obtained for the analysed parameters were low.

As presented in Table 6 it appears that the use of RTSF translated into a reduction of the tensile splitting strength of approximately 16%, when compared to the reference mixture, MR_N. However, when comparing the ductility, the 0.5FRC_EAFS 8D1 mixture proved to be quite advantageous, overcoming the fact of showing lower tensile splitting strength. As revealed in Fig. 5, the reference mixture MR_N showed a brittle behaviour, whereas the rupture mode of 0.5FRC_EAFS 8D1 mixture was characterized by a strain-softening behaviour.

The tensile splitting stress-crack width representative relationships can be seen in Fig. 6, where completely different performances between these two mixtures were observed. Reference mixture presented a brittle behaviour when rupture occurs, while

Table 6 Results of the tensile splitting tests obtained for the reference mixture MR_N and for the concrete designer mixture developed with RTSF at 28 days

Mixtures	f_{ctm} (MPa)			$\delta_{fctm,max}$ (mm)			$w_{fctm,max}$ (μm)		
	C1	C2	C3	C1	C2	C3	C1	C2	C3
MR_N	1.78	1.8	1.81	1.40	1.44	1.25	10.56	20.62	21.95
0.5FRC_EAFS 8D1	1.66	1.50	1.39	1.02	1.32	1.37	10.31	14.10	14.60

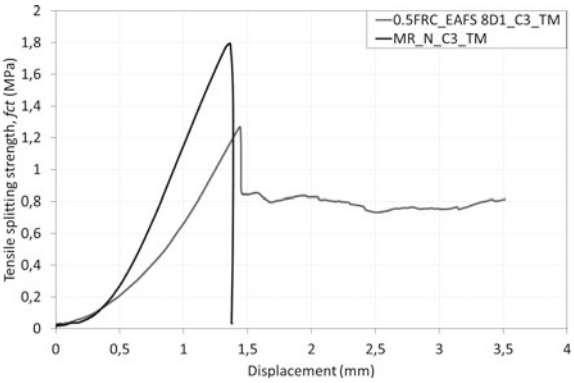

Fig. 5 Representative tensile splitting stress vs axial displacement curves for MR_N and FRC_EAFS mixtures at 28 days

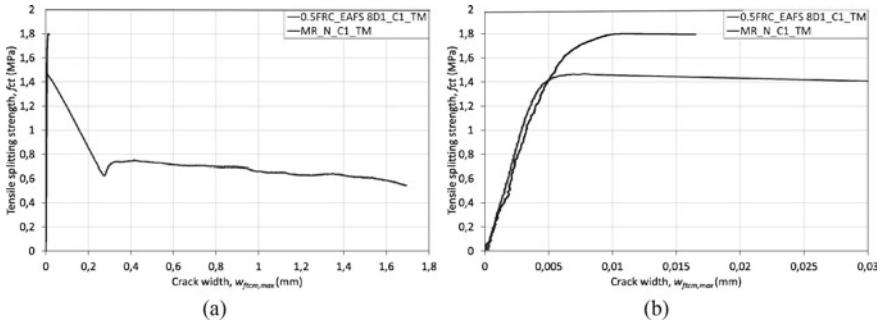

Fig. 6 Tensile splitting stress-crack width representative relationships for MR_N and FRC_EAFS mixtures at 28 days; **a** general crack width responses obtained; **b** crack width responses for smaller crack widths

0.5FRC_EAFS mixture 8D1 showed the ability to retain a significant residual tensile stress.

4 Conclusions

Changing the constituents of concrete may have environmental benefits, because it reduces the environmental impact and may have economic benefits; nevertheless, it can result in lower strengths and less durability compared to traditional concrete. Thus, it is necessary to balance all these factors in order to achieve an optimal equilibrium between the direct environmental benefit and the functionality of the structural concretes.

In the present research, a structural concrete mixture was developed with the incorporation of electric arc furnace slag (EAFS) aggregates and fly ash (FA) having in consideration a conventional concrete mixture, MR_N. Additionally, the incorporation of RTSF in the EAFS mixture was carried out. By using the modified Andreasen and Andersen particle-packing model it was possible to optimize the quantities of materials for an EAFS concrete mixture with the highest compactness and strength capacity, according to the predefined requirements of reference mixture MR_N. The main conclusions of EAFS structural concrete are:

(1) The EAFS 8D1 concrete mixture can be described as a potentially sustainable structural concrete due to the replacement of a large parcel of its natural constituents with large quantities of industrial by-product aggregates, whose replacement percentages are around 70% of EAFS aggregates and 10% of FA fine powder.
(2) C20/25 and C25/30 strength classes were obtained for the 0.5FRC_EAFS 8D1, EAFS 8D1 and MR_N mixtures, which represented a difference in its characteristic compressive strength at 28 days ranging from 3 to 4 MPa. However, this difference was not very significant because the 0.5FRC_EAFS 8D1 mixture reached mean residual strain values 2 times greater than the non-reinforced mixtures EAFS 8D1 and MR_N, resulting in an increase in its ductility that somewhat compensates the reduction in both tensile and compressive strengths.
(3) The significant relative amount of tyre rubber present in this type of recycled fibres has likely resulted in the decrease of 0.5FRC_EAFS 8D1 mixture compressive and tensile strengths. However, the reductions observed were not significant, considering the added value associated to the possibility of applying the tire waste directly and without further treatment, which would imply the reduction of the energetic and resources efficiency of the mixture.

Acknowledgements The first author thanks FCT (Fundação para a Ciência e a Tecnologia) for the scholarship with the reference number SFRH/BD/135790/2018, DST company and to the project "Next generation monitoring of coastal ecosystems in a scenario of global change", NORTE-01-0145-FEDER-000032, that was co-funded by Fundo Europeu de Desenvolvimento Regional (FEDER), with Programa Operacional Regional do Norte (NORTE2020).

References

1. Torgal, F.P., Jalali, S.: Sustentabiliade - Tendências para a sustentabilidade dos materiais de construção. Engenharia e Vida, pp. 2–5 (2008)
2. Eurostat—Statistics Explained, Material flow accounts—flows in raw material equivalents. Eurostat—Statistics Explained (2016). http://ec.europa.eu/eurostat/statistics-explained/index.php/Material_flow_accounts_-_flows_in_raw_material_equivalents. Accessed 28 Mar 2017
3. Eurostat—Statistics Explained, Industry and construction statistics—short-term indicators. Eurostat—Statistics Explained (2017). http://ec.europa.eu/eurostat/statistics-explained/index.php/Industry_and_construction_statistics_-_short-term_indicators#Construction. Accessed 28 Mar 2017

4. Rodrigues, I.P.: Dissertação de Mestrado em Engenharia Civil - Ligantes de baixo impacto ambiental e baixo custo, baseados na ativação química de escórias de aciaria. Escola de Engenharia da Universidade do Minho (2015)
5. Yu, R., Spiesz, P., Brouwers, H.J.H.: Development of an eco-friendly Ultra-High Performance Concrete (UHPC) with efficient cement and mineral admixtures uses. Cem. Concr. Compos. **55**, 383–394 (2015)
6. Torgal, F.P., Jalali, S.: Eco-eficiência dos materiais de construção. Revista da Associação Portuguesa de Empresas de Betão Pronto, pp. 48–55 (2010)
7. Pacheco, A.: Dissertação de Mestrado em Engenharia Civil-Estudo da viabilidade da utilização de escórias de aciaria (ASIC) em betão denso, Faculdade de Engenharia da Universidade do Porto (2012)
8. Vu, H.M., Forth, J.P., Toropov, V.V.: The use of glycerol and cooking oil in masonry unit production. ICE Institution Civ. Eng. Publ., p. 14 (2015)
9. Aiello, M.A., Leuzzi, F.: Waste tyre rubberized concrete: properties at fresh and hardened state. Waste Manag **30**(8–9), 1696–1704 (2010)
10. Sousa Coutinho, A.: Fabrico e Propriedades do Betão. LNEC - Lab. Nac. Eng. Civ. **1** (1988)
11. S. (Grupo E. CPPE - Companhia Portuguesa de Produção de Electricidade, "Cinzas Volantes - Aplicações em Cimentos e Betões," Boletim da Sociedade Portuguesa de Química, Correntes de Despolorizção Termostimuladas, Mar-1995
12. Web Page: The balance small business. https://www.thebalancesmb.com/the-importance-of-tire-recycling-2878127. Accessed 29 Jan 2020
13. Pilakoutas, K., Neocleous, K., Dipl-ing, H.T., Inge, B.: Reuse of tyre steel fibres as concrete reinforcement. Eng. Sustain. **E53**, 131–138 (2004)
14. Fauzan, F., Sandi, R., Melinda, A.P.: The effects of steel fibers extracted from waste tyre on concrete containing palm oil fuel ash. Int. J. GEOMATE **44**, 142–148 (2018)
15. Aiello, M.A., Leuzzi, F., Centonze, G., Maffezzoli, A.: Use of steel fibres recovered from waste tyres as reinforcement in concrete: pull-out behaviour, compressive and flexural strength. Waste Manag **29**, 1960–1970 (2009)
16. Andreasen, A.H.M., Andersen, J.: Über die Beziehung zwischen Kornabstufung und Zwischenraum in Produkten aus losen Körnern (mit einigen Experimenten). Kolloid-Zeitschrift **50**(3), 217–228 (1930)
17. Funk, J.E., Dinger, D.: Predictive Process Control of Crowded Particulate Suspensions: Applied to Ceramic Manufacturing. Springer, US (1994)
18. Husken, G.: A Multifunctional Design Approach for Sustainable Concrete—with Application to Concrete Mass Products. Eindhoven University of Technology, The Netherlands (2010)
19. Yu, R., Spiesz, P., Brouwers, H.J.H.: Mix design and properties assessment of Ultra-High Performance Fibre Reinforced Concrete (UHPFRC). Cem. Concr. Res. **56**, 29–39 (2014)
20. Yu, R., Tang, P., Spiesz, P., Brouwers, H.J.H.: A study of multiple effects of nano-silica and hybrid fibres on the properties of Ultra-High Performance Fibre Reinforced Concrete (UHPFRC) incorporating waste bottom ash (WBA). Constr. Build. Mater. **60**, 98–110 (2014)
21. Yu, R., Spiesz, P., Brouwers, H.J.H.: Static properties and impact resistance of a green Ultra-High Performance Hybrid Fibre Reinforced Concrete (UHPHFRC): experiments and modeling. Constr. Build. Mater. **68**, 158–171 (2014)
22. EN 12350-2, "EN 12350-2," in Testing fresh concrete—Part 2: slump-test, European Standard, p. 8 (2009)
23. EN 12390, "EN 12390," in Testing hardened concrete, European Standard (2009)
24. NP EN 206-1, "NP EN 206-1," in Betão - Parte 1: Especificação, desempenho, produção e conformidade, CEN (Comité Europeu de Normalização), p. 84 (2007)
25. EN 1992-1-1, "EN 1992-1-1," in Design of concrete structures—Part 1-1: general rules and rules for buildings, European Standard, p. 230 (2004)